

Important Notice

This copy may be used only for the purposes of research and private study, and any use of the copy for a purpose other than research or private study may require the authorization of the copyright owner of the work in question. Responsibility regarding questions of copyright that may arise in the use of this copy is assumed by the recipient.

UNIVERSITY OF CALGARY

An Investigation of the Role of Low Frequencies in Seismic Impedance Inversion

by

Heather Jeanne Eileen Lloyd

A THESIS

SUBMITTED TO THE FACULTY OF GRADUATE STUDIES
IN PARTIAL FULFILMENT OF THE REQUIREMENTS FOR THE
DEGREE OF MASTER OF SCIENCE

DEPARTMENT OF GEOSCIENCE

CALGARY, ALBERTA

JUNE, 2013

© Heather Jeanne Eileen Lloyd, 2013

Abstract

Acoustic seismic impedance inversion is investigated using a migrated, stacked, reflectivity image. Basic inversion formulae are derived and sensitivity to the bandwidth of the reflectivity is analyzed. It is shown that high frequencies are responsible for the detail in the impedance image and low frequencies are responsible for the trend, where the low frequencies must be acquired from an external data type.

External data must be matched to the reflectivity image. Methods for data amplitude balancing and phase rotation are discussed. A Hilbert envelope calibration algorithm is designed to calibrate the time-depth curves between the seismic reflectivity and the external data. Both the use of well logs and stacking impedances are explored, and while well logs produce the most accurate images, a combination of the two types is also acceptable. Inversions are sensitive to the amount of external data that is added and reliable impedance images can be produced by using just 1.5-2.5 Hz of the external data.

Acknowledgements

First, I would like to thank my supervisor Dr. Gary Margrave for all of his guidance support and wisdom. In my undergrad, he convinced me that writing a thesis was simple and that all I had to do was write CREWES reports every year and each one could simply be turned into a chapter. He lied. However, my graduate program was a rewarding and valuable experience. I could not have asked for a better supervisor throughout this degree. Thank you for everything.

I would like to acknowledge all of the academic guidance I received from professors at the University of Calgary and the associated faculty of CREWES. Thank you to Dr. Larry Lines for his advice on my 701 and for all his other insight during CREWES technical talks as well as agreeing to be on my defense committee. I would like to thank Dr. Kris Inannen for his guidance on my 701 and suggestions during technical talks. Thank you to Dr. Don Lawton for his conversations on carbon dioxide sequestration. Thank you to Dr. Brian Russell for his suggestions on well tying. I would also like to thank Dr. Ian Gates for agreeing to be my external examiner and posing thought-provoking questions during my defense.

I would like to express my great appreciation to Roy Lindseth. It is not common that you get to meet the person who invented the topic that you are working on. I not only have had the privilege of meeting Roy, but I also had the privilege of working with him and, without his insight, this thesis would not have been possible.

I am grateful to CREWES sponsors and Carbon Management Canada for their financial support. I would like to thank Husky Energy, INOVA and Geokinetics for their assistance in acquiring the Hussar low-frequency data set, and thank you to PennWest for

the use of the Violet Grove well logs. Thank you to the SIS team at Schlumberger for my current employment and enabling me to complete my Masters Thesis.

I would like to thank all of the technical support staff at CREWES, especially Kevin Hall for not only his technical support on computers. He also took me under his wing to show me object oriented programming in MATLAB. Together we developed some useful MATLAB tools and, without him, I would have lost many days struggling with technical issues. I would like to thank Dr. Helen Isaac for her help in understanding the processing of the Hussar data, and Dr. Rolf Maier for his help with editing my thesis. Thank you to Malcolm Bertram for making experiences in the field entertaining and Kevin Bertram for printing the never ending pile of posters that we needed for conferences.

I would especially like to thank Laura Baird for all of the hard work that she does at CREWES. Laura is basically responsible for making sure that CREWES runs like a well-oiled machine but she also she takes a personal interest in the student's well-being and tries to ensure that we have everything we need to succeed. Laura, our friendship is one of a kind, and thank you for not letting me quit when things got hard.

There are two fellow students who have been with me since my undergrad. Peter Gagliardi, who shared my geophysics classes with me and helped me work out any problems that I had with my data, an algorithm or MATLAB code. He is an incredible source of inspiration and a pleasure to work with him. I would also like to thank Keith Darcy who shared my geology undergrad, and kept me informed on all the new advances in science. We had a lot of fun and the summers camping and attempting to do geology field work.

I would like to thank all of my office mates and fellow students at CREWES and the University of Calgary for all of your helpful suggestions and comments during my time at the University. I would especially like to thank Dr. Faranak Mahmoudian, Jessie Arthur and Diane Lespinasse for all of our conversations on science and the fun we had during our conference travels. I'd also like to thank Steve Kim, Chris Bird, Vanja Vracar, Patricia Gavotti, Melissa Hernandez, Virginia Vera, Thalia Aspeslet, Mahdi Al-Mutlaq, Dawson Holloway and Glen Young for all of the science you have taught me.

I would like to thank my Auntie Chrystal, Uncle John and Auntie Tina for their support, encouragement and for believing in me. A special thank you to my sisters Kim and Crystal-Lynn for their cheering and helpfulness. Papa, you believed that I was going to be in school forever and now, with pride, I get to say I am done (at least for now). Thank you to all my family in northern BC, my family in Ontario and all my adopted family in southern Alberta for your support and encouraging words.

This thesis would not have been possible without the support at home and for that I would like to thank Al Stanford. He helped me whenever he could even if it was just to cook me a meal so that I could carry on. I appreciate everything he did for me.

*To Roy Lindseth, not only has your wisdom guided this thesis but I also have the privilege
of calling you a friend. Thank-you*

Table of Contents

Abstract	ii
Acknowledgements	iii
Table of Contents	vii
List of Tables	ix
List of Figures and Illustrations	x
List of Symbols, Abbreviations and Nomenclature	xxii
CHAPTER ONE: INTRODUCTION	1
1.1 Reflectivity and impedance	1
1.2 Bandlimited wavelet	4
1.3 Data processing required before inversion	12
1.4 Interpretation of impedance sections versus reflectivity sections	23
1.5 History of Impedance Inversion	25
1.6 Overview of Chapters	27
1.7 MATLAB Software and Development	28
1.8 Original Contributions	28
CHAPTER TWO: HUSSAR FIELD EXPERIMENT	31
2.1 Introduction	31
2.2 Data Processing	33
2.3 Well Preparation	36
2.4 Well Ties	40
2.4.1 Well Tying experiment	40
2.4.1.1 Introduction	40
2.4.1.2 Time-depth curves without Check-shots or VSP data	42
2.4.1.3 Creating Synthetic Reflection Coefficients	44
2.4.1.4 Wavelet Estimation	48
2.4.1.5 Why phase rotations are needed in inversion processing	50
2.4.2 Hussar Well Ties	57
2.5 Final Results	65
2.6 Summary	66
CHAPTER THREE: BLIMP METHOD FOR INVERSION	68
3.1 Introduction	68
3.2 Theory	69
3.2.1 New method for calculating the scaling factor	74
3.2.2 BLIMP low-frequency input	77
3.3 Low-frequency data type: well logs	80
3.3.1 Qualitative analysis of impedance images	80
3.3.2 Low-frequency cut-off determination	83
3.4 Low-frequency data type: stacking velocities	93
3.4.1 Formatting stacking velocities to stacking impedance	93
3.4.2 Testing for optimal low-frequency cut off	103
3.4.3 BLIMP impedance inversions using stacking impedance	107
3.5 Low-frequency data type: combination of well logs and stacking velocities	110

3.6 Summary	119
CHAPTER FOUR: TIME-LAPSE CO ₂ STUDY	121
4.1 Introduction.....	121
4.2 Violet Grove CO ₂ Sequestration Model	122
4.2.1 Area Background.....	122
4.2.2 Well Preparation.....	123
4.2.3 Gassmann Fluid-Substitution	129
4.2.3.1 Theory.....	129
4.2.3.2 Methodology.....	133
4.2.4 Synthetic-Seismic production.....	138
4.3 Inversions Using BLIMP	143
4.3.1 Introduction	143
4.3.2 Supercritical Carbon Dioxide Model.....	144
4.3.3 Gaseous Carbon Dioxide Model	148
4.4 Inversions Using Low-Frequency Data	152
4.5 Model of A Thin Cardium Reservoir.....	156
4.6 Summary.....	158
CHAPTER FIVE: CONCLUSIONS	160
REFERENCES	164
APPENDIX A: MATLAB WELL-TYING PROGRAMS	169
A.1. Introduction.....	169
A.2. WaveletEstimator.....	169
A.3. StretchWell	171
A.4. EnvelopeMatch	174

List of Tables

Table 2.1: The match interval calibration data used for the Hilbert envelope well matching method.....	57
Table 2.2: Goodness of fit measurements for phase rotated data. Θ_I represents phase rotations made using individual well comparisons. Θ_A represents rotations using the average phase rotations and Θ_{LS} represents using the rotations calculated by the least squares method.	60
Table 3.1: Percent errors calculated between filtered impedance logs and inversions for various low-frequency cut offs. The percent errors are calculated for four, 200 millisecond time windows.	119
Table 4.1: Bulk modulus and density properties of fluids and minerals in the Cardium formation.....	135

List of Figures and Illustrations

Figure 1.1: When a source emits energy into the subsurface a wave is formed. When the wave crosses a layer boundary some of the energy is returned to the surface in the reflected wave and the rest of the energy continues downward through the next layer in the transmitted wave.	4
Figure 1.2: The effect of a dynamite source, 10Hz geophone and attenuation ($Q=50$) on a signal. The dynamite source signal is depicted in black with the damping effect of the geophone shown in grey. As deeper reflections are recorded at greater travel times, the amount of high frequency signal is reduced due to attenuation. For this example the signal band decreases from 150Hz at 0.5 seconds to 50 Hz at 2 seconds.....	6
Figure 1.3: The effect of a Vibroseis source, 10Hz geophone and attenuation ($Q=50$) on a signal. The Vibroseis sweep was between 10 to 100 Hz and is depicted in black with the damping effect of the geophone shown in grey. As deeper reflections are recorded the amount of high frequency signal is reduced due to attenuation. For this example the signal band decreases from 100Hz at 0.5 seconds to 50 Hz at 2 seconds.....	7
Figure 1.4: Impedance inversions using various wavelet bandwidths. The black curve is the true impedance and the red curve is the inversion using the trace integration formula (Equation 1.5).....	11
Figure 1.5: Impedance inversions testing the low end of the bandwidth. The black curve is the true impedance where the red curve is the inversion result. This trace continues to 2000 seconds which ensures a sample rate of 0.005 in the frequency domain.....	11
Figure 1.6: Basic processing flow needed for inversion.....	13
Figure 1.7: Raw shot record of Hussar data. Color limits have been adjusted to show seismic events.	15
Figure 1.8: Fully processed Hussar data with time variant amplitude balancing and time variant phase rotations. The preparation of the Hussar seismic data is discussed in Chapter 2.	15
Figure 1.9: Inversions for data with signal to random noise ratios ranging from one to eight. The black curve is the true impedance and the red curve is the inversion result.....	17
Figure 1.10: Inversions for primary reflection data, primaries plus multiples data, primary data scaled by a constant scale factor of 0.75, and primary data with AGC applied. The black curve is the true impedance and the red curve is the inversion result. For Panel C, the reflection coefficients were scaled by a factor of 0.75 before the impedance inversion was computed. For Panel D, the	

operator length for the AGC was 750 ms, and was scaled by a factor of 0.44 which was the maximum reflection coefficient.	17
Figure 1.11: When the seismic is not zero phase the inversions that are produced are incorrect. Black is the true impedance and red is the inversion result.	20
Figure 1.12: Example of a point diffraction hyperbola being migrated to produce the point diffractor.	22
Figure 1.13: A) A wedge model in impedance, B) the wiggle trace display of the seismic produced from the wedge model. C) the variable density display of the seismic, D) the impedance inversion result. (Modified from Latimer et al, 2000).....	24
Figure 1.14: A) stacked channel model in impedance, B) the wiggle trace display of the seismic produced from the stacked channel model. C) the variable density display of the seismic, D) the impedance inversion result.....	25
Figure 2.1: Location of the seismic line area near Hussar, Alberta, Canada indicated by the red marker.	32
Figure 2.2: The location of the line and wells. The color scale shows the common midpoint number.	33
Figure 2.3: Seismic after processing and migration. The shallow section have lower amplitudes than seen else in the section and in the well logs. A synthetic seismogram from well 14-27 is plotted on each side of the section, separated by dashed lines to show that the amplitudes in the upper section are low.....	35
Figure 2.4: Seismic after time variant balancing using well 14-27. A synthetic seismogram from well 14-27 is plotted on each side of the section, separated by dashed lines, to show how the amplitudes in the upper section were restored by using time variant scaling.	35
Figure 2.5: Well logs for well 12-27 including the p-wave velocity log, density log both of which are shown with the overburden and underburden applied and the gamma ray log.....	37
Figure 2.6: Well 14-27 p-wave velocity and density log with overburden and underburden applied as well as the gamma ray log.	38
Figure 2.7: Well 14-35 showing the p-wave velocity log and density log both of which have an overburden and underburden applied. The gamma ray log is also shown.	39
Figure 2.8: Hilbert envelopes of the synthetic and seismic traces before and after matching.....	43
Figure 2.9: Synthetic and trace matching using the Hilbert envelope method.	44

Figure 2.10: The velocity, density and attenuation values for the 10 layer model.	46
Figure 2.11: Original sonic log, sonic adjustment and calibrated sonic log, used to compute synthetic seismograms for well ties.	46
Figure 2.12: Well ties for the stretched sonic log method (left) and the altered time- depth curve method (right) compared to the real seismic trace (middle).	47
Figure 2.13: The cross-correlation plot for each method. The ideal method would have the largest maximum with the smallest shift from zero.	47
Figure 2.14: Reflectivity, signal and deconvolution using stationary methods.	52
Figure 2.15: Reflectivity, signal and deconvolution using nonstationary operators.	52
Figure 2.16: Phase rotations calculated for the stationary and nonstationary case. The yellow zone indicates the design window for the deconvolution.	53
Figure 2.17: Signal at 1 seconds that shows the signal before and after phase rotations for both the stationary and nonstationary trace. The black signal is a zero phase band limited trace, which represents the ideal bandlimited solution.	53
Figure 2.18: Reflectivity, signal and deconvolution using stationary methods.	55
Figure 2.19: Reflectivity, signal and deconvolution using nonstationary methods.	55
Figure 2.20: Phase rotations calculated in 200 ms windows centered at each strong event and then calculated for a set of 200 ms gaussian windows.	56
Figure 2.21: Signal at 1 second that shows the signal before and after phase rotations for both the stationary and nonstationary trace. The black signal is a zero phase band limited trace, which represents the ideally bandlimited solution.	56
Figure 2.22: Seismic and synthetic well ties after Hilbert envelope matching process.	58
Figure 2.23: Time variant phase rotations calculated for each trace-well pair and the average of the three, as well as the least squares solution. well 12-27 corresponds to trace 848, well 14-27 corresponds to trace 681 and well 14-35 corresponds to trace 266.	61
Figure 2.24: Well ties and Phase rotated seismic traces using phase angles calculated at each well location.	62
Figure 2.25: Well ties and phase rotated seismic traces using the average phase angles.	63
Figure 2.26: Well ties and phase rotated seismic traces using the least squares calculated phase angles	64

Figure 2.27: Time variant phase rotated seismic, with the average well synthetic trace plotted on both sides for comparison.	65
Figure 2.28: Final corrected seismic section and well ties.	66
Figure 3.1: The low frequencies from a well log can be added to the seismic frequencies that have been integrated by the recursion formula to obtain an impedance inversion.	69
Figure 3.2: Impedance log before and after the linear trend is removed.	70
Figure 3.3: Seismic trace and the Pseudo-Impedance calculated using the recursion formula for a bandpass filter starting at 4.5 Hz to 75 Hz.....	71
Figure 3.4: Integrated sonic and well impedance log before and after scaling.....	72
Figure 3.5: Integrated seismic and filtered well impedance are added together to form the impedance inversion without the linear trend. The low-frequency cut-off chose was 4.5 Hz.....	73
Figure 3.6: BLIMP impedance result with and without linear trend.	73
Figure 3.7: Various low-frequency data types with linear trends. The linear trend is a least squares fit to the data from 0 seconds to 4 seconds, so it does not always fit the data in the best way possible. For the well with the bad trend the linear trend was calculated from 200 to 600 ms.....	75
Figure 3.8: The frequency spectrum of the residual impedance data type. Data types with a bad linear trend have high power in the low frequencies where a linear trend with a good fit has lower in the low frequencies.	76
Figure 3.9: Scaling values calculated for various low-frequency scaling cut offs. Threshold values help stabilize the effect of a bad linear fit.	77
Figure 3.10: The contribution from the low-pass well contribution and linear trend. The blue curve is the impedance inversion. The red curve is the amplitude spectrum of the linear trend and the green curve contribution from the low-pass filtered log, filtered with a [0 0 5 10] low-pass filter. This has been zoomed in to show detail at the low frequencies. Both the impedance inversion and linear trend continue to an amplitude of 6.7×10^{10} at 0 Hz.	79
Figure 3.11: Panel A shows the true impedance in green and the low-pass filtered ([0 0 75 100] impedance log in black. Panel B shows an inversion where just the linear trend is used in blue and the low-pass filtered log in black. Panel C shows the inversion using the BLIMP method in red and the low-pass filtered impedance log in black.	79

Figure 3.12: This figure shows the effects of an impedance section when the low-frequency cut off is too low (0.5 Hz). Noise from the pump jack can be seen in the ellipse labeled A. The impedance values of the layers indicated by the ellipse labelled B are much higher than the impedance values from the well log. The well log used for the low-frequency contribution is shown on either side of the section and are separated by a dashed black line. Ellipse C indicates that the layers are not continuous for this section. Since these are strong reflections continuous reflectors would be expected.	81
Figure 3.13: This inversion has a cut-off that is a reasonable range (3 Hz). In Ellipse A there is slight pump jack noise. In Ellipse B the impedance values of the section are close to the impedance values of the well log that is shown on the sides of the inversion separated by the dashed lines. In Ellipse C the reflections are continuous.	82
Figure 3.14: This inversion shows a case where the low-frequency cut-off is too high. Ellipse A shows very slight noise from the pump jack located near trace 681. Ellipse B shows impedance values that are within the range of the well log shown on either side of the impedance section and separated by dashed black lines. Ellipse C shows where events not present in the seismic image but present in the well logs are starting to appear in the impedance section.	83
Figure 3.15: BLIMP impedance inversions using trace 848 and well 12-27 for various low-frequency cut offs. On the sides of the section is a low-pass filtered impedance log from well 12-27 for reference.	85
Figure 3.16: BLIMP impedance inversions using trace 681 and well 14-27 for various low-frequency cut offs. On the sides of the section is a low-pass filtered impedance log from well 14-27 for reference.	85
Figure 3.17: BLIMP impedance inversions using trace 266 and well 14-35 for various low-frequency cut offs. On the sides of the section is a low-pass filtered impedance log from well 14-35 for reference.	86
Figure 3.18: BLIMP impedance inversions using the average trace and average well impedance log for various low-frequency cut offs. On the sides of the section is a low-pass filtered average impedance log for reference.	86
Figure 3.19: The normalized difference between adjacent inversions. Inversion stability is found when the low-frequency cut-off between 3 and 4 Hz.	87
Figure 3.20: BLIMP impedance inversions using the average impedance well log for different frequency cut offs ranging from 1.5 Hz to 4Hz.	88
Figure 3.21: Impedance inversion calculated using well 12-27 and a low frequency cut-off of 2.5 Hz. Low-pass filtered impedance log from well 12-27 is displayed on the sides for reference.	89

Figure 3.22: Impedance inversion calculated using well 14-27 and a low frequency cut-off of 2.5 Hz Low-pass filtered impedance log from well 14-27 is displayed on the sides for reference.	89
Figure 3.23: Impedance inversion calculated using well 14-35 a low frequency cut-off of 2.5 Hz. Low-pass filtered impedance log from well 14-35 is displayed on the sides for reference.	90
Figure 3.24: Impedance inversion calculated using the average well impedance log and a low frequency cut-off of 2.5 Hz. Low-pass filtered average impedance log is displayed on the sides.	90
Figure 3.25: Cross validation plot that compares the inversion calculated using the impedance log from well 12-27 (Red) with the filtered well impedances (Black). Error is calculated in the interval from 0.2 seconds to 1.05 seconds.	91
Figure 3.26: Cross validation plot that compares the inversion calculated using the impedance log from well 14-27 (Red) with the filtered well impedances (Black). Error is calculated in the interval from 0.2 seconds to 1.05 seconds.	91
Figure 3.27: Cross validation plot that compares the inversion calculated using the impedance log from well 14-35 (Red) with the filtered well impedances (Black). Error is calculated in the interval from 0.2 seconds to 1.05 seconds.	92
Figure 3.28: Cross validation plot that compares the inversion calculated using the average impedance log (Red) with the filtered well impedances (Black). Error is calculated in the interval from 0.2 seconds to 1.05 seconds.	92
Figure 3.29: Stacking velocity picks made during processing. The picks have good time coverage at the zone of interest but poor spatial coverage. Each point is the location of the pick and the color refers to the stacking velocity at that pick.	94
Figure 3.30: A linear interpolation of the stacking velocity picks on a 25 ms by 250 meter grid. Linear interpolation can only interpret velocity points between picks so the white regions represent where there are no picks.	95
Figure 3.31: This shows the different interpolation methods available and their accuracy, The PCHIP approximation is the best choice as it follows the trend of the data in the lower times and does not overshoot at high times.	96
Figure 3.32: This figure shows the extrapolation results for three different methods when extrapolating the time direction (t-interp) and the horizontal direction (x-interp).	97
Figure 3.33: Extrapolated stacking velocities using the PCHIP method. The exaggerated elevation profile is shown to assess where residual statics could be affecting the stacking velocities.	98

Figure 3.34: Interval velocities calculated from smoothed stacking velocities using Dix (1955) equations.....	99
Figure 3.35: Gardner parameters determined by well logs for each set of tops.	100
Figure 3.36: Densities calculated using Gardner parameters and interval velocities.	101
Figure 3.37: Impedance section constructed from stacking velocities	101
Figure 3.38: Impedance inversion using a low-frequency cut off of 4 Hz, and using the stacking impedance section for low-frequency input. The filtered average impedance well log is located on the sides of the impedance section for reference.....	102
Figure 3.39: Mean stacking impedance which was calculated by averaging all stacking impedance traces and the preferred stacking impedance which was calculated by averaging traces 1 to 300 only.	103
Figure 3.40: BLIMP impedance inversions using average trace and the mean stacking impedance for various low-frequency cut offs. On the sides of the section is the low-pass filtered average impedance well log for reference.....	104
Figure 3.41: BLIMP impedance inversions using average trace and the preferred stacking impedance for various low-frequency cut offs. On the sides of the section is the low-pass filtered average impedance well log for reference.....	104
Figure 3.42: The normalized difference between adjacent inversions.	105
Figure 3.43: BLIMP impedance inversions using the preferred stacking impedance trace for different frequency cut offs ranging from 0.5 Hz to 3Hz. The filtered average impedance well log is displayed on both sides of the inversion for reference.....	106
Figure 3.44 : Impedance inversion calculated using the mean stacking impedance trace and a low frequency cut-off of 1 Hz. Low-pass filtered average impedance log is displayed on the sides.....	108
Figure 3.45: Impedance inversion calculated using the mean stacking impedance trace and a low frequency cut-off of 1 Hz. Low-pass filtered average impedance log is displayed on the sides.	108
Figure 3.46: Cross validation plot that compares the inversion calculated using the mean stacking impedance (Red) with the filtered well impedances (Black). Error is calculated in the interval from 0.2 seconds to 1.05 seconds.	109
Figure 3.47 : Cross validation plot that compares the inversion calculated using the preferred stacking impedance (Red) with the filtered well impedances (Black). Error is calculated in the interval from 0.2 seconds to 1.05 seconds.....	109

Figure 3.48: Preferred stacking impedance, average well impedance, and the combination impedance plotted with their linear trends. The combination trace is the average well impedance from 0 to 1.054 seconds and the mean stacking impedance from 1.054 seconds to 4 seconds. 1.054 seconds is the end of the well.....	111
Figure 3.49: Fourier transform of the preferred stacking impedance, average well impedance, and the combination impedance.	111
Figure 3.50: BLIMP impedance inversions using average trace and the preferred stacking impedance for various low-frequency cut offs. On the sides of the section is the low-pass filtered average impedance well log for reference.....	113
Figure 3.51: The normalized difference between adjacent inversions for the combination trace.....	113
Figure 3.52: BLIMP impedance inversions using the combination impedance trace for different frequency cut offs ranging from 0.5 Hz to 3Hz. The filtered average impedance well log is displayed on both sides of the inversion for reference.....	115
Figure 3.53: Impedance inversion calculated using combination impedance and a low frequency cut-off of 1.5 Hz. The filtered average impedance log is displayed on each side for reference.	116
Figure 3.54: Cross validation plot that compares the inversion calculated using the combination impedance (Red) with the filtered well impedances (Black). Error is calculated in the interval from 0.2 seconds to 1.05 seconds.	116
Figure 3.55: Impedance inversion calculated using combination impedance and a low frequency cut-off of 2 Hz. The filtered average impedance log is displayed on each side for reference.	117
Figure 3.56 Cross validation plot that compares the inversion calculated using the combination impedance (Red) with the filtered well impedances (Black). Error is calculated in the interval from 0.2 seconds to 1.05 seconds.	117
Figure 3.57: Impedance inversion calculated using combination impedance and a low frequency cut-off of 2.5 Hz. The filtered average impedance log is displayed on each side for reference.	118
Figure 3.58 Cross validation plot that compares the inversion calculated using the combination impedance (Red) with the filtered well impedances (Black). Error is calculated in the interval from 0.2 seconds to 1.05 seconds.	118
Figure 4.1: Well 102/08-14-48-9W5, with gamma ray, sonic and density logs, recorded from 308 m to 2220 m.	126

Figure 4.2: Well 102/07-11-48-9W5, with gamma ray, sonic and shear sonic recorded from 260m to 1670 m.	127
Figure 4.3: P-wave velocity and S-Wave linear relationships. The color bar indicates the depth of the log measurements. The Cardium formation is indicated by the red asterisk.	128
Figure 4.4: Volume of shale, p-wave velocity, s-wave velocity and density logs before and after the homogenous reservoir was created.	129
Figure 4.5: Fluid saturation for the three stages of field development. Phase 1- original fluids in place, Phase 2- after water injection, Phase 3- after carbon dioxide injection.....	134
Figure 4.6: Phase diagram for carbon dioxide. The Cardium formation plots in the supercritical phase. TP is the triple point where at this temperature and pressure solid, liquid and gaseous phases exist in equilibrium. CP represents the critical point where the carbon dioxide enters into the supercritical phase. (Modified from Bachu, 2000)	135
Figure 4.7: Velocity, density and impedance signatures in the Cardium reservoir for phase 1: original fluids, phase 2: water injection and phase 3: injection of supercritical carbon dioxide.....	137
Figure 4.8: Velocity, density and impedance (P-wave) signatures in the Cardium reservoir for phase 1: original fluids, phase 2: water injection and phase 3: injection of gaseous carbon dioxide.....	138
Figure 4.9: Log placement for creating the velocity and density model for the fluid substituted reservoir. P1 is the phase 1 logs that contain original fluids, P2 is the phase 2 logs which model the fluids after water injection, P3 is the phase 3 logs which model the fluids after the carbon dioxide injection.....	139
Figure 4.10: Impedance model using supercritical carbon dioxide. The horizontal grey lines near 1600m depth represent the top and bottom of the Cardium reservoir. If the carbon dioxide spread radially about the well bore this model would simulate the sequestration of about 58000 metric tonnes of supercritical carbon dioxide.....	140
Figure 4.11: Impedance model using gaseous carbon dioxide. The horizontal grey lines near 1600m depth represent the top and bottom of the Cardium reservoir. If the carbon dioxide spread radially about the well bore this model would simulate the sequestration of about 8200 metric tonnes of gaseous carbon dioxide.....	140
Figure 4.12: Synthetic seismic for supercritical model using a [8 10 50 125] zero phase Ormsby wavelet. The Cardium reservoir is located at about 1 second.....	141

Figure 4.13: Synthetic seismic for supercritical model using a [8 10 50 125] zero phase Ormsby wavelet. This has been zoomed in to view the Cardium reservoir in more detail at about 1 second.	141
Figure 4.14: Synthetic seismic for gaseous model using a [8 10 50 125] zero phase Ormsby wavelet. The Cardium reservoir is located at about 1 second.....	142
Figure 4.15: Synthetic seismic for gaseous model using a [8 10 50 125] zero phase Ormsby wavelet. This has been zoomed in to view the Cardium reservoir in more detail at about 1 second.....	142
Figure 4.16: True filtered impedance for the supercritical carbon dioxide model. The filtered impedance at 1500 meters is plotted on each side of the impedance section for reference.....	145
Figure 4.17: BLIMP inversion using the baseline impedance log and a low-frequency cut off of 9 Hz for the supercritical carbon dioxide model. The filtered baseline log is plotted at each side for reference.....	146
Figure 4.18: Cross validation plots for the baseline impedance log and a low-frequency cut off of 9 Hz for the supercritical carbon dioxide model. The black curve represents the true impedance and the red curve represents the inversion. Error is calculated between 0.8 and 1.2 seconds.....	146
Figure 4.19: BLIMP inversion using the monitor impedance log and a low-frequency cut off of 9 Hz for the supercritical carbon dioxide model. The filtered monitor log is plotted at each side for reference.....	147
Figure 4.20: Cross validation plots for the monitor impedance log and a low-frequency cut off of 9 Hz for the supercritical carbon dioxide model. The black curve represents the true impedance and the red curve represents the inversion. Error is calculated between 0.8 and 1.2 seconds.....	147
Figure 4.21: True filtered impedance for the gaseous carbon dioxide model. The filtered impedance at 1500 meters is plotted on each side of the impedance section for reference. The artifacts that are part of this section only appear in time and are pull down effects of the carbon dioxide plume.	148
Figure 4.22: BLIMP inversion using the baseline impedance log and a low-frequency cut off of 9 Hz for the gaseous carbon dioxide model. The filtered baseline log is plotted at each side for reference.	150
Figure 4.23: Cross validation plots for the baseline impedance log and a low-frequency cut off of 9 Hz for the gaseous carbon dioxide model. The black curve represents the true impedance and the red curve represents the inversion. Error is calculated between 0.8 and 1.2 seconds.....	150

Figure 4.24: BLIMP inversion using the monitor impedance log and a low-frequency cut off of 9 Hz for the gaseous carbon dioxide model. The filtered monitor log is plotted at each side for reference.	151
Figure 4.25: Cross validation plots for the monitor impedance log and a low-frequency cut off of 9 Hz for the gaseous carbon dioxide model. The black curve represents the true impedance and the red curve represents the inversion. Error is calculated between 0.8 and 1.2 seconds.....	151
Figure 4.26: Seismic data for the low-frequency gaseous carbon dioxide model. The wavelet used was a zero phase [1.5 2 50 125] Hz Ormsby wavelet.	153
Figure 4.27: True filtered impedance for the gaseous carbon dioxide model. The filtered impedance at 1500 meters is plotted on each side of the impedance section for reference. The artifacts that are part of this section only appear in time and are pull down effects of the carbon dioxide plume.	153
Figure 4.28: BLIMP inversion using the baseline impedance log and a low-frequency cut off of 2 Hz for the low-frequency gaseous carbon dioxide model. The filtered baseline log is plotted at each side for reference.	154
Figure 4.29: Cross validation plots for the baseline impedance log and a low-frequency cut off of 2 Hz for the low-frequency gaseous carbon dioxide model. The black curve represents the true impedance and the red curve represents the inversion. Error is calculated between 0.8 and 1.2 seconds.....	154
Figure 4.30: BLIMP inversion using the monitor impedance log and a low-frequency cut off of 2 Hz for the low-frequency gaseous carbon dioxide model. The filtered monitor log is plotted at each side for reference.	155
Figure 4.31: Cross validation plots for the baseline impedance log and a low-frequency cut off of 2 Hz for the low-frequency gaseous carbon dioxide model. The black curve represents the true impedance and the red curve represents the inversion. Error is calculated between 0.8 and 1.2 seconds.....	155
Figure 4.32: Seismic data for the thin Cardium reservoir. The wavelet used was a [3 5 100 125] Hz zero phase Ormsby wavelet. The Cardium reservoir is located at 1 second.	157
Figure 4.33: A close up of the seismic data showing the signature of the supercritical carbon dioxide plume.....	157
Figure 4.34: BLIMP inversion using the baseline impedance log and a low-frequency cut off of 4 Hz for the thin Cardium reservoir supercritical carbon dioxide model.....	158
Figure A.1: The interface for <i>WaveletEstimator</i> . The zone that is used in calculating the amplitude spectra from the trace is indicated in yellow on the left-hand side.	

The amplitude spectra of the seismic trace and the estimated wavelet are shown in top right-hand corner, and in decibels just below. The wavelet is shown in the bottom right-hand corner in time. In the center are the wavelet options. Each wavelet type is identified by a separate color, which can be seen in each of the displays. 170

Figure A.2: The interface of *StretchWell*. The synthetic seismogram is shown in blue and the seismic data is shown in red. The two sonic curves are shown in the upper left hand corner of the display. 174

Figure A.3: The *EnvelopeMatch* interface has several features including the ability to toggle modified sonic log display and the time-depth curve change display. The seismic Hilbert envelope is displayed in red while the synthetic seismogram Hilbert transform is displayed in dark blue..... 175

List of Symbols, Abbreviations and Nomenclature

Symbol	Definition
AEC	Automatic Envelope Correction
AGC	Automatic Gain Correction
API (GR)	Gamma Ray Units
API (Oil)	Oil gravity
BLIMP	BandLimited IMPedance inversion
CMP	Common midpoint
CREWES	Consortium of Research in Elastic Wave Exploration Seismology
EOR	Enhanced Oil Recovery
FWI	Full waveform inversion
GOR	Gas Oil Ratio
GR	Gamma Ray
Hz	Hertz, a unit of frequency
I	Impedance
Kg	Kilograms
m	Meters
ms	milliseconds
NMO	Normal Move-Out
Peaks	Positive reflection coefficients
P-wave	Compressional wave
Q	Attenuation
R	Reflectivity
RMS	Root mean squares
S	Seconds
SAIL	Seismic Approximate Impedance Log
S-wave	Shear wave
t	Time vector
Troughs	Negative reflection coefficients
V	Velocity
VD	Variable density display
V _p	P-wave or Compressional velocity
V _s	S-wave or shear velocity
VSP	Vertical Seismic Profile
WTVA	Wiggle trace variable area display
ρ	Density

Chapter One: **Introduction**

1.1 Reflectivity and impedance

The subsurface of the Earth can be modelled as a series of rock layers. These rock layers vary in thickness from centimeters to hundreds of meters. Each layer has unique properties including P-wave velocity, S-wave velocity and density. Both p-wave velocity and density are dependent on the amount of porosity or fluid filled space in the rock matrix (Sheriff and Geldart, 1995). Impedance, which is the product of p-wave velocity and density, is also dependent on the porosity of a rock layer.

Seismic exploration looks for rocks that contain hydrocarbons which usually have high porosity. Hydrocarbon filled rocks tend to produce lower impedances than similar rocks. If a picture of the subsurface could be obtained where lower impedances were identified then finding hydrocarbons could become easier. Currently it is only possible to directly measure rock properties in the subsurface at well locations. While these measurements do provide insight to the rocks in detail they do not show the structure of the subsurface. Seismic reflection surveys are a commonly used exploration method that produces an image of the subsurface. This type of survey measures reflection coefficients that are an interface property instead of a layer property. Reflection coefficients are related to impedance.

Consider a 1D earth with properties defined as a function of time. Let impedance be defined as a piecewise constant function

$$I(t) = I_k, t_k < t \leq t_{k+1}, k \in [0,1,2, \dots \infty], \quad 1.1$$

where t_k represents the time at the k th layer boundary and t_{k+1} represents the time at the next layer boundary. The times of the layer boundaries are not necessarily regularly

spaced. Typically, $t_0 = 0$, and it is assumed that $I = 0$ for $t < t_0$. As defined here, the impedance function represents a sequence of layers where each has a characteristic (constant) impedance. The reflectivity (r) is defined in terms of the impedance as

$$r(t) = \begin{cases} r_k = \frac{I_k - I_{k-1}}{I_k + I_{k-1}}, & t = t_k, k \in [1, 2, \dots, \infty] \\ 0, & \text{otherwise} \end{cases}. \quad 1.2$$

This gives the reflectivity, which is a time series of isolated spikes located at the layer boundaries. The magnitude of each spike is equal to the normal incidence reflection coefficient between the two impedance layers adjacent to the layer boundary. Since the reflectivity is at the layer boundaries there will be one less reflection coefficient than there are impedance layers. Equation 1.2 can be applied to the 3D earth if we assume that the waves have a normal incidence to the layer boundary. This assumption is appropriate for the most common seismic image, known as a “stack”. For other incidence angles the reflection coefficients are more complicated and need to be calculated using a different formula, which is given by Aki and Richards (2002).

The estimation of impedance from reflectivity data is called seismic impedance inversion. This can be done by either prestack using offset information, or poststack using the normal incidence assumption. This thesis will focus on poststack seismic impedance inversion. From Equation 1.2 impedance can be expressed in terms of reflectivity by

$$I_k = I_{k-1} \left(\frac{1+r_k}{1-r_k} \right). \quad 1.3$$

This is also known as the impedance recursion formula, as the next layer in the sequence is dependent on the impedance of the layer above it. Applying this formula recursively results in

$$I_k = I_0 \prod_{j=1}^k \left(\frac{1+r_j}{1-r_j} \right), \quad 1.4$$

where I_0 is the impedance at the surface. It is common for reflection coefficients to have magnitudes much less than one, therefore an approximation of $\frac{1+r_j}{1-r_j} \sim 1 + 2r_j \sim e^{2r_j}$ can be used for reflection coefficients less than 0.3 (eg. Oldenburg et al, 1983). By using this approximation Equation 1.4 then becomes

$$I_k = I_0 \prod_{j=1}^k e^{2r_j} = I_0 e^{2 \sum_0^k r_j}. \quad 1.5$$

If time intervals becomes infinitesimally small then Equation 1.2 can be rewritten as

$$r(t) = \frac{1}{2} \frac{dI}{I}(t) = \frac{1}{2} d \ln \left(\frac{I(t)}{I_0} \right), \quad 1.6$$

where \ln is the natural logarithm and the ratio $\frac{I(t)}{I_0}$ is required to ensure that the argument is dimensionless. Solving Equation 1.6 for impedance gives

$$I(t) = I_0 e^{2 \int_0^t r(t)} \quad 1.7$$

Equation 1.5 is commonly used to convert reflectivity into impedance and will be referred to as the trace integration formula because of the form it takes (Equation 1.7) in the limit of continuously changing impedance. To achieve accurate impedance results the reflection coefficients must be broadband in frequency. For seismic impedance inversions this is seldom possible as reflection coefficients from seismic data are bandlimited in frequency.

1.2 Bandlimited wavelet

During a reflection survey, a source of energy is used to create waves in the subsurface. When the waves reach a layer boundary, most of the energy continues downward but the rest reflects on the surface and moves back to the surface to be recorded by receivers (Figure 1.1). One type of receiver is called the geophone, which contains a mass on a spring mechanism that produces a voltage when displaced that is then recorded (eg. Evans,1997). The voltage produced for a given reflection is recorded at the elapsed time between when the source started to when the event was measured at the geophone. The receiver, source and the earth all affect the wave and remove important information that is needed to calculate an accurate impedance inversion. The result is a bandlimited seismic trace.

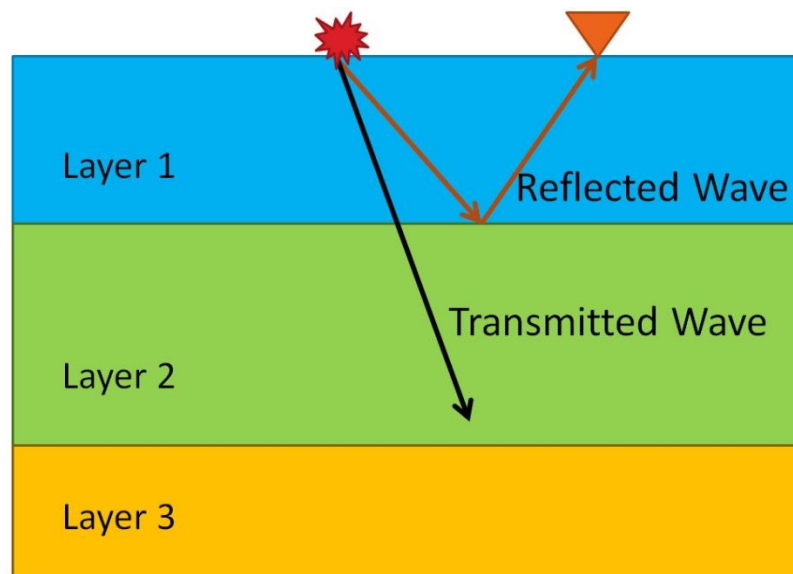


Figure 1.1: When a source emits energy into the subsurface a wave is formed. When the wave crosses a layer boundary some of the energy is returned to the surface in the reflected wave and the rest of the energy continues downward through the next layer in the transmitted wave.

While well measurements of rock properties can obtain a very broad bandwidth of frequency information for a localized area around the well, measuring a similar bandwidth of seismic reflection data is not typically possible. The seismic field system, including sources, receivers and recording instruments, is responsible for removing low frequencies from the signal, whereas earth effects, sources, and the recording system are responsible for removing (or not generating) the high-frequencies. Figure 1.2 shows the effects for a simulated dynamite source, where the dynamite source spectrum is based on observation rather than theory and is only meant to suggest a general case. The dynamite source has significant power for frequencies over 6 Hz, but declines rapidly for frequencies below 6 Hz. A geophone damping effect is also shown, which reduces the power of the signal for frequencies below the natural frequency (10 Hz in this case) of the geophone. This response can be modeled with a second order minimum-phase Butterworth filter, (Bertram and Margrave, 2010). The earth removes high frequencies through attenuation (Aki and Richards, 2002). This is shown with the wavelet that is recorded at various times. Each curve labelled with a time is the product of three things: geophone response, source spectrum, and an attenuation curve (discussed below). For shallow events more high-frequency data can be recorded and for deeper events more high-frequency data is attenuated and is not recorded. Figure 1.3 shows the amplitude versus frequency response of the signal when a Vibroseis source is used. Vibroseis sweeps have a start and a stop frequency, so the frequency of the source signal is inherently bandlimited. Hence, the seismic data that is recorded will be bandlimited, with no frequencies present below the start frequency or above the stop frequency of the sweep. The signal band is the range of data that is available for analysis; this is defined

as data that has signal power above the noise floor. Figure 1.2 and Figure 1.3 demonstrate that the signal band decreases for increasing depth or time.

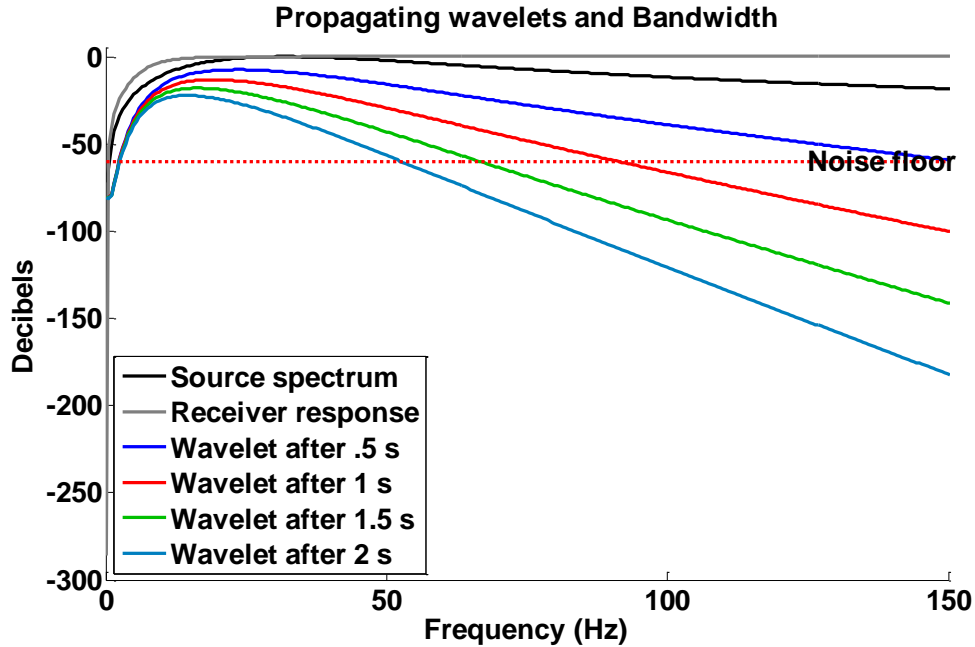


Figure 1.2: The effect of a dynamite source, 10Hz geophone and attenuation ($Q=50$) on a signal. The dynamite source signal is depicted in black with the damping effect of the geophone shown in grey. As deeper reflections are recorded at greater travel times, the amount of high frequency signal is reduced due to attenuation. For this example the signal band decreases from 150Hz at 0.5 seconds to 50 Hz at 2 seconds.

The choice of source is important in determining the bandwidth that is sent into the ground. Sources such as vibrator trucks are limited in the amount of low-frequencies they can produce. For light weight EnviroVibe trucks frequencies up to 8Hz can physically damage the truck (Hall et al., 2009), whereas for larger trucks the operating band of frequencies can be lower. Some enhanced vibrator trucks are made for low-frequency output but can still only operate as low as 1-2 Hz (Wei and Phillips, 2011). Dynamite is a better choice as it produces the most energy and the largest bandwidth of

all source types (Evans, 1997), but can be expensive and may not be permitted in certain areas.

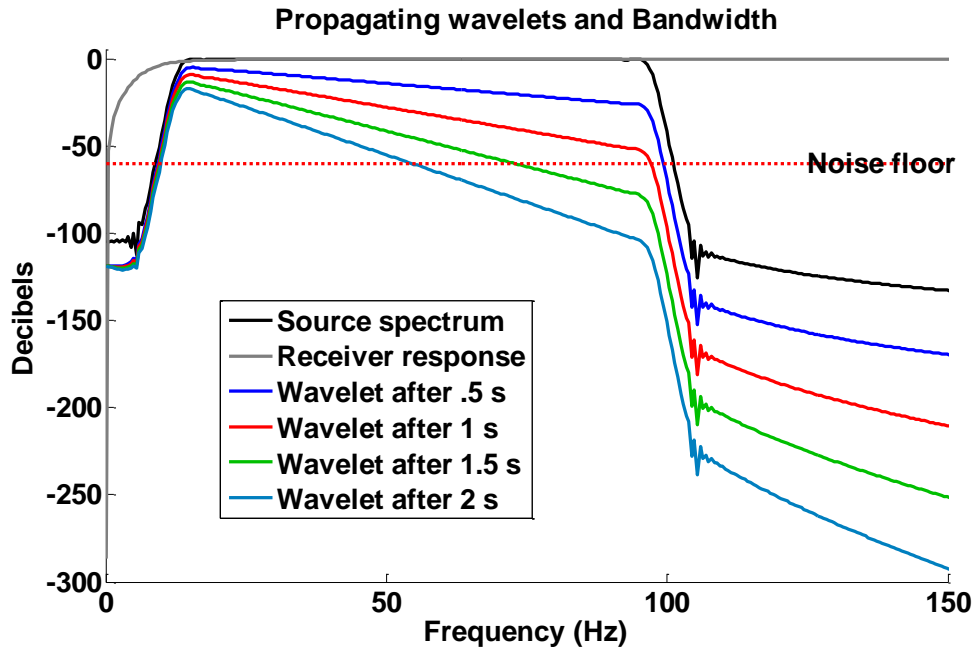


Figure 1.3: The effect of a Vibroseis source, 10Hz geophone and attenuation ($Q=50$) on a signal. The Vibroseis sweep was between 10 to 100 Hz and is depicted in black with the damping effect of the geophone shown in grey. As deeper reflections are recorded the amount of high frequency signal is reduced due to attenuation. For this example the signal band decreases from 100Hz at 0.5 seconds to 50 Hz at 2 seconds.

Even if it was possible to emit a full bandwidth source at high power we would not be able to record all the frequencies due to the limitations of the recording system. Geophones have a damping effect at low frequencies due to the resistance of their electrical components (Evans, 1997). Accelerometers, another type of receiver, suffer from $1/\text{frequency}$ noise which can mask weak signals in the low frequencies (Margrave et al, 2012). In 2011, Hall and Margrave observed that earthquakes do produce enough power at low frequencies to overcome the geophone dampening effect and $1/\text{frequency}$ noise. Unfortunately to produce the amount of energy that an earthquake does, a nuclear

bomb would be needed (Lowrie, 1997). Since explosions of that magnitude are very rarely used in surveying, it is unlikely that the damping effect of geophones can be sufficiently overcome by the power of a typical seismic survey source.

The high frequencies of the signal can be lost due to a process called attenuation which is always associated with velocity dispersion. There are two types of attenuation, the first being caused by intrinsic rock attenuation and consequent transference of seismic energy into heat and the second being an apparent attenuation caused by finely layered stratigraphic units (O'Doherty and Anstey, 1971). Attenuation always affects high frequencies more than low frequencies, thus reducing the amplitude of the signal unevenly. While there is no completely accepted theory for intrinsic attenuation, both effects can be approximately modelled as an exponential decay in both time and frequency (Aki and Richards, 2002). This relationship is

$$A_{t_1}(f) = A_{t_0}(f)e^{-\frac{\pi t_1 f}{Q}} \quad 1.8$$

where A_{t_1} is the amplitude spectrum of the wave after a time t_1 , A_{t_0} is the amplitude spectrum at time zero, f is the frequency, and Q is attenuation (eg. Aki and Richards, 2002). This relationship significantly reduces the amount of high frequency data that can be recorded. Stratigraphic velocity dispersion reduces the high frequencies in a different way. The high frequency component of the wave front has a shorter wavelength and reflects off of these boundaries whereas the low frequency component of the wave front, with a long wavelength, passes through the thin beds. This results in the high frequencies becoming delayed by random, chaotic amounts of time. These high-frequency wave fronts destructively interfere with one another causing an apparent

attenuation of the high frequencies (O'Doherty and Anstey, 1971). When recorded at the surface the signal looks the same as if it had been affected by an attenuative homogenous layer. There is no known way to separate intrinsic and apparent attenuation, so we will consider the combined affects as an effective attenuation.

The signal bandwidth after the attenuation of low and high frequencies that is imposed on the reflection coefficients is referred to as the wavelet amplitude spectrum. The wavelet phase spectrum is also important to the wavelet shape in the time domain. Ideally for easy interpretation, the wavelet should be zero phase, where the dominant energy of the wavelet is centered on the reflection coefficient location in time. For a Vibroseis source the phase of the wavelet is designed to be zero phase after correlation, but when mixed with minimum phase attenuation, becomes mixed phase (Margrave, 2010a). For an impulse source, such as dynamite, the wavelet is causal and is often modeled as minimum phase. A raw trace contains surface waves, spherical spreading, multiples, attenuation, noise, and reflectivity. To isolate the reflectivity as much as possible, surface waves, spherical spreading and multiples need to be removed from the raw trace data. Once this is accomplished the signal can be modelled by the convolutional model (Sheriff and Geldart, 1995).

$$S(t) = r(t) * w(t) + n(t) \quad 1.9$$

where $S(t)$ is the signal, $r(t)$ is the reflectivity, $w(t)$ is the wavelet and $n(t)$ is noise, and $*$ is a convolution.

Figure 1.4 shows the effect of different wavelets during impedance inversion using the trace integration formula (Equation 1.5). Using the full bandwidth (Figure 1.4 A) of the reflectivity produces the exact impedance solution. This impedance result is

ideal but would be impossible to obtain using seismic data. Using a wavelet for 7-50 Hz (Figure 1.4 B) produces a result that has inflections at the right points but does not correctly estimate the impedance layers. This impedance result shows the limitations of using seismic data alone. Using a wavelet for 7-250 Hz (Figure 1.4 C) produces a similar result to the 7-50 Hz wavelet but with sharper boundaries. The 0-50 Hz wavelet (Figure 1.4 D) produces an impedance result where the impedance layers are correct but the boundaries are not crisp. This impedance result would be similar to an impedance inversion computed using the seismic data and external low-frequency impedance data, such as well-log data or stacking velocities. This shows that the low frequencies are essential to producing an accurate inversion, and the high frequencies are essential to producing a precise and detailed inversion.

Recording as much low-frequency content as possible in seismic data is important so that when an impedance inversion is calculated it is not overly influenced by the external source of low frequencies. Even though all frequencies are important to the inversion, the most influential frequency is at zero Hertz. This is also known as the DC spike and is the average of the time domain series. Without the information provided by the DC spike, the impedance inversion will not be accurate. Figure 1.5 shows inversions using bandwidths that approach 0 Hz. Even seismic signals that include frequencies down to 0.01 Hz produce slight errors in the inversion. It is likely that the information contained in the DC spike will always have to be imported from well logs, velocity estimates or by other means.

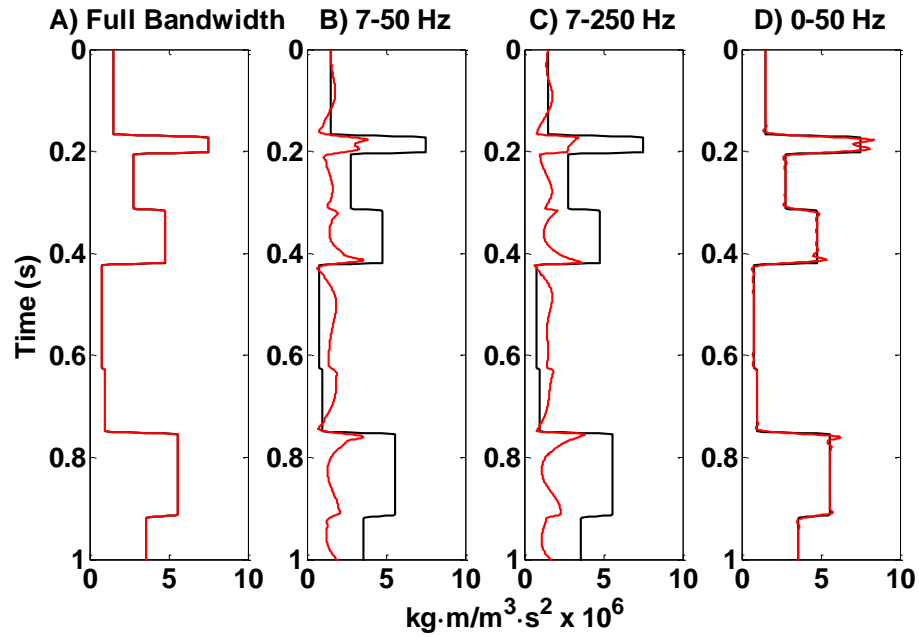


Figure 1.4: Impedance inversions using various wavelet bandwidths. The black curve is the true impedance and the red curve is the inversion using the trace integration formula (Equation 1.5).

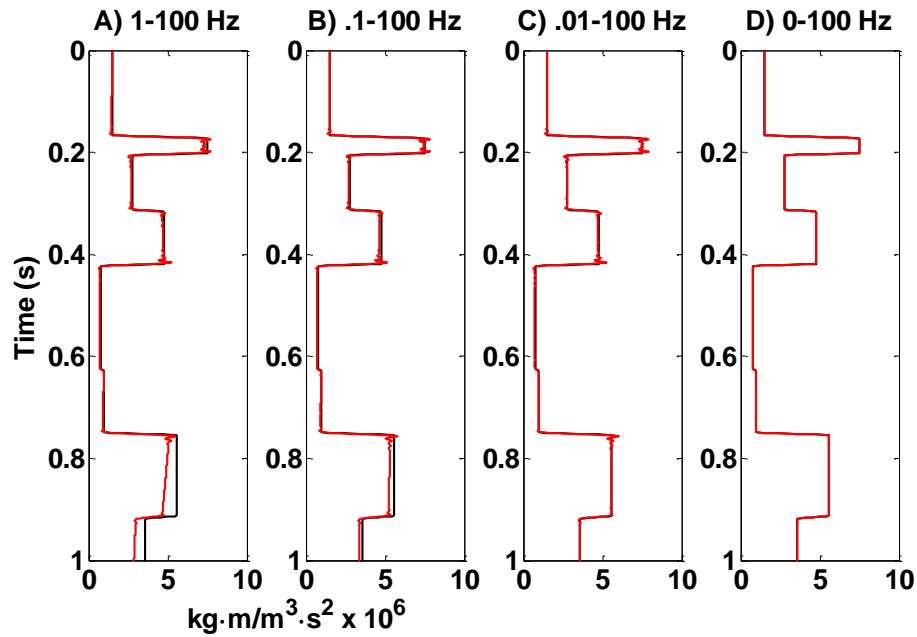


Figure 1.5: Impedance inversions testing the low end of the bandwidth. The black curve is the true impedance where the red curve is the inversion result. This trace continues to 2000 seconds which ensures a sample rate of 0.005 in the frequency domain.

1.3 Data processing required before inversion

Seismic data acquisition is often modeled to be very simple, where the wavelet is known, and the output is predictable. When actual seismic data is acquired it contains an abundance of complexities. Some of these complexities such as shot strength, receiver coupling, distance from the shot, and distance from the receiver can be compensated for by using geometrical spreading corrections and surface consistent methods (Yilmaz, 2001). Other complexities such as transmission loss and velocity dispersion require too much detailed information about the subsurface to be fully compensated for. Ideally, data should be processed for true amplitude recovery of the reflection coefficients. This is most likely impossible, especially when considering how complicated the subsurface is. What may be possible is to recover true relative amplitudes of the reflection coefficients. True relative amplitudes can be assumed to differ from true amplitudes by a constant scale factor, but sometimes the scale factor may need to be a time dependent function in order to accommodate for attenuation. Also, for acoustic impedance inversion the data needs to be normal incidence, which requires the use of post-stack data. The following basic processing flow (Figure 1.6) attempts to achieve true relative amplitude, normal incidence, and zero phase seismic data, as required to calculate satisfactory impedance inversions.

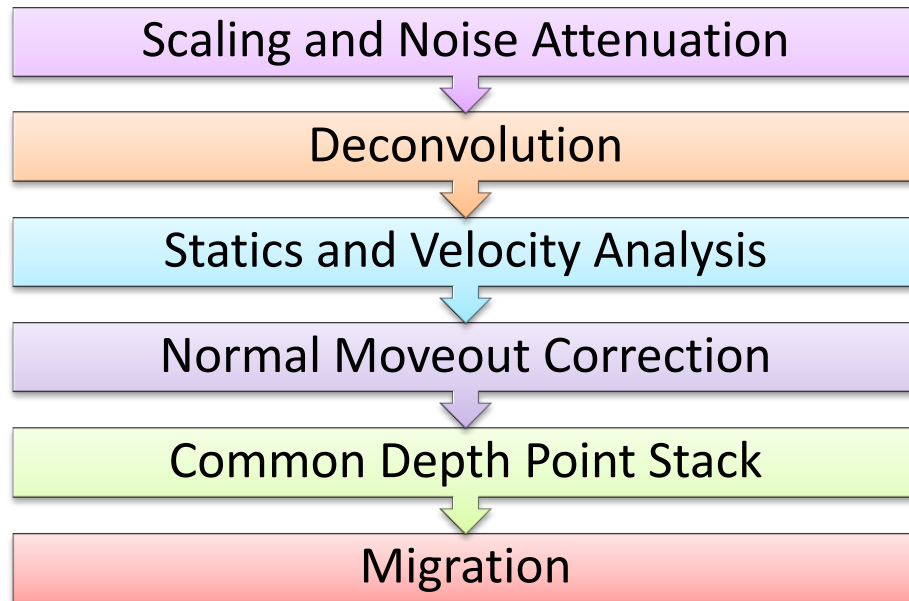


Figure 1.6: Basic processing flow needed for inversion.

The seismic processing required to convert raw seismic data (Figure 1.7) to an inversion ready state (Figure 1.8) requires a series of important steps (Figure 1.6). The first step is to remove as much noise as possible and scale the amplitudes of the reflections to remove the first-order effects of spherical spreading, transmission losses, and similar phenomena. Noise attenuation is incredibly important, as noise can interfere with the reflections. Some sources of noise include random noise such as wind, predictable noise such as the noise caused by power lines or pump jacks, coherent source generated noise such as ground roll, and coherent subsurface generated noise such as multiples and converted waves. All types of noise, if not removed appropriately, can cause errors in the inversion process. Often, a high-pass filter that removes low frequencies up to 10 Hz is applied to remove effects such as ground roll. This is problematic if an accurate impedance inversion is to be calculated after this processing.

Better noise attenuation methods need to be used to ensure the preservation of signal in the low frequencies while still reducing the amount of noise in the section. Examples include coherent noise attenuation methods and radial filtering (Henley, 2003). Figure 1.9 shows the effect on inversion of additive random noise for different signal-to-noise ratios. The random noise was generated using a random number generator with the same seed number for each signal to noise ratio. When the noise has the same power as the signal, the inversion is very poor, but when the signal to noise ratio is increased the inversion becomes more accurate.

Seismic reflection data contains both primary reflections as well as multiple reflections. Primary reflections occur when the wave front reflects off of a layer interface and travels to the surface where it is recorded. Multiple reflections occur when the wave front reflects off two or more layers in the subsurface before it is recorded at the surface. Multiples are usually fairly weak with respect to primary reflections, except in marine settings where strong multiples are produced between the water-air interface and the water-sea bottom interface. These marine multiples are strong as the amplitudes of the multiples are products of the reflection coefficients. The water-air boundary has a reflection coefficient of nearly -1 whereas the water-sea bed reflection coefficient has a coefficient greater than 0.3. Reflection coefficients at rock layer boundaries are usually less than 0.3 making the marine multiples stronger than most rock layer multiples. It is very important that the multiples are attenuated before impedance inversion as they act as reflection coefficients and produce inaccurate inversions as shown in Figure 1.10. Most short-path multiples are attenuated by deconvolution, while long-path multiples are attenuated by CMP (Common MidPoint) stacking.

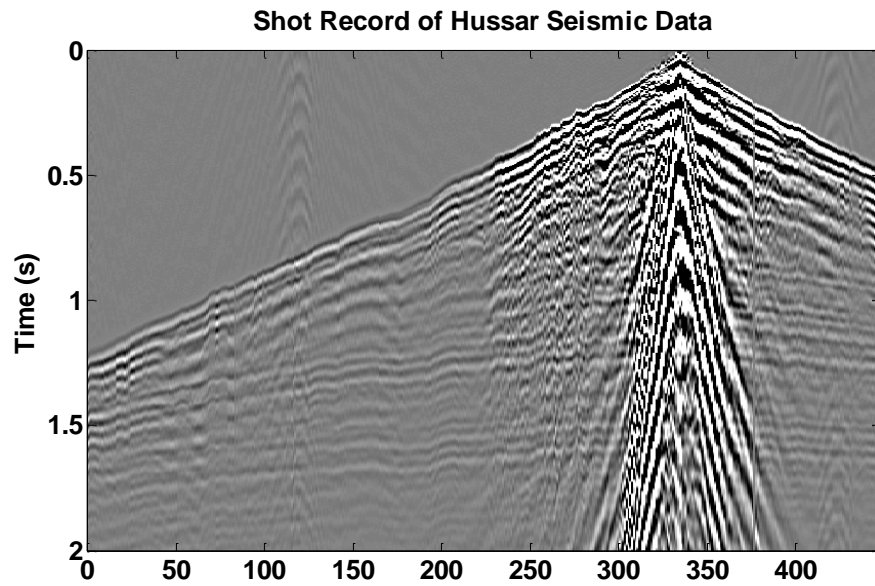


Figure 1.7: Raw shot record of Hussar data. Color limits have been adjusted to show seismic events.

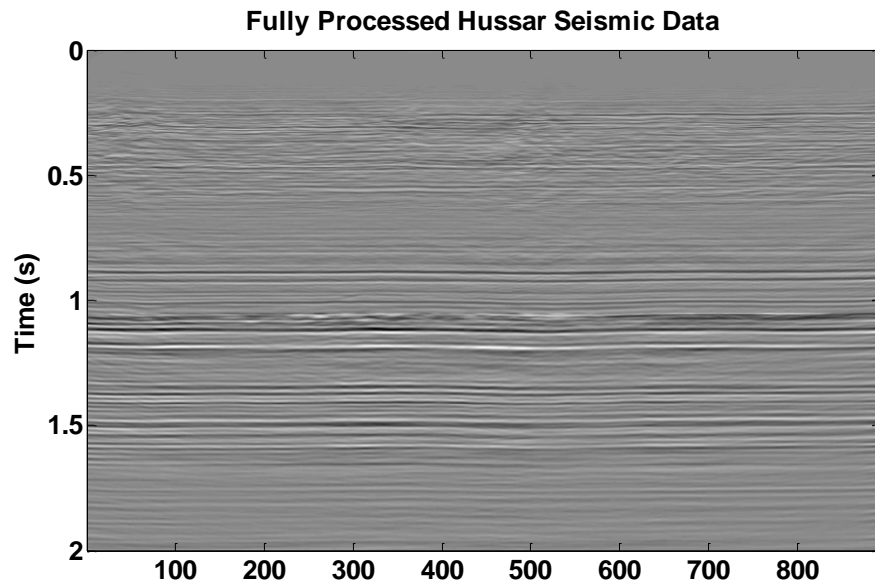


Figure 1.8: Fully processed Hussar data with time variant amplitude balancing and time variant phase rotations. The preparation of the Hussar seismic data is discussed in Chapter 2.

Amplitude scaling is also crucial to an accurate inversion. Figure 1.7 shows how unevenly the energy of the events is distributed on a raw seismic record. The high energy

events occur near the shot location and in noise such as ground roll. The desired events such as reflections have less energy. A scaling operator must be applied in order to boost the energy of the reflection events. An AGC (Automatic Gain Correction) is often used for this purpose. One type of AGC is the Automatic Envelope Correction (AEC). This method works by calculating the Hilbert envelope of the seismic trace, smoothing the envelope with a chosen smoother length, and then dividing by the envelope (Margrave, 2010a). A RMS (root mean squares) AGC works by calculating the RMS amplitude in a time window and then incrementing the time window by one time sample. This produces an amplitude model which the trace is then divided by (Yilmaz, 2001). Very different results are obtained depending on the width of the window (or the smoother length in AEC), also known as the operator length. For more physical results the operator length should be very long. Since this method is trying to equalize the amplitudes along the trace it is not respecting the true amplitudes of the reflectivity. Therefore using other scaling operators such as physics-based geometric spreading corrections, balancing or surface consistent scaling are better options.

Figure 1.10 shows an inversion where the amplitudes of the trace were not scaled correctly. The scaled primary result has a constant but incorrect scaling factor applied. All the events either overestimate or underestimate the impedance by the same factor. The inversion result with the AGC applied before inversion is similar to the true impedance but is not related by a simple scalar. Correcting these amplitudes would be difficult as a simple scalar or function would not fix these amplitude inconsistencies. This shows that even though an AGC can make seismic reflection data look good the amplitudes do not reflect the true amplitudes of the earth.

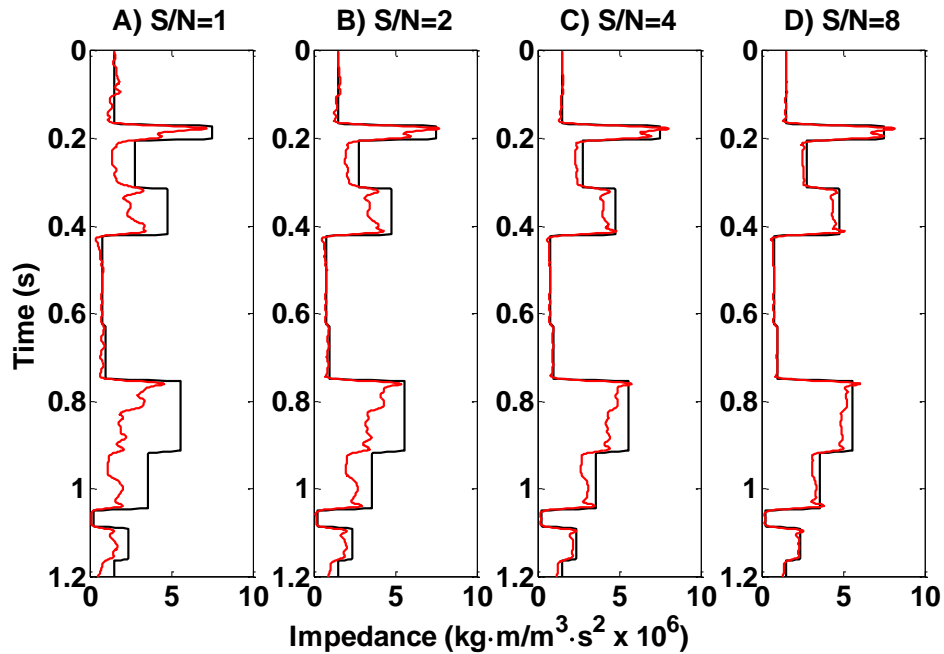


Figure 1.9: Inversions for data with signal to random noise ratios ranging from one to eight. The black curve is the true impedance and the red curve is the inversion result.

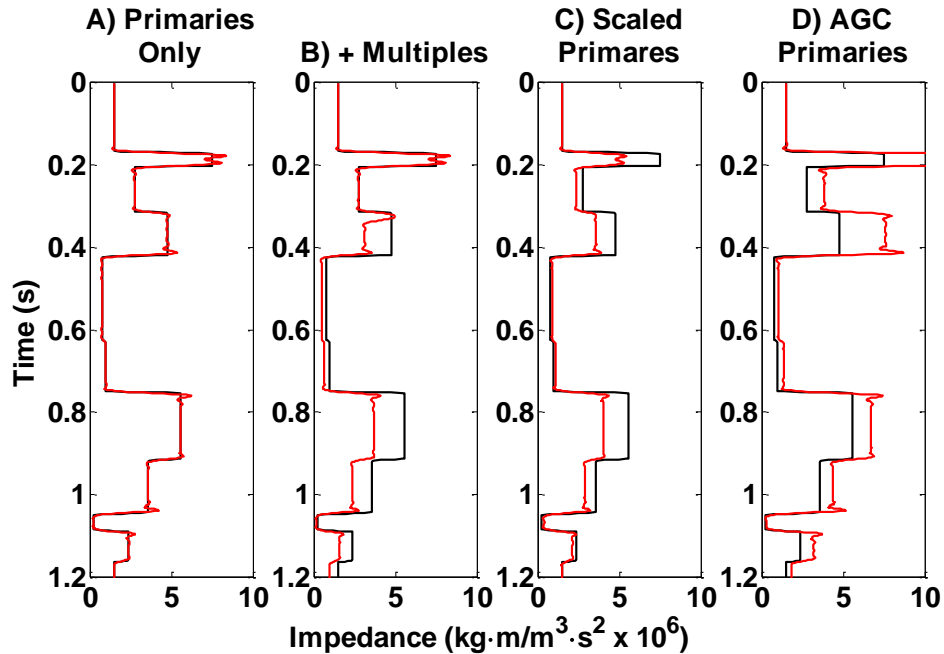


Figure 1.10: Inversions for primary reflection data, primaries plus multiples data, primary data scaled by a constant scale factor of 0.75, and primary data with AGC applied. The black curve is the true impedance and the red curve is the inversion result. For Panel C, the reflection coefficients were scaled by a factor of 0.75 before the impedance inversion was computed. For Panel D, the operator length for the AGC was 750 ms, and was scaled by a factor of 0.44 which was the maximum reflection coefficient.

Ideally the data needs to be zero phase as it is easier to interpret and is needed for accurate inversions. Zero phase means that the dominant energy of the wavelet is centered at zero time and the wavelet is symmetrical about zero. When this type of wavelet is convolved with reflectivity all the major peaks should correspond to the peaks of the reflectivity sequence and similarly for troughs (however, the bandlimited nature of the data means that the wavelet has side lobes which can potentially be confused with small reflection coefficients.). Since raw seismic data contains a minimum or a mixed phase wavelet, deconvolution is needed. Deconvolution is a process that removes the wavelet by collapsing it into a spike (Yilmaz, 2001). The wavelet needs to be estimated from the seismic data, and it can be challenging to obtain a good wavelet estimate. There are many types of deconvolution but all have the same goal which is to recover the reflectivity function from the seismic trace (Sheriff and Geldart, 1995).

Deconvolution generally has several assumptions including that the signal is stationary, that the wavelet is minimum phase, and that the spectrum of the reflection coefficients is white, meaning that the amplitude spectrum of the reflectivity is essentially constant for all frequencies. The use of “white” here is in analogy to white light which has equal amounts of all colour or frequencies (Sheriff and Geldart, 1995). By assuming the amplitude spectrum of the reflectivity is white the amplitude spectrum of the wavelet is equal to the amplitude spectrum of the trace multiplied by a constant. As shown previously seismic data is not stationary due to attenuation. The wavelet loses high frequencies with increasing distance travelled. This means that the wavelet in the shallow section is not the same as the wavelet in a deeper section. Having the most accurate inversion at the reservoir depth is important, so the wavelet is often extracted

from this zone of interest. This means there is always a residual wavelet in the zones above and below the reservoir. Phase is very difficult to estimate and seismic data is not always minimum phase. This leads to residual phase being left in the deconvolved wavelet and thus contributing to the residual wavelet. No matter how much noise attenuation is applied to a seismic signal it is impossible to remove it all. This noise will also cause inaccuracies when estimating the wavelet and contribute to the residual wavelet in all zones. Finally, deconvolution assumes that the reflection coefficients have a white spectrum. This assumption does not hold for many reflectivity series due to the cyclical nature of geologic formations.

Since the seismic wavelet is always non-stationary and the deconvolution operator is usually stationary, the residual wavelet in the reflectivity estimate is non-stationary. Thus it will have some time-variant amplitude spectral differences, but most importantly the residual wavelet will not be zero phase, except perhaps in the zone where the operator was designed. Figure 1.11 shows inversions where the data was zero phase, minimum phase, 90° out of phase and 180° out of phase. This result shows that it is crucial that the data be as close to zero phase as possible when computing impedance inversions and that deconvolution is an important step in achieving this.

Statics analysis and velocity analysis are important as both methods estimate the velocity of the subsurface. Statics are responsible for the near surface estimation and need to be as accurate as possible to obtain a good velocity model for the entire section. The near surface layer tends to have a lot of velocity variation and topography. Statics are crucial to remove the effects of this highly variable weathering layer and topography. It is common to iterate the statics and velocity calculations so that a stable model can be

estimated, as the statics affect the velocity model and the velocity model can affect the statics. It may be tempting to use the velocity model to estimate impedance instead of computing an impedance inversion from the data. Unfortunately, the velocities calculated for the velocity model are very smoothed, are error prone, and are dominated by low-frequencies. Therefore the velocity model can be used as a low-frequency source for impedance inversion but is too lacking in high-frequency information to be used alone.

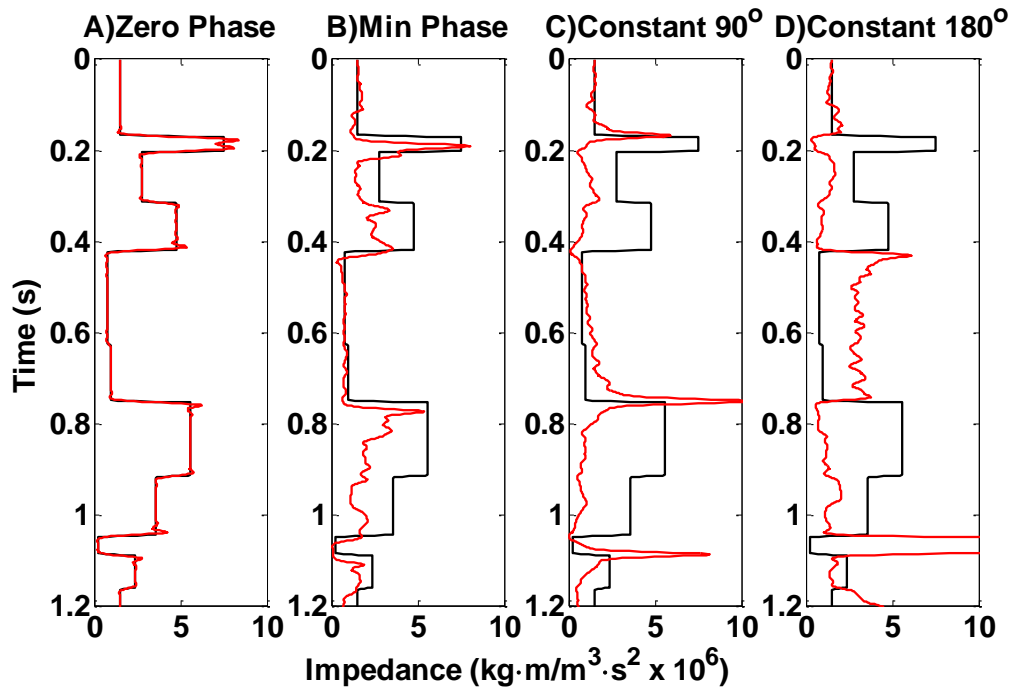


Figure 1.11: When the seismic is not zero phase the inversions that are produced are incorrect. Black is the true impedance and red is the inversion result.

Once the velocity model is created it is used for NMO (Normal Move-Out) corrections. When the reflection from a horizontal layer is recorded on the surface in a shot record it can be approximated by a hyperbola,

$$t_H^2 = t_0^2 + \frac{H^2}{v^2} \quad 1.10$$

where t_H is the time that the event is recorded at a distance H from the shot, t_0 is the time that it takes the wavefront to travel to the reflector and back at normal incidence, v is the RMS (Root Mean Squares) velocity from the surface to the reflector (eg. Margrave, 2010a). The NMO correction applies time shifts to the shot record to flatten the hyperbolic event.

When seismic data is recorded, the shot records contain data from different offsets and incidence angles. Since the data needs to be normal incident for post stack acoustic impedance inversions, the data must be stacked. Here “stacking” refers to a sum over offsets (at constant source-receiver midpoint) after normal moveout removal. Common midpoints are calculated as the distance half way between the source and receiver for each trace. Once each trace has been assigned a midpoint bin the traces in each bin are then summed (stacked) together to form a single stacked trace (Sheriff and Geldart, 1995). These stacked traces form the normal incidence reflectivity image. While this image has the correct normal incidence traveltimes, its amplitude is usually an average over offset which may deviate from the true normal incidence response. Stacking also eliminates noise and increases the gain of reflection events, while suppressing multiple energy. While there are other types of inversion that do not require stacked data, this dissertation will focus on post stack acoustic impedance inversion.

When data are viewed in time, dipping events have a geometric distortion and a spatial positioning shift. Also point diffractions or edges have unfocused data. A migration collapses diffractions and returns dipping events to their true dip (Yilmaz,

2001). An example of a point diffractor is shown in Figure 1.12. This point diffractor caused a hyperbolic event in the normal incidence time section. A Kirchhoff migration was used to collapse the diffraction into a single point. This is important to inversion as it ensures the structure in the seismic image is spatially focussed.

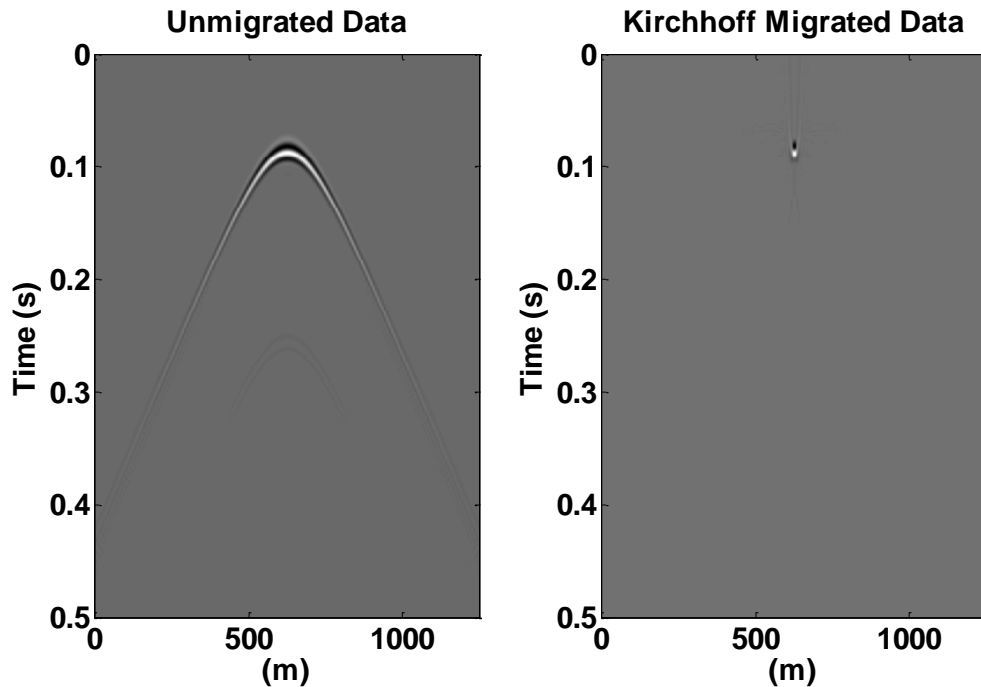


Figure 1.12: Example of a point diffraction hyperbola being migrated to produce the point diffractor.

The preceding discussion has outlined a basic processing flow, but it is common to repeat steps such as scaling and noise attenuation throughout the flow. Additional processing steps may be needed to correct for residual phase distortions or amplitude inconsistencies. These types of corrections usually require well control. Methods for correcting for residual phase distortions and amplitude inconsistencies will be discussed in Chapter 2.

1.4 Interpretation of impedance sections versus reflectivity sections

Normally seismic data, after it has been processed, is a reflectivity image that is interpreted, and decisions of where to drill a well are based on that interpretation.

Reflectivity images are not always easily interpreted and details may be missed that become obvious when interpreting an impedance image (Pendrel, 2006). Figure 1.13 shows simulated reflectivity and impedance images collected over a wedge of low-velocity sand. Reflectivity images are often viewed as wiggle trace variable area (WTVA) or variable density (VD) displays. The WTVA displays can be difficult to identify troughs (negative reflection coefficients) so picking peaks (positive reflection coefficients) tends to be easier. VD displays can make it easy to pick troughs or peaks but it can still be difficult to tell what lithology is being picked. This is illustrated by a stacked sand channel model, Figure 1.14, where it is more difficult to see the feature on the reflectivity image than the impedance image. When the impedance image is computed it becomes obvious in both the wedge example and the stacked channel example that the event is low-velocity sand which potentially could contain hydrocarbons. Another advantage to interpreting the impedance image is that it shows subtleties such as gradients which are very difficult to see on the reflectivity image (Latimer et al, 2000).

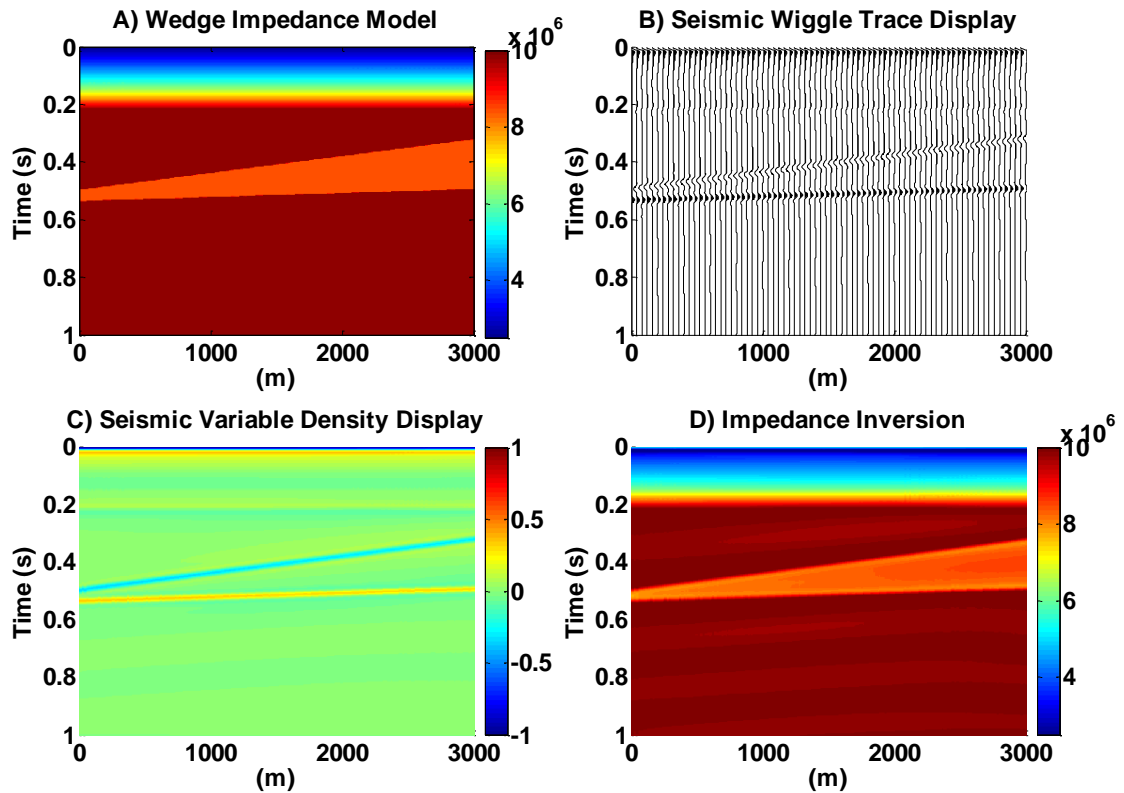


Figure 1.13: A) A wedge model in impedance, B) the wiggle trace display of the seismic produced from the wedge model. C) the variable density display of the seismic, D) the impedance inversion result. (Modified from Latimer et al, 2000)

By computing an impedance image, it is easy to obtain rock properties such as porosity, density, velocity, and lithology by using empirical relationships (Latimer et al., 2000). Acoustic impedance sections can also be used to calculate a time depth curve by relating the density to velocity using Gardner's rule (Gardner et al, 1974) and then solving for velocity (Lloyd et al., 2012).

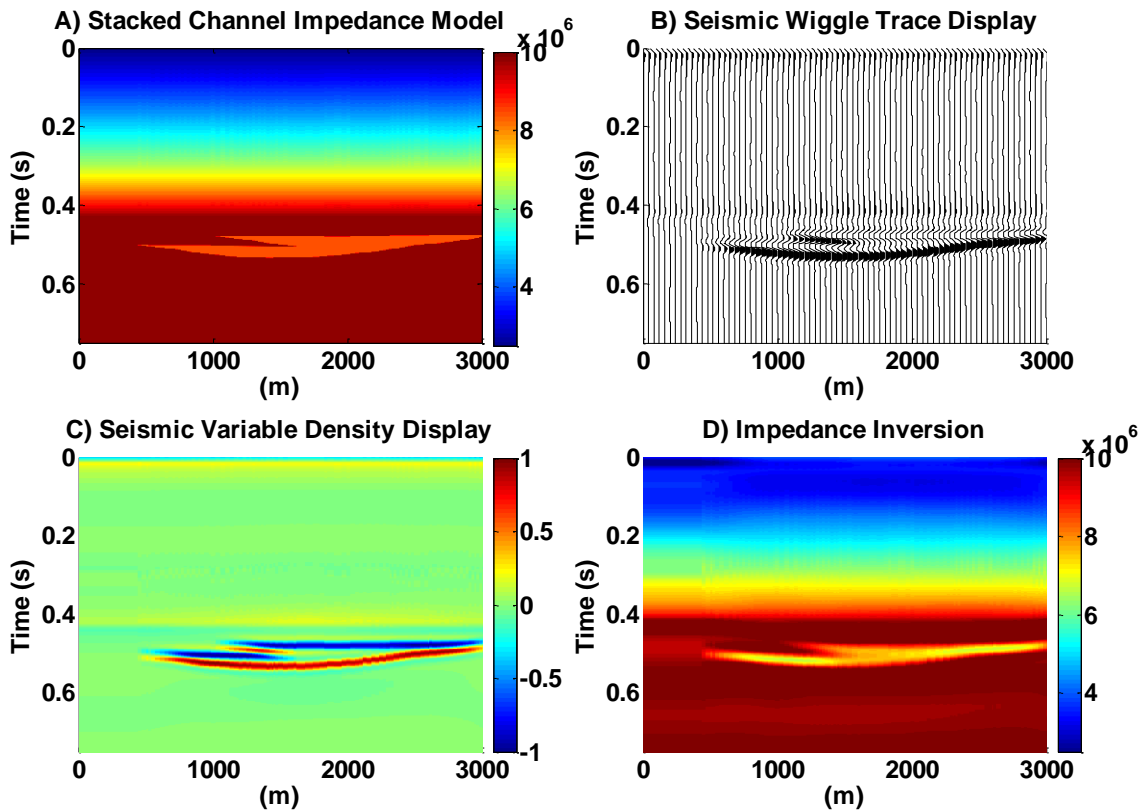


Figure 1.14: A) stacked channel model in impedance, B) the wiggle trace display of the seismic produced from the stacked channel model. C) the variable density display of the seismic, D) the impedance inversion result.

1.5 History of Impedance Inversion

In 1972, Lindseth published the first paper that solved for impedance by substituting the low frequencies in well logs for the low frequencies in seismic data. Later in 1979, Lindseth described his method that applied a low-pass filter to the well impedance log and added it to the integrated seismic trace using Equation 1.7. This produced a pseudo impedance log for every seismic trace from which rock properties such as porosity could be estimated. In 1975 Lavergne suggested using stacking velocity information to replace the low frequencies in seismic data. In the late 1970's and early

1980's various other post stack inversion methods were developed such as the autoregressive method using Burg prediction filters in 1983 by Oldenburg et al., and the generalized linear method also in 1983 by Cooke and Schneider. From the late 1980's to the present these methods, as well as more complex methods were utilized by commercial software allowing any user to compute an impedance section.

In 1996, Ferguson and Margrave created the BLIMP (BandLimited IMPedance) inversion algorithm. This algorithm is a variation on the Lindseth method (1979). It first removes a linear trend from the well log before filtering. It also calculates a scalar to boost the amplitudes of the integrated seismic trace. This method allows relative amplitudes to be used, and also provides stabilization of the inversion method by removing the linear trend before calculating the low-pass filter needed for the well log and adding the linear trend back in after the scaling process. This algorithm will be discussed further in Chapter 3.

In the early 1980's, Lailly (1983) and Tarantola (1984) brought the idea of full waveform inversion (FWI) to the table. This is different from acoustic impedance inversion as it uses the full wave equation to predict what the data will look like from a model of p-wave velocities and can be extended to include densities as well. The model is then updated in an iterative process such that the data misfit function (true data – modeled data) is minimized (eg. Margrave et al, 2010b). The result is a direct prediction of the impedance image without having to first create a reflectivity image. Full waveform inversion has at least three large problems to overcome. The first problem is that the solutions to the full wave equation must contain sufficient realism to reasonably match the recorded data. It is not clear if simpler physics can lead to reliable models.

Secondly, the starting model must contain enough detail to compensate for the low frequencies that are missing in seismic data. It is not clear how to get such a model in routine practice. Finally, the computational power that full waveform inversion requires is immense. In recent years, there has been an amazing increase in computational power but still parallel clusters are needed to run these algorithms.

Even though full waveform inversion is more sophisticated, this dissertation will focus on the acoustic impedance inversion methods as they are fast, reliable and do not require any specialized computer equipment.

1.6 Overview of Chapters

This thesis is presented in 5 chapters. Chapters 2 and 3 discuss acoustic impedance inversions using data collected near Hussar, Alberta. Chapter 4 discusses using a time-lapse model based on a carbon dioxide sequestration project near Violet Grove, Alberta, to compare low-frequency well log input of a baseline and monitor survey.

In Chapter 2 the Hussar data set is introduced, processing methods are discussed and well tying procedures are analyzed.

In Chapter 3 the theory of the BLIMP (Band-Limited IMPedance) inversion method is discussed. Low frequency input from well logs and stacking velocities are also explored.

In Chapter 4 the time lapse model of Violet Grove is outlined and results for using well logs before fluid substitution and after fluid substitution are compared. Finally, in Chapter 5 the conclusions from chapters 2-4 are summarized.

Appendix A contains descriptions of MATLAB tools that were created for well tying.

1.7 MATLAB Software and Development

The main software used in this thesis is MATLAB® which is a high-level programming language developed by MathWorks. This software is optimized for matrix algebra, which is ideal for seismic data. CREWES (Consortium of Research in Elastic Wave Exploration Seismology) developed a toolbox with a variety of processing, modeling and utility functions that can be used for seismic data processing. This toolbox was used extensively in this thesis. Many MATLAB tools were designed as a result of this thesis and are indicated in the next section.

1.8 Original Contributions

Processing the seismic reflectivity data for inversion is a very important step in the inversion process. Tools for time variant phase rotations and time variant balancing were created to correct for processing artifacts. These methods are described in sections 2.2 and 2.4.2.

Connecting the seismic reflection data to the well logs is important in ensuring that the low-frequency well data will match with the signal band data. Wavelets are necessary to bandlimit the well reflectivity in the same way as the seismic data is bandlimited. *WaveletEstimator*, a for estimating wavelets using polynomials was created for this purpose. It is described in detail in Appendix A and is utilized in section 2.4.1.4. Calibrating the well log time-depth curve is essential for connecting the seismic reflection data which is in time to the well logs which are in depth. *StretchWell* and *EnvelopeMatch* were created for calibrating the time-depth curve by adding or

subtracting slowness from an interval of the sonic log. *StretchWell* creates the intervals by matching reflection events on both the synthetic trace and the real seismic trace. The second tool creates the intervals by matching lobes of each trace's Hilbert envelope. The second method provides a better calibration as it is independent of phase rotations. The idea of the *StretchWell* is very common but the *EnvelopeMatch* appears to be a new calibration method. Both calibration methods are discussed in Appendix A, and *EnvelopeMatch* is used in section 2.4.1.2.

The BLIMP inversion method is used extensively in Chapter 3. This algorithm calculates a scalar that it multiplies the integrated trace spectra. Previously this calculation of the scalar was difficult to understand and unpredictable. Modifications to the scalar were made using L_2 norms. When very low frequency cut offs are chosen the scalar can become very large. To help reduce the frequency dependence of the scalar a threshold option was also added. When the threshold option is in effect the scalar will be calculated using frequencies from the threshold frequency to the high frequency cut-off. This cut off produces a more reliable inversion result. These changes to the BLIMP method can be found in section 3.2.1.

Estimating the low-frequency cut-off needed for inversion is a difficult task. Calculating an impedance trace using different low-frequency cut offs, subtracting the adjacent trace and summing the difference produces an L-curve type plot. The corner of the L is thought to be the preferred low-frequency cut-off. For the Hussar data set this works quite well but for the Violet Grove data set it does not work as well. The Hussar data is real field data with embedded noise whereas the Violet-Grove model is noise free synthetic data. This indicates is that the low-frequency cut off is a noise indicator. At the

corner frequency, the signal is no longer dominated by the noise. Examples for this method can be found in section 3.3.2.

Chapter Two: **Hussar Field Experiment**

2.1 Introduction

In September 2011, CREWES initiated a seismic experiment with the goal was to push the low-frequency content of seismic down as low as possible. This project was located near Hussar, Alberta, which is about 100km east of Calgary, Alberta, Figure 2.1. The line was 4.5km long and intersected three wells 12-27, 14-27 and 14-35, shown in Figure 2.2 (Margrave et al, 2012). The seismic experiment implemented several receiver and source types. The receiver types that were used included 3-component 10Hz SM-7 (Ion Sensor) Geophones with 10 meter spacing, 3-component Vectorseis (MEMS) accelerometers with 10 meter spacing and 1-component 4.5Hz geophones with 20 meter spacing (Margrave et al, 2012). For sources, a 2kg charge of dynamite at 15 meters, a low dwell sweep using a standard production vibrator (Failing Y2400) and the INOVA AHV-IV (model 364) vibrator (INOVA 364) both a low-dwell sweep and a linear sweep were used (Margrave et al, 2012). The INOVA 364 has a reinforced base plate which allows it to vibrate at high power at low frequencies, this allows the INOVA 364 to complete a linear sweep whereas the Failing Y2400 could not do this type of sweep.

While CREWES initiated this project, it would not have been possible without the help of Husky Energy, Geokinetics and INOVA. Husky Energy managed this project as if it were their own by choosing the site, providing land access and shooting the data. Geokinetics provided the experiment with a seismic crew, recorder and the accelerometers used in the experiment. INOVA provided the INOVA 364 to Hussar, AB from Houston, TX just for this project.

While all of the data sets are of interest, this dissertation will focus on the dynamite source recorded with the 10Hz geophones as this data set contained the most signal at low-frequencies out of all data sets.

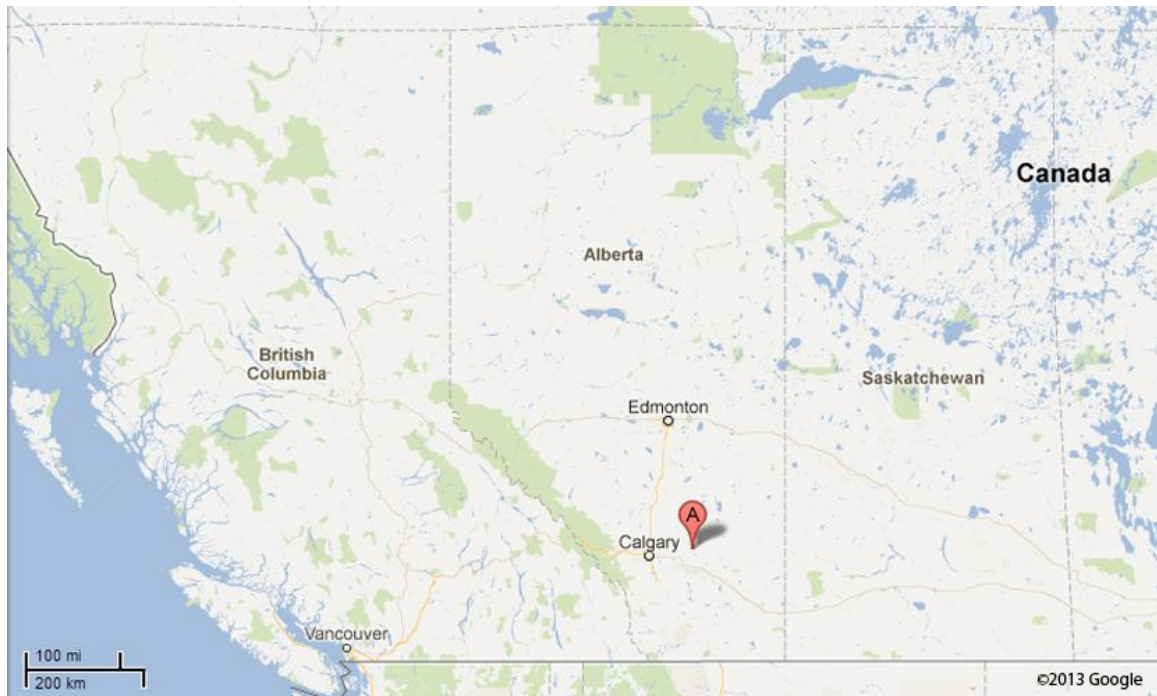


Figure 2.1: Location of the seismic line area near Hussar, Alberta, Canada indicated by the red marker.

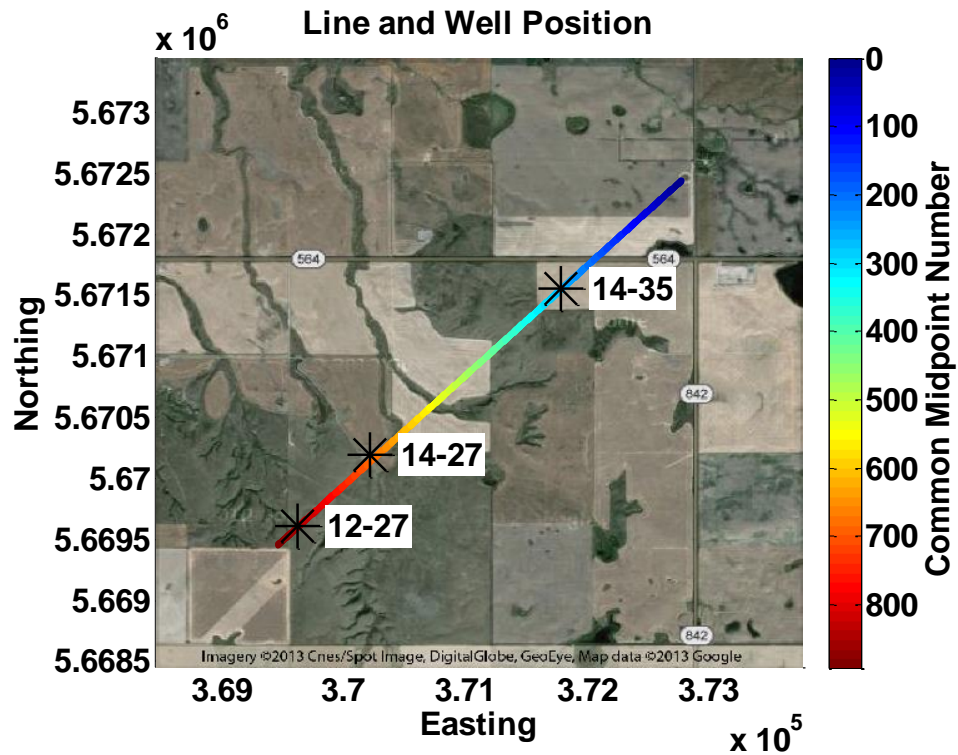


Figure 2.2: The location of the line and wells. The color scale shows the common midpoint number.

2.2 Data Processing

The objective of this data set to recover as much low-frequency information as possible, so CGG Veritas implemented a specialized processing flow. Normally a high-pass filter is applied to the data to remove noise such as ground roll. This high-pass filter can be as high as 10 Hz. To keep the integrity of the low-frequencies, different noise attenuation was needed. Some of these methods were as follows: removing sinusoidal noise caused by power lines and pump-jacks, attenuating coherent noise and attenuating anomalous high amplitude frequencies. These noise attenuation procedures were repeated several times during the processing flow. Scaling was also specialized as

common trace equalization, such as an AGC was undesired. Geometrical spreading gain recovery and surface consistent scaling was implemented instead.

Phase coherence, which is an indicator of coherent signal at a particular frequency, was measured by CREWES and reflection signal was estimated to be present down to frequencies as low as 1 to 5 Hz in the dynamite data (Isaac et al, 2012). The fully processed section, Figure 2.3 , when compared to the well reflectivity, has underestimated amplitudes from 0 to 1 second. This may be a result of trying to reduce the noise in the near surface and inadvertently reduced the signal amplitudes as well. This needs to be corrected for but cannot be done with conventional scaling operators such as an AGC as this adversely affects the phase coherence of the data (Isaac et al, 2012) by boosting noise present in the low frequencies that the specialized noise attenuation attempted to reduce. An AGC also equalizes the energy on the trace which does not keep the true relative reflectivity intact. Scaling was achieved by tying well 14-27, using a bulk shift, to the seismic and computing a time variant balancing algorithm with a window size of 50 ms and an increment of 10 ms. The resulting seismic section is shown in Figure 2.4.

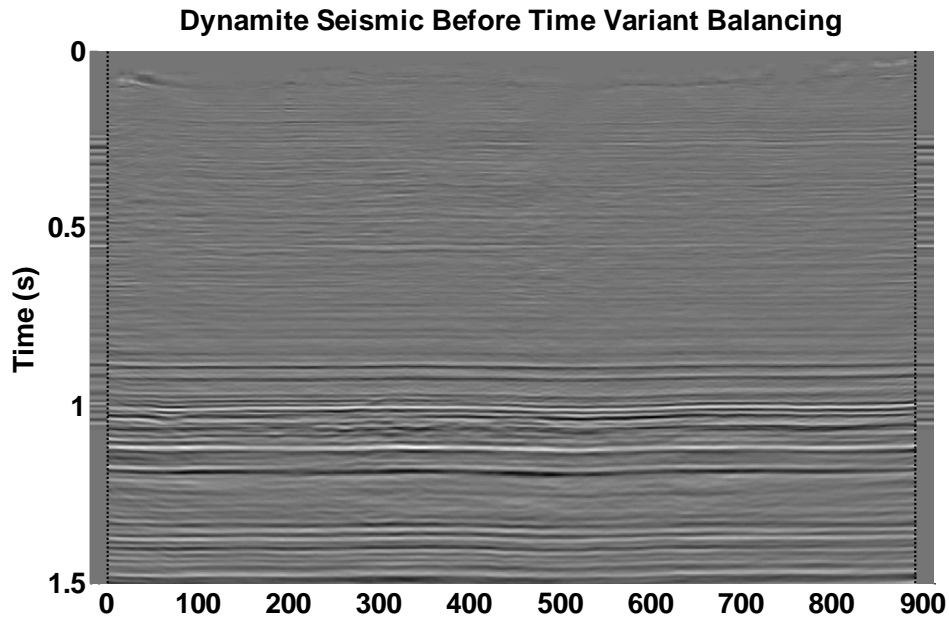


Figure 2.3: Seismic after processing and migration. The shallow section have lower amplitudes than seen else in the section and in the well logs. A synthetic seismogram from well 14-27 is plotted on each side of the section, separated by dashed lines to show that the amplitudes in the upper section are low.

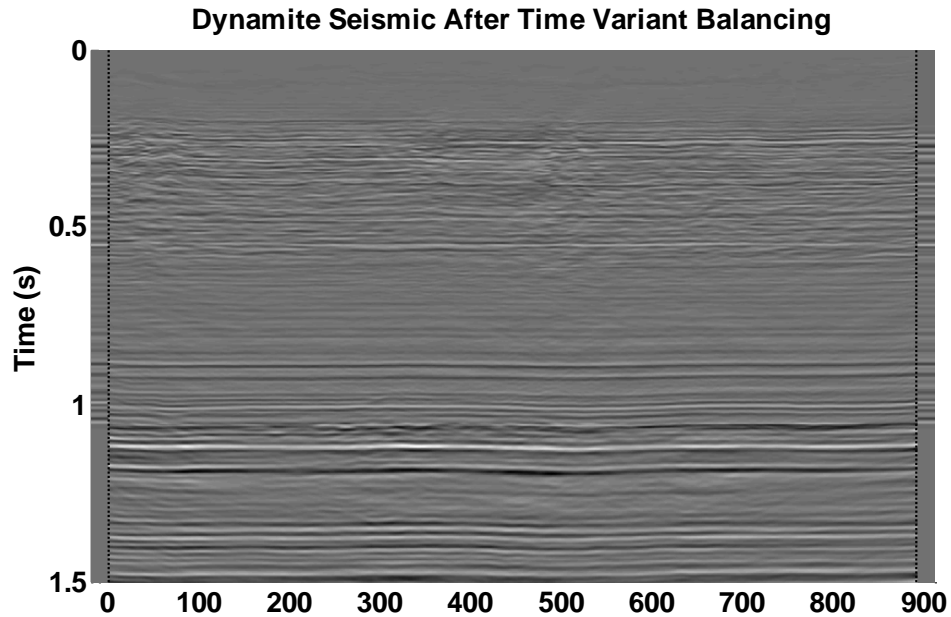


Figure 2.4: Seismic after time variant balancing using well 14-27. A synthetic seismogram from well 14-27 is plotted on each side of the section, separated by dashed lines, to show how the amplitudes in the upper section were restored by using time variant scaling.

2.3 Well Preparation

Before the wells can be tied to the seismic data they must first have an overburden and underburden applied. The overburden extends the wells to the surface and makes the well tying process easier. The underburden allows that the well seismogram to be calculated to a full 4 seconds which ensures a fine sample rate in the frequency domain. An overburden was modeled using a linear gradient for the P-wave velocity and density. The surface value for the P-wave velocity was obtained from first break analysis (1101 m/s) and the end value of the gradient blended into the top of the well log. The density surface value was chosen to simulate unconsolidated dirt at the surface (1500 kg/m^3). The underburden that was chosen was the linear trend of the well logs. Since the linear trend is already present in the data, using it as the underburden minimizes the distortion to the frequency domain. The logs for well 12-27, 14-27 and 14-35 are displayed in Figure 2.5, Figure 2.6, and Figure 2.7, respectively.

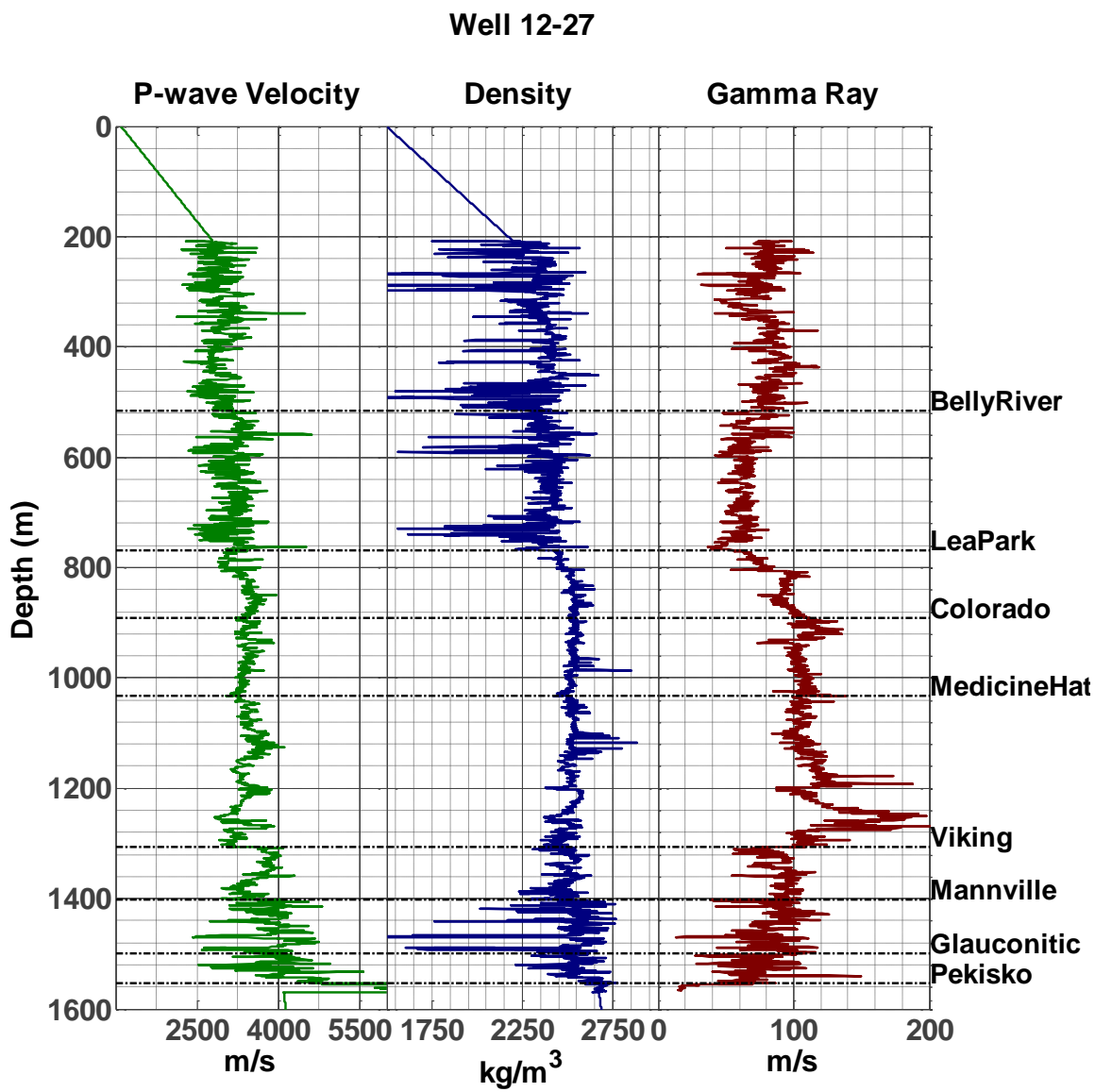


Figure 2.5: Well logs for well 12-27 including the p-wave velocity log, density log both of which are shown with the overburden and underburden applied and the gamma ray log.

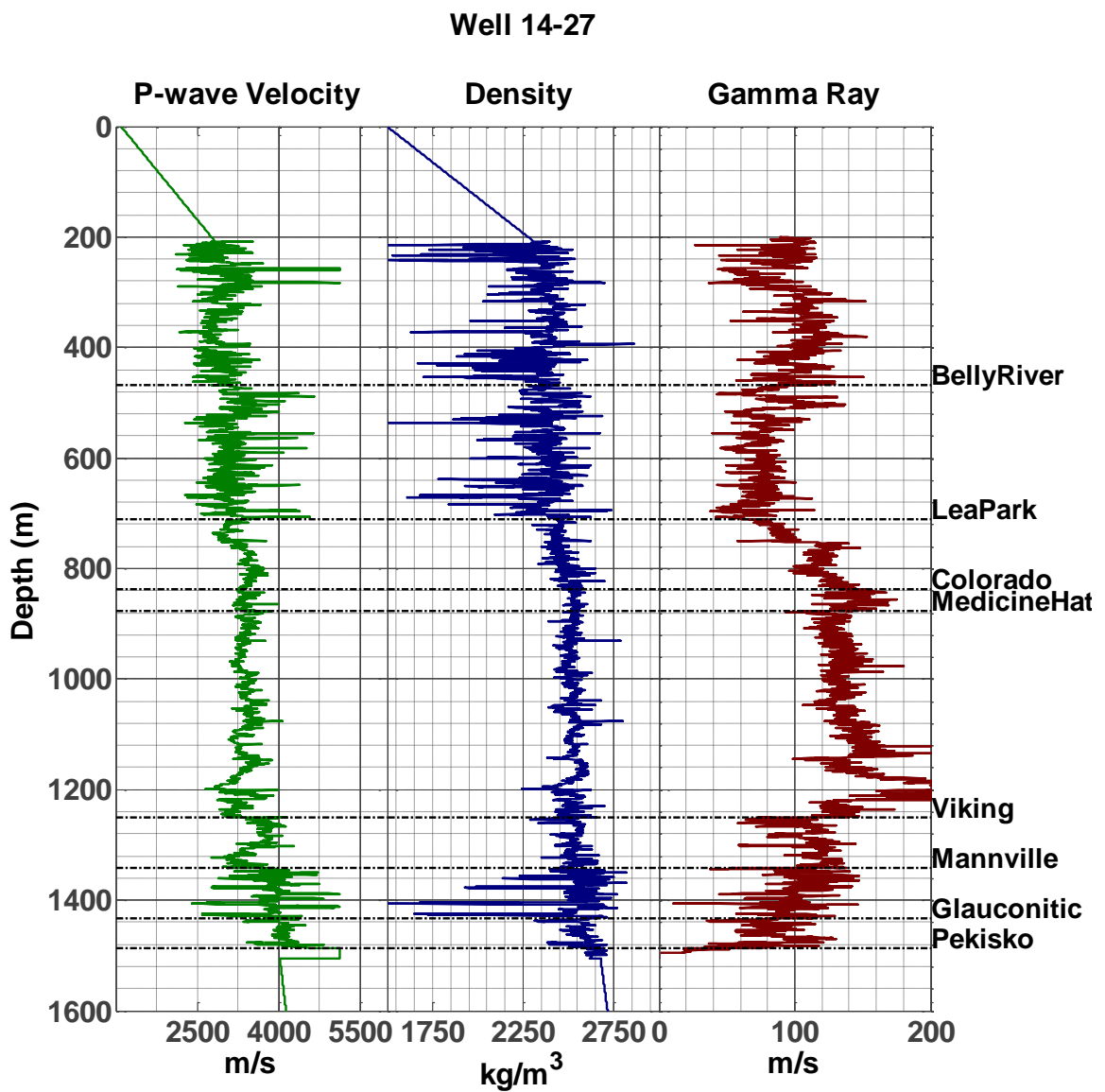


Figure 2.6: Well 14-27 p-wave velocity and density log with overburden and underburden applied as well as the gamma ray log.

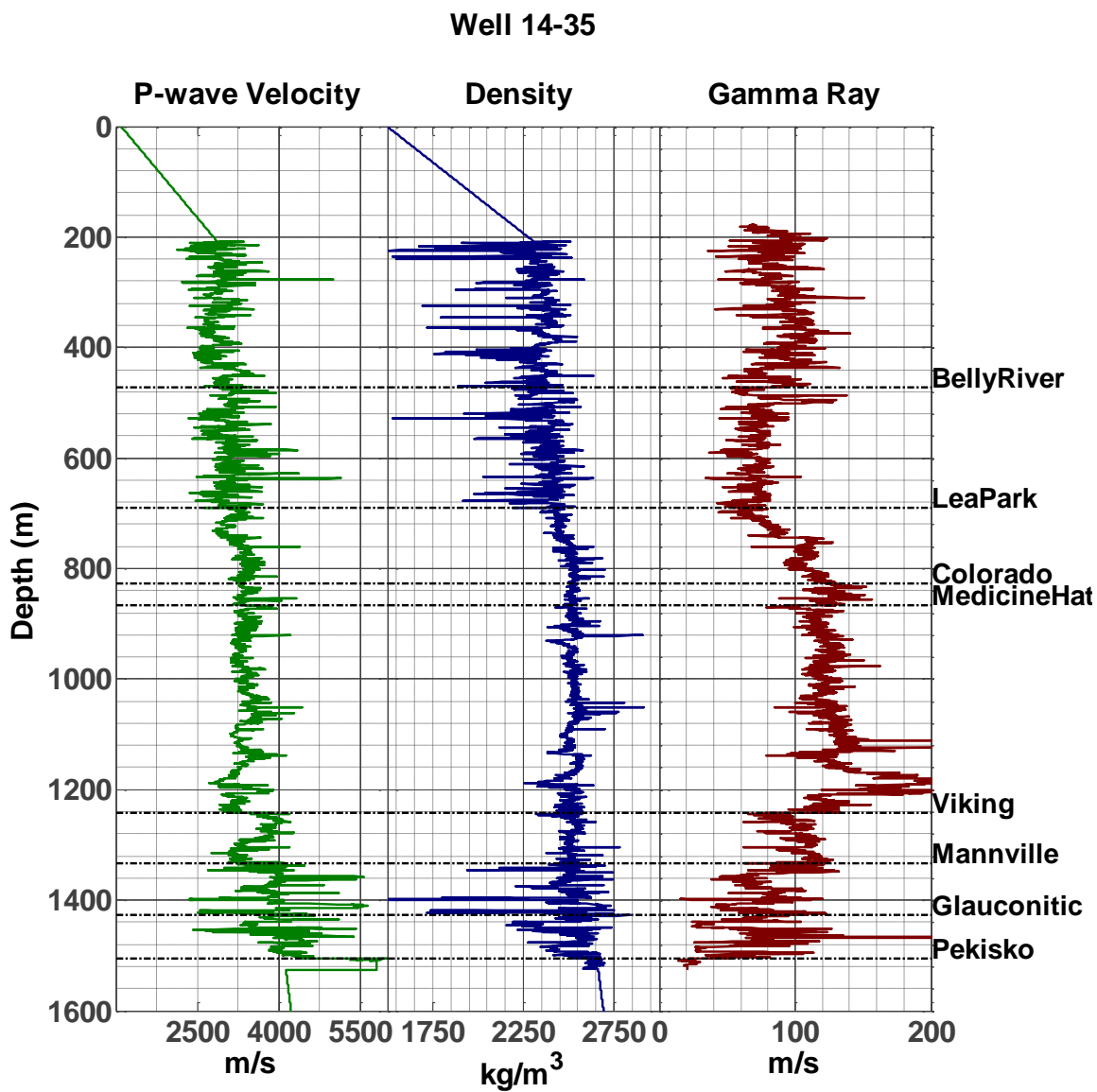


Figure 2.7: Well 14-35 showing the p-wave velocity log and density log both of which have an overburden and underburden applied. The gamma ray log is also shown.

2.4 Well Ties

2.4.1 Well Tying experiment

2.4.1.1 Introduction

Tying well logs to seismic is an important process in interpretation and to compute viable inversions, where well logs are being used for their low-frequency content. This process involves the following steps modified from White and Simm (2003):

1. Edit the sonic and density logs.
2. Calibrate the sonic log to check shot or VSP (Vertical Seismic Profile) times.
3. Create the synthetic reflection coefficients using the calibrated logs in two way time
4. Determine the best match location and estimate wavelet at the location

The first step removes spurious events and cycle skipping. This is often done by smoothing the sonic and density logs. It may be necessary to clip spurious events to a reasonable level, this could include sonic or density values that are less than zero or higher than an acceptable value for the interval. This step could also involve computing local averages of the sonic log using the Backus average to account for the stratigraphically induced velocity dispersion caused by the disparity between the seismic and sonic frequencies (White and Simm, 2003).

The second step is the most important as this effects the timing of the synthetic. A mismatch in time is significantly more detrimental than a mismatch in amplitudes (White, 1997). Ideally this involves calibrating the integrated sonic times with measured

check shot or VSP times, but other methods as described in 2.4.1.2 can also be used. To create a time-depth relationship the integrated sonic times and the check shot or VSP times are compared at equal depths. These depth points are also known as knee points and should correspond to a reflector to reduce artificial coefficients being introduced in the corrected sonic log. The difference between the integrated sonic log and the check shot or VSP times is known as the drift curve. Ideally this curve should be smooth and have small time changes with depth.

This calibration step is necessary as the velocity that seismic waves experience is not the same as the velocity that sonic logging tools estimate. This is because of the basic theory of wave propagation in an attenuating medium which predicts that velocity must depend upon frequency. Seismic velocity and logging velocity are related by

$$V(f) \approx V_o \left(1 + \frac{1}{\pi Q} \ln \left| \frac{f}{f_o} \right| \right) \quad 2.1$$

where V is velocity, Q is attenuation, f is the frequency of the current wavefield, f_o is the dominant frequency of the reference wavefield and V_o is the velocity measured by the reference wavefield (eg. Margrave, 2010a). What this equation shows is the seismic data (frequencies of 0 Hz to 70 Hz) will measure a slower velocity than the sonic tool (frequencies $\sim 10^4$ Hz). Drift curves are commonly around 2 ms per 1000ft or 304 meters but can be as high as 7 ms per 1000ft (Stewart et al, 1984). In the near surface these drift curves are less reliable and can have shifts that are positive or negative ranging from -8 ms to 8 ms (Stewart et al, 1984). Once the drift curve has been calculated it and the sonic log are used to create a time-depth relationship.

2.4.1.2 Time-depth curves without Check-shots or VSP data

Data that is available for academic purposes rarely contains check shots or VSP data. This requires that other means are used to create the time-depth relationship. One common method is stretching and squeezing the sonic log. While this approach is often labeled as unscientific (White and Simm, 2003) and imprecise (White et al., 1998) it can be used when other methods for calibration are not available as long as reasonable knee points are chosen. Prior to this step, a wavelet needs to be estimated that captures the amplitude spectra and the phase spectra of the seismic as much as possible. Ensuring the phase of the seismic data and the phase of the synthetic match before stretching or squeezing is necessary as phase rotations can cause event mis-match and forcing them to match leads to errors.

Matlab based programs were designed to allow the user to choose knee points and then add or subtract slowness from the sonic log to produce the time-depth relationship. These programs are described in further detail in Appendix A.

A robust way to pick the match points and produce the time-depth curves is to match the Hilbert envelopes of the synthetic and real seismic traces. The Hilbert envelope is formed by

$$HE = \sqrt{tr^2 + tr_q^2} \quad 2.2$$

where HE is the Hilbert Envelope, tr is the trace and tr_q is the quadrature of the trace (rotated 90 degrees) (eg. Claerbout, 1976). This envelope is independent of constant phase rotations and thus any constant phase rotations in the data can be ignored. For this to work, the wavelet still needs to be estimated but the phase spectrum of the wavelet is

less important for this method. Figure 2.8 shows the Hilbert Envelopes before corrections and after corrections. In Figure 2.8 B, it is apparent that a good match can be obtained for the envelope even if the amplitudes of the seismic Hilbert envelope and synthetic Hilbert envelope do not match. Figure 2.9 shows the synthetic and seismic trace before the calibration process. The event at about 0.48 seconds on the synthetic trace is now lined up with the event on the seismic trace, even though they may not be in the same phase.

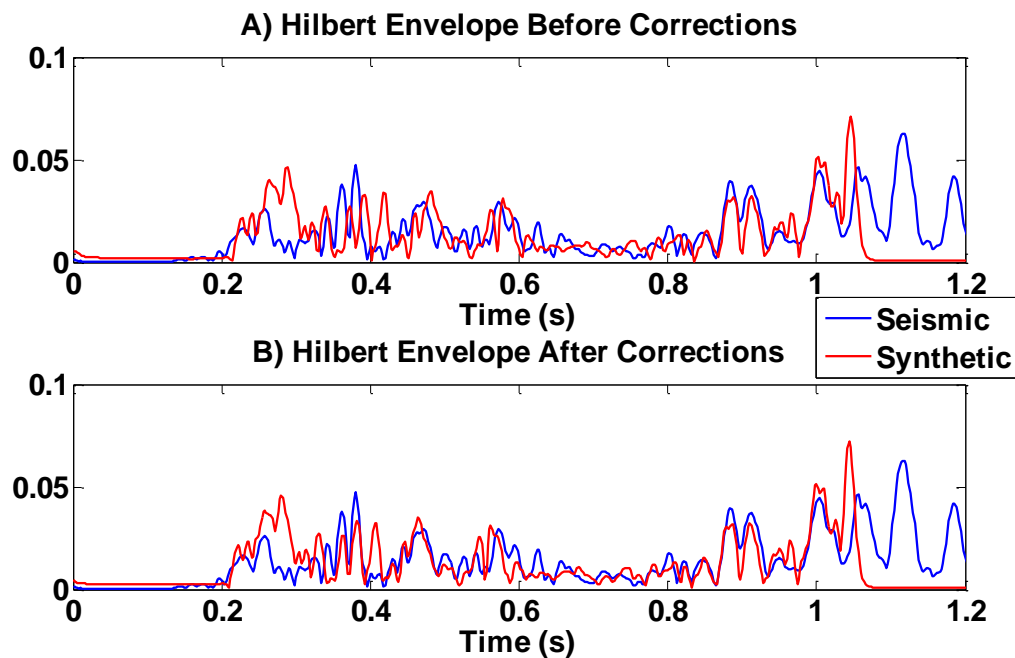


Figure 2.8: Hilbert envelopes of the synthetic and seismic traces before and after matching.

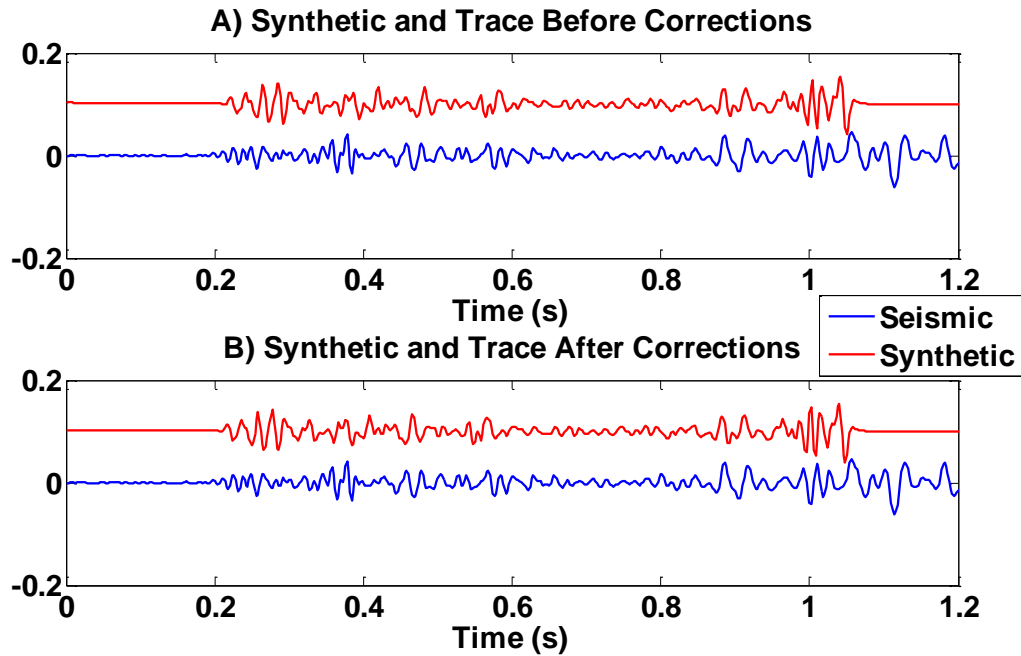


Figure 2.9: Synthetic and trace matching using the Hilbert envelope method.

2.4.1.3 Creating Synthetic Reflection Coefficients

Well log measurements are measured in depth and need to be converted to time to match the well synthetic with the seismic data. There are two methods in which to do this. The first method is to use the calibrated sonic log to create the reflection coefficients and convert the logs into time (Method 1). This would mean that some of the reflections could potentially have a larger or smaller value depending on how much the sonic log was adjusted during calibration. The other method is to use the original sonic log for the reflection coefficients and to then convert to time by calculating the time-depth curves using the calibrated sonic log (Method 2).

A model was created with 10 layers with varying velocity, density and attenuation values (Figure 2.10), to evaluate if there is significant difference between using Method 1

and Method 2. Since sonic tools have a high frequency source the values were estimated using Equation 2.2. A synthetic trace using the sonic log was calibrated to a trace made using the initial seismic velocity and the envelope matching program in MATLAB. The original sonic is compared with the calibrated sonic and their difference in Figure 2.11. Both methods for creating reflection coefficients were explored and the results can be seen in Figure 2.12. The results are very similar and match up with all events, but the amplitudes of the reflections may be slightly different. This can normally be corrected for by using a time variant balancing algorithm. The cross correlation for each method was calculated (Figure 2.13). A negligible time shift was suggested for both synthetics but the correlation factor was slightly larger Method 2. Since the correlation factor was minimally different, further testing is needed to see if Method 2 is always superior, however; in intervals where the attenuation is high, Method 1 is still valid as it would account for velocity differences occurring between the seismic and the sonic log.

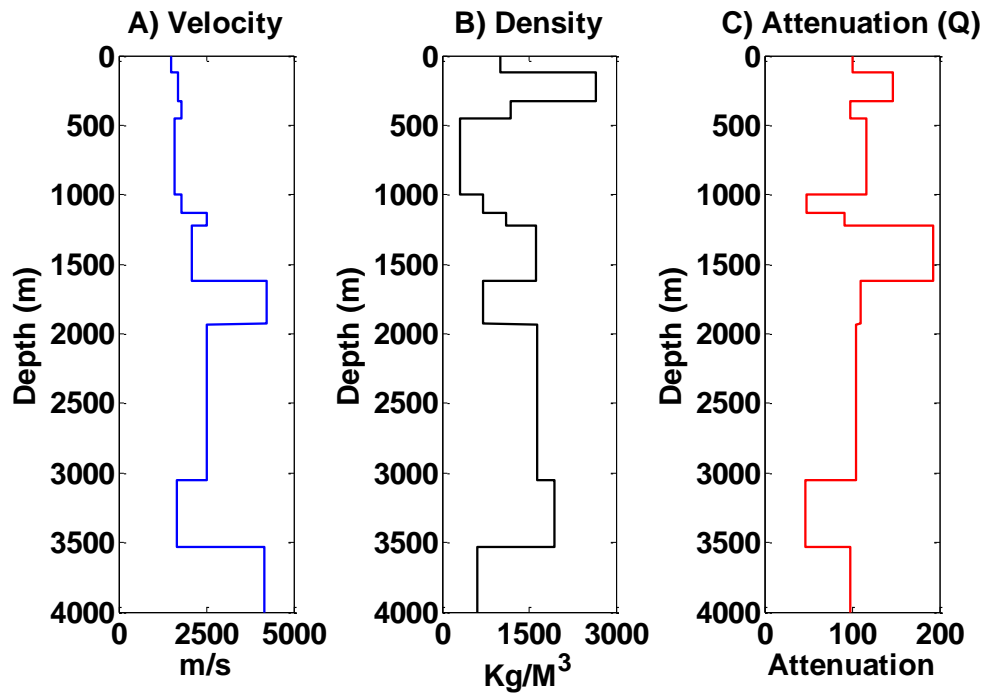


Figure 2.10: The velocity, density and attenuation values for the 10 layer model.

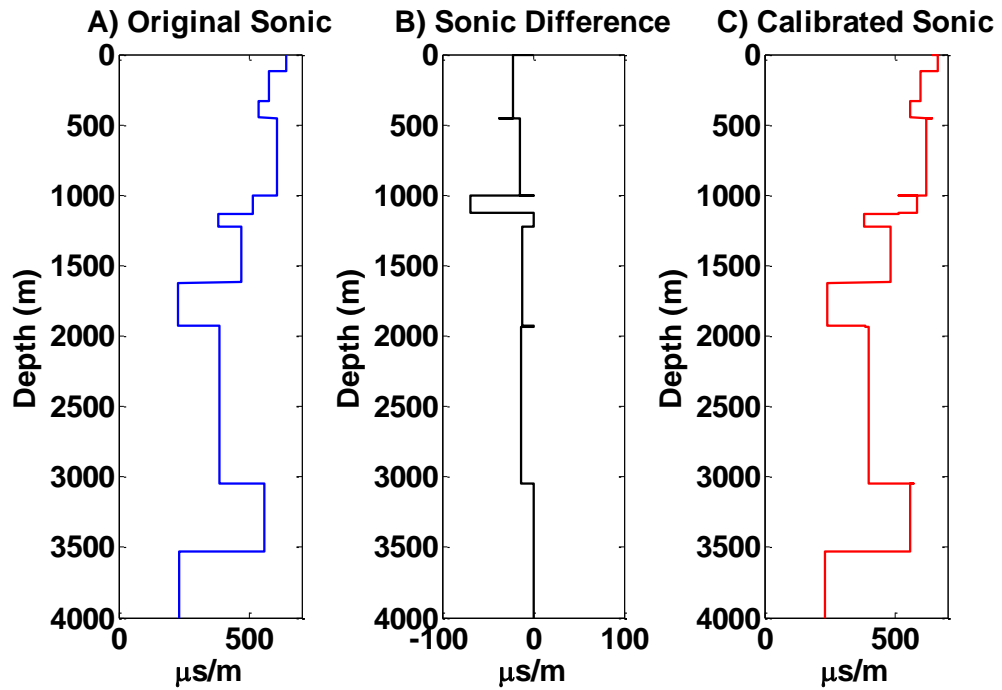


Figure 2.11: Original sonic log, sonic adjustment and calibrated sonic log, used to compute synthetic seismograms for well ties.

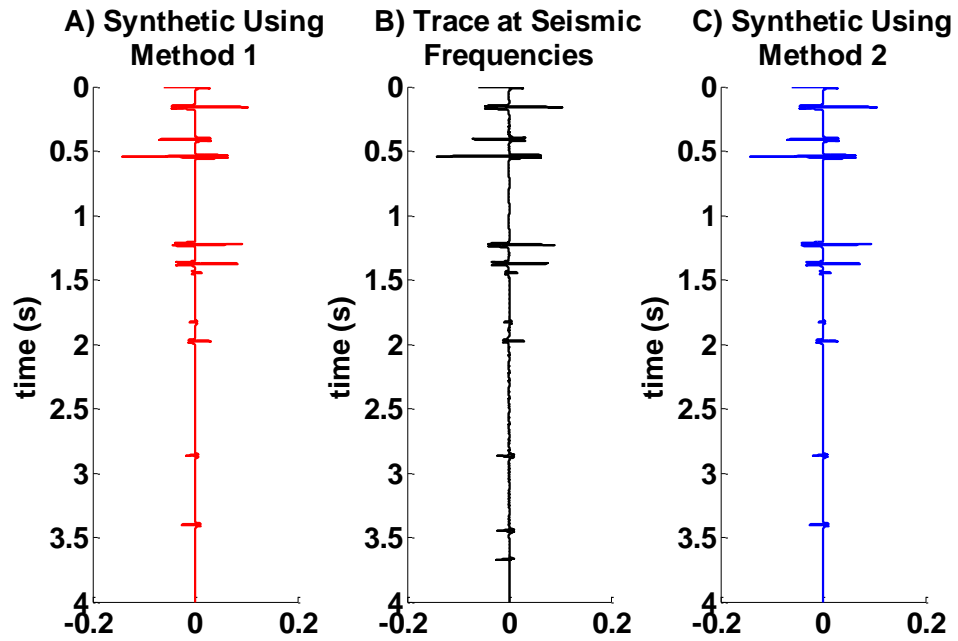


Figure 2.12: Well ties for the stretched sonic log method (left) and the altered time-depth curve method (right) compared to the real seismic trace (middle).

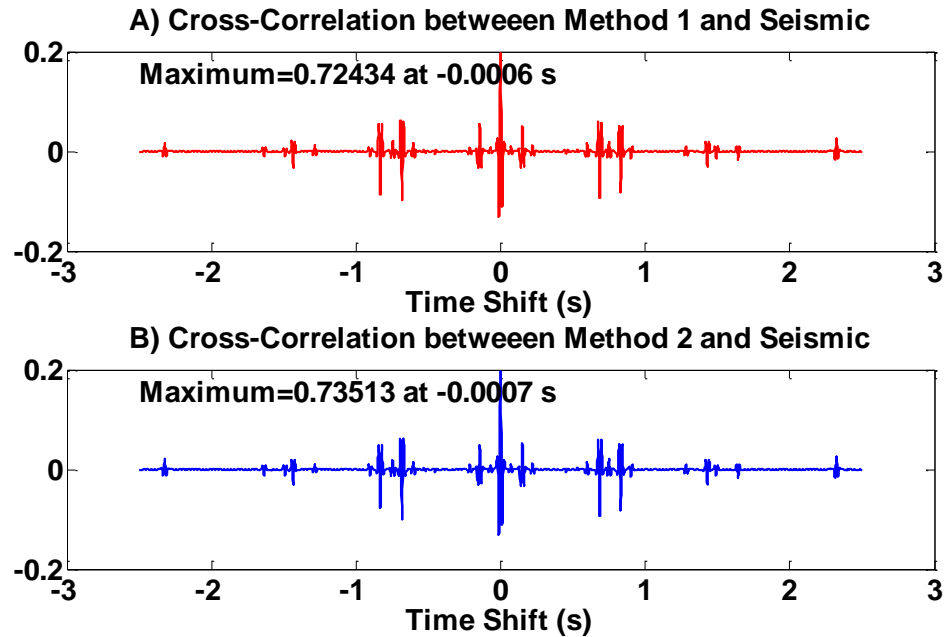


Figure 2.13: The cross-correlation plot for each method. The ideal method would have the largest maximum with the smallest shift from zero.

2.4.1.4 Wavelet Estimation

Once the synthetic seismogram has been calibrated to the sonic, the final wavelet can be estimated. Since the phase of reflectivity is very complicated it is best that the final wavelet is estimated after all corrections so that the phase can be estimated properly. When estimating a wavelet it is important that no assumptions are applied to the wavelet such as its appearance or timing (White and Simm, 2003), including the phase. For wavelet estimation there are several ways of estimating the amplitude spectra such as modeling it with a spline, a polynomial or computing a more statistical amplitude spectrum such as the method defined in White (1980). The phase can also be estimated, but it is more difficult to get a good model as it is very sensitive to effects such as noise. Therefore it is common practice to assume a phase model. Since this discussion is about the inversion of migrated sections, it is fair to assume that the data have already been deconvolved. This implies that only residual wavelet phase remains and the common industrial model for that is that it is constant (independent of frequency). If the wavelet model is assumed to be minimum phase the phase spectra must be formed from a minimum phase operator. If phase is assumed to be constant than a zero phase wavelet can be rotated to accommodate the phase. If the phase is assumed to be time variant, then constant phase rotations can be calculated in Gaussian windows and then applied to the synthetic or the seismic data.

Constant phase rotations can be computed using a Fourier multiplier method

$$S_{rot}(t) = \int_{\mathbb{R}} e^{i\varphi \text{sgn}(\omega)} \hat{S}(\omega) e^{i\omega t} d\omega \quad 2.3$$

where S_{rot} is the rotated trace, $e^{i\varphi \text{sgn}(\omega)}$ is the Fourier multiplier that contains the constant phase rotation φ , $\text{sgn}(\omega)$ is the sign of the frequency, $\hat{S}(\omega)$ is the input trace in the frequency domain and $e^{i\omega t}$ is the Fourier kernel. The Fourier multiplier can be expanded to

$$\begin{aligned} e^{i\varphi \text{sgn}(\omega)} &= \cos(\varphi \text{sgn}(\omega)) + i \sin(\varphi \text{sgn}(\omega)) = \cos(\varphi) + i \sin(\varphi) \text{sgn}(\omega) \\ &= \cos(\varphi) + \sin(\varphi) e^{i\pi/2 \text{sgn}(\omega)} \end{aligned} \quad 2.4$$

where $e^{i\pi/2 \text{sgn}(\omega)}$ is a 90 degrees phase rotation. This result can be substituted back into Equation 2.3

$$\begin{aligned} S_{rot}(t) &= \int_{\mathbb{R}} (\cos(\varphi) + \sin(\varphi) e^{i\pi/2 \text{sgn}(\omega)}) \hat{S}(\omega) e^{i\omega t} d\omega \\ &= \cos(\varphi) S(t) + \sin(\varphi) S^\perp(t) \end{aligned} \quad 2.5$$

where $S^\perp(t) = \int_{\mathbb{R}} e^{i\pi/2 \text{sgn}(\omega)} \hat{S}(\omega) e^{i\omega t} d\omega = \mathcal{H}(S)(t)$, which is the Hilbert Transform (\mathcal{H}).

To find the best phase rotation that matches one trace S_1 to S_2 , the L_2 Norm needs to be minimized:

$$\mu = \|S_{1:rot} - S_2\|^2 = \left\| aS_1 + \sqrt{1-a^2} S_1^\perp - S_2 \right\|^2 \quad 2.6$$

where $a = \cos(\varphi)$. This can be expanded and simplified to

$$\mu = a^2 \sigma_1 + 2a\sqrt{1-a^2} \sigma_{11}^\perp + (1-a^2)\sigma_1^\perp - 2a\sigma_{21} - 2\sqrt{1-a^2} \sigma_{21}^\perp + \sigma_2 \quad 2.7$$

where

$$\begin{aligned}\sigma_1 &= \int S_1^2 dt, \quad \sigma_{11}^\perp = \int S_1 S_1^\perp dt, \quad \sigma_1^\perp = \int S_1^{\perp 2} dt, \\ \sigma_{21} &= \int S_2 S_1 dt, \quad \sigma_{21}^\perp = \int S_2 S_1^\perp dt, \quad \sigma_2 = \int S_2^2 dt.\end{aligned}\tag{2.8}$$

To find the minimum, the derivative of Equation 2.7 is taken and then set to zero

$$\frac{d\mu}{da} = 2a\sigma_1 + 2a\sqrt{1-a^2}\sigma_{11}^\perp - \frac{2a^2}{\sqrt{1-a^2}}\sigma_{11}^\perp - 2a\sigma_1^\perp - 2\sigma_{21} + \frac{2a}{\sqrt{1-a^2}}\sigma_{21}^\perp = 0.\tag{2.9}$$

This can be expanded and results in a fourth-order polynomial that the roots can be solved for. Each root must then be tested to determine which gives the actual minimized result. Once ϕ has been solved for Equation 2.5 can be used to calculate the rotated trace.

2.4.1.5 Why phase rotations are needed in inversion processing

Phase rotations are needed after deconvolution to move the central peak of the wavelet to the position of the reflection coefficient. Deconvolution is rarely perfect in its attempt to produce a zero-phase wavelet from a minimum-phase, nonstationary signal. Usually deconvolution estimates a wavelet from an interval along the trace so at this location the deconvolution is as accurate as it can be. Above this interval the events become over-whitened and the high frequencies are boosted. Below this interval the events become underwhitened and the lower frequencies are dominant. The phase component in these events is not equal so they need a time variant rotation to correct for the deconvolution operator and rotate the wavelet so that the maximum energy is centered at the reflection coefficient.

To illustrate the effect of deconvolution on a nonstationary signal, a model of five reflection coefficients was made. All the reflection coefficients have absolute value of 0.2 but the second and fourth reflection coefficients are negative. A very weak noise

signal was added to help stabilize the deconvolution operator as it is meant for a random reflectivity sequence. The reflectivity is shown in Figure 2.14. The stationary trace was built using a 30 Hz minimum-phase wavelet and then deconvolved using a Weiner deconvolutional operator with 40 lags used in the autocorrelation. The design window used in the deconvolution was from 1.8 seconds to 2.2 seconds. The nonstationary trace shown in Figure 2.15 was formed by using the same 30 Hz minimum phase wavelet combined with a minimum-phase forward Q operator having a Q value of 100. The Weiner deconvolution was again performed using 40 lags and a time window of 1.8 seconds to 2.2 seconds for the operator design. A linear amplitude gain was applied to the signal expressed by $gained\ signal = 2.5 * t * signal$.

The purpose of computing and removing phase rotations is so that the events line up with the ideal trace, a stationary zero phase trace with the same amplitude spectra as the deconvolved data. This ideal or reference trace was calculated for each of the stationary and nonstationary cases. Phase rotations were then calculated between the reference trace and the deconvolved traces. These phase rotations were calculated by using least squares method in a 200 ms Gaussian window centered on each event. The phase rotations are shown in Figure 2.16, where the stationary example has a constant (with time) phase rotation and the nonstationary example has a time-variant phase rotation. The phase rotations are applied and the results are shown in Figure 2.17. Ideally, the phase rotations should shift the energy of the wavelet so that the most energy lines up with the center of the zero phase wavelet. For the stationary example there is no real improvement but for the nonstationary case there is significant improvement. This is

important to inversion as the central peak of the wavelet needs to line up with the reflection coefficient.

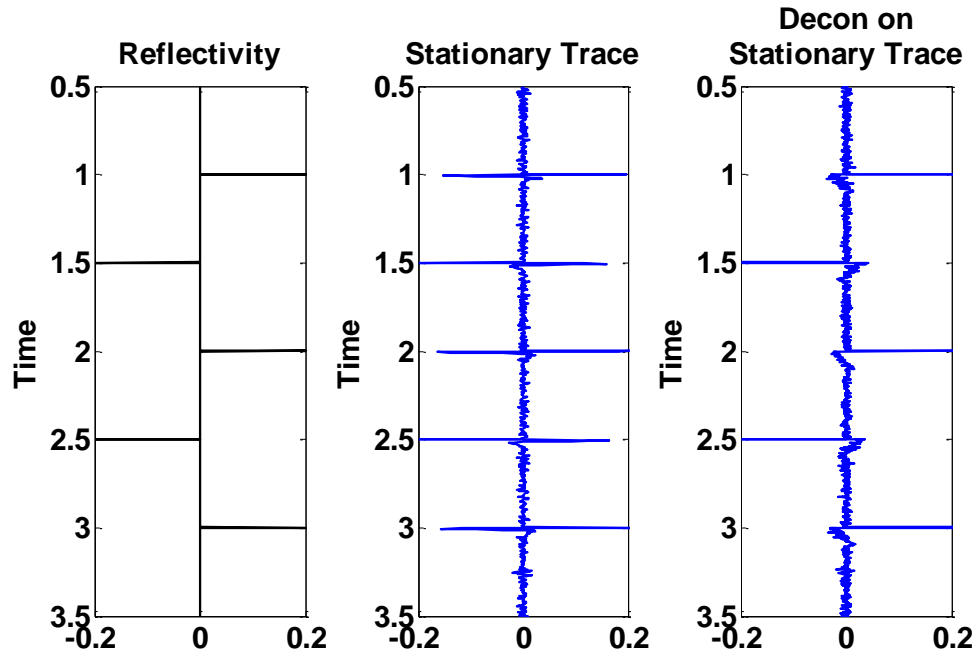


Figure 2.14: Reflectivity, signal and deconvolution using stationary methods.

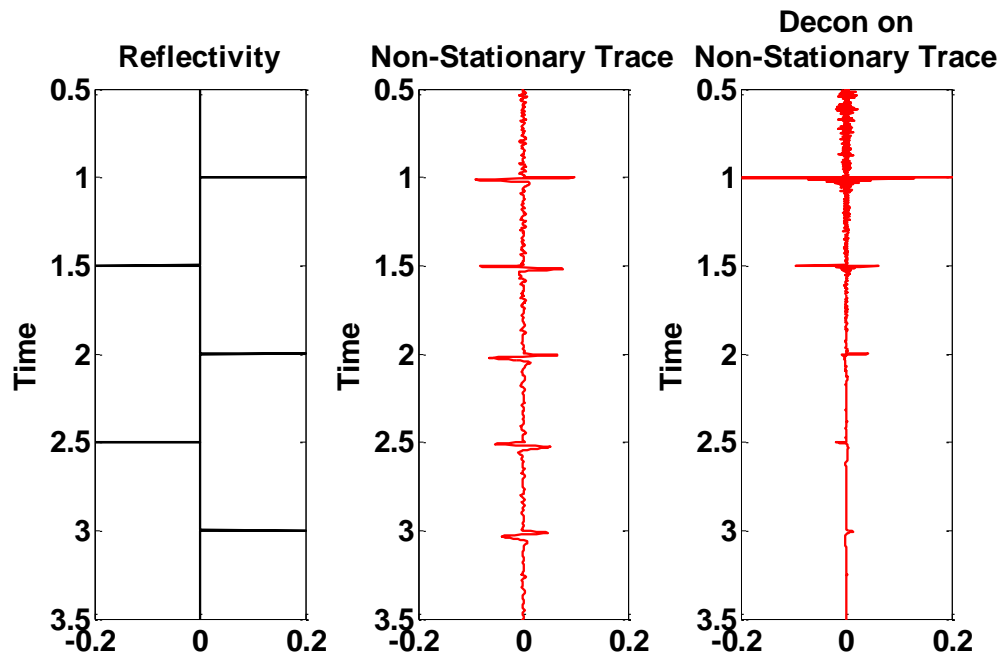


Figure 2.15: Reflectivity, signal and deconvolution using nonstationary operators.

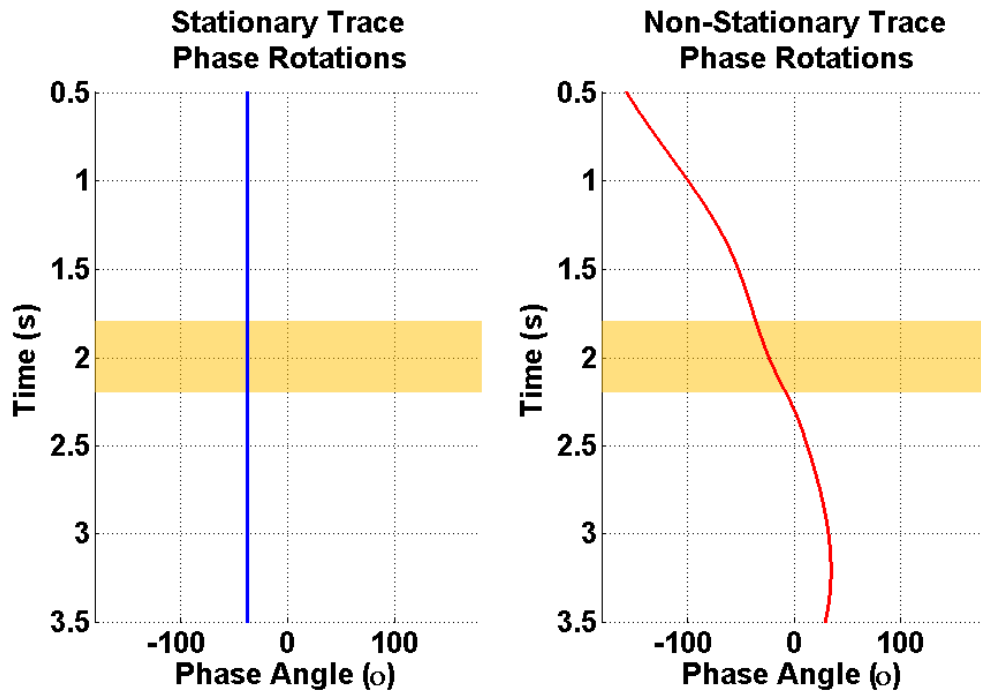


Figure 2.16: Phase rotations calculated for the stationary and nonstationary case. The yellow zone indicates the design window for the deconvolution.

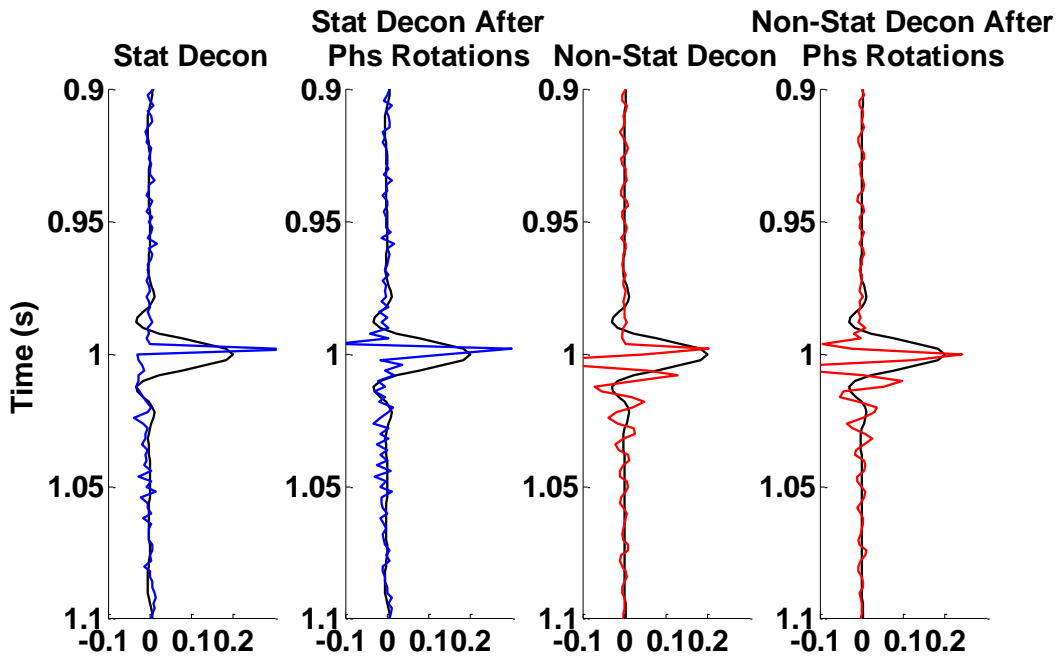


Figure 2.17: Signal at 1 seconds that shows the signal before and after phase rotations for both the stationary and nonstationary trace. The black signal is a zero phase band limited trace, which represents the ideal bandlimited solution.

A second example was created where there are still five strong reflection coefficients along a random spread of comparable reflection coefficients, Figure 2.18 and Figure 2.19. The same procedure was used as before but on this more complicated series. Phase rotations were calculated by centering a 200 ms window on the strong events and by also using 200 ms Gaussian windows incremented every 10 ms, Figure 2.20. Both methods of phase calculation match up very well. Figure 2.21, shows the phase rotated stationary and nonstationary trace after deconvolution for the event at 1 second. The stationary trace was mostly centered at the correct location to begin with but the nonstationary trace has now been slightly shifted such that the maximum energy is located at the correct position.

These examples show that when a nonstationary signal is deconvolved using the common stationary Wiener algorithm then time-variant residual phase remains in the data. It is important to correct for this as inversion requires that the maximum amount of energy in the wavelet be centered at the reflection coefficient. If this is not corrected for, the inversion will contain errors that can be misinterpreted. These errors are produced by phase rotations in the data up to 180 degrees. Even when the trace is stationary, a time-constant phase rotation can be detected although it may be very small. For real seismic data the data should be rotated with phase corrections determined by comparison to the well synthetic as the well synthetic, after calibration, will be held as the true solution and can be satisfactorily designed to be zero phase.

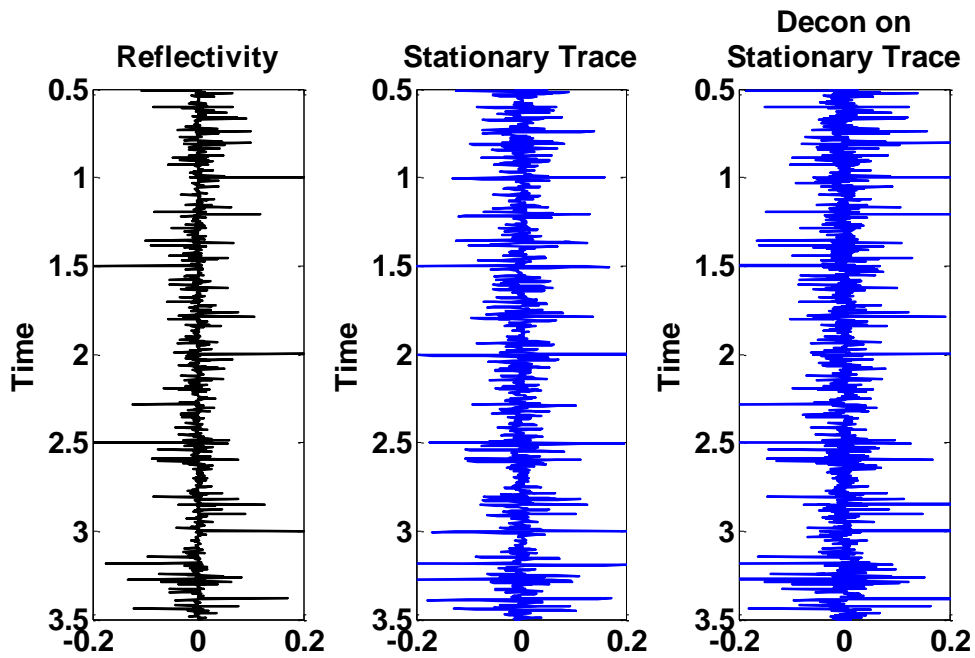


Figure 2.18: Reflectivity, signal and deconvolution using stationary methods.

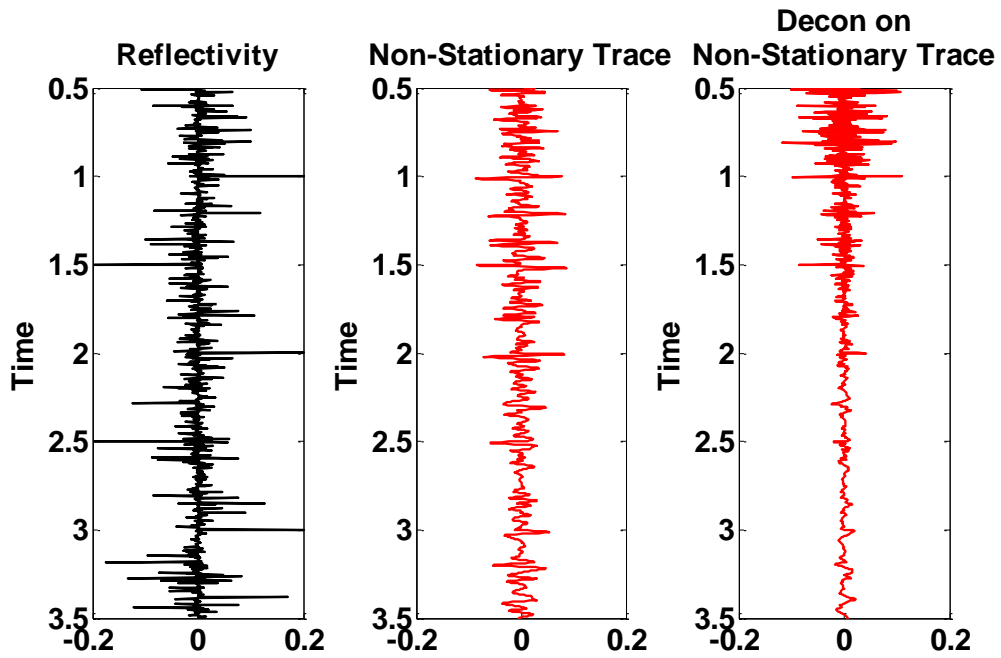


Figure 2.19: Reflectivity, signal and deconvolution using nonstationary methods.

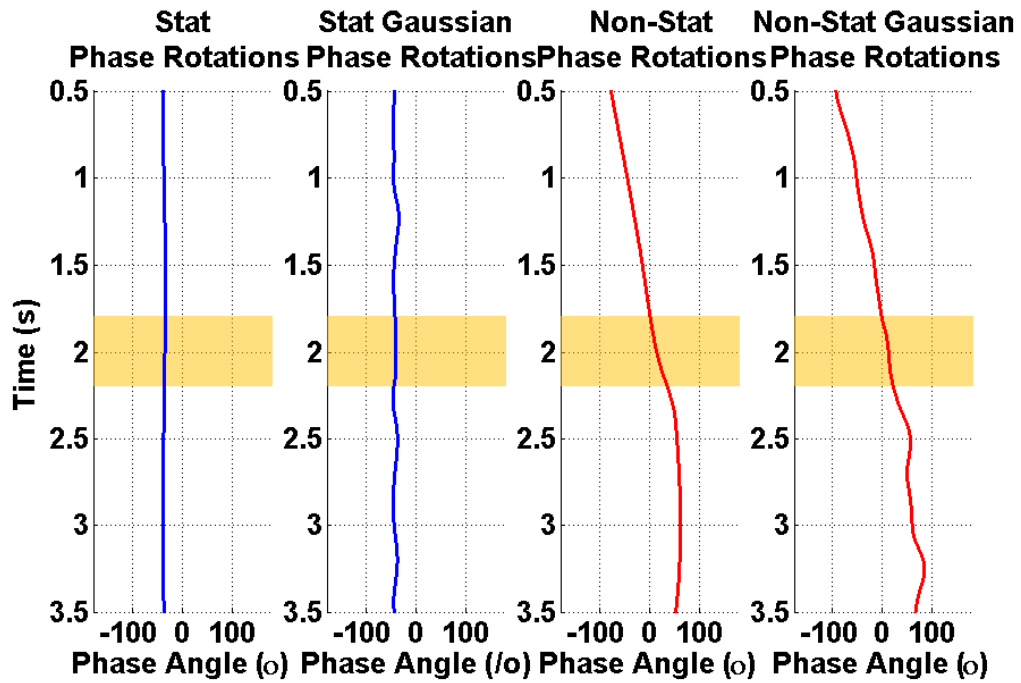


Figure 2.20: Phase rotations calculated in 200 ms windows centered at each strong event and then calculated for a set of 200 ms gaussian windows.

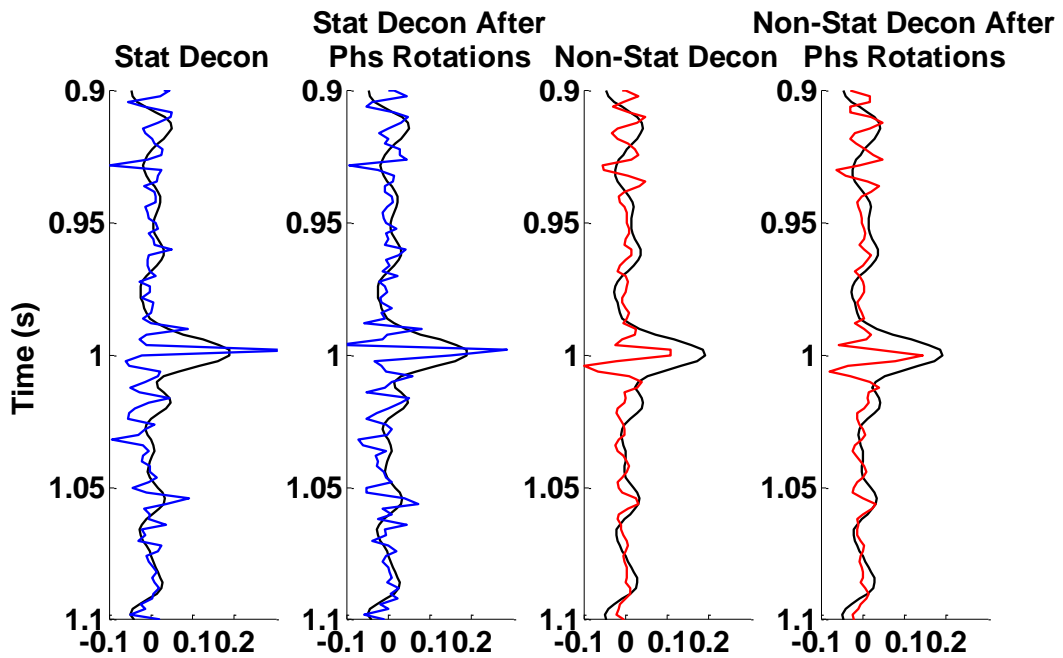


Figure 2.21: Signal at 1 second that shows the signal before and after phase rotations for both the stationary and nonstationary trace. The black signal is a zero phase band limited trace, which represents the ideally bandlimited solution.

2.4.2 Hussar Well Ties

For the Hussar data set, the synthetic bandlimited reflection coefficients and five seismic traces, averaged near the well location, were calibrated by using the Hilbert envelope method. Only two intervals were needed to get a good match, the first match interval targeted the overburden. Changes that occur in this interval can be large to correct for any surface inconsistencies between the well locations. The second match interval was similar for all wells (Table 2.1) at about 0.560 seconds. The adjustment needed was between 10 to 20 ms which is much higher than the values suggested by Stewart et al. (1984). The rock type in that interval is known to be shale, therefore with this in mind, the adjustment is accepted and would suggest a large attenuation in the interval.

Table 2.1: The match interval calibration data used for the Hilbert envelope well matching method.

	Match Interval 1	Difference	Match interval 2	Difference
Well 12-27	0.100 to 0.200 s	-0.020 s	0.570 to 0.880 s	0.010 s
Well 14-27	0.100 to 0.270 s	0.020 s	0.550 to 0.880 s	0.010 s
Well 14-35	0.080 to 0.270 s	0.020 s	0.560 to 0.890 s	0.020 s

To create the Synthetic seismograms, the reflection coefficients were calculated using the non-calibrated sonic log. They were then converted to time using the calibrated sonic to match the events with the seismic, these calibrated synthetics can be compared with the seismic trace in Figure 2.22.

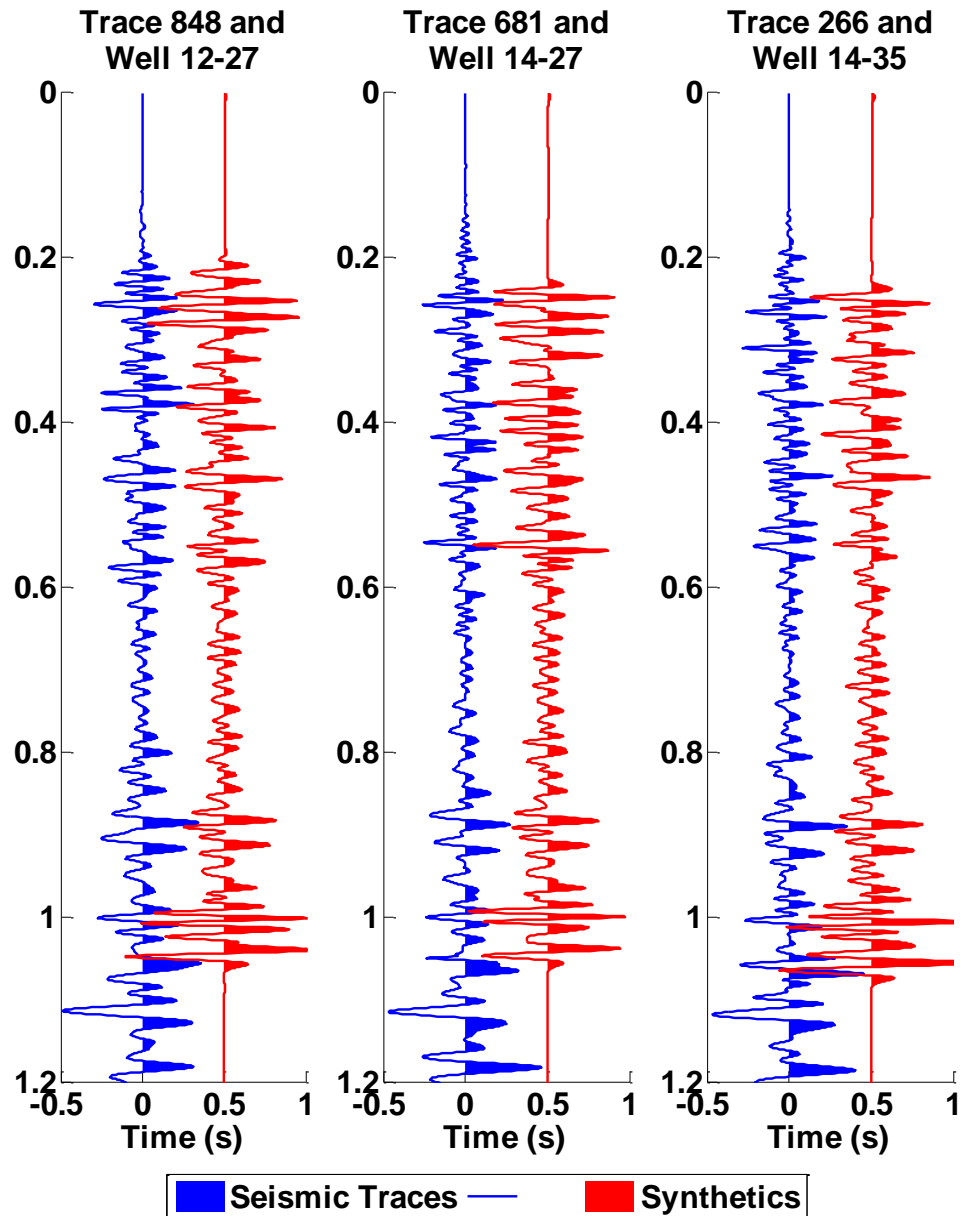


Figure 2.22: Seismic and synthetic well ties after Hilbert envelope matching process.

Since this result is meant to be used with inversion, the seismic data needs to be zero phase. Figure 2.22, shows the result after calibration and while the reservoir zone (0.880 – 1.050 seconds) matches up very nicely, events around 0.37 seconds appear to be 180° out of phase. This is evidence that there may be time-variant residual phase

rotations left over from the deconvolution process. Since there is a good match at the reservoir but not in the upper section a time variant phase rotation will be needed to match the data to the well.

To determine the best phase rotation to apply to phase rotate the seismic data, three different calculations were used to calculate the phase rotation angle. The first set of rotations used angles that were calculated by using the synthetic bandlimited reflection coefficients and the averaged five traces at each well location. The phase-rotated seismic traces and well-derived synthetic traces are compared in Figure 2.24. The phase angles that were used can be seen in Figure 2.23.

This method was the most accurate as shown in Table 2.2, where it has the lowest residual energy/ trace energy and the highest correlation at zero lag. If this well-tie method was to be used, then a laterally variant phase rotation would be applied to the seismic line. This is considered a dangerous interpretation practice because it can cause apparent stratigraphic changes where there are none. Unless there is very good evidence for applying a laterally variant phase rotation to the seismic a single phase rotation is preferred. To achieve this, the average of the individual phase rotations and a least squares phase rotations were calculated, Figure 2.25 and Figure 2.26, respectively. These phase rotations can also be found in Figure 2.23. The least squares method was calculated by creating one super trace that appended the three comparison traces end to end and then calculated the phase rotations by comparing the super trace to a super synthetic that appended the three synthetics end-to-end. The least squares solution is the better choice as it has a larger correlation at zero lag and less residual energy when compared to the

average phase rotations. The least square phase rotations were used to rotate the entire seismic section which can be seen in Figure 2.23.

Table 2.2: Goodness of fit measurements for phase rotated data. Θ_I represents phase rotations made using individual well comparisons. Θ_A represents rotations using the average phase rotations and Θ_{LS} represents using the rotations calculated by the least squares method.

	Residual Energy / Trace Energy			Correlation at Zero Lag		
	Θ_I	Θ_A	Θ_{LS}	Θ_I	Θ_A	Θ_{LS}
Well 12-27 and Trace 848	0.391	0.620	0.533	1.000	0.557	0.924
Well 14-27 and Trace 681	0.512	0.776	0.554	1.000	0.508	1.000
Well 14-35 and Trace 266	0.454	0.680	0.703	1.000	0.744	0.652

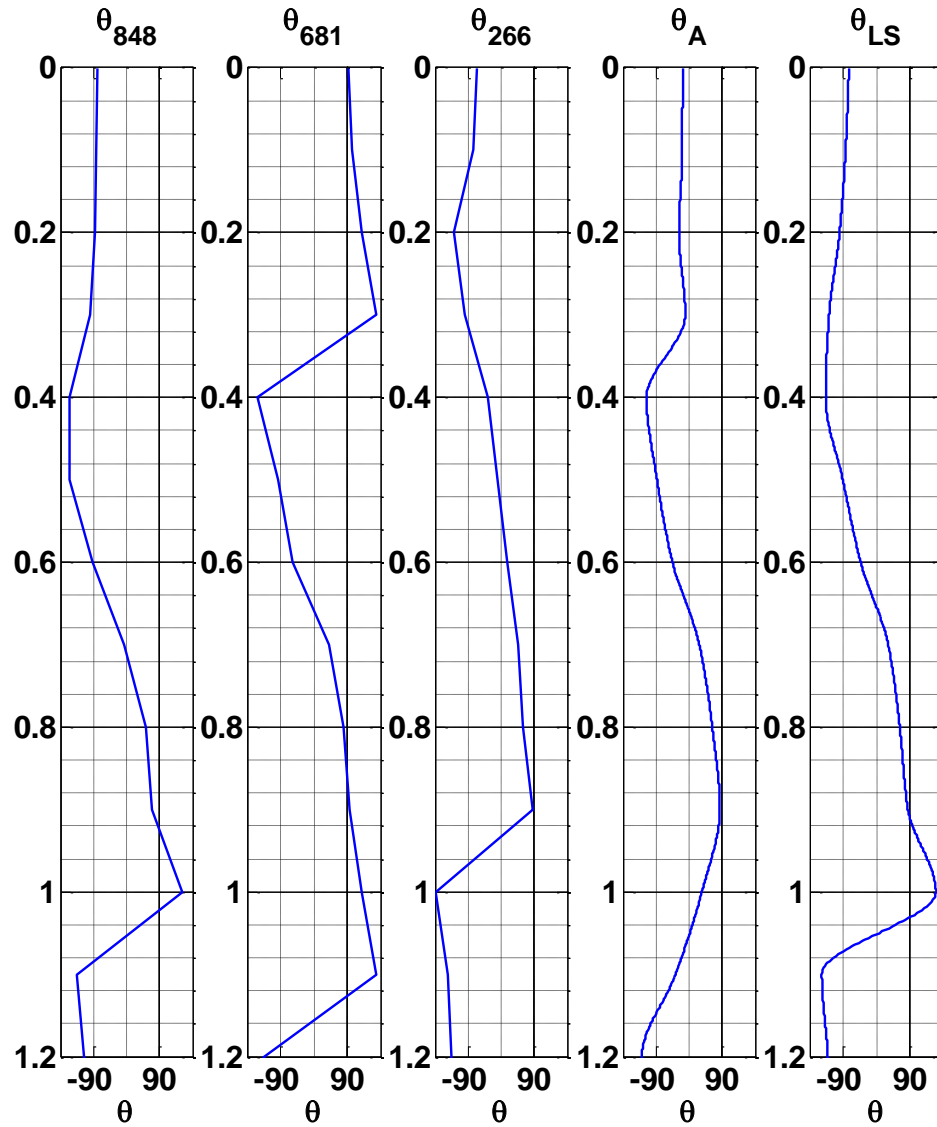


Figure 2.23: Time variant phase rotations calculated for each trace-well pair and the average of the three, as well as the least squares solution. well 12-27 corresponds to trace 848, well 14-27 corresponds to trace 681 and well 14-35 corresponds to trace 266.

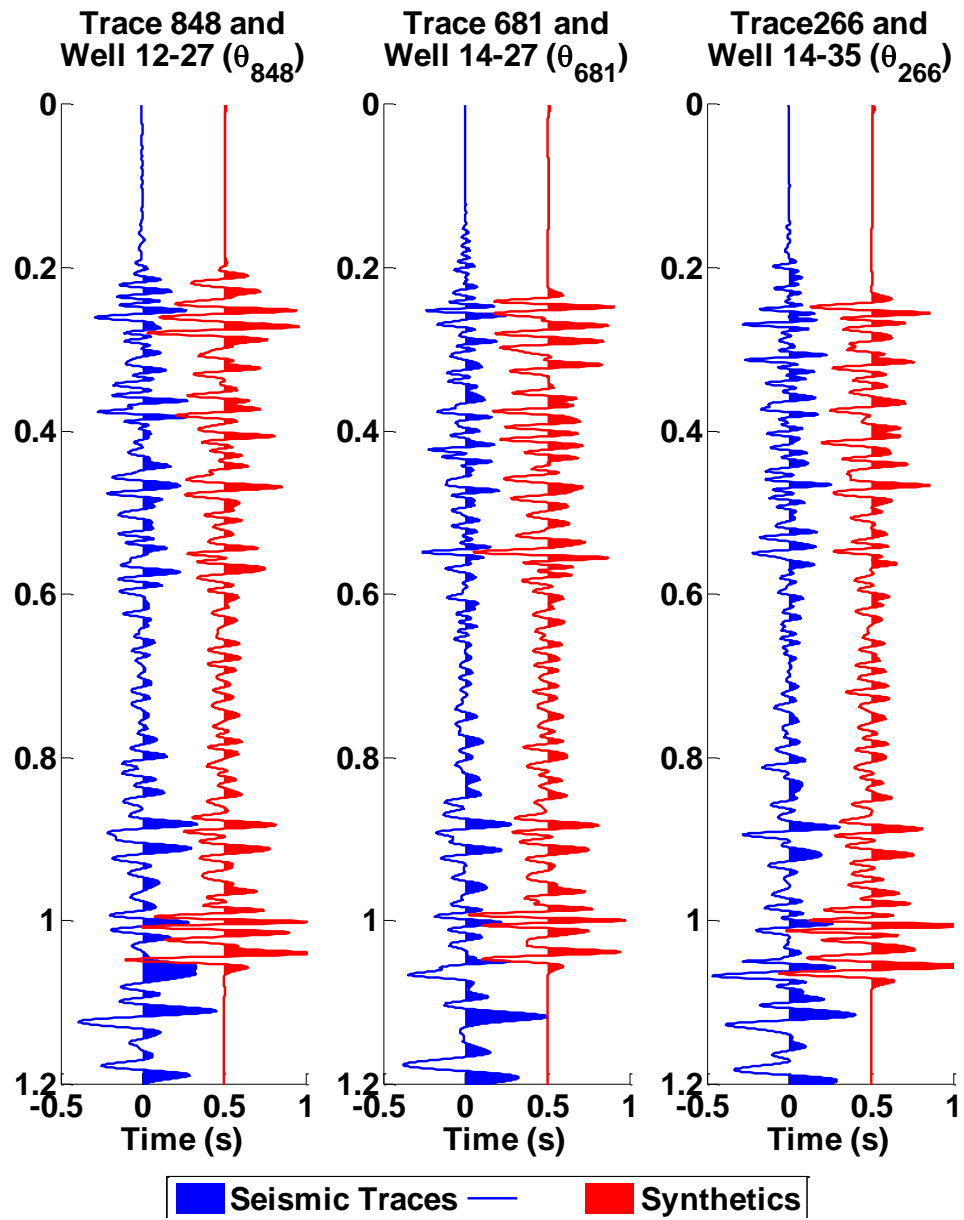


Figure 2.24: Well ties and Phase rotated seismic traces using phase angles calculated at each well location.

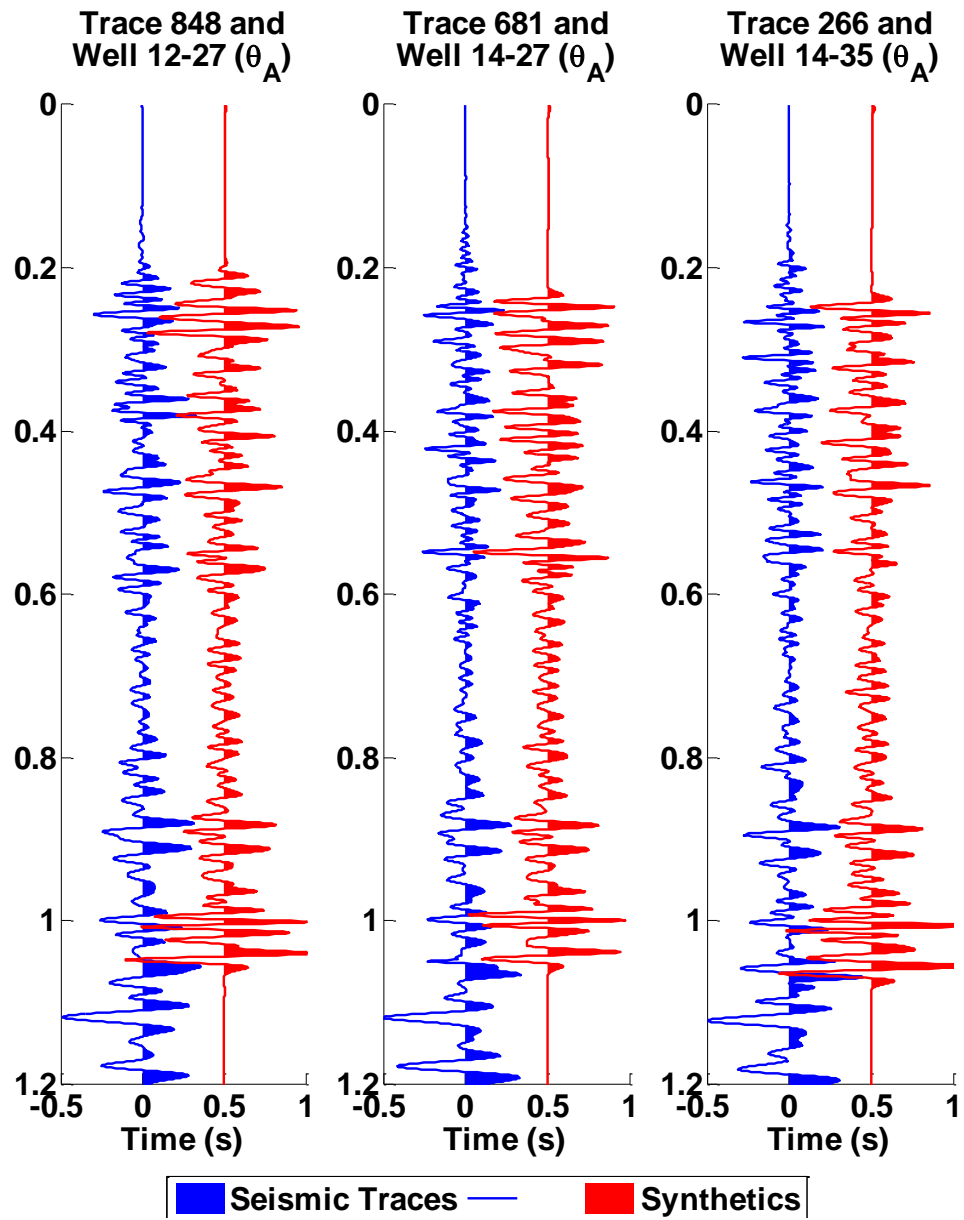


Figure 2.25: Well ties and phase rotated seismic traces using the average phase angles.

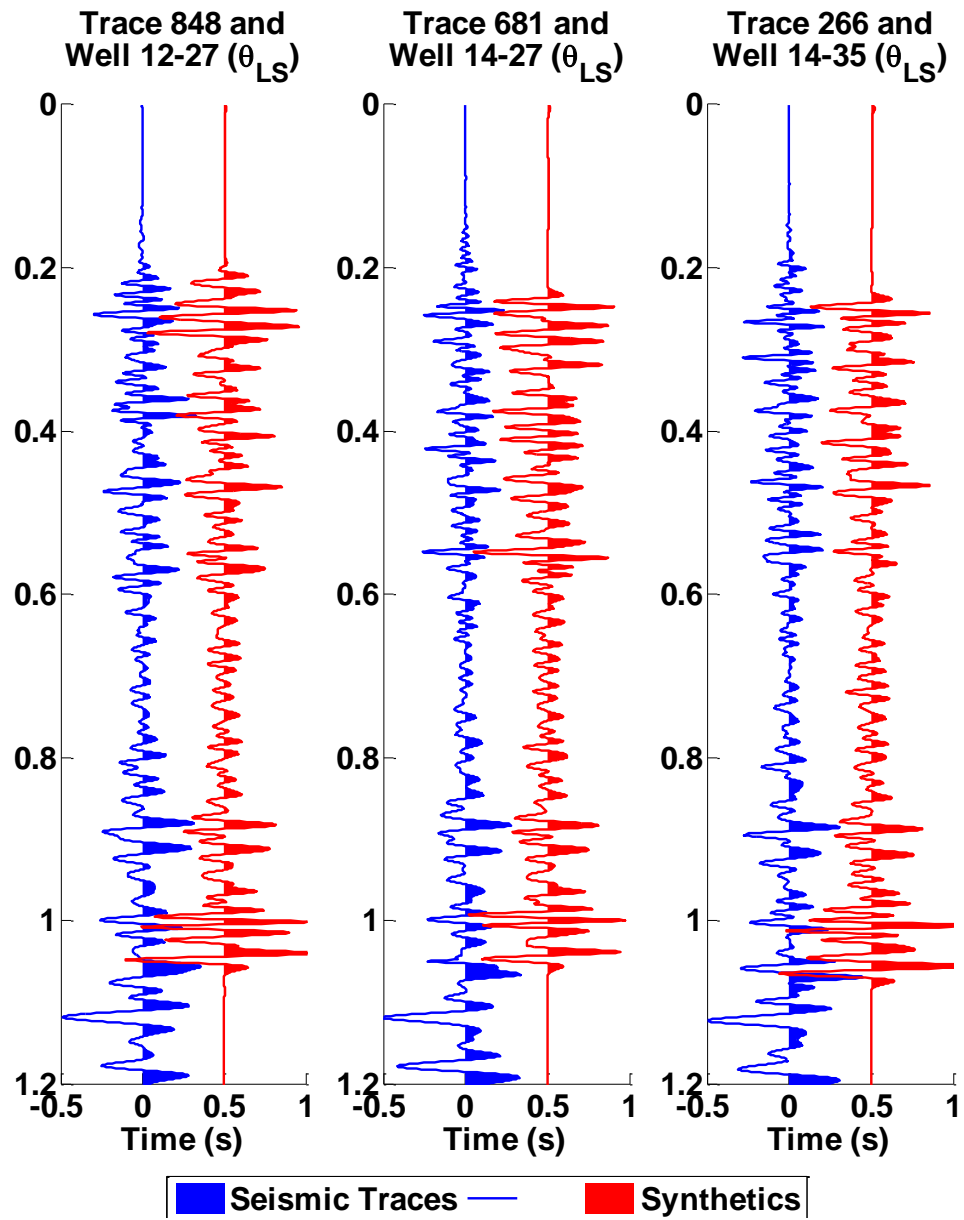


Figure 2.26: Well ties and phase rotated seismic traces using the least squares calculated phase angles .

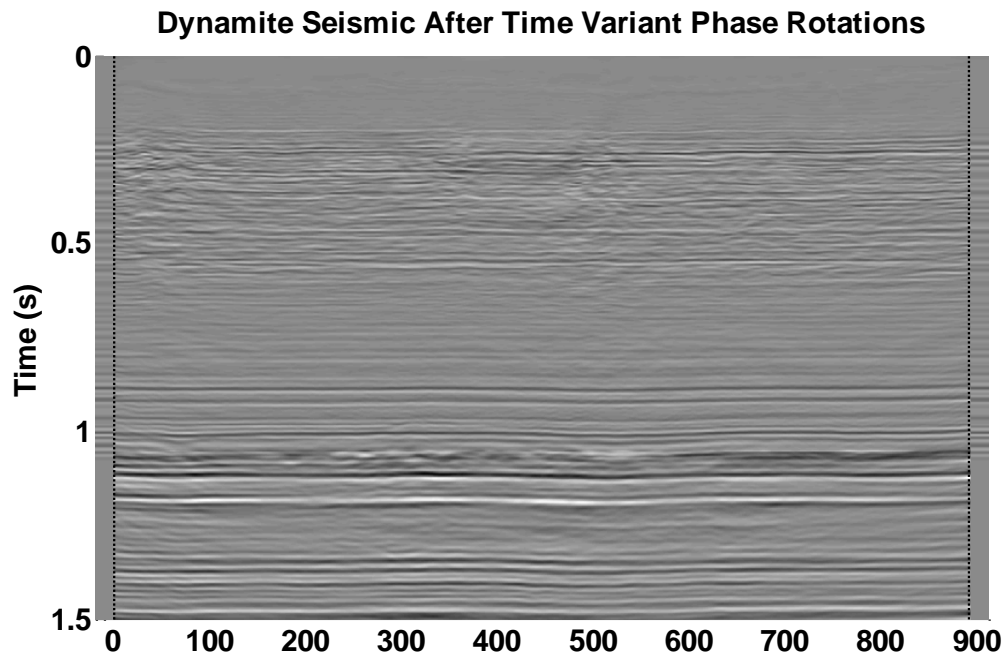


Figure 2.27: Time variant phase rotated seismic, with the average well synthetic trace plotted on both sides for comparison.

2.5 Final Results

The final corrected seismic section and well ties are shown in Figure 2.28. Many useful MATLAB programs were designed for the process of well tying and seismic amplitude and phase corrections. These are listed with a short description of their role in Appendix A. The process of computing an accurate well tie and conditioning the data can be very tedious but is extremely important to obtaining good results.

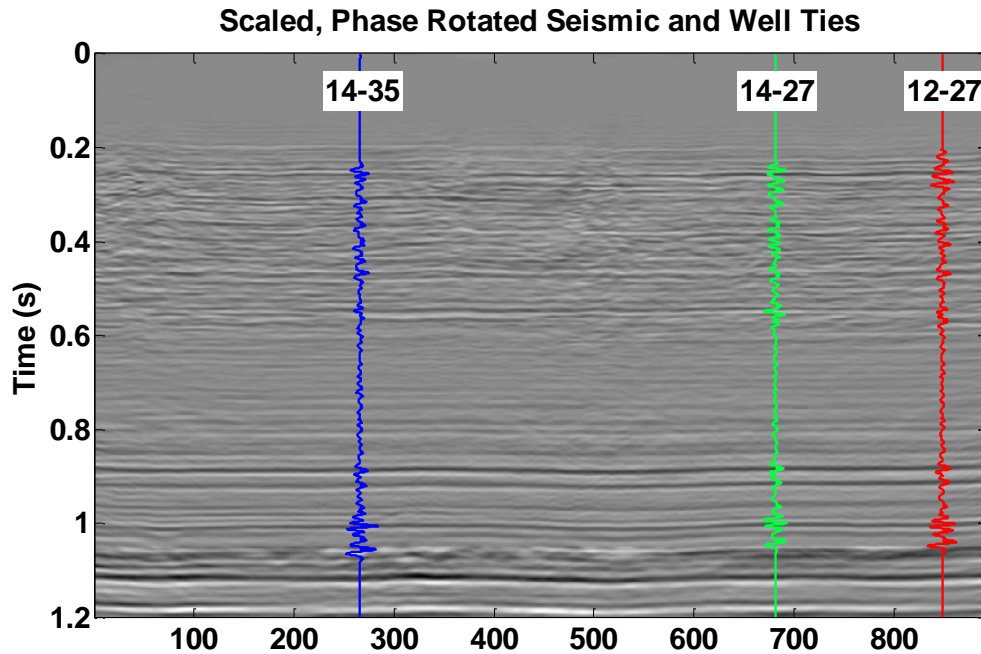


Figure 2.28: Final corrected seismic section and well ties.

2.6 Summary

- Processing can invalidate the amplitudes of seismic reflection events. Using time variant balancing with a reference well log can be a valid way of restoring the amplitudes.
- Reasonable overburdens need to be applied to well logs to assist in the well tying process. It is preferable to use a linear gradient so that artificial reflection coefficients are not created.
- Reasonable underburdens should be applied to well logs to lengthen the logs to match the seismic length. For convenience this can be done in the time domain.
- Anomalous log values need to be removed by either clipping or smoothing operations.

- Calibration of the time-depth relationship is essential for producing accurate impedance inversions. When VSP or check-shot data is not available using reflection event matching or Hilbert envelope lobe matching programs can be used.
- Hilbert envelope lobe matching produces better calibration than reflection event matching as it is insensitive to constant phase errors.
- Polynomials can be used to fit the amplitude spectra of the seismic reflectivity data when estimating a wavelet. Using a fourth order polynomial fit to the log of the amplitude spectra produces a very good result.
- Deconvolution causes time variant phase rotation errors. This can be corrected for using time-variant phase rotations. It is preferred that the same phase rotation is used on the entire reflectivity section so phase angles calculated using a least squares method for all wells is preferred.

Chapter Three: **BLIMP Method for Inversion**

3.1 Introduction

In 1978, Waters created SAIL (Seismic Approximate Impedance Log) which integrates the trace in the frequency domain to create an approximate impedance inversion. The results are very similar to using trace integration formula (Equation 1.5). This method lacks the introduction of low-frequency information from other data types and therefore only produces an approximate impedance log. In 1977, Lavergne and Willm, proposed using normal move out velocities to contribute low frequency information into the impedance version. They suggested using a linear trend as part of the low-frequency component. In 1979, Lindseth published an algorithm that added integrated traces to a filtered low-frequency data type. This method combines low-frequency information from well logs with the integrated trace in the time domain, Figure 3.1.

The BLIMP (BandLimited IMPedance) method (Ferguson and Margrave, 1996) is a simple but very powerful acoustic impedance technique. This method combines the integrated trace with low-frequency information from other data types in the frequency domain. While there are other methods, the BLIMP algorithm allows the user to input low-frequency information from any data type and uses the available signal band of the seismic to compute the impedance inversion. This method does not use additional high-frequency information from the well logs or other data types therefore the impedance inversion will always be under detailed when compared to the well impedance.

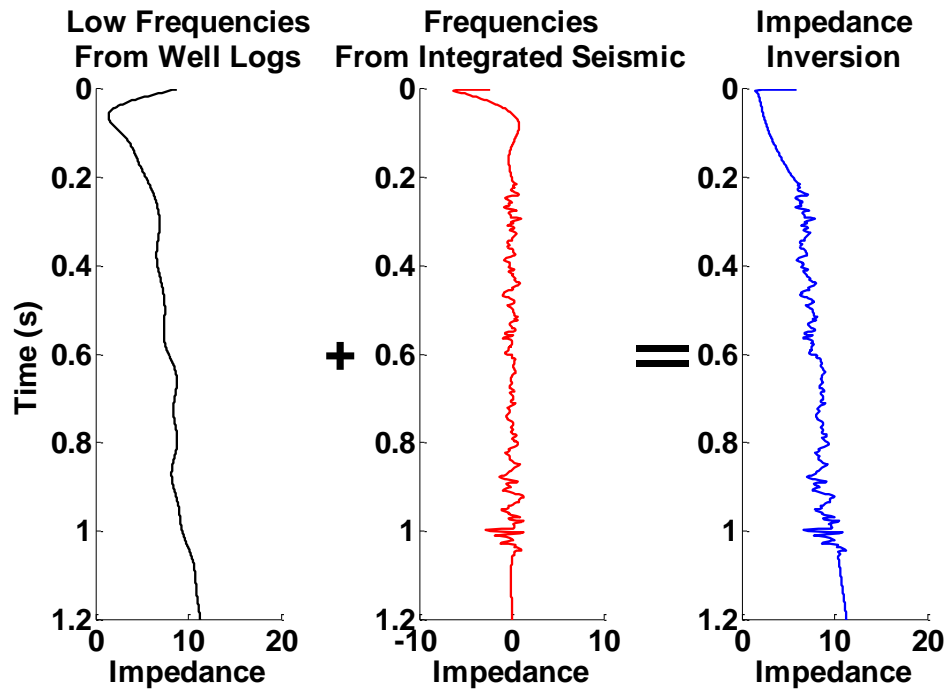


Figure 3.1: The low frequencies from a well log can be added to the seismic frequencies that have been integrated by the recursion formula to obtain an impedance inversion.

The method described by Lindseth (1979) is very similar to BLIMP where it combines low frequency content from the wells with the integrated seismic data using the recursion formula. The difference is that BLIMP removes a linear trend before filtering and scales the seismic trace to match the expected amplitude range of bandlimited reflectivity. It is not clear what kind of scaling is involved in the Lindseth method (1979). The low-frequency content from the well data type and the scaled integrated seismic are combined in the frequency domain. This result is then converted back into the time domain where the linear trend is then added to the inversion.

3.2 Theory

While the BLIMP method can use any low-frequency data type including well logs, stacking velocities and regional impedance trends, well logs will be used as the

example when describing the steps of the method. The BLIMP method uses the following steps to compute the inversion:

Step 1: If there is any structure in the area an impedance model must be created with spatially interpolated well logs (representing impedance) that follow the structure of the subsurface. Each trace in the section would then use the corresponding model data type. If there is no obvious structure the same well log can be used for the entire section.

Step 2: The second step is to remove the linear trend from the well log (Figure 3.2). This trend will later be added to the solution. Since the trend-removed log and the seismic trace are both zero mean, they can be compared to estimate the scale factor calculated in step 6.

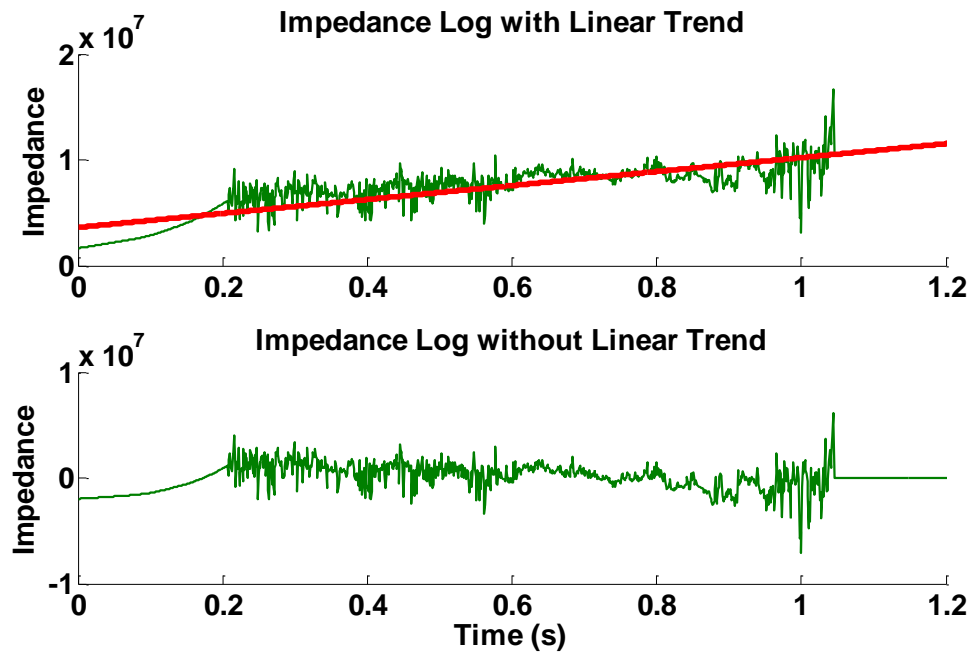


Figure 3.2: Impedance log before and after the linear trend is removed.

Step 3: The third step is to compute the Fourier spectrum of the de-trended impedance log. This step is important as the combination of the well log and seismic trace occurs in the frequency domain.

Step 4: The seismic trace is filtered using a high-pass filter whose lower limit is the low-frequency cut off (f_c) which is selected by the user. The optimal low-frequency cut off can be difficult to determine and methods for its selection will be discussed in section 3.3.2. The filtered trace is then integrated and exponentiated using the trace integration formula (Equation 1.5). The filtering in this step is important so that the power of samples outside the filter limits are minimized. This step is shown in Figure 3.3.

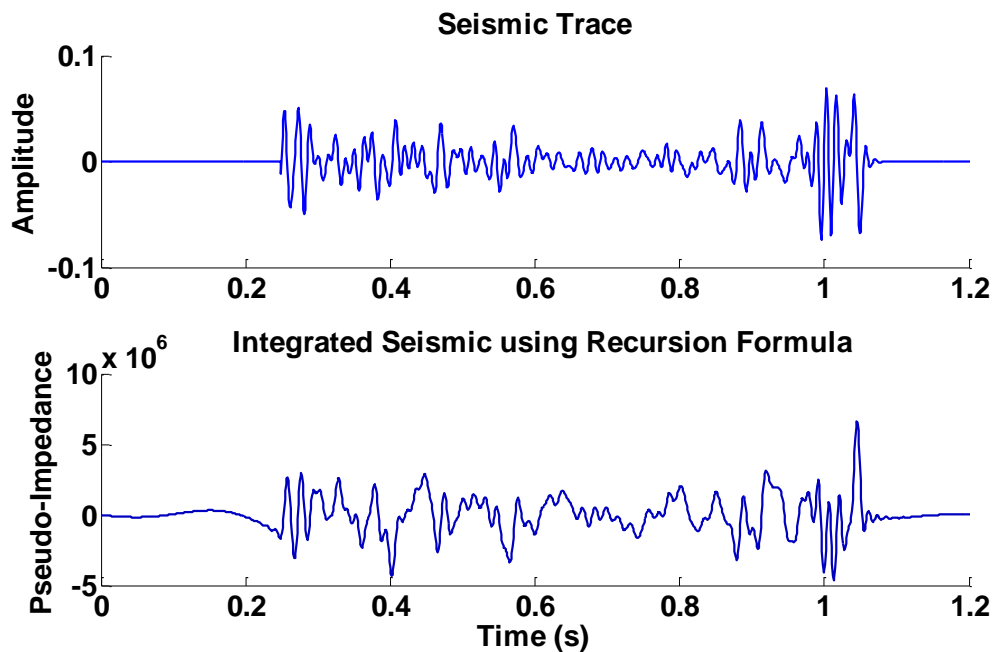


Figure 3.3: Seismic trace and the Pseudo-Impedance calculated using the recursion formula for a bandpass filter starting at 4.5 Hz to 75 Hz.

Step 5: The result from step 4 is transformed into the Fourier domain

Step 6: The amplitude spectrum of the seismic trace needs to be scaled to match the amplitude spectrum of the impedance log. This is done by calculating the mean power of the amplitude spectra and multiplying the amplitude spectrum of the trace by the scaling factor, Figure 3.4.

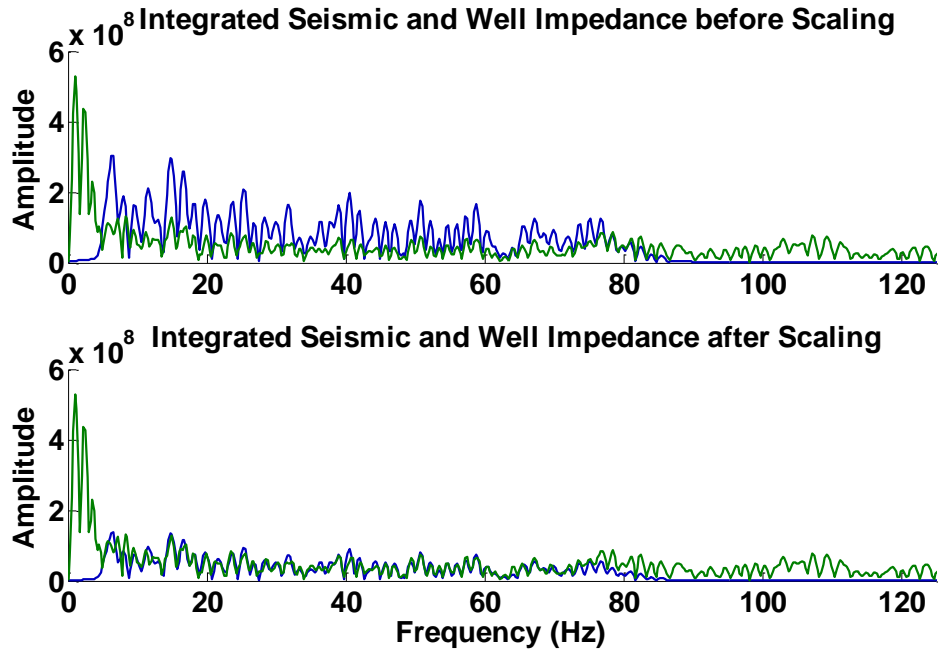


Figure 3.4: Integrated sonic and well impedance log before and after scaling.

Step 7: The next step is to apply a low-pass filter to the impedance log amplitude spectrum. This removes all of the high-frequency information of the impedance log and keeps the low-frequency information that is needed for the inversion. The low-pass value is called the low-frequency cut-off (f_c) and is selected by the user. This result is then added to the result from step 6, Figure 3.5 . This filter is chosen to be compatible with the high-pass filter applied to the seismic data such that they sum to unity.

Step 8: Once the well log low-frequency information has been combined with the scaled and integrated seismic data, the result is inverse Fourier transformed back into the time domain.

Step 9: The linear trend that was removed in step 2 is then added to the result of step 8, shown in Figure 3.6. This completes the impedance inversion.

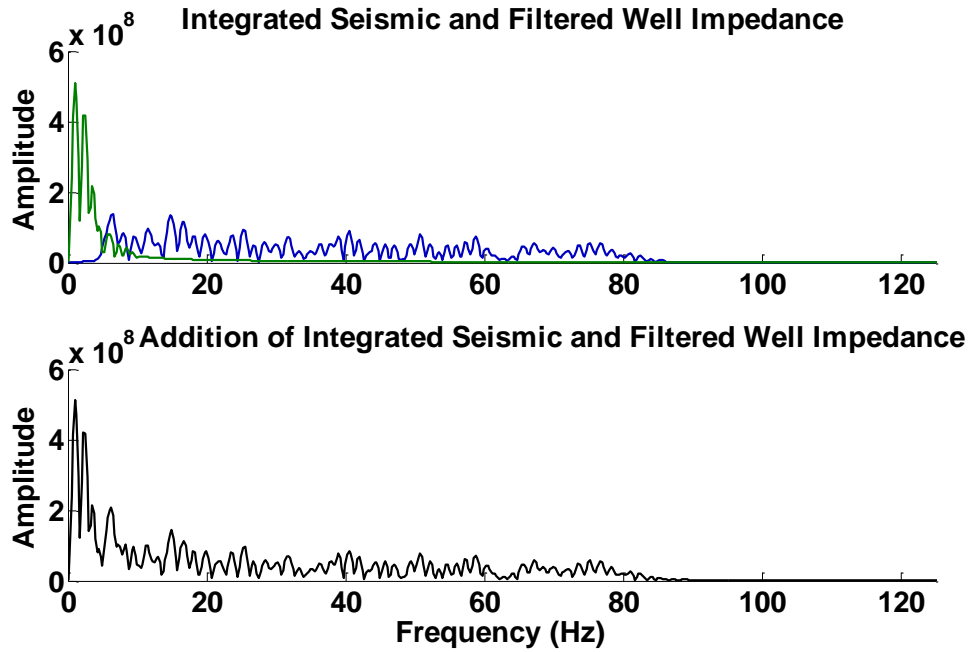


Figure 3.5: Integrated seismic and filtered well impedance are added together to form the impedance inversion without the linear trend. The low-frequency cut-off chose was 4.5 Hz.

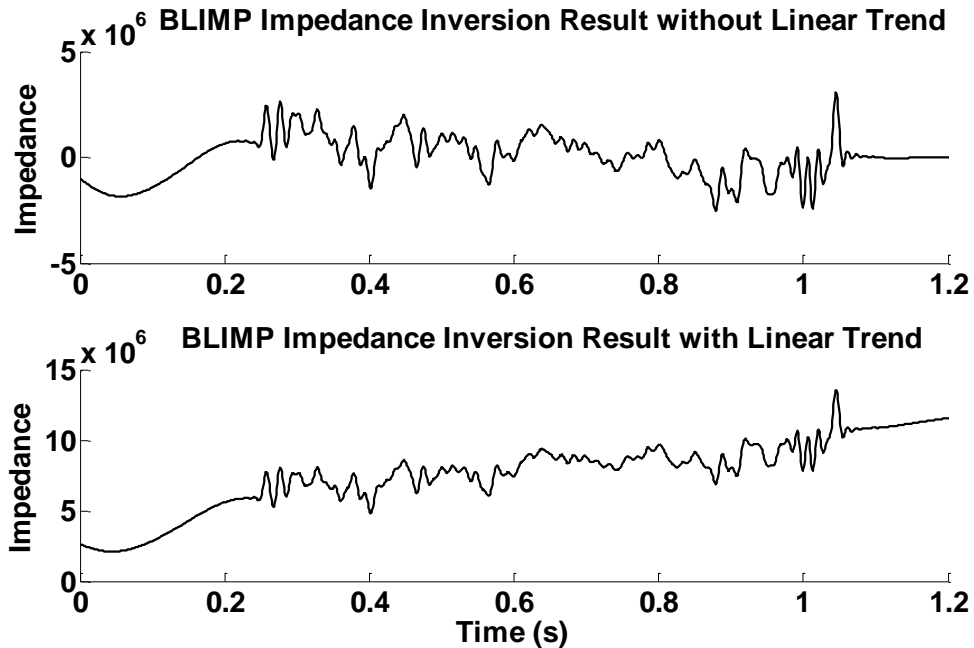


Figure 3.6: BLIMP impedance result with and without linear trend.

3.2.1 New method for calculating the scaling factor

In step 6 of the BLIMP method a scaling factor is determined and applied to the integrated trace. This factor is calculated in the frequency domain by finding the scalar that best matches the amplitude spectra of the well log and the integrated trace over the seismic frequency band. A simple equation to compute this scalar is

$$scalar == \frac{norm(b*I_S)}{norm(b*I_R)}, \quad 3.1$$

where norm is the L2 norm, b is a band pass filter that selects the seismic bandwidth, I_S is the the data type impedance (usually a well log), I_R is the integrated seismic data, and $*$ means convolution. Equation 3.5 can be computed in either the time for frequency domains since the L2 norm (i.e. power) is the same in both domains (Bracewell 2000, p119). This method works best if I_S is fully defined over the seismic bandwidth, which is true for well logs but not for other data types like stacking velocities.

When the linear trend that is calculated in step 2 is a good match to the well impedance this scalar produces good inversion results, however when the difference between the linear trend and well impedance is high, the scalar does not produce good inversion results. Linear trends have a significant amount of power in the low frequencies so when the linear trend is not a good match to the low-frequency data type, the residual (difference between the low-frequency data type and the linear trend) also has significant power in the low frequencies. Figure 3.7 shows well impedance with a linear trend that has a good fit, well impedance where the linear trend has a bad fit (the bad fit refers to the high error between the well impedance and the linear trend) to the data and the least squares fit to the stacking velocities. The linear trend that has the bad fit

was only fitted to the impedance well data between 200 and 600 ms, resulting in a trend that does not honor the whole impedance trace. Figure 3.8 shows the amplitude spectrum for the residual between the low-frequency data types and their linear trend. The data types with the bad fitting linear trends have higher amplitudes than a data type that has a good fit.

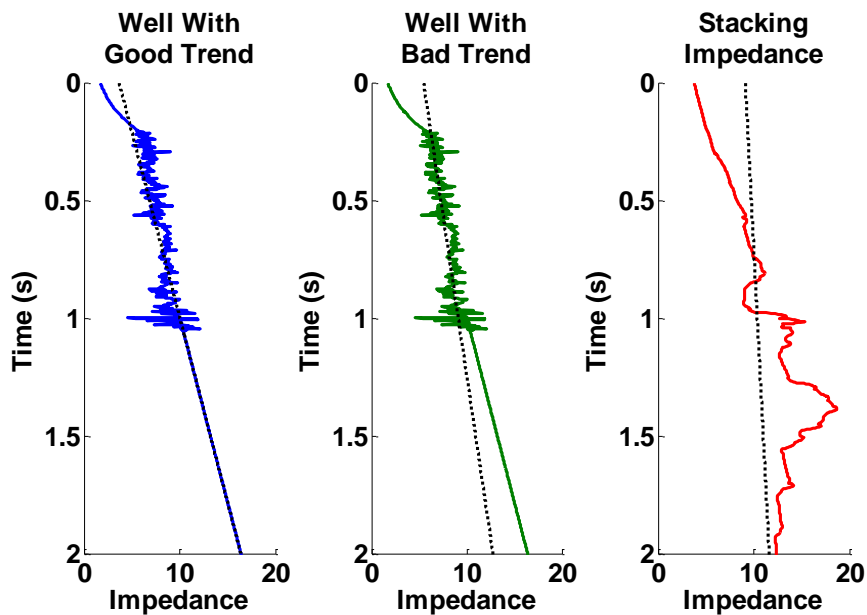


Figure 3.7: Various low-frequency data types with linear trends. The linear trend is a least squares fit to the data from 0 seconds to 4 seconds, so it does not always fit the data in the best way possible. For the well with the bad trend the linear trend was calculated from 200 to 600 ms.

When the scalar is calculated using a bad fitting linear trend the whole integrated trace is amplified by the scalar. This causes high amplitudes in the low frequencies as well as the high frequencies causing large errors in the inversion. To help with reducing the effect of the low-frequency power a threshold option has been implemented in BLIMP. If the low-frequency cut off is below the threshold the scalar will be calculated using the filtered data type spectrum from the threshold value to the high-frequency cut

off. This threshold is only used for calculating the scalar. The original low-frequency cut off is still used in applying a low pass filter to the impedance data type and adding it to the scaled integrated trace.

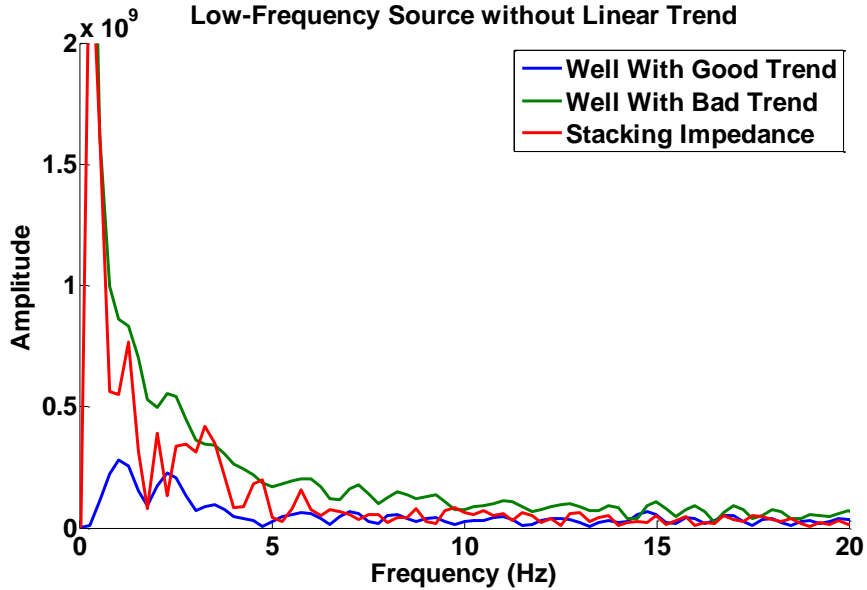


Figure 3.8: The frequency spectrum of the residual impedance data type. Data types with a bad linear trend have high power in the low frequencies where a linear trend with a good fit has lower in the low frequencies.

Figure 3.9 shows the scaling factor computed without a threshold when the linear fit is bad. This shows that the scalar is highly variable with the choice of the cut-off value. This is not desirable as the scaling of the integrated trace should be independent of the low-frequency cut-off. For well data it is common for the scaling value to stabilize at about 20 Hz. For impedance from stacking velocities the threshold value may need to be lower than 20 Hz as the stacking impedance tends to contain less high-frequency information than well logs causing the scaling factor to become unstable for low-frequency cut offs above 20 Hz.

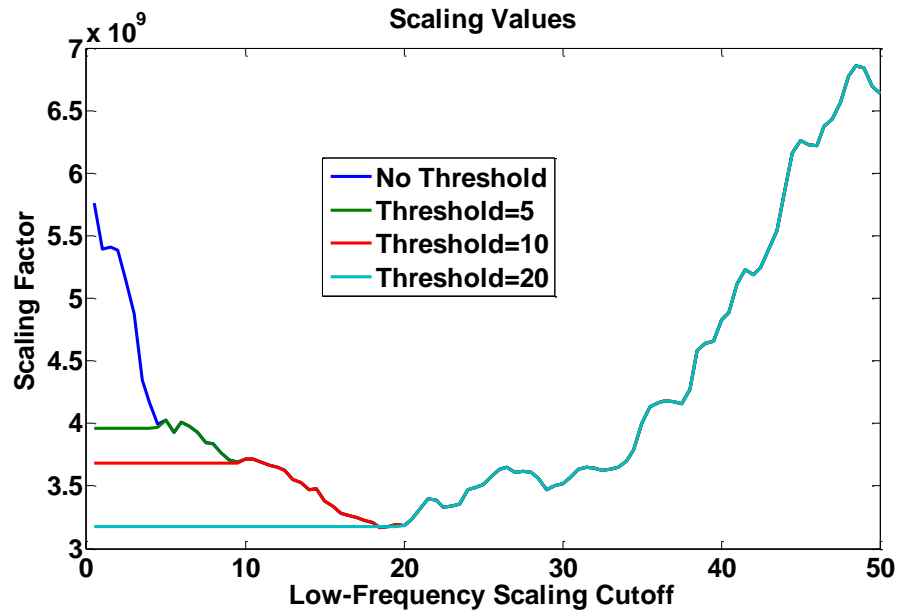


Figure 3.9: Scaling values calculated for various low-frequency scaling cut offs. Threshold values help stabilize the effect of a bad linear fit.

For all of the impedance inversions, unless otherwise noted, will be calculated using the new scaling threshold method. It produces more stable inversions at low frequencies which is important when pushing the low-frequency cut off as low as possible.

3.2.2 *BLIMP low-frequency input*

The BLIMP method inputs low-frequency information into the inversion at two different stages. The first way BLIMP imports low-frequency information is in the low-pass frequencies from the well log input. This information is computed from the trend-removed log. The second way BLIMP imports low-frequency information is adding the linear trend, removed in step 2, back into the inversion. The filter keeps the low frequencies from 0 Hz to the low-frequency cut off and then applies a taper on the high end of the filter. This taper was selected to be 0.25 Hz for all inversion in this chapter so

the filter would remain stable but the additional low-frequencies added by the taper would be minimal. These low frequencies are important for inputting character into the impedance inversion, see section 1.2. To compute an accurate inversion the low-frequency cut-off must be chosen with care. If the cut-off is too low, low-frequency noise from the seismic data will contaminate the inversion. If the cut-off is too high, the inversion is overwhelmed by well information and subtle details from the seismic data cannot be seen.

Without the low-frequency input from a well log or stacking impedance data type the impedance inversion will not be correct. Figure 3.10a shows the contribution of the low-pass well impedance and linear trend. Even though the low-pass well impedance has less amplitude at low-frequencies than the linear trend it is still essential in producing an accurate impedance inversion.

The second way low frequencies are added to the inversion is the linear trend. The linear trend contains high amplitude low-frequency information including the necessary amplitudes at 0 Hz, also known as the DC Spike. A linear trend contains strong low-frequency content ranging from zero to about 20 Hz. Most of this energy is focused from about 0 Hz to about 6 Hz (Figure 3.10b). The DC Spike is responsible for the largest influence on the inversion without it the impedance inversion will not have the proper trend. Even with a correct linear trend the impedance still needs the low-pass well contribution. Figure 3.11 shows that an impedance inversion only using the linear trend for low frequencies is significantly different from the filtered well impedance at 1.2 seconds. The BLIMP inversion that contains both the linear trend and the low-pass well contribution produces a more accurate inversion.

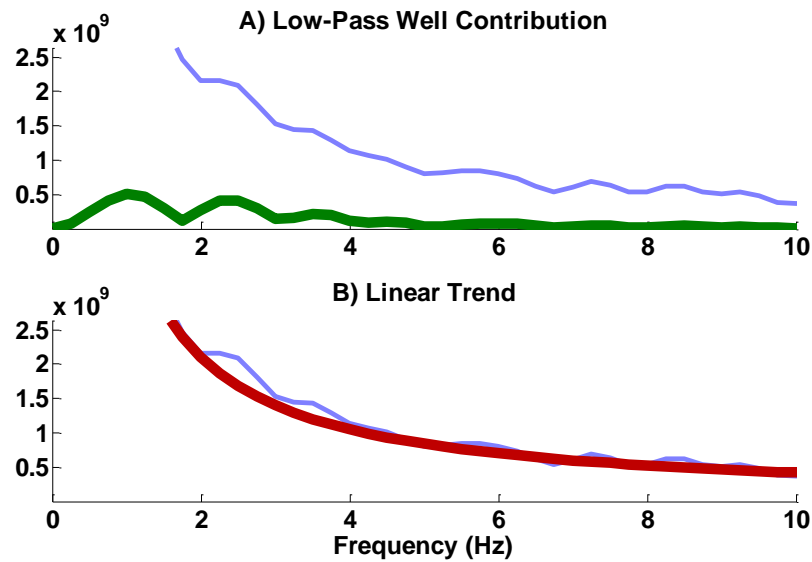


Figure 3.10: The contribution from the low-pass well contribution and linear trend. The blue curve is the impedance inversion. The red curve is the amplitude spectrum of the linear trend and the green curve contribution from the low-pass filtered log, filtered with a [0 0 5 10] low-pass filter. This has been zoomed in to show detail at the low frequencies. Both the impedance inversion and linear trend continue to an amplitude of 6.7×10^{10} at 0 Hz.

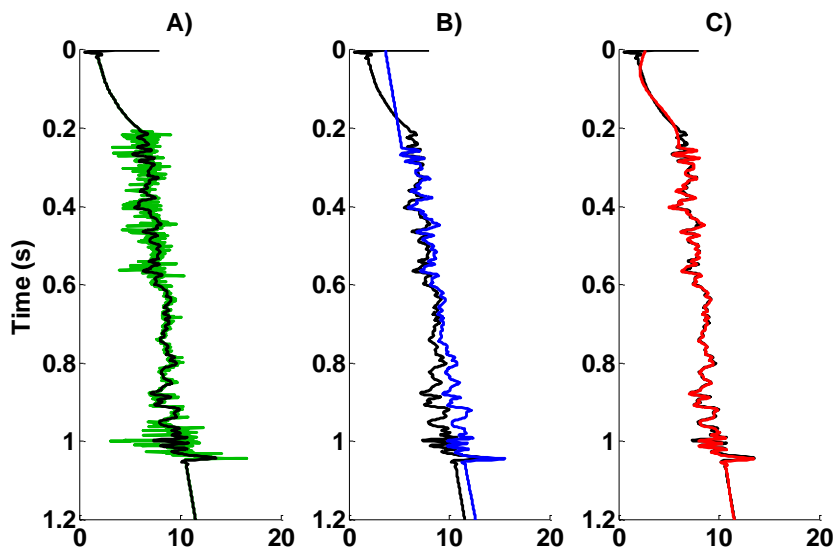


Figure 3.11: Panel A shows the true impedance in green and the low-pass filtered ([0 0 75 100] impedance log in black. Panel B shows an inversion where just the linear trend is used in blue and the low-pass filtered log in black. Panel C shows the inversion using the BLIMP method in red and the low-pass filtered impedance log in black.

3.3 Low-frequency data type: well logs

As described in the section 3.2, well logs can be used for low-frequency input in acoustic impedance inversion, in the BLIMP method. As part of the impedance inversion process choosing a low-frequency cut off is essential to an accurate and reliable impedance inversion. Choosing this low-frequency cut off can be very difficult and may require additional tools to analyze the optimal low-frequency cut off.

3.3.1 Qualitative analysis of impedance images

Figure 3.12, Figure 3.13, and Figure 3.14 illustrate what occurs when the low-frequency cut off is either too low, in the right range, or too high, respectively. The low-frequency input was from an average impedance well log which was prepared by matching key events from the impedance well logs and then averaging them. When the low-frequency cut off is too low noise is more noticeable such as the pump jack noise indicated by Ellipse A. Layer boundaries are also discontinuous indicated by Ellipse C and the impedance values are dissimilar from the impedance values of the well logs. If the layer boundaries are not continuous this signifies that the seismic data still has significant noise at the cut off frequency. For convenience the impedance section plots contain a well log on the sides of the impedance image separated by black dashed lines. This is to aid in the interpretation and determine the quality of the inversion.

When the low-frequency cut off is in the optimal range (Figure 3.13) the seismic dominates the section and the wells only provide a small amount of information such as trend. This results in the acoustic impedance inversion being true to the seismic. These sections can still contain noise such as the pump jack signature shown in Ellipse A. When the impedance is in the right range the horizons become continuous as seen in the

seismic. The impedance values of the section are also similar to the impedance values in the wells showing that the inversion is a good approximation to the subsurface impedance.

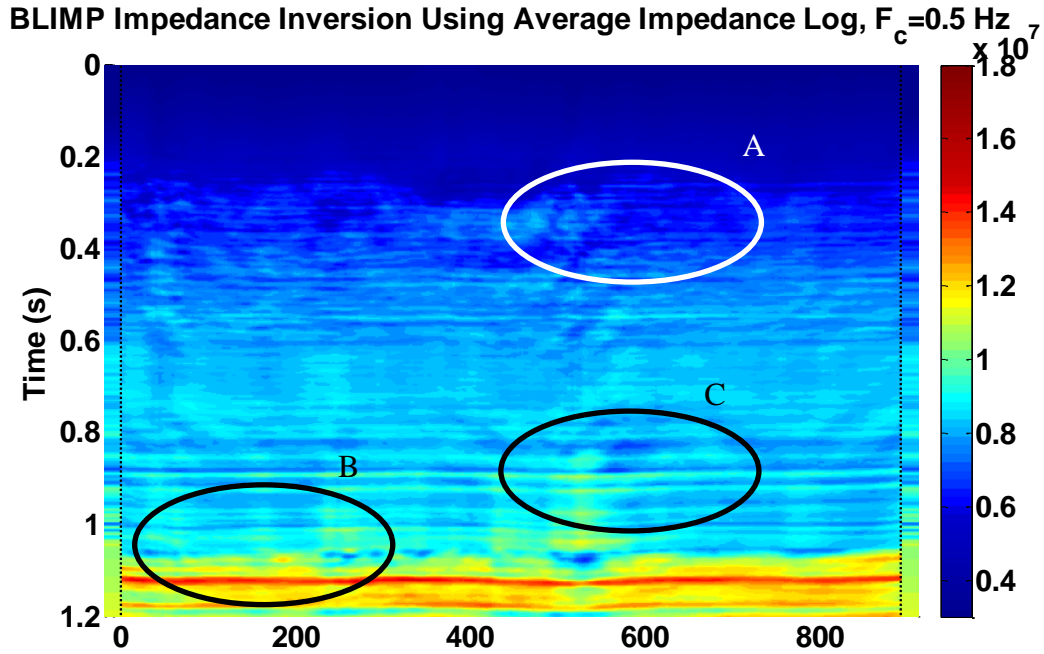


Figure 3.12: This figure shows the effects of an impedance section when the low-frequency cut off is too low (0.5 Hz). Noise from the pump jack can be seen in the ellipse labeled A. The impedance values of the layers indicated by the ellipse labelled B are much higher than the impedance values from the well log. The well log used for the low-frequency contribution is shown on either side of the section and are separated by a dashed black line. Ellipse C indicates that the layers are not continuous for this section. Since these are strong reflections continuous reflectors would be expected.

When a low-frequency cut off is chosen to be too high the section becomes very consistent by matching the well impedance too closely (Figure 3.13). In this impedance image the pump jack noise is more attenuated than in the two previous sections. The impedance values of the image are very close to the impedance values seen in the impedance log. The most concerning event is shown by Ellipse C. In this area a horizon

that is seen in the well log begins to show in the impedance image. This event was not seen in the seismic. This means that the low-frequency seismic information has been overridden by the well information. This can lead to the impedance image missing subtleties that are important in interpretation processes.

While these qualitative judgements are useful to determine the quality of an inversion at a glance more quantitative methods are needed to determine if the choice of cut off frequency is appropriate.

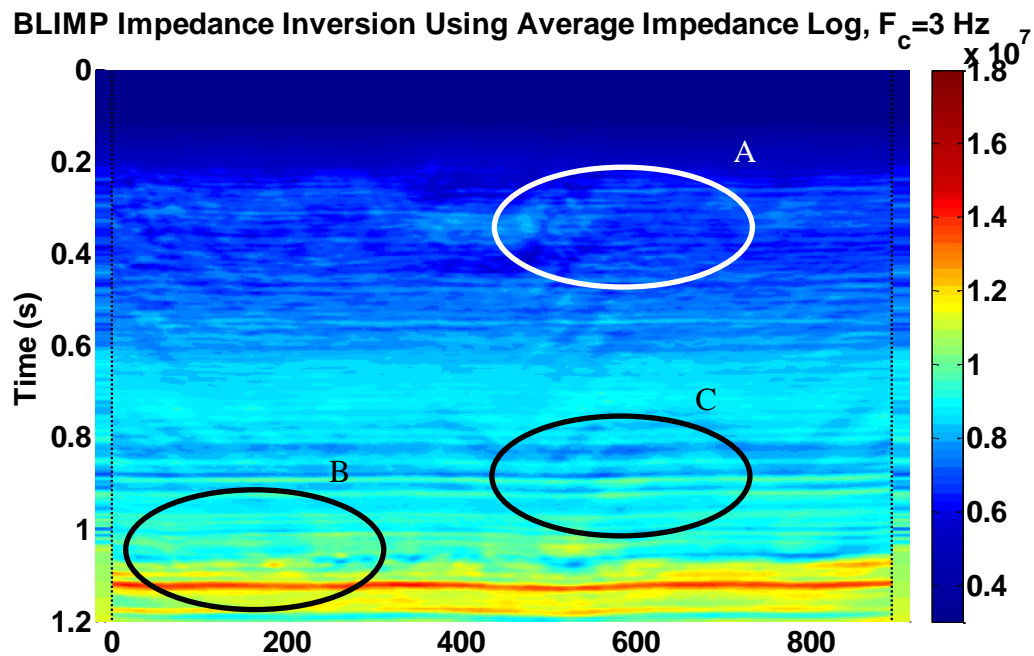


Figure 3.13: This inversion has a cut-off that is a reasonable range (3 Hz). In Ellipse A there is slight pump jack noise. In Ellipse B the impedance values of the section are close to the impedance values of the well log that is shown on the sides of the inversion separated by the dashed lines. In Ellipse C the reflections are continuous.

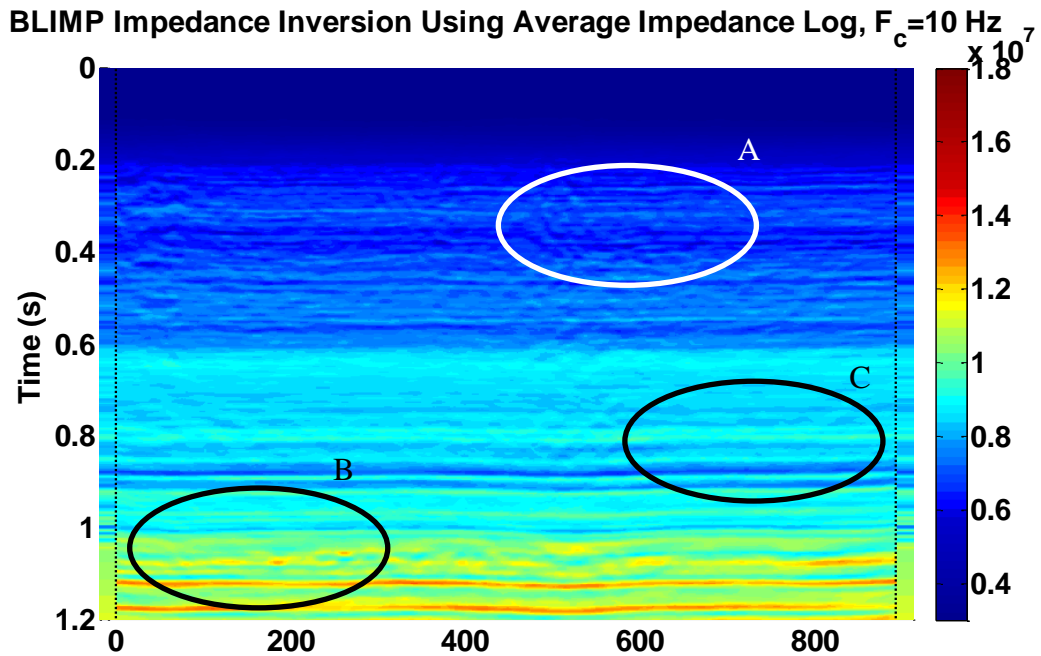


Figure 3.14: This inversion shows a case where the low-frequency cut-off is too high. Ellipse A shows very slight noise from the pump jack located near trace 681. Ellipse B shows impedance values that are within the range of the well log shown on either side of the impedance section and separated by dashed black lines. Ellipse C shows where events not present in the seismic image but present in the well logs are starting to appear in the impedance section.

3.3.2 Low-frequency cut-off determination

To determine at which cut-off frequency the inversion becomes stable, impedance inversions are computed using one trace and well pair for various low-frequency cut offs. Figure 3.15, Figure 3.16, Figure 3.17, and Figure 3.18 show these tests using well 12-27 and trace 848, well 14-27 and trace 681, well 14-35 and trace 266, and using an average impedance log and an average trace, respectively. The average trace was prepared by taking five traces from each well location matching key events and then averaging them. The rate of change between each inversion is very high when the cut off is too low but become very stable when the cut off is very high. The optimal low-frequency cut off for

the well trace pair occurs where there is transition from the rapid change to stability.

Figure 3.19 shows the normalized difference between one low-frequency cut off inversion and the next for all trace-well pair's. This normalized curve forms an L shape so the optimal low-frequency cut off would be at the corner of the L-curve, for this data the cut off would be between 2 and 3 Hz.

Figure 3.20 shows BLIMP impedance inversions for sections using cut offs between 1.5 Hz and 4 Hz. This is another way to analyze if a low-frequency cut off is suitable. Ideally the low-frequency cut off would be the lowest frequency for which reliable impedance sections are produced. The 4 Hz result looks like the low-frequencies in the seismic signal band are being overridden, so it does not make the best use of the seismic data. The 2.5 Hz, 3 Hz and 3.5 Hz impedance inversions all look very similar so it could be argued that a cut off of 2.5 Hz is acceptable for this inversion.

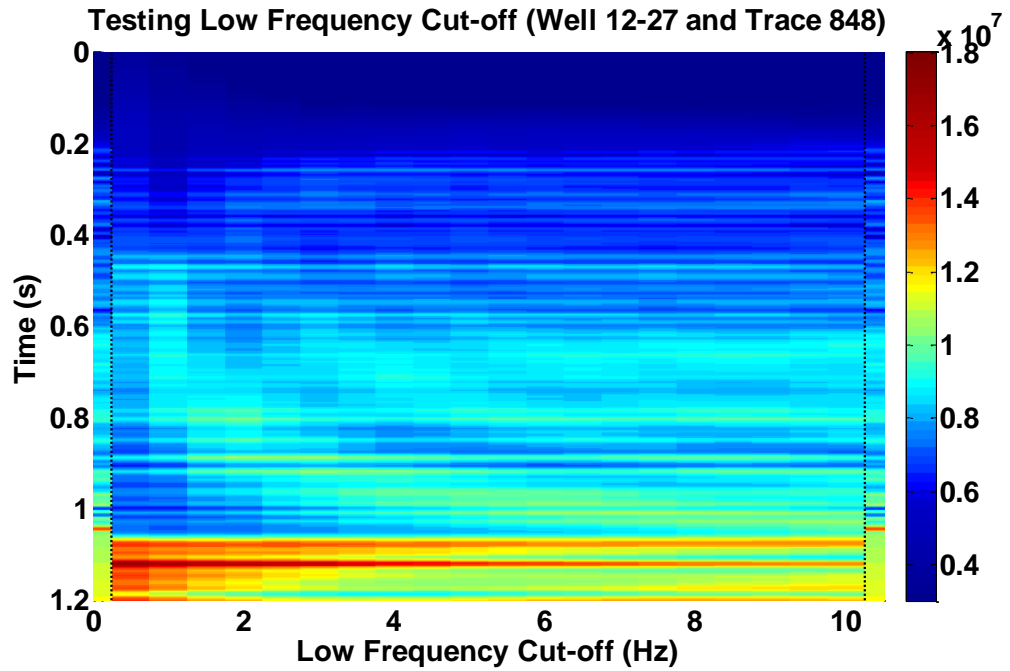


Figure 3.15: BLIMP impedance inversions using trace 848 and well 12-27 for various low-frequency cut offs. On the sides of the section is a low-pass filtered impedance log from well 12-27 for reference.

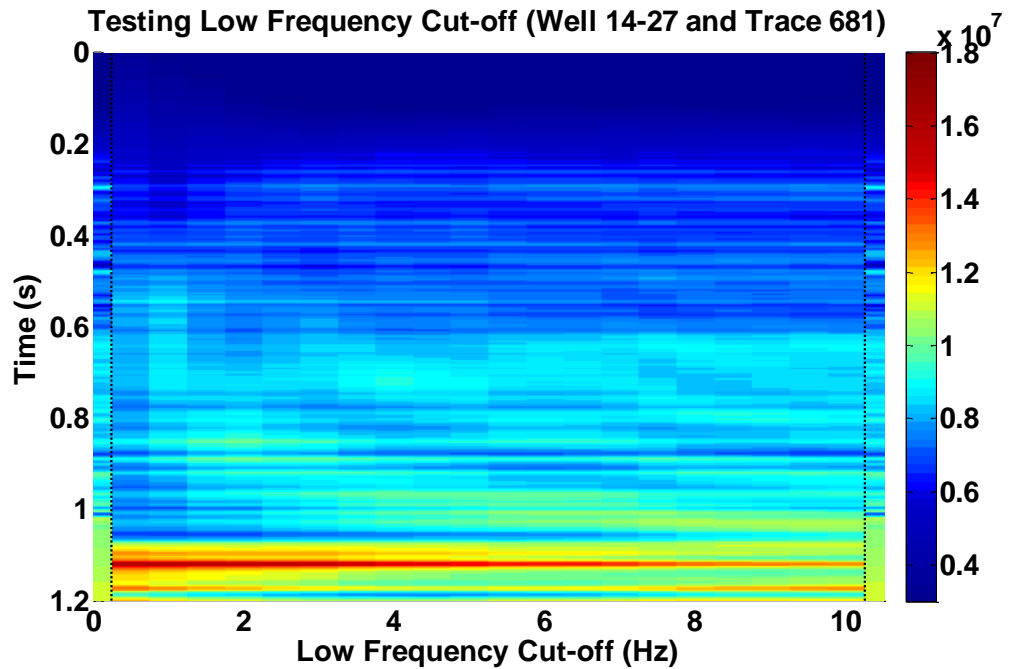


Figure 3.16: BLIMP impedance inversions using trace 681 and well 14-27 for various low-frequency cut offs. On the sides of the section is a low-pass filtered impedance log from well 14-27 for reference.

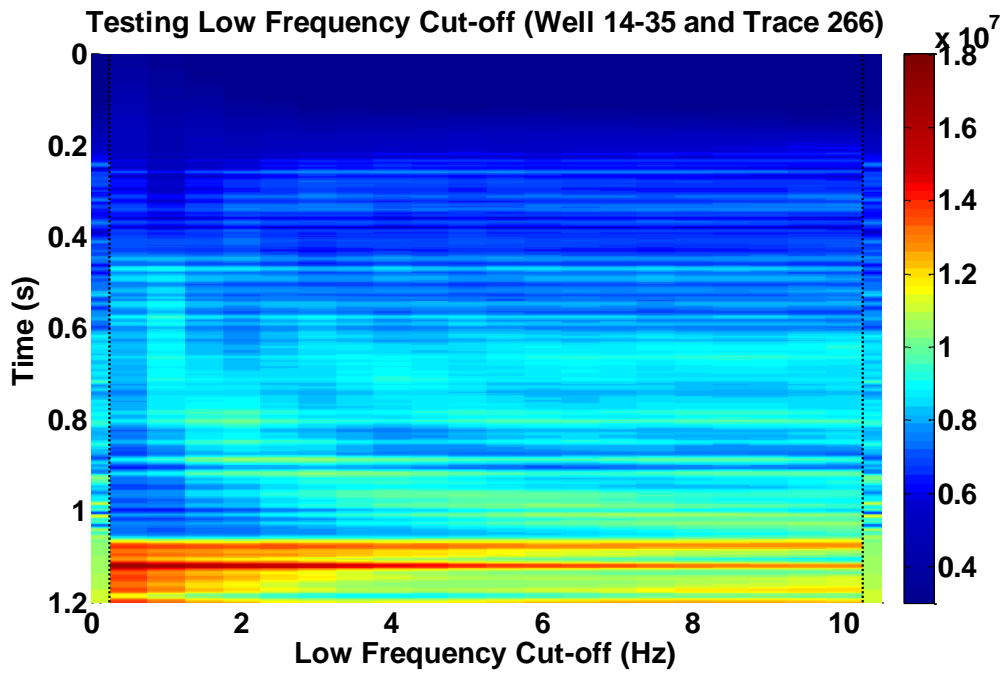


Figure 3.17: BLIMP impedance inversions using trace 266 and well 14-35 for various low-frequency cut offs. On the sides of the section is a low-pass filtered impedance log from well 14-35 for reference.

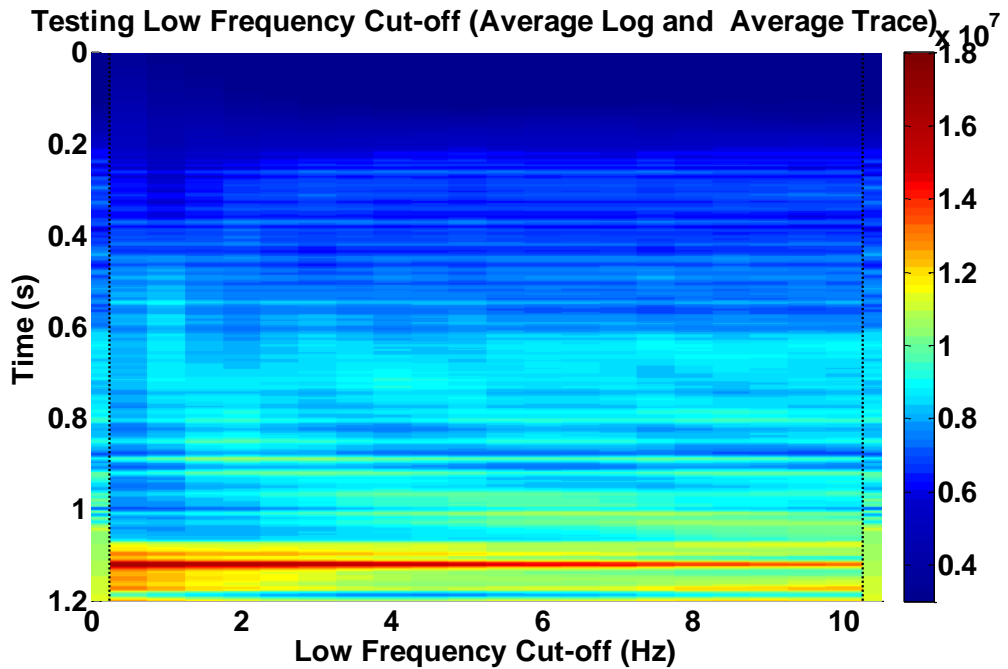


Figure 3.18: BLIMP impedance inversions using the average trace and average well impedance log for various low-frequency cut offs. On the sides of the section is a low-pass filtered average impedance log for reference.

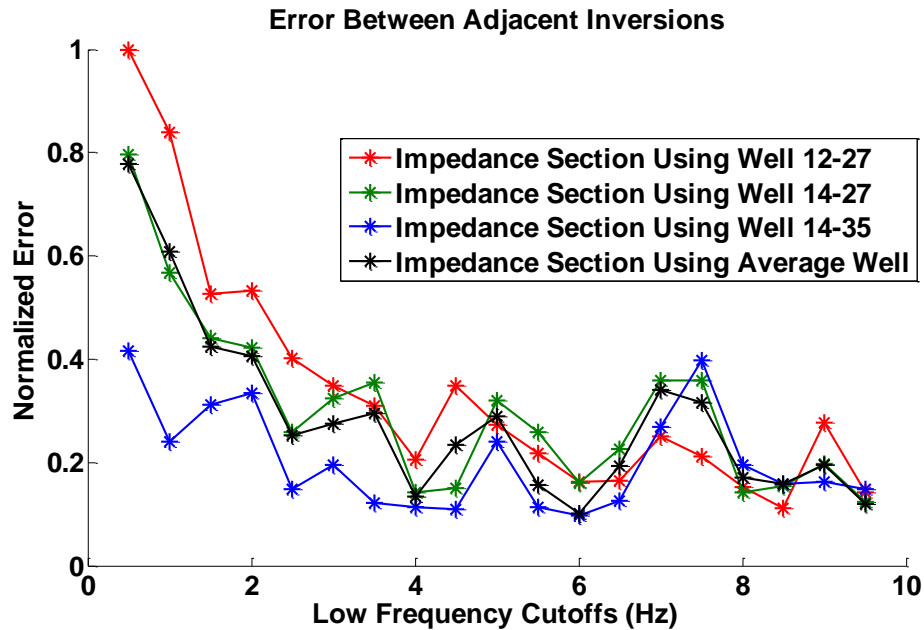


Figure 3.19: The normalized difference between adjacent inversions. Inversion stability is found when the low-frequency cut-off between 3 and 4 Hz.

BLIMP impedance inversions were calculated using a low-frequency cut off of 2.5 Hz and impedance logs from wells 12-27, 14-27 , 14-35 and the average impedance log, Figure 3.21, Figure 3.22, Figure 3.23 and Figure 3.24, respectively. These inversions visually look very similar. To evaluate whenever the inversion is accurate, cross validation plots are used. These plots (Figure 3.25, Figure 3.26, Figure 3.27 and Figure 3.28) compare the impedance inversion using one well to filtered well logs at the locations of the other wells. That is, we are seeing how well an inversion driven by one well can predict the measured impedance at another well. It is important that the well logs are filtered with a low pass filter as BLIMP does not restore high frequency content. Mean percent error was calculated for each cross validation by

$$Error = \frac{1}{n} \sum_{i=0}^n \frac{I_{well} - I_{inversion}}{I_{well}} \times 100. \quad 3.2$$

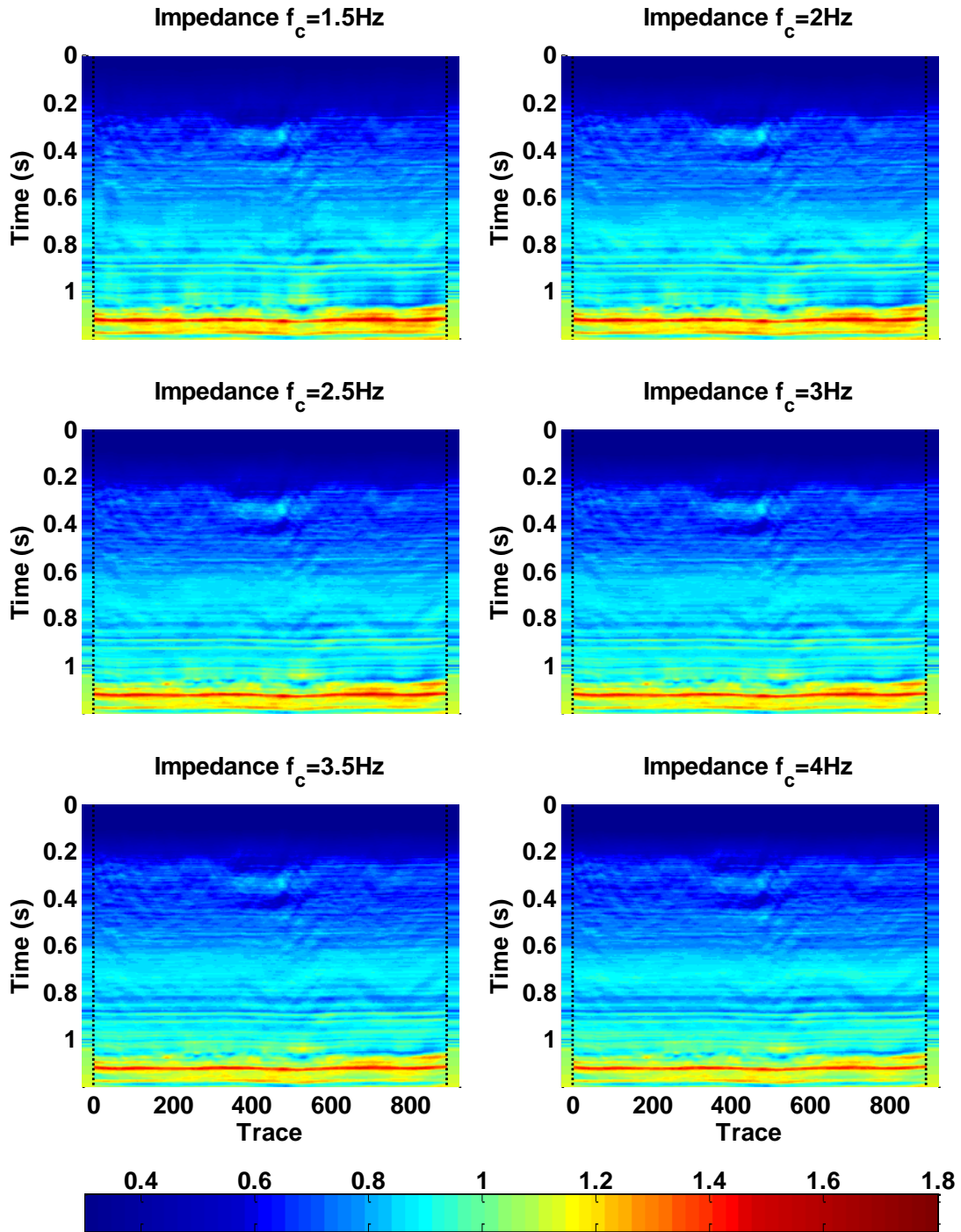


Figure 3.20: BLIMP impedance inversions using the average impedance well log for different frequency cut offs ranging from 1.5 Hz to 4Hz.

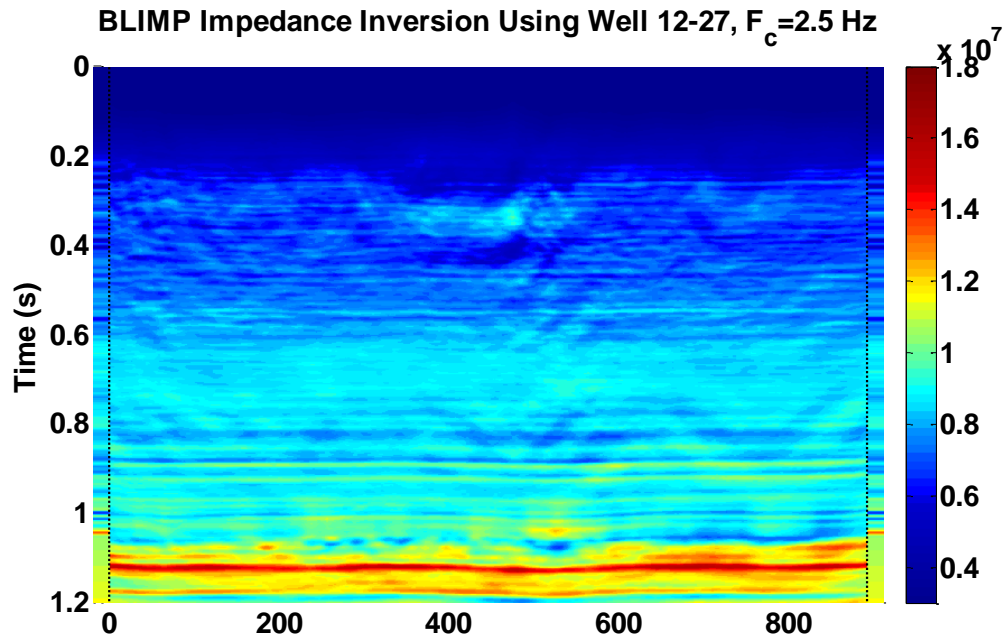


Figure 3.21: Impedance inversion calculated using well 12-27 and a low frequency cut-off of 2.5 Hz. Low-pass filtered impedance log from well 12-27 is displayed on the sides for reference.

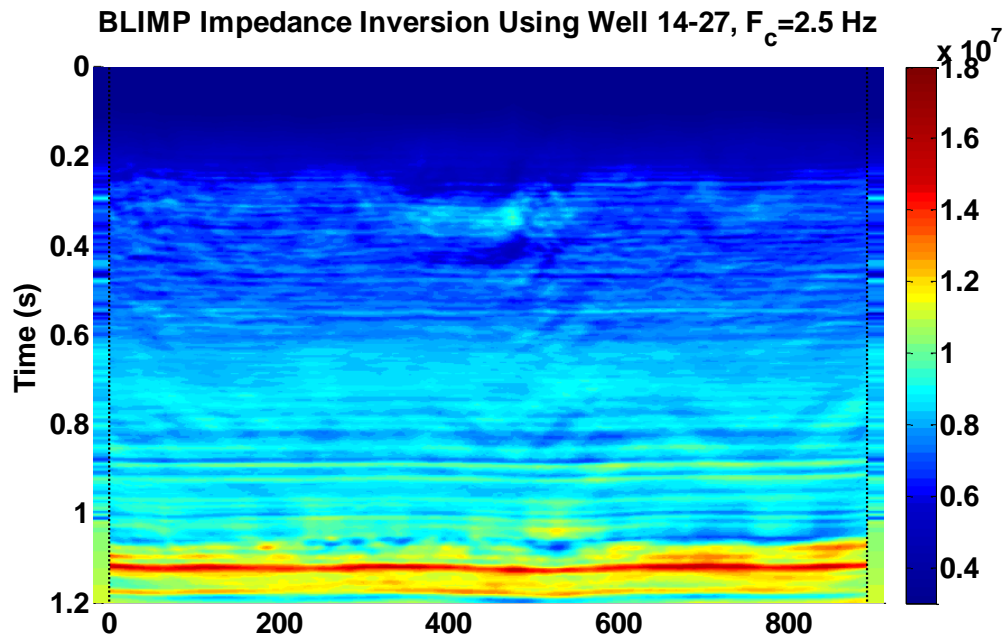


Figure 3.22: Impedance inversion calculated using well 14-27 and a low frequency cut-off of 2.5 Hz. Low-pass filtered impedance log from well 14-27 is displayed on the sides for reference.

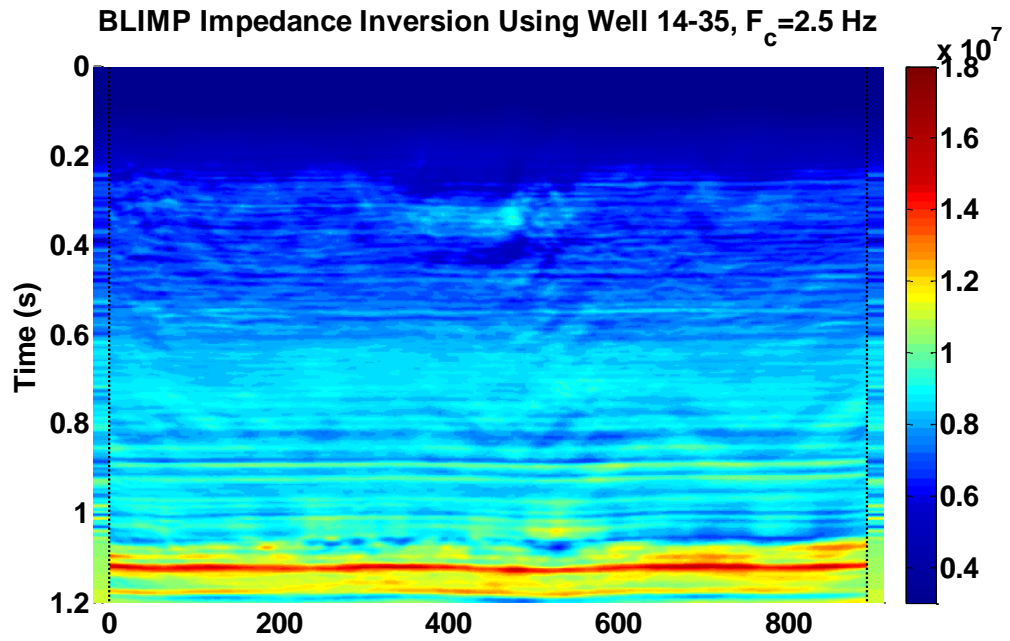


Figure 3.23: Impedance inversion calculated using well 14-35 a low frequency cut-off of 2.5 Hz. Low-pass filtered impedance log from well 14-35 is displayed on the sides for reference.

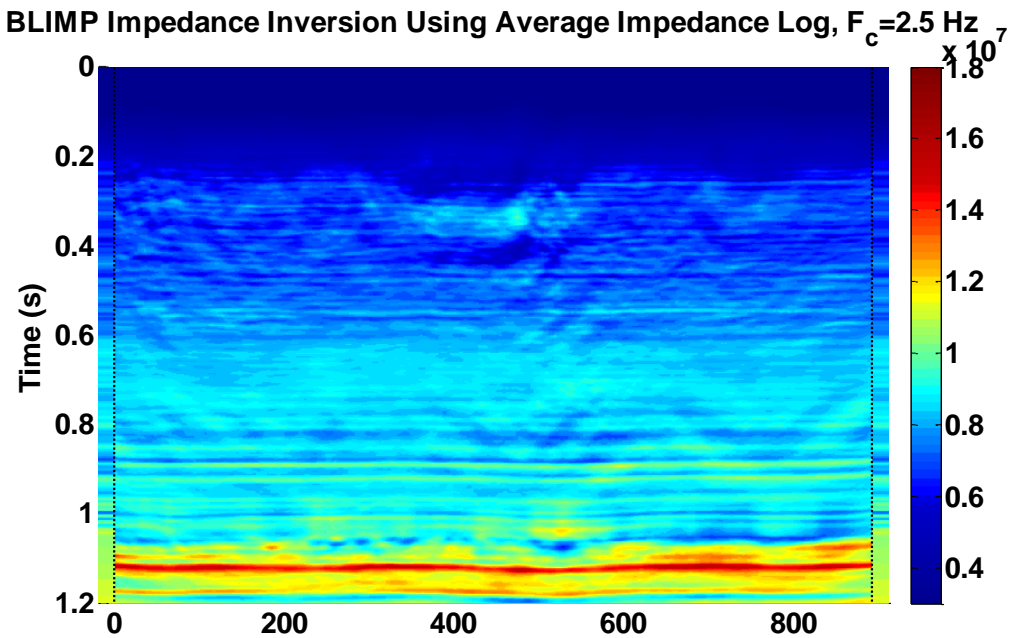


Figure 3.24: Impedance inversion calculated using the average well impedance log and a low frequency cut-off of 2.5 Hz. Low-pass filtered average impedance log is displayed on the sides.

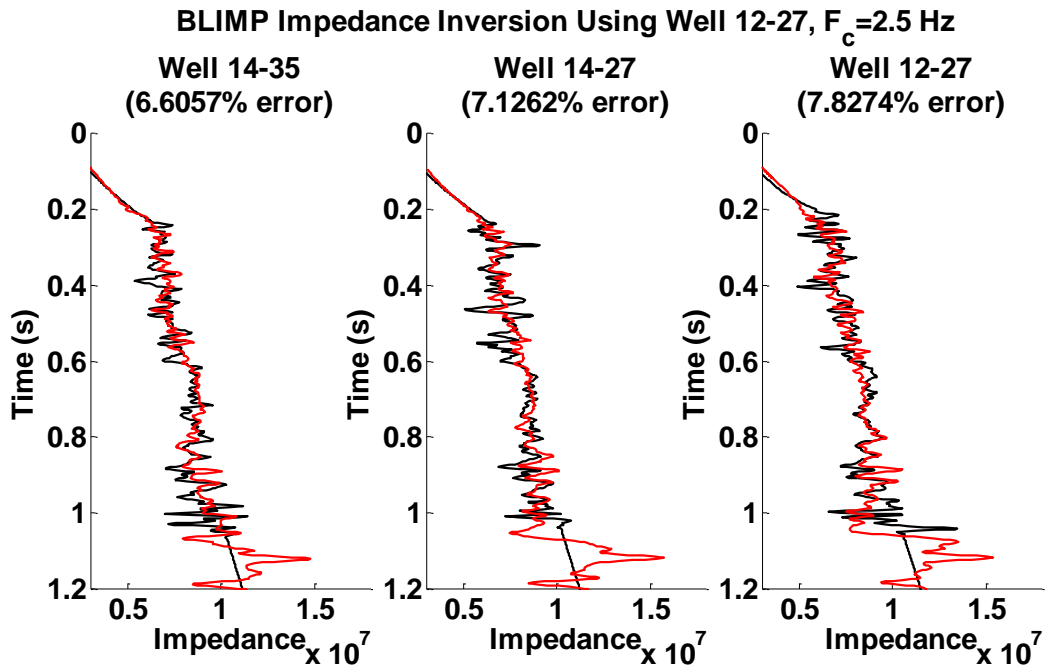


Figure 3.25: Cross validation plot that compares the inversion calculated using the impedance log from well 12-27 (Red) with the filtered well impedances (Black). Error is calculated in the interval from 0.2 seconds to 1.05 seconds.

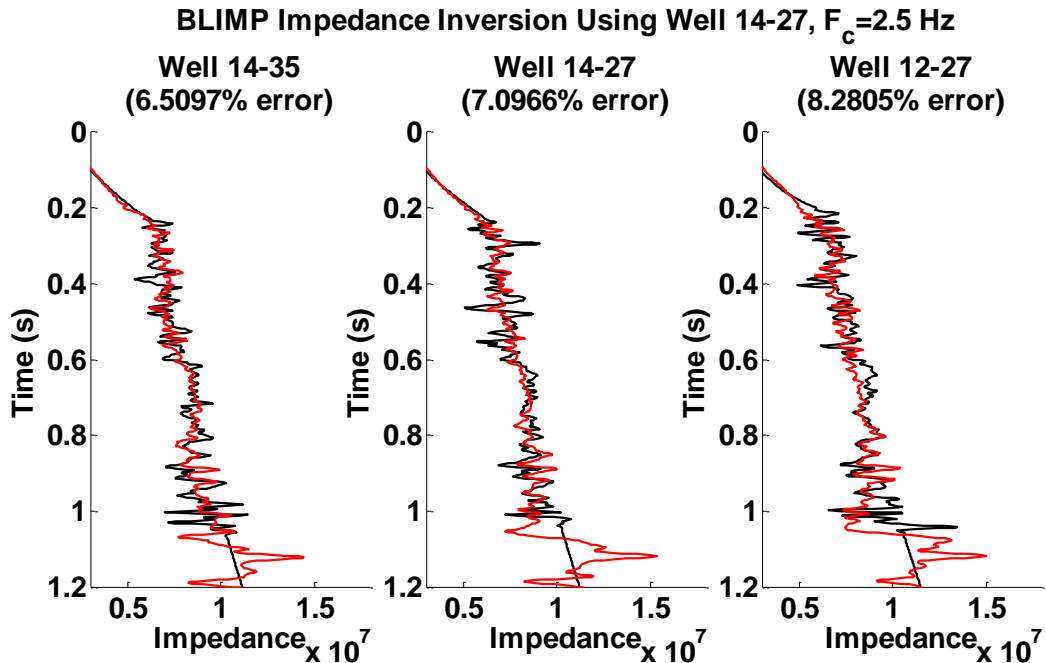


Figure 3.26: Cross validation plot that compares the inversion calculated using the impedance log from well 14-27 (Red) with the filtered well impedances (Black). Error is calculated in the interval from 0.2 seconds to 1.05 seconds.

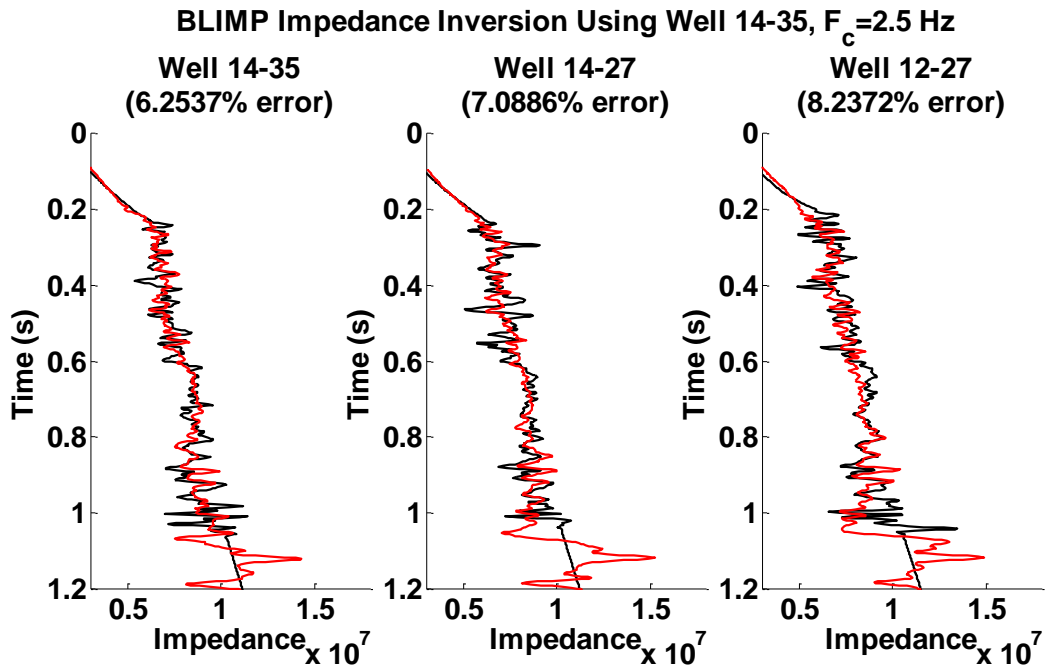


Figure 3.27: Cross validation plot that compares the inversion calculated using the impedance log from well 14-35 (Red) with the filtered well impedances (Black). Error is calculated in the interval from 0.2 seconds to 1.05 seconds.

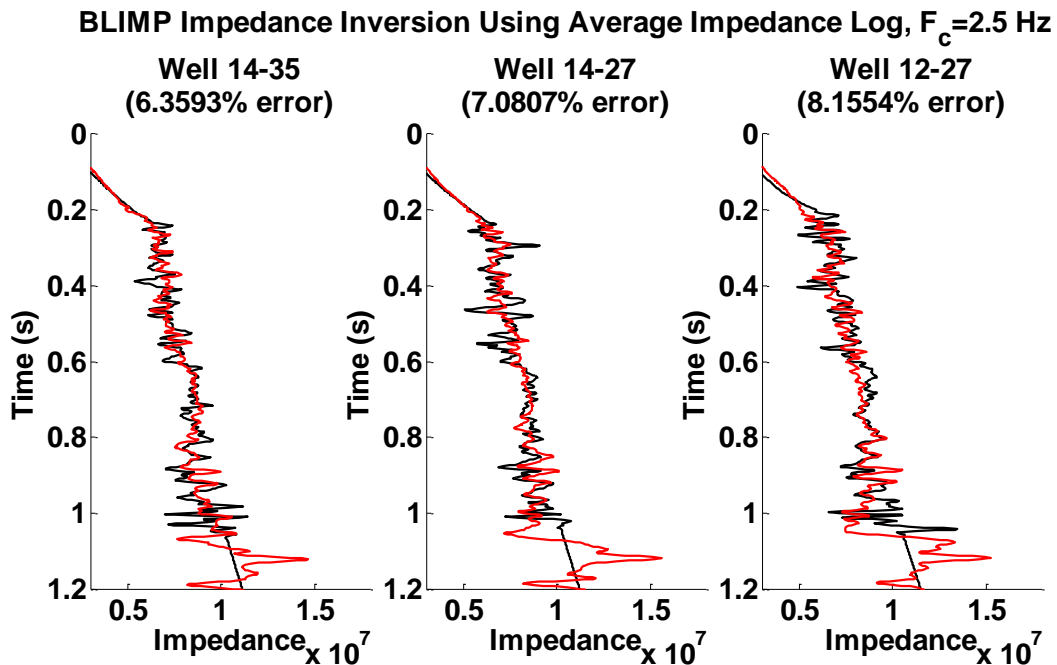


Figure 3.28: Cross validation plot that compares the inversion calculated using the average impedance log (Red) with the filtered well impedances (Black). Error is calculated in the interval from 0.2 seconds to 1.05 seconds.

The cross validation plots show a range of impedance errors from 6.25 to 6.61% at the location of well 14-35, 7.08 % to 7.13% at the location of well 14-27 and 7.83% to 8.28% at the location of well 12-27. With the errors varying by 2 % across the section there may be a slight difference in the frequency content in the lateral direction especially close to the location of well 12-27 where the seismic “fold” is low (“fold” is an integer counting the number of prestack traces contributing to a single stacked trace). Normally it would be expected that the cross validation plots would show a lower error for the well that was being used as the impedance data type. This is not the case as similar errors are seen for each inversion suggesting that 2.5 Hz is a stable frequency for this data set.

3.4 Low-frequency data type: stacking velocities

3.4.1 Formatting stacking velocities to stacking impedance

Stacking velocities can be converted into a low-frequency data type. These velocities are picked during processing for normal moveout corrections. These picks are sparsely chosen, in this case every 50 traces and roughly every 200ms and therefore are coarsely sampled when compared to the temporal sample rate of the seismic data. . Prior to inversion, the stacking velocities are “conditioned” using approximations to fill the stacked section volume using the same time and trace locations as the seismic data.

Figure 3.29 represents how sparse the stacking velocity picks are in the data. The first step to condition the stacking velocities is to interpolate the temporally irregular picks to a regularly spaced grid in time using a linear operator. A time grid sampled at 25 milliseconds was used (Figure 3.30). The next step was to interpolate the data onto the

same spatial and temporal grid as the seismic data.. Three different MATLAB® algorithms were analyzed to determine the best method for this purpose.

The first technique was fitting a cubic polynomial to the velocities. The algorithm that was used in MATLAB was *polyfit* with a polynomial order of three. This method tries to fit a global cubic to the velocities so the true velocities are not always honored by this method (Figure 3.31). Figure 3.32 shows that this method creates an anomalous low velocity region at 3.5 seconds. Since stacking velocities almost always increase with time this is not a satisfactory response so the cubic polynomial method was not chosen.

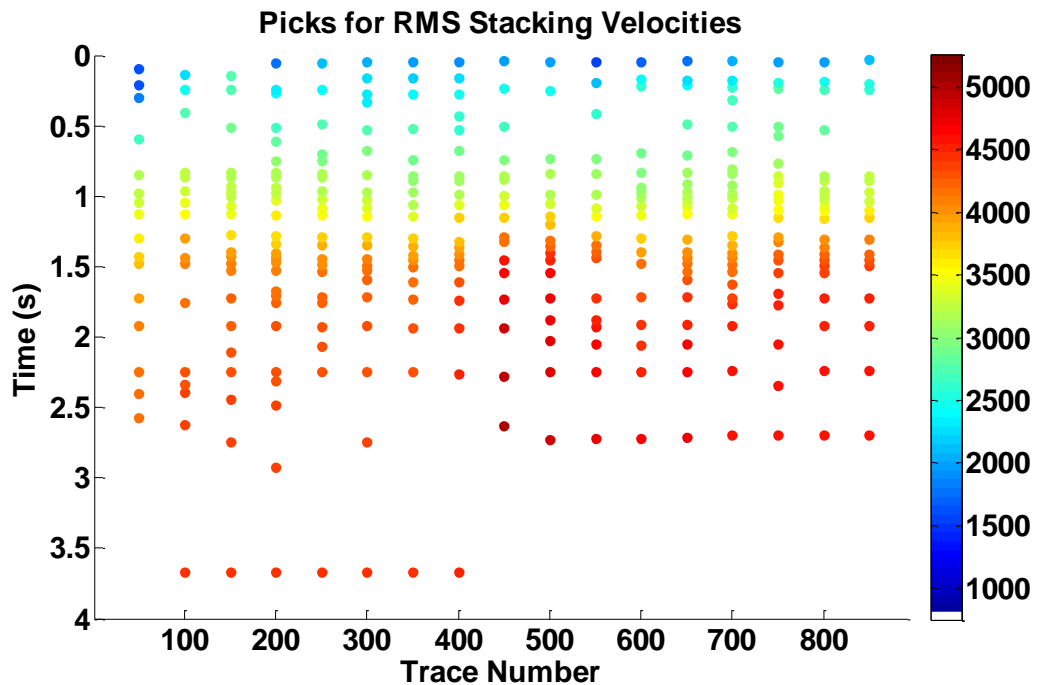


Figure 3.29: Stacking velocity picks made during processing. The picks have good time coverage at the zone of interest but poor spatial coverage. Each point is the location of the pick and the color refers to the stacking velocity at that pick.

The next technique was using a cubic spline to fit the data. This algorithm uses a series of polynomials to interpolate the data and connects them smooth continuous

manner. The spline method is true to the data where there is data and then attempts to extrapolate where there is no data. Figure 3.31 shows how the spline method can veer off when there is no data. Figure 3.32 shows the results when using the spline method for both the time direction and the horizontal direction. Anomalous high events occur at 0 and 4 seconds at approximately 50 traces. This indicates that the spline method may not be the best choice in an extrapolation method.

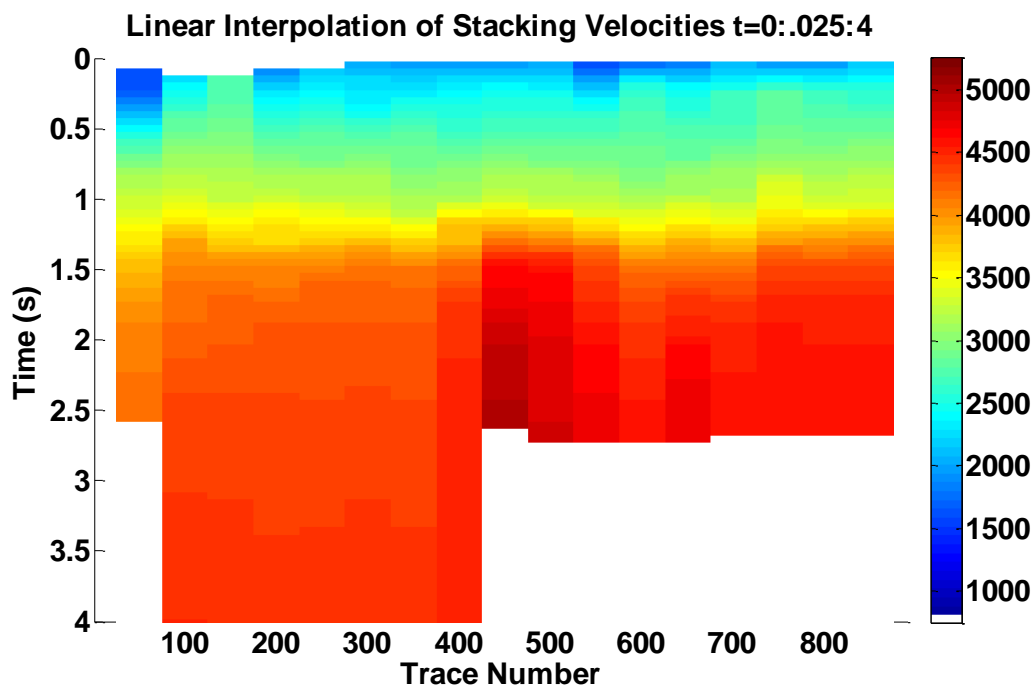


Figure 3.30: A linear interpolation of the stacking velocity picks on a 25 ms by 250 meter grid. Linear interpolation can only interpret velocity points between picks so the white regions represent where there are no picks.

The last technique is the PCHIP (Piecewise Cubic Hermite Interpolating Polynomial) algorithm (Fritsch and Carlson, 1980). This method is very similar to the spline method where it uses a series of cubic polynomials to interpolate the data but connects the polynomials in a way that is not always smooth, for example using straight

lines instead of a smooth curve. This method is true to the velocities where there are picks and tries to extrapolate outside the picks in an appropriate manner (Figure 3.31). This method was chosen as it produces the most reasonable result, with the stacking velocities consistently increasing with depth.

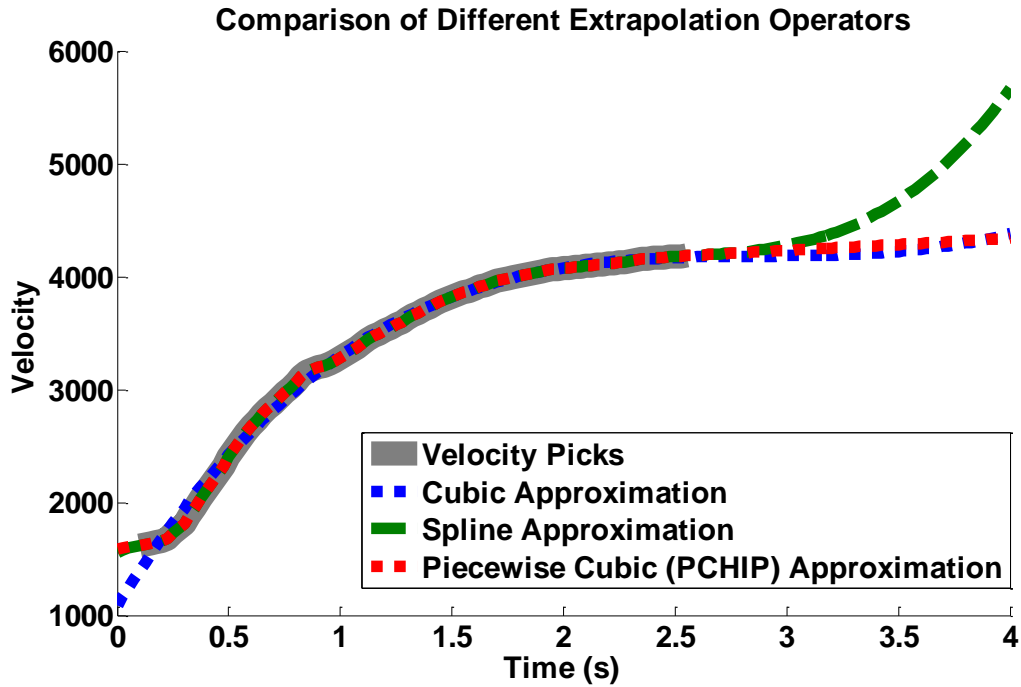


Figure 3.31: This shows the different interpolation methods available and their accuracy, The PCHIP approximation is the best choice as it follows the trend of the data in the lower times and does not overshoot at high times.

Once the stacking velocities have been extrapolated to fill a grid with the same temporal and horizontal sampling rates as the seismic, further conditioning may be needed. In Figure 3.33 a high velocity anomaly near trace 450 and 2 seconds is present. This anomaly may be a result of residual statics (Oldenburg et al., 1984), or possibly a bias from the topography. Ideally this should be minimized using smoothing or other techniques. Smoothing however reduces the bandwidth of the velocities. With

experimentation smoothing was found to remove key events in the data so the stacking velocities will be used without any smoothing.

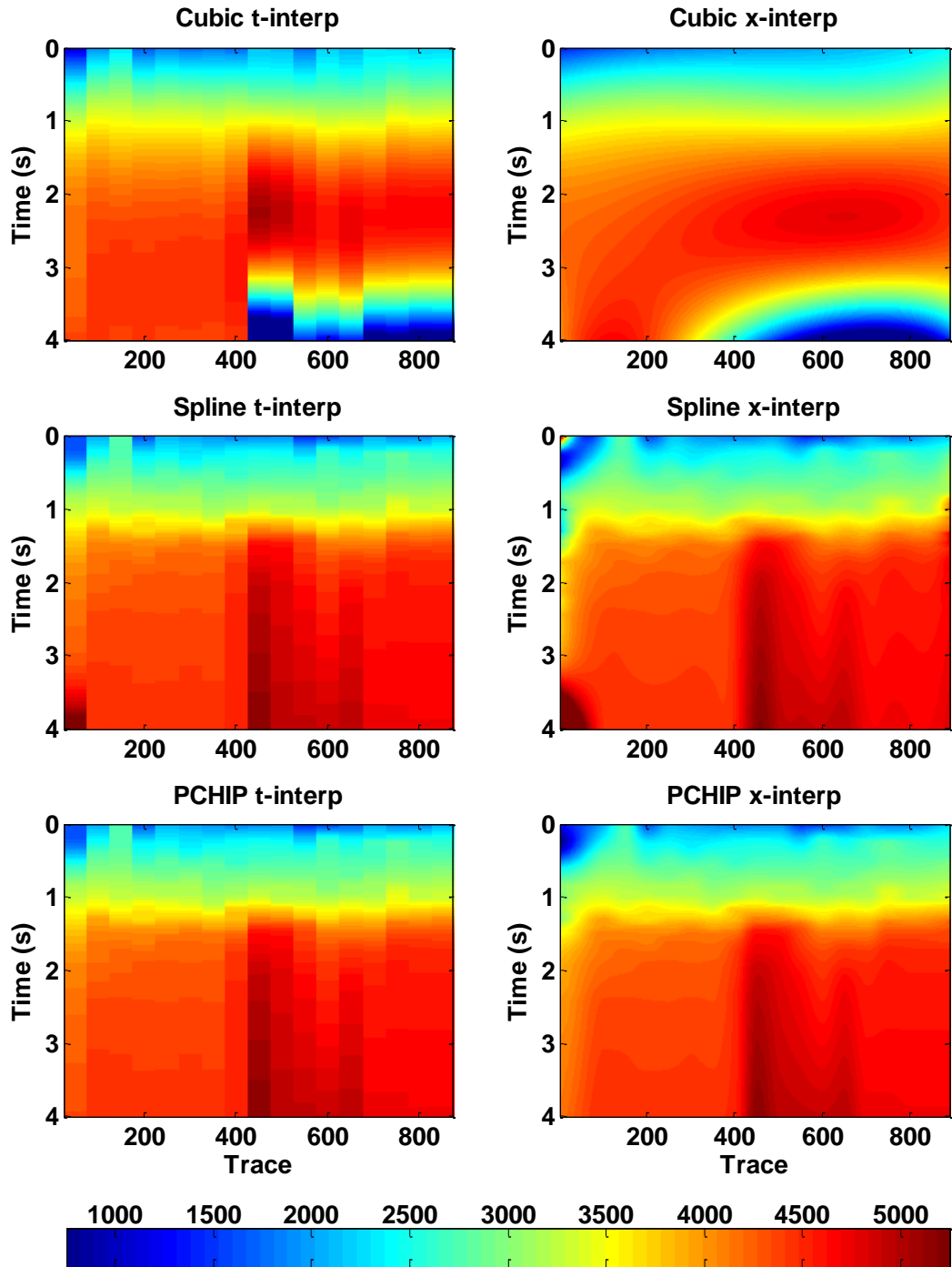


Figure 3.32: This figure shows the extrapolation results for three different methods when extrapolating the time direction (t-interp) and the horizontal direction (x-interp).

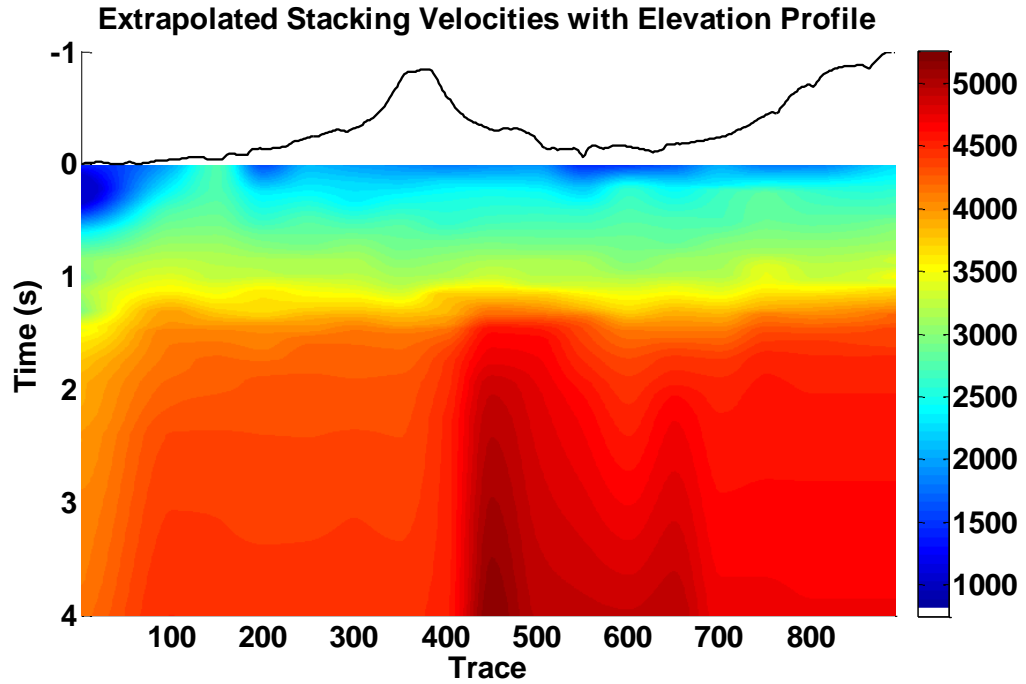


Figure 3.33: Extrapolated stacking velocities using the PCHIP method. The exaggerated elevation profile is shown to assess where residual statics could be affecting the stacking velocities.

The stacking velocities are approximately an RMS average of the interval velocities (Dix, 1955) but the interval velocity of each layer is needed to calculate impedance. This can be achieved by calculating interval velocities using the standard Dix (1955) interval velocity calculation equations

$$V_{int_k}^2 = \frac{V_{rms_{k+1}}^2(t_{k+1} - t_o) - V_{rms_k}^2(t_k - t_o)}{(t_{k+1} - t_k)} \quad 3.3$$

where V_{rms} are the stacking velocities, V_{int} are the Dix interval velocities, t is the time and t_o is the starting time (zero in this case), (e.g. Margrave, 2010). It is common that a small error in the stacking velocities can cause a large error in the interval velocities so ensuring the stacking velocities are reasonable is important. Figure 3.34, shows the calculated interval velocities. The velocities vary significantly in the lateral direction

which may not be indicative of the geology present in the subsurface. Instead of using the whole section for the inversion it may be desirable to calculate one impedance trace by averaging the section.

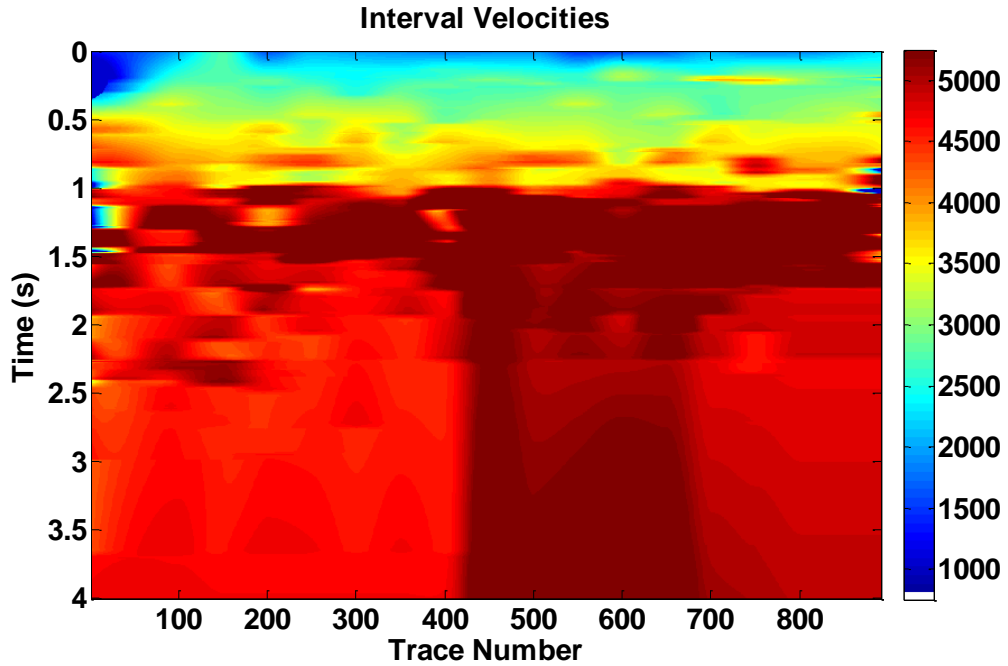


Figure 3.34: Interval velocities calculated from smoothed stacking velocities using Dix (1955) equations.

The next step in the process of converting the stacking velocities into impedance is to estimate the density. Gardner et al. (1974) suggested using an empirical relationship between density (ρ) and velocity (V_{int})

$$\rho = m * V_{int}^a \quad 3.4$$

where m is the Gardner scalar and a is the Gardner Exponent. The Gardner exponent is calculated by plotting velocity versus density on a log-log plot. The slope of the line is the exponent. The Gardner scalar is calculated by averaging the scalars needed to make density and V_{int}^a match. The Gardner parameters were calculated using well logs and a

different set of parameters were calculated for each interval identified in the well logs by tops, Figure 3.35. The density section was then calculated using these parameters and the interval velocities, Figure 3.36.

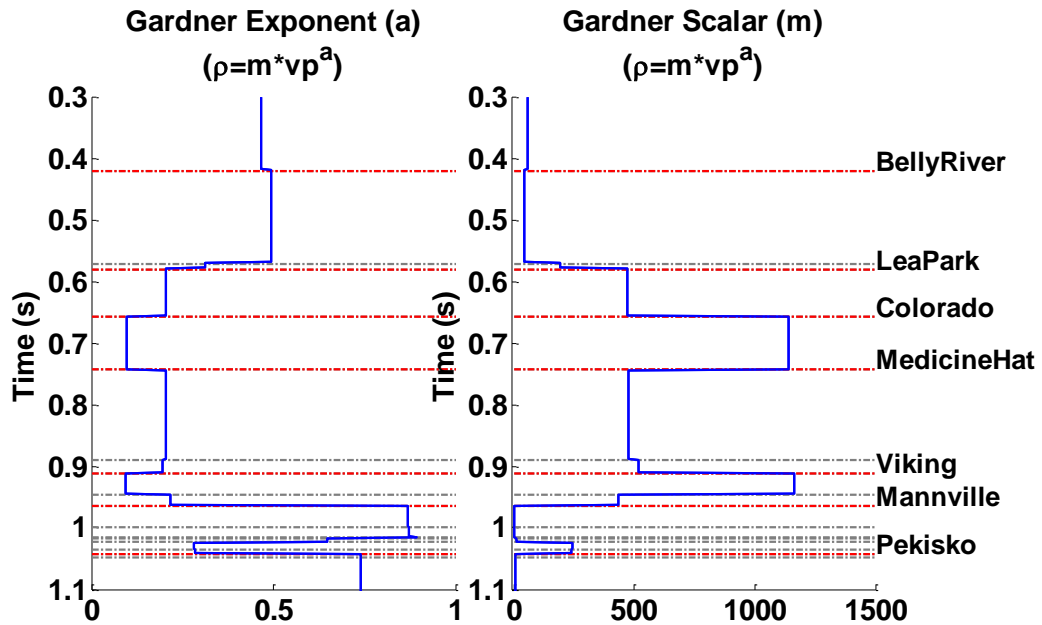


Figure 3.35: Gardner parameters determined by well logs for each set of tops.

Now that the interval velocities and densities have been calculated the impedance section can be produced. Figure 3.37, shows the calculated impedance section. The impedance section is very irregular but these events are predominantly high-frequency events and will be filtered out when the inversion is computed. The impedance section still varies rapidly in the lateral direction, where the geology does not indicate these changes. Figure 3.38, shows an impedance inversion using the stacking impedance. The result is very irregular. Instead of using the whole section it is preferred to use an average of the impedance section.

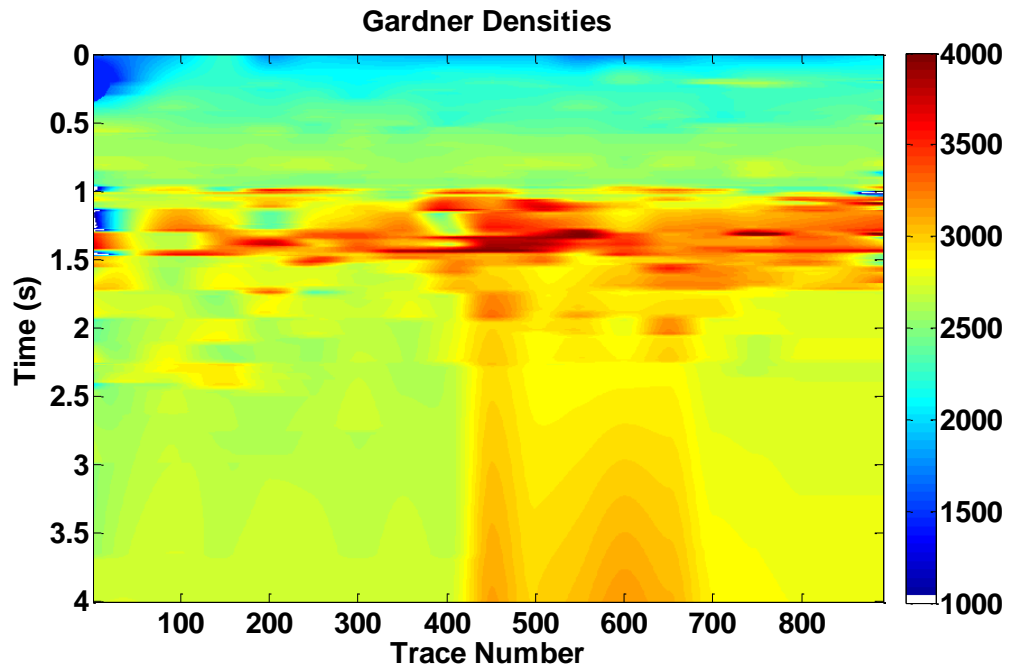


Figure 3.36: Densities calculated using Gardner parameters and interval velocities.

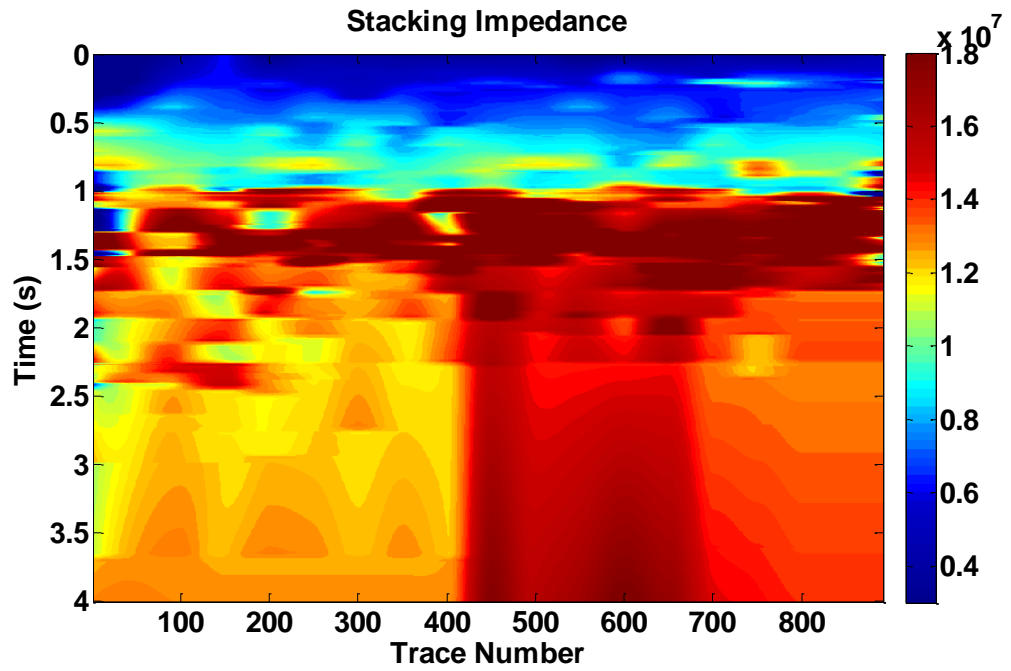


Figure 3.37: Impedance section constructed from stacking velocities

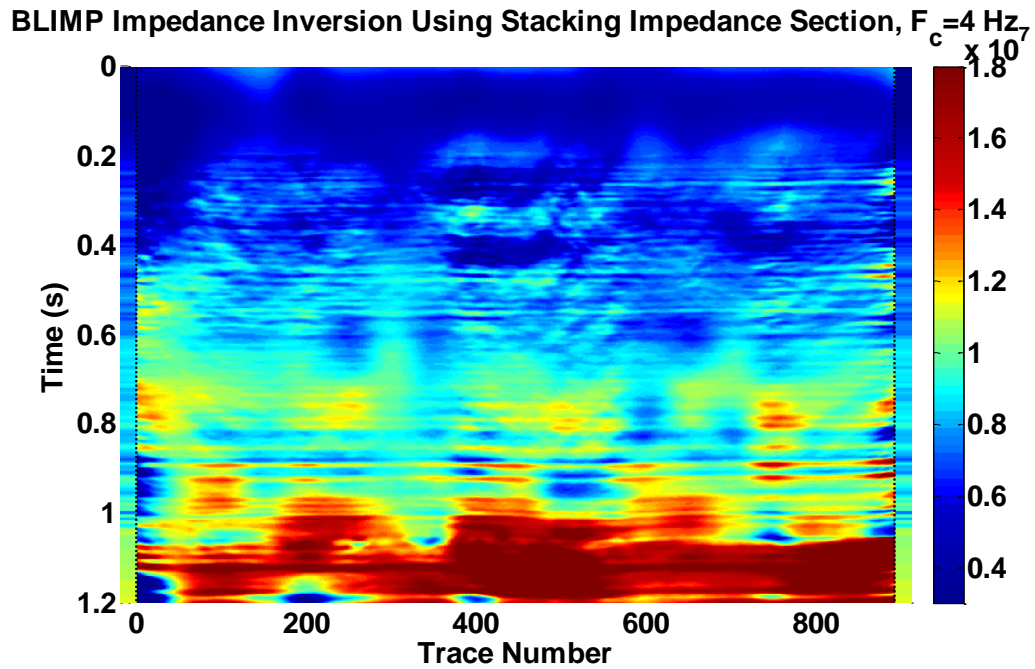


Figure 3.38: Impedance inversion using a low-frequency cut off of 4 Hz, and using the stacking impedance section for low-frequency input. The filtered average impedance well log is located on the sides of the impedance section for reference.

Two average stacking impedances were determined (Figure 3.39). The mean stacking impedance averages all traces in the section whereas the preferred stacking impedance only averages traces 1 to 300. The range for the preferred stacking impedance was selected as it was outside the high amplitude area. These average impedance traces will be used in the following BLIMP inversions.

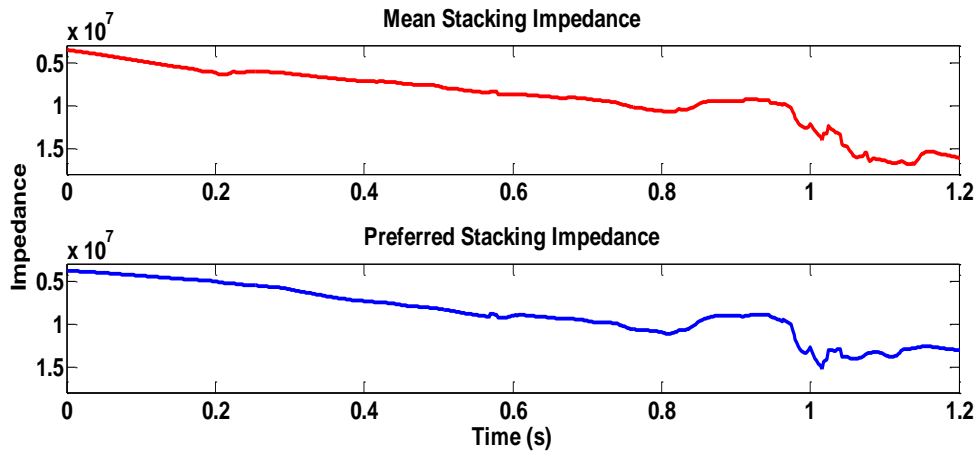


Figure 3.39: Mean stacking impedance which was calculated by averaging all stacking impedance traces and the preferred stacking impedance which was calculated by averaging traces 1 to 300 only.

3.4.2 Testing for optimal low-frequency cut off

Both the mean stacking impedance and the preferred stacking impedance were used in BLIMP inversions for various low-frequency cut offs. The scaling threshold value used was 5 Hz instead of 20 Hz, as there is less high frequency content in stacking impedance than there is in well impedance. In both Figure 3.40 and Figure 3.41 anomalous high impedance occurs after .9 seconds for low-frequency cut off s above 3 Hz. It is important that the low frequency cut off is not higher than 3 Hz because the stacking impedances start to dominate the inversion. By looking at the error between adjacent inversions, Figure 3.42, a low-frequency cut off between 1 Hz and 2.5Hz is indicated as optimal. Figure 3.43 shows the BLIMP inversion results using low-frequency cut offs of 0.5 to 3 Hz. From this display it can be seen that 0.5 Hz is too volatile but 1 Hz is more stable. The 1.5 Hz and 2 Hz results look very similar to the 1 Hz result, where the 2.5 Hz and 3 Hz results look substantially different. Therefore 1Hz is a suitable cut off to be used with the stacking impedances.

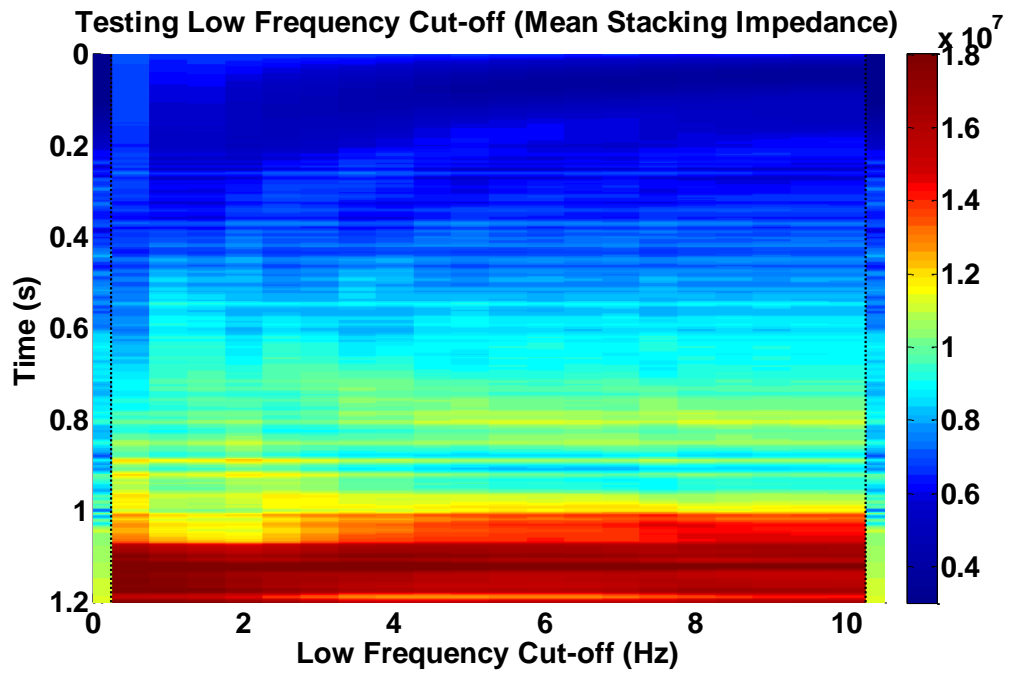


Figure 3.40: BLIMP impedance inversions using average trace and the mean stacking impedance for various low-frequency cut offs. On the sides of the section is the low-pass filtered average impedance well log for reference.

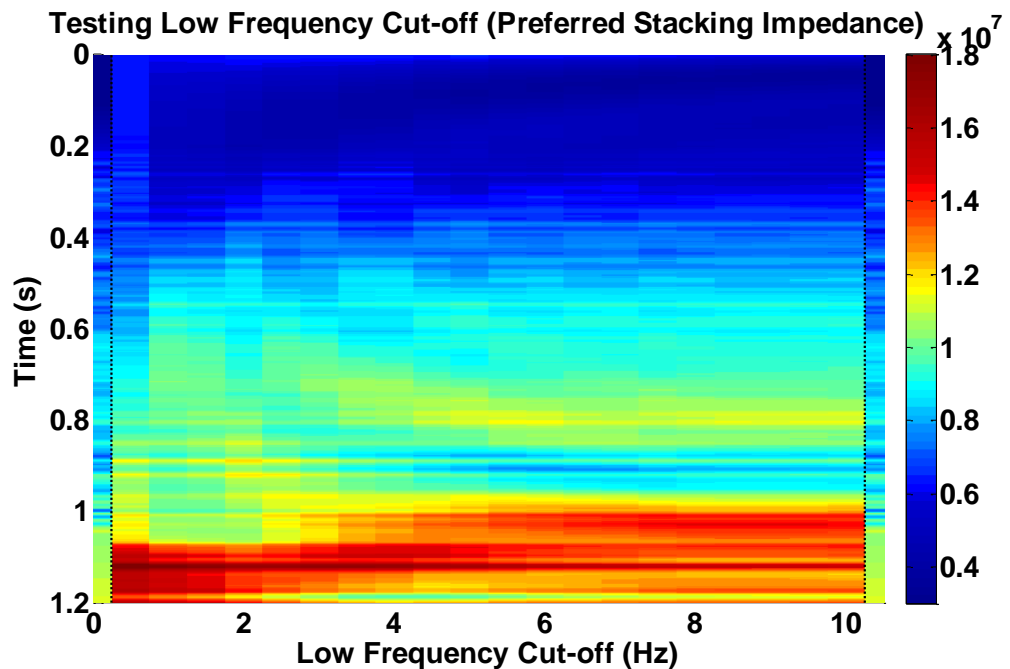


Figure 3.41: BLIMP impedance inversions using average trace and the preferred stacking impedance for various low-frequency cut offs. On the sides of the section is the low-pass filtered average impedance well log for reference.

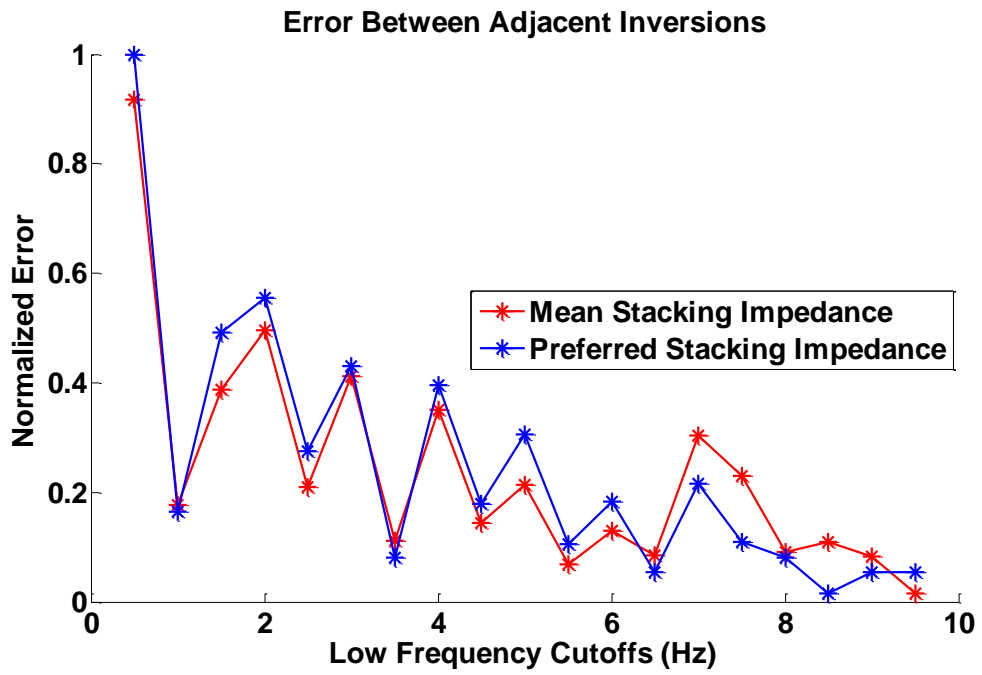


Figure 3.42: The normalized difference between adjacent inversions.

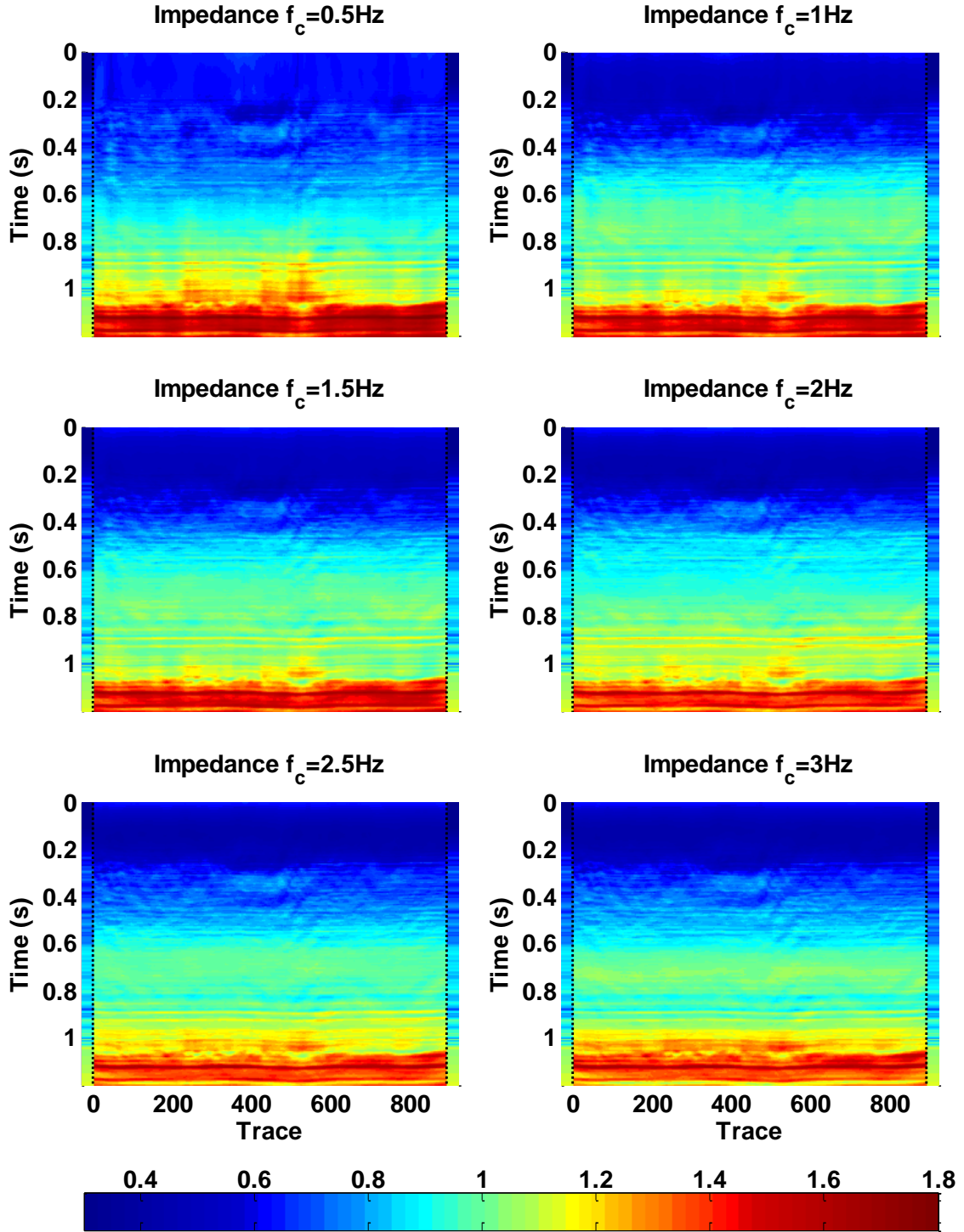


Figure 3.43: BLIMP impedance inversions using the preferred stacking impedance trace for different frequency cut offs ranging from 0.5 Hz to 3Hz. The filtered average impedance well log is displayed on both sides of the inversion for reference.

3.4.3 BLIMP impedance inversions using stacking impedance

Figure 3.44 and Figure 3.45 show the mean stacking impedance inversion and the preferred stacking impedance inversion with a low-frequency cut off of 1 Hz, respectively. This inversion is more unreliable than the BLIMP inversions using well logs, but still produces a result that can be interpreted. Figure 3.46 and Figure 3.47 show cross validation plots for each of the stacking impedance inversions. The error ranging from 12.2% to 13.87% for the mean stacking impedance inversion and the errors ranging from 14.98% to 15.96% for the preferred stacking impedance inversion are much higher than the well log inversions. Inversions using the mean stacking impedance tend to be more accurate than the preferred stacking impedance. Both of the stacking inversions tend to have higher error in the midsection between 0.5 and 0.9 seconds. It can be concluded that using stacking velocities alone may not be optimal for producing accurate inversions however a ballpark impedance section can be created using stacking impedance inversions.

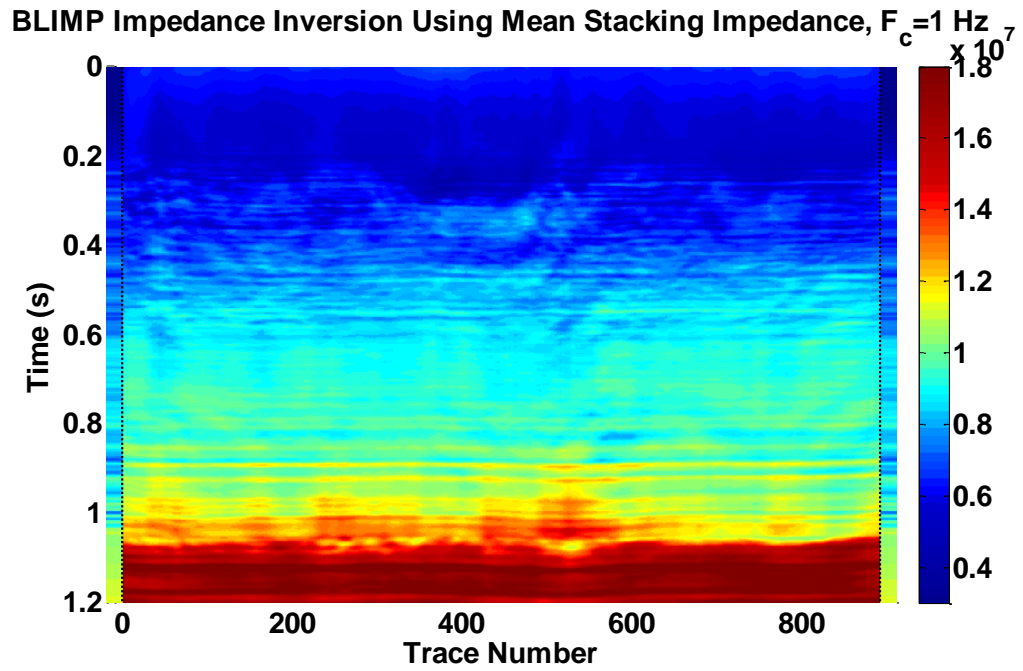


Figure 3.44 : Impedance inversion calculated using the mean stacking impedance trace and a low frequency cut-off of 1 Hz. Low-pass filtered average impedance log is displayed on the sides.

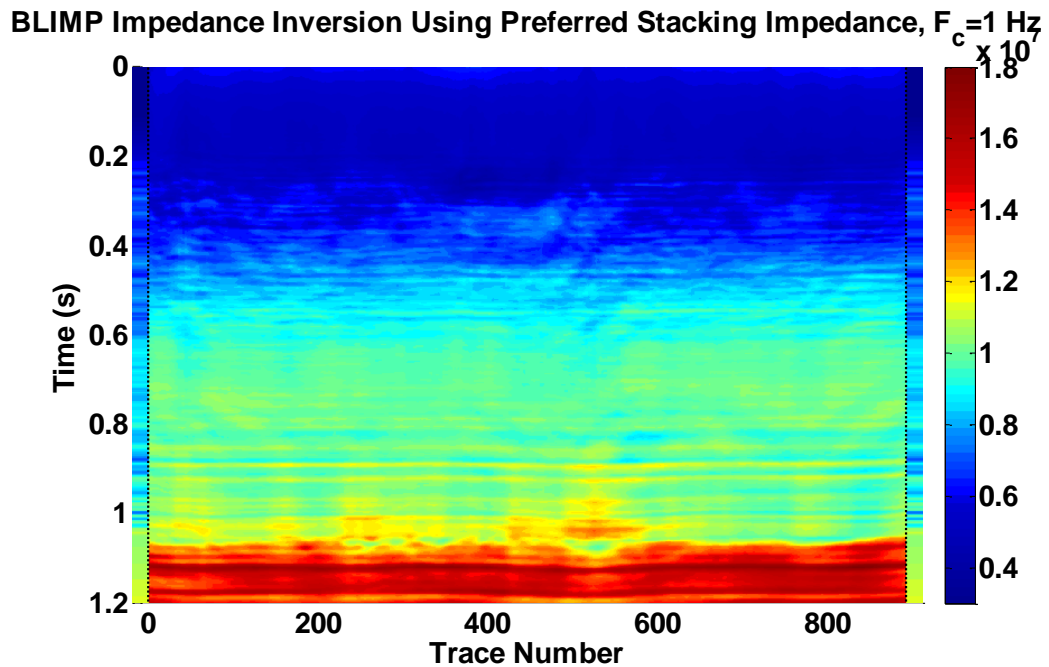


Figure 3.45: Impedance inversion calculated using the mean stacking impedance trace and a low frequency cut-off of 1 Hz. Low-pass filtered average impedance log is displayed on the sides.

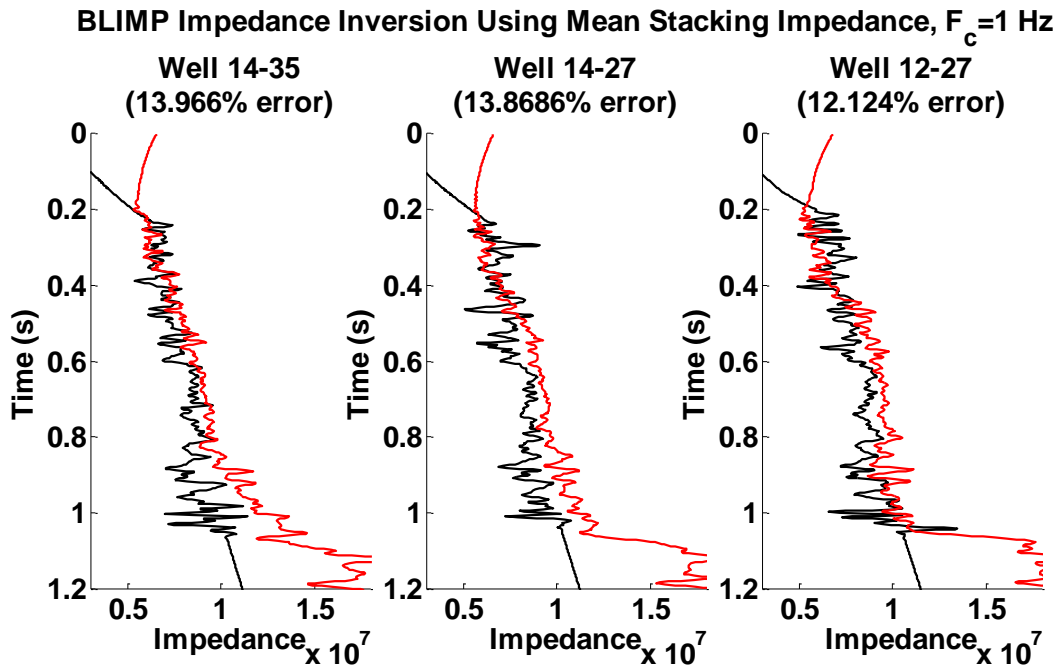


Figure 3.46: Cross validation plot that compares the inversion calculated using the mean stacking impedance (Red) with the filtered well impedances (Black). Error is calculated in the interval from 0.2 seconds to 1.05 seconds.

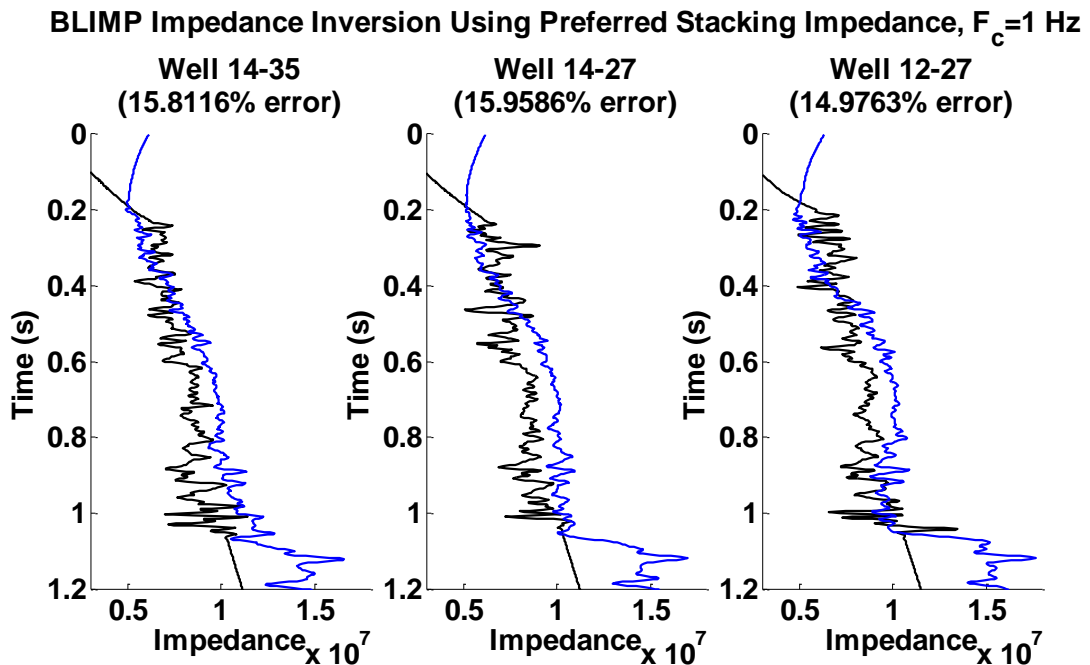


Figure 3.47 : Cross validation plot that compares the inversion calculated using the preferred stacking impedance (Red) with the filtered well impedances (Black). Error is calculated in the interval from 0.2 seconds to 1.05 seconds.

3.5 Low-frequency data type: combination of well logs and stacking velocities

It can be noted that the stacking impedances were able to use a low frequency cut off of 1 Hz whereas the well impedances needed a cut off of 2.5 Hz. The main reason for this is that the linear trend of the stacking impedances is different from the linear trend of the well impedances, Figure 3.48. The linear trend for the well impedance fits the impedance very well whereas the linear trend for the stacking impedance does not. When transformed to the frequency domain the amplitude of the stacking impedance is greater than the amplitude of the well impedance, Figure 3.49. The threshold scaling method tries to reduce this effect to some degree but even at 5 Hz the amplitude spectrum of the stacking impedance has higher amplitudes than that of the well logs. This causes the integrated seismic to have a larger scalar applied when using the stacking impedance than when using the well impedance. The low-frequencies in the integrated seismic become amplified, requiring less information from the stacking impedance to be used.

To determine if a more accurate inversion can be computed using the stacking impedance a combination trace was created that uses the average well log impedances from 0 seconds to 1.054 seconds and the mean stacking impedance between 1.054 seconds to four seconds, Figure 3.48. 1.054 seconds is the bottom of the well in time. This procedure is reasonable as the stacking impedance has a similar trend to the well impedance from 0 to .8 seconds. Therefore the stacking impedance is being replaced with impedance values that have a similar trend but are more detailed.

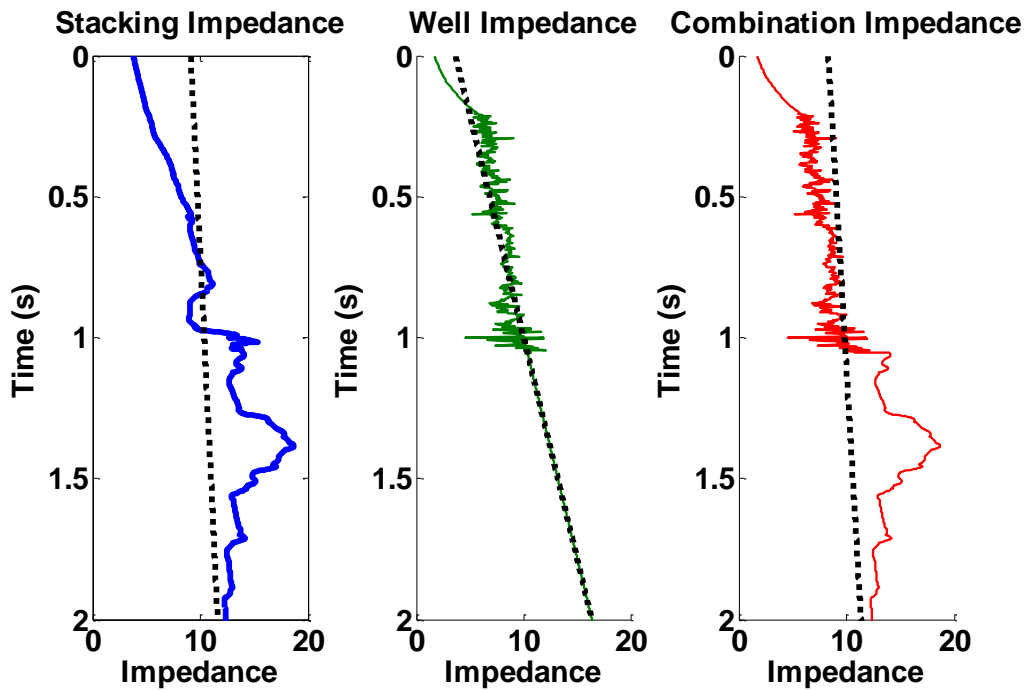


Figure 3.48: Preferred stacking impedance, average well impedance, and the combination impedance plotted with their linear trends. The combination trace is the average well impedance from 0 to 1.054 seconds and the mean stacking impedance from 1.054 seconds to 4 seconds. 1.054 seconds is the end of the well.

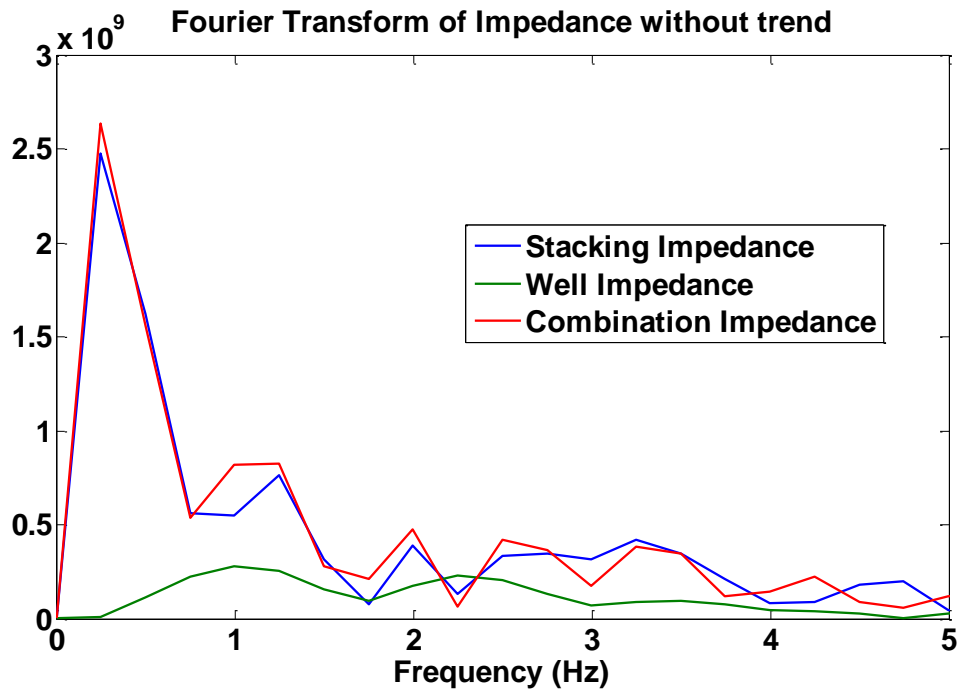


Figure 3.49: Fourier transform of the preferred stacking impedance, average well impedance, and the combination impedance.

A low frequency test was computed using the combination impedance for low-frequency cut offs between .5 and 10 Hz, Figure 3.50. The difference between one cut off inversion test and the next was summed between .2 and 1.05 seconds, Figure 3.51. This plot indicates that the optimal low-frequency cut off is between 1 Hz and 2.5 Hz. Figure 3.52 shows impedance inversions using cut offs from 0.5 Hz to 3 Hz. This plot shows that the 2.5 Hz result is very similar to the 1.5 and 2 Hz results.

To investigate how the error changes between these three cut offs inversions and cross-validation plots were prepared. For the cut off of 1.5 Hz the impedance inversion, Figure 3.53, shows that events are mostly continuous except between 0.6 and 0.8 seconds. According to the well logs, this interval contains shales so continuous impedance contrasts are not likely to occur. The cross validation plot, Figure 3.54, shows that the inversion matches up to the well impedance for wells 12-27 (8.5%) and 14-27(8.1%), but has a 9.4% error when compared to well 14-35. The impedance inversion was also calculated for a low-frequency cut off of 2 Hz, Figure 3.55. The cross validation plot, Figure 3.56, shows that this inversion had errors of 8.4 % for well 14-35, 7.9% for well 14-27 and 9.0% for well 12-27. The inversion using a cut off of 2.5 Hz, Figure 3.57, was found to produce errors of 9.0% in well 14-35, 6.8% in well 14-27 and 7.5% in well 12-27, Figure 3.58.

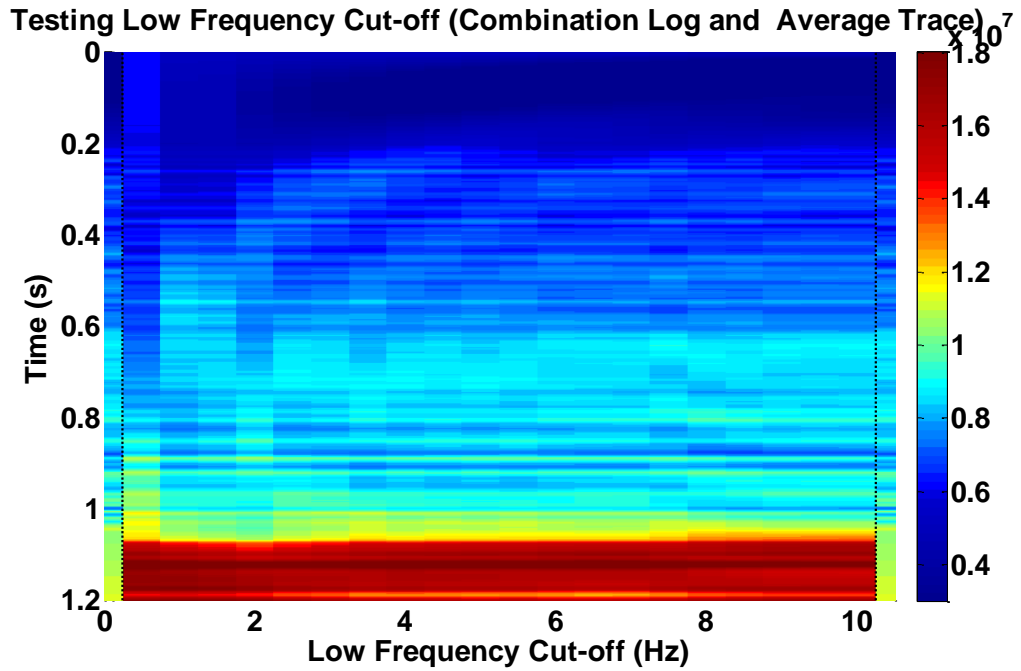


Figure 3.50: BLIMP impedance inversions using average trace and the preferred stacking impedance for various low-frequency cut offs. On the sides of the section is the low-pass filtered average impedance well log for reference.

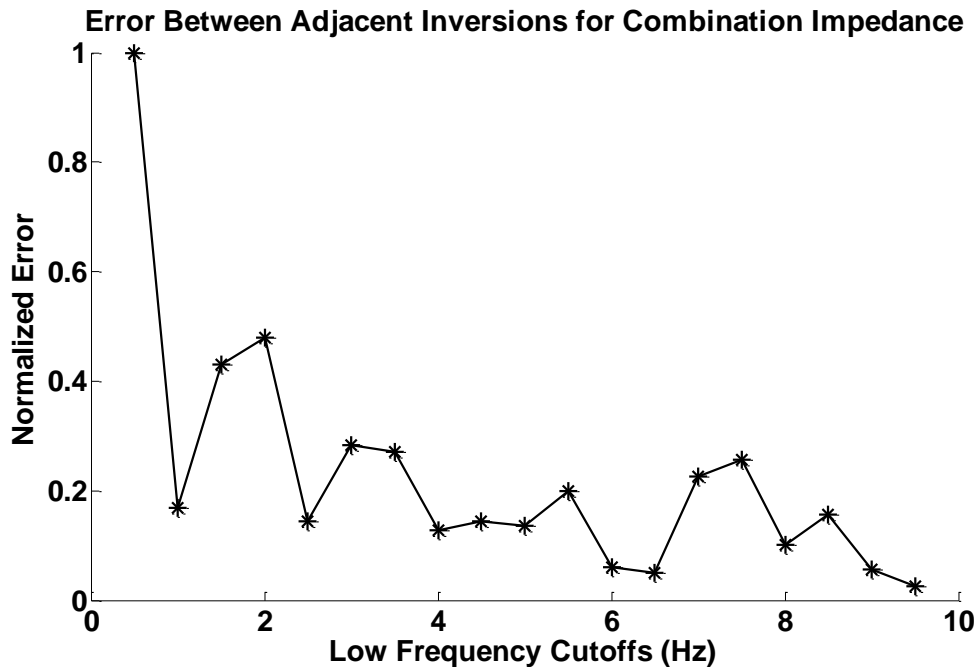


Figure 3.51: The normalized difference between adjacent inversions for the combination trace.

The error for each well does not consistently decrease when a higher frequency cut off is used. This could mean that there is time variant low-frequency content in the data. Table 3.1 shows the percent error for low-frequency cut offs from 1 Hz to 4 Hz. The percent error is calculated in 200 millisecond time windows including 0.2 to 0.4 seconds, 0.4 to 0.6 seconds, 0.6 to 0.8 seconds and 0.8 to 1.0 seconds. The error for the time window between 0.2 to 0.4 seconds, averaging about 10% for all tests, is much higher than the error for the time window between 0.6 and 0.8 seconds, averaging only 4% for all tests. The percent error calculated for windows 0.6 to 0.8 seconds and 0.8 to 1.0 seconds appears to stabilize at a low-frequency cut off of about 1.5 Hz. The percent error for the shallow section does not stabilize until a low-frequency cut off of 3 Hz. This shows that the low-frequency content of the hussar data set varies with time. The cause of this is most likely caused by the smaller amount of fold at the shallow section than the deep section. Higher levels of fold increases signal to noise ratio, thus reducing the amount of noise in the deeper section. These tests show that the optimal low-frequency cut off when using the combination impedance is 1.5 Hz for the deeper section and up to 3 Hz for the shallow section.

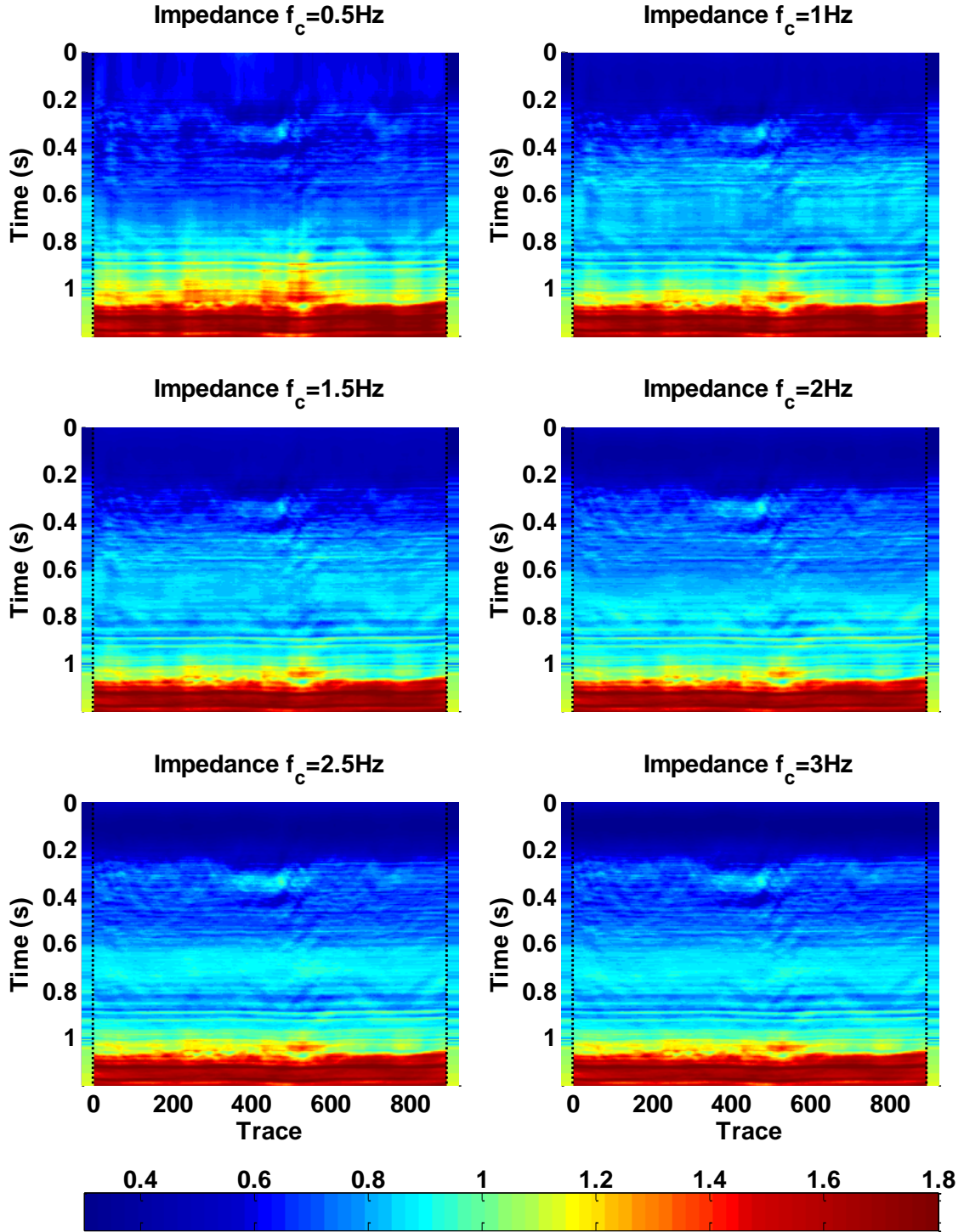


Figure 3.52: BLIMP impedance inversions using the combination impedance trace for different frequency cut offs ranging from 0.5 Hz to 3Hz. The filtered average impedance well log is displayed on both sides of the inversion for reference.

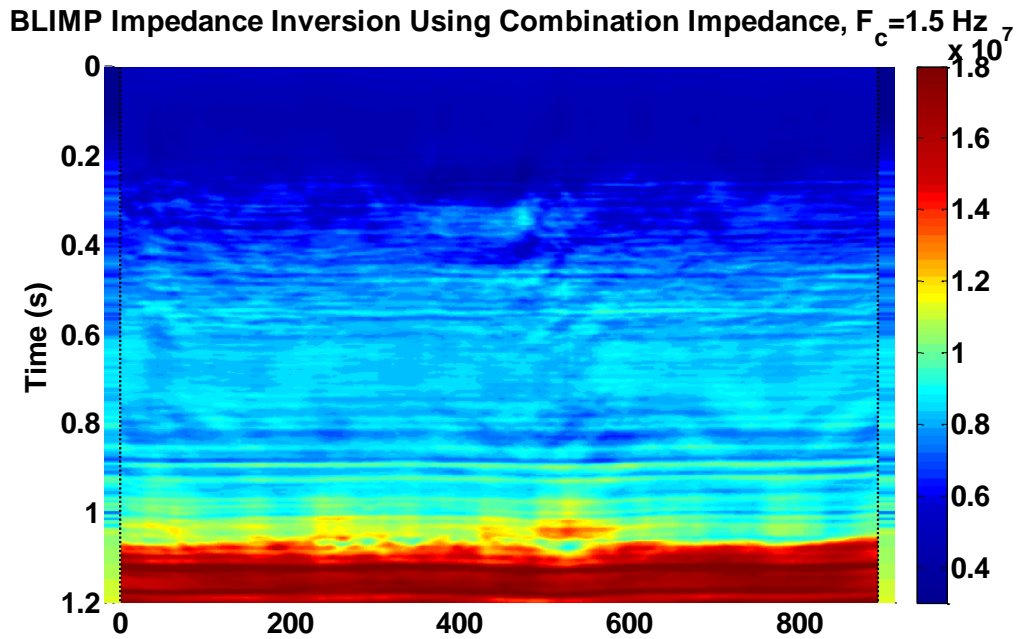


Figure 3.53: Impedance inversion calculated using combination impedance and a low frequency cut-off of 1.5 Hz. The filtered average impedance log is displayed on each side for reference.

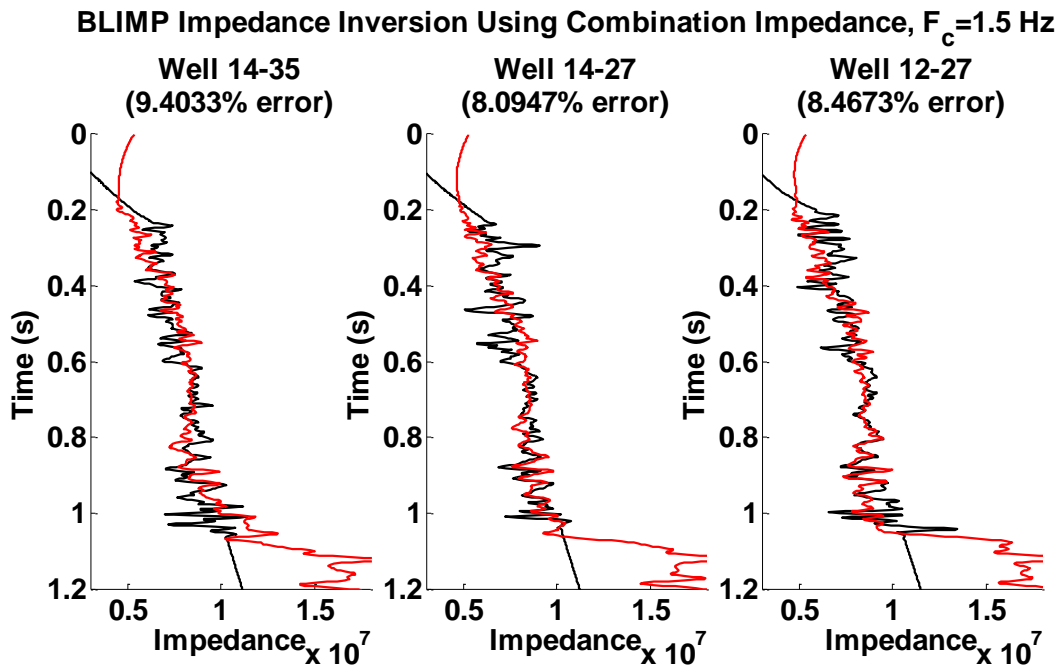


Figure 3.54: Cross validation plot that compares the inversion calculated using the combination impedance (Red) with the filtered well impedances (Black). Error is calculated in the interval from 0.2 seconds to 1.05 seconds.

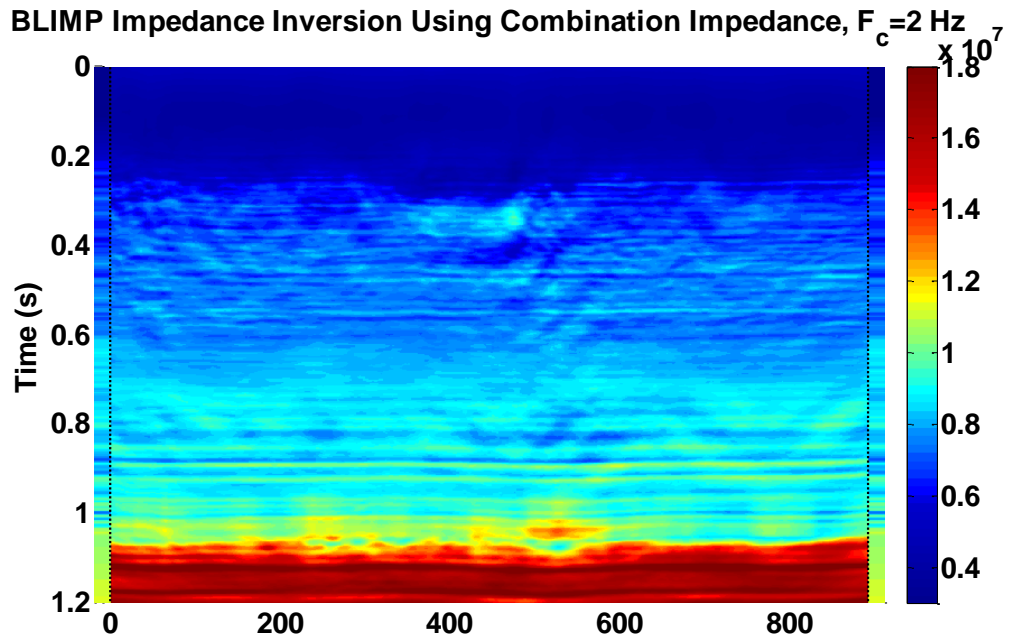


Figure 3.55: Impedance inversion calculated using combination impedance and a low frequency cut-off of 2 Hz. The filtered average impedance log is displayed on each side for reference.

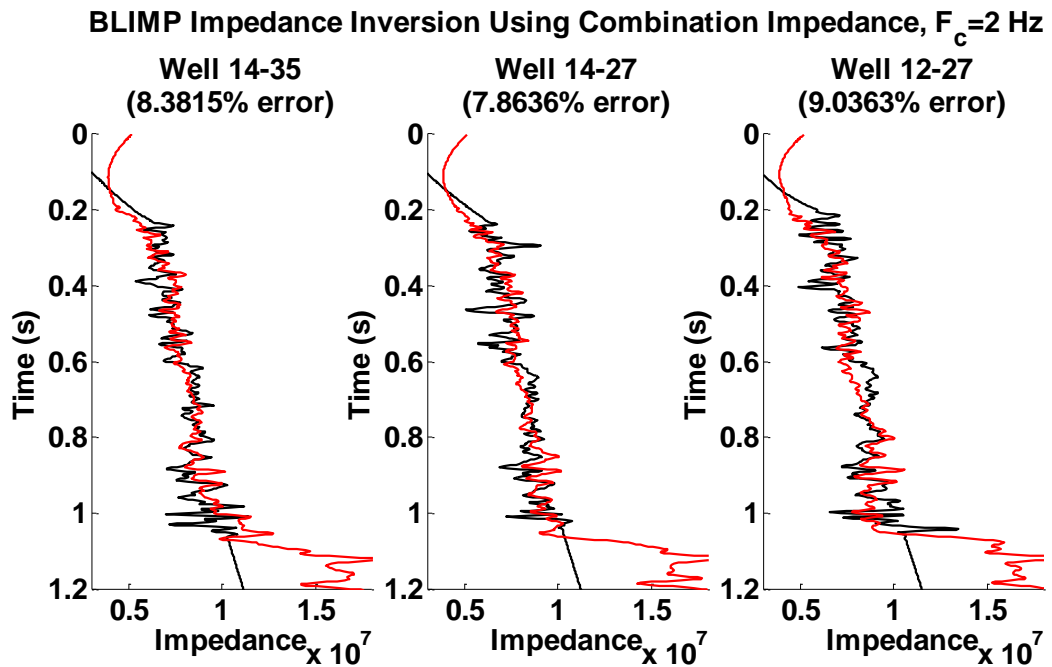


Figure 3.56 Cross validation plot that compares the inversion calculated using the combination impedance (Red) with the filtered well impedances (Black). Error is calculated in the interval from 0.2 seconds to 1.05 seconds.

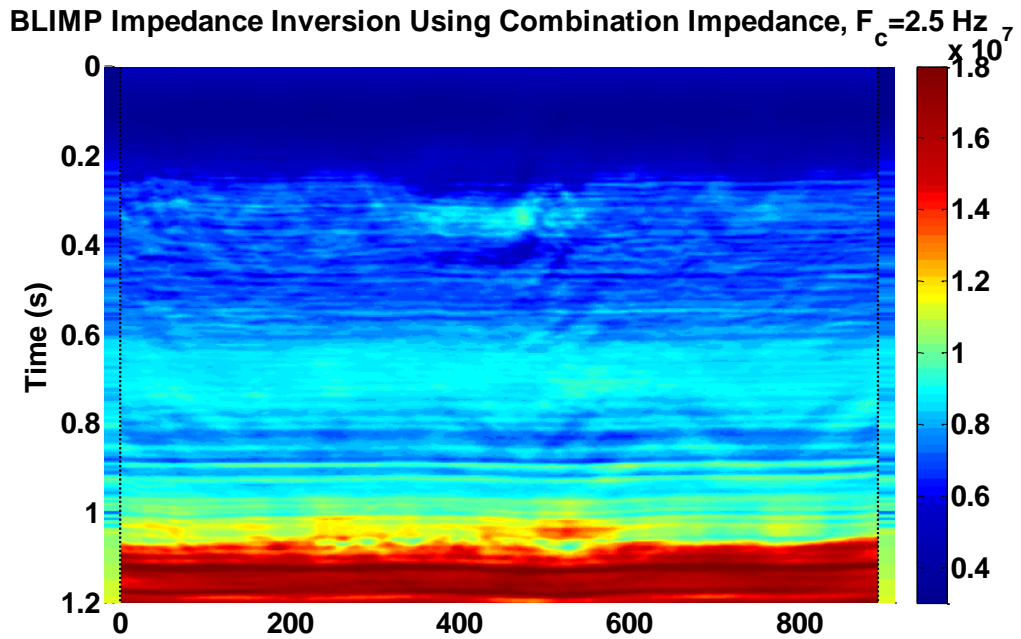


Figure 3.57: Impedance inversion calculated using combination impedance and a low frequency cut-off of 2.5 Hz. The filtered average impedance log is displayed on each side for reference.

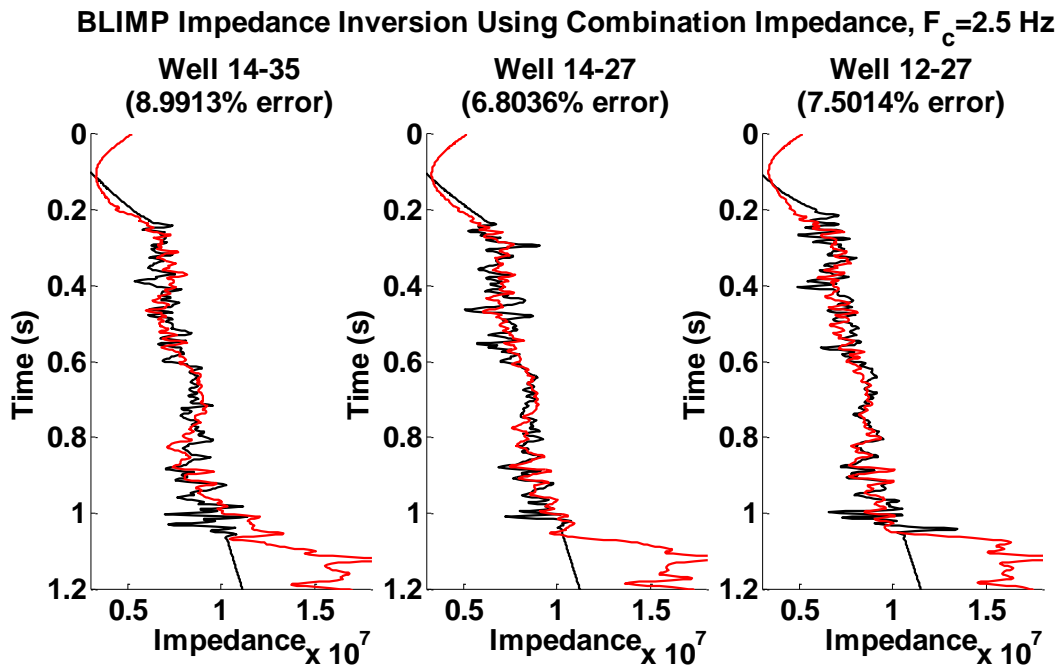


Figure 3.58 Cross validation plot that compares the inversion calculated using the combination impedance (Red) with the filtered well impedances (Black). Error is calculated in the interval from 0.2 seconds to 1.05 seconds.

Table 3.1: Percent errors calculated between filtered impedance logs and inversions for various low-frequency cut offs. The percent errors are calculated for four, 200 millisecond time windows.

	Low-frequency cut off (Hz)	Percent error from 0.2 to 0.4 seconds	Percent error from 0.4 to 0.6 seconds	Percent error from 0.6 to 0.8 seconds	Percent error from 0.8 to 1.0 seconds
Inversion compared with filtered impedance log from well 14-35	1	11.16	8.35	5.78	10.21
	1.5	12.77	8.71	3.77	8.53
	2	11.40	6.94	4.42	7.54
	2.5	9.72	7.66	5.16	8.81
	3	6.85	6.94	4.18	7.34
	3.5	6.24	7.58	5.83	6.03
	4	6.65	6.63	3.53	6.14
Inversion compared with filtered impedance log from well 14-27	1	11.64	13.69	4.35	4.52
	1.5	11.36	12.46	3.91	4.95
	2	9.52	9.61	5.25	7.05
	2.5	8.11	9.84	4.06	4.82
	3	7.01	10.25	3.91	4.26
	3.5	6.22	10.39	4.59	4.28
	4	7.13	8.88	4.50	4.15
Inversion compared with filtered impedance log from well 12-27	1	16.50	11.93	3.48	8.82
	1.5	13.96	9.31	2.97	6.36
	2	11.79	8.58	6.59	8.03
	2.5	10.63	8.96	3.33	5.90
	3	10.19	9.32	3.03	5.96
	3.5	10.21	8.82	4.26	5.83
	4	9.36	8.44	3.89	6.28

3.6 Summary

- The BLIMP algorithm is similar to the Lindseth method (1979) except it removes the linear trend and then applies a scalar to the integrated seismic data in the frequency domain. The linear trend is then added to the inversion result.
- The BLIMP algorithm adds low frequencies in two stages by estimating and removing the linear trend from the well impedance and adding it back to the

inversion and by adding low-pass frequencies from the well impedance to the inversion.

- The low-frequency cut off used in the low pass filter applied to the well impedance is very important. Selecting this value to be too low the impedance inversion will be unreliable. Selecting the value too high will cause the seismic data to be overwritten with information from the well logs, causing subtleties in the seismic to be erased.
- The BLIMP algorithm can be used with low-frequency information supplied by impedance logs from wells, impedance calculated from stacking velocities and a combination of stacking impedance and well impedance.
- The BLIMP algorithm applies a scalar to the integrated seismic. If this scalar is large enough it can amplify the low frequencies of the seismic and allow the cut off to be lower than it would be if the scalar was smaller. This only applies to seismic data that contain very low frequencies.
- The low frequency cut off is a rough indicator of the low-frequency content of the seismic data.
- In the Hussar data set, the low frequency content is time variant. For the shallow section the low-frequency content is about 3 Hz whereas for the deeper section the low-frequency content can be determined to be between 2 to 2.5 Hz. If the amplitude of the low-frequencies is boosted the low frequency content can be pushed down to 1.5 Hz.

Chapter Four: **Time-lapse CO₂ Study**

4.1 Introduction

Over the last century there has been an increase to the mean global temperature of about 0.4-0.6°C (Bachu, 2000). As much as 64 % of this change can be attributed to rising carbon dioxide levels (Bachu, 2000). While there may be other mechanisms for the observed warming trend, the increase in carbon dioxide can be attributed to human activity (Bachu, 2000). The use of fossil fuels to produce energy and transportation are large contributors to the production of carbon dioxide. Reducing the amount of carbon dioxide in the atmosphere is important in reducing the anthropogenic source of carbon dioxide emissions.

There are several ways to reduce carbon dioxide in the atmosphere including mineralization, biomass usage and geological storage (Bachu, 2000). Mineralization of carbon dioxide is a permanent form of storage; however it takes significant geologic time for the geochemical reactions to occur. Using forests to convert the carbon dioxide into growth and oxygen requires a significant amount of time and land use. Therefore geological storage is a very attractive long term carbon dioxide storage method.

The Alberta basin in western Canada is one of the most viable carbon dioxide sequestration sites (Bachu, 2002). Many depleted hydrocarbon fields are ideal storage sites as the producing formation is geologically sound and contains an adequate seal. Carbon dioxide sequestration can also aid in the production of hydrocarbons through fluid injection. This method is used worldwide and can enhance recovery of up to 40% of the residual oil in the formation, after primary production and water flooding has occurred (Bachu, 2000).

It is essential that sequestration projects are monitored to determine how quickly the carbon dioxide is moving through the reservoir and to determine its migration path to map any possible leakage (Cairns et al, 2010). Seismic surveys are commonly used for time lapse monitoring projects. The seismic data from the survey however tends to be noisy and difficult to interpret; computing acoustic impedance inversions provides more accurate interpretations (Latimer et al., 2000).

Acoustic impedance inversions need low-frequency information from an external source, such as well logs or stacking velocities (Latimer et al., 2000). In the previous chapters it is evident that well logs provide more reliable information so they will be used here. Well logs are usually recorded when a well is drilled. This measures the original properties of the formation and fluids. Therefore, most well logs do not represent the fluid properties after water or carbon dioxide is injected. This chapter will determine if re-logging a well is necessary for producing accurate impedance inversions in a reservoir with active fluid injection.

4.2 Violet Grove CO₂ Sequestration Model

4.2.1 Area Background

Carbon dioxide emissions have been attributed to adversely affecting the environment. To help reduce carbon dioxide emissions sequestration projects are being investigated. Violet Grove, located approximately 120 km south west of Edmonton, Alberta, was chosen as a pilot project for enhanced oil recovery and carbon dioxide sequestration, where 60,000 tons of carbon dioxide was injected between 2004 and 2009 (Alshuhail, 2011). Violet Grove is part of the Pembina oil field, which is the largest conventional oil field in North America covering an area of about 4000 km² and

containing an estimated 7.4 billion barrels of original oil in place (Alshuhail, 2011). Other oil recovery methods such as water flooding were done prior to the carbon dioxide sequestration (Chen, 2006). The main oil producer in this area is the Cretaceous sandstone in the Cardium formation, which contains thin beds of clean sandstone separated by thin layers of shale (Alshuhail, 2011). Fluid tends to flow along the upper sand layer but it is only separated from the middle sand by a thin layer of shale, which is not an effective permeability barrier (Alshuhail, 2011). The lower Cardium sand is separated by a much larger shale interval and can be assumed to be isolated from the other Cardium sands. This dissertation will create a time-lapse model based on the fluid properties and changes in the Violet Grove area. The model will go through the three stages of oil recovery seen at Violet Grove, and will use well logs and available fluid and mineral properties, but is not meant to be a fully realistic simulation of the Violet Grove EOR Project.

4.2.2 Well Preparation

In the Violet Grove field there were two wells that had extensive logging. Well 102/08-14-48-9W5 (08-14) was drilled in 1985 to a depth of 2225 meters and was logged to include a gamma ray, sonic and density, Figure 4.1. Well 102/07-11-48-9W5 (07-11) was drilled in 2004 to a depth of and was logged to include gamma ray, sonic and dipole sonic, Figure 4.2. Since well 08-14 includes a density log and is the longest, it will be used as the model well.

Castagna et al. , (1993) characterizes the relationship between p-wave velocity (V_p) and s-wave velocity (V_s) as linear. The most commonly used relationship is the mudrock line,

$$V_s (m/s) = .8621 V_p - 1172.4. \quad 5.1$$

However, since most of the lithology besides the Cardium is shale the relationship for shale

$$V_s (m/s) = .7700 V_p - 867.4. \quad 5.2$$

was used as it provided more accurate results. The Cardium formation was not well characterized by either standard relationship so a custom relationship

$$V_s (m/s) = .4831 V_p - 412.6. \quad 5.3$$

derived from the logs in well 07-11 was used for the formation. Figure 4.3 shows log data as well as the three linear relationships described above.

When wells are drilled they are rarely logged for the entire length of the well. At best they start at about 200 meters down due to the casing and continue to the reservoir. For modeling this means that an overburden and underburden need to be applied to the wells. To create the overburden a seismic shot record was selected from the Violet Grove time-lapse survey and first break analysis was completed to get a starting velocity of 1103 m/s or 906 μ s/m. A linear gradient was applied to the sonic starting at 0 m and continuing to the beginning of the well log at 308 meters, using the result from the first break analysis. The density overburden was applied using a Gardner based relationship for shale from Castagna et al. (1993)

$$\rho (kg/m^3) = 175 V_p(m/s)^{.265} \quad 5.4$$

The linear trend of the P-wave velocity and density was used for the underburden of each of the p-wave and density logs. The S-wave velocity overburden and underburden was calculated using the shale $V_p \propto V_s$ relationship.

To better characterize the mineralogy of the Cardium formation an estimate of the volume of shale is needed. The Volume of shale can be calculated from the gamma ray log (Rider, 2008)

$$v_{sh}^* = \frac{GR - \min(GR)}{\max(GR) - \min(GR)} \quad 5.5$$

where GR is the gamma ray. This result needs to be corrected as v_{sh}^* tends to overestimate the volume of shale using

$$v_{sh} = 0.33(2^{2v_{sh}^*} - 1) \quad 5.6$$

from (Rider, 2008).

08-14 Well Logs

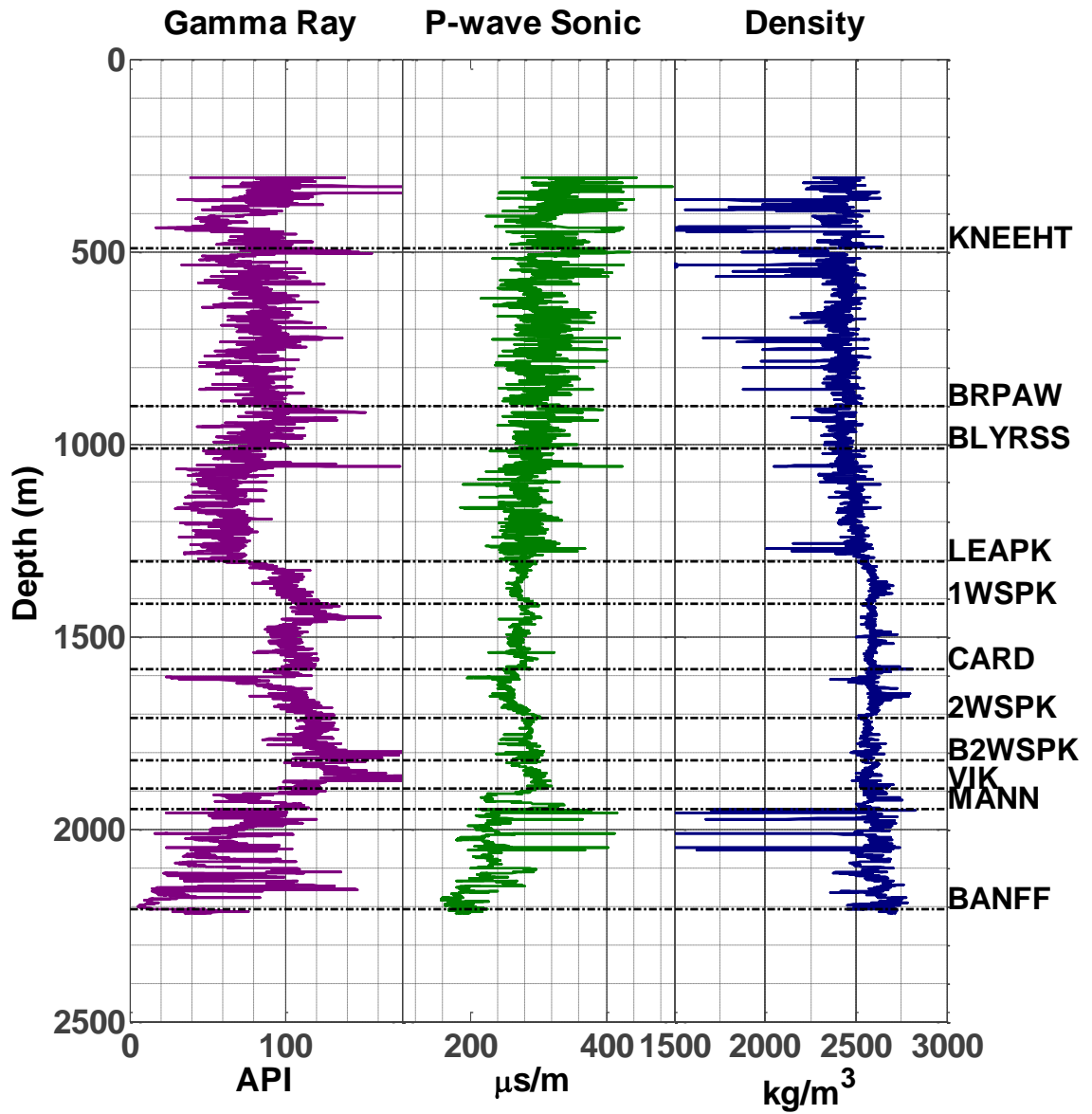


Figure 4.1: Well 102/08-14-48-9W5, with gamma ray, sonic and density logs, recorded from 308 m to 2220 m.

07-11 Well Logs

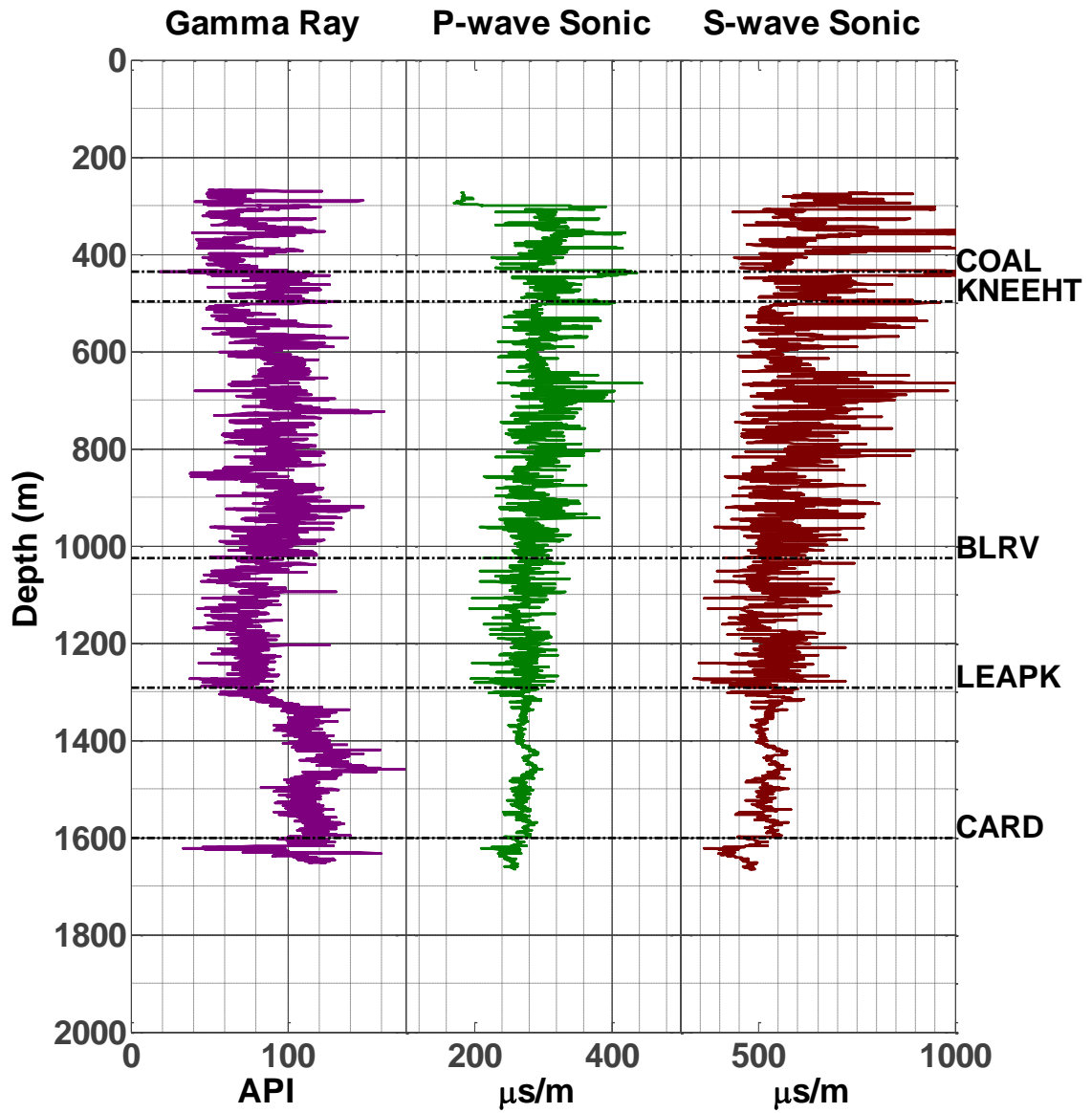


Figure 4.2: Well 102/07-11-48-9W5, with gamma ray, sonic and shear sonic recorded from 260m to 1670 m.

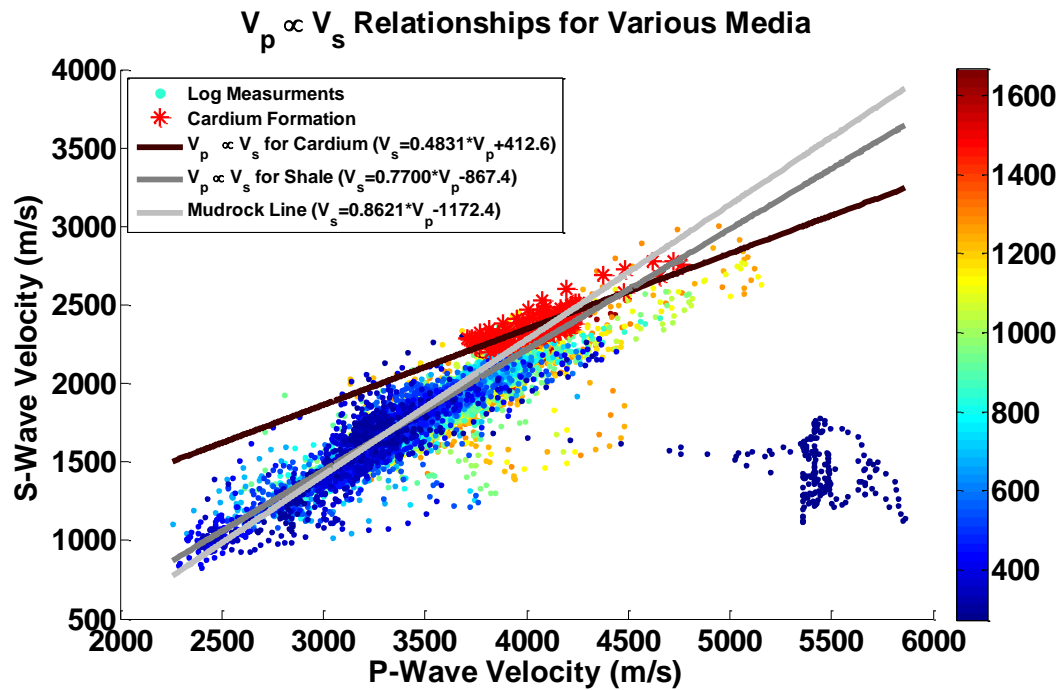


Figure 4.3: P-wave velocity and S-Wave linear relationships. The color bar indicates the depth of the log measurements. The Cardium formation is indicated by the red asterisk.

The Cardium consists of three sand beds separated by shale layers; this creates very thin (~4 m) sand beds that are isolated from each other. Modeling the reservoir as the thin sand beds proved difficult as they were not imaged very well in the seismic survey. To overcome the imaging difficulties the entire Cardium formation, at depths from 1587 meters to 1629 meters, was chosen as the fluid substitution interval. It is convenient to create a homogenous reservoir for fluid substitution, so the properties from a clean high porosity sand at 1610 meters was used to fill the homogenous reservoir. Figure 4.4 shows the recorded logs and the logs with the homogeneous reservoir. This modelling assumption creates a simplified reservoir scenario that will exaggerate the actual Cardium's ability to sequester CO₂.

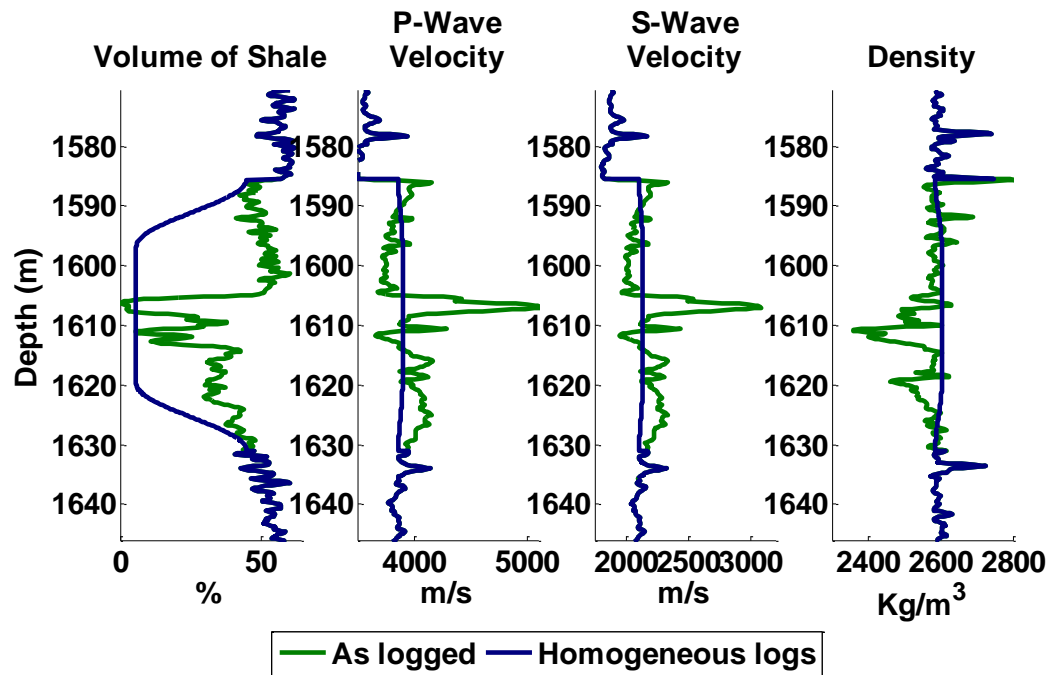


Figure 4.4: Volume of shale, p-wave velocity, s-wave velocity and density logs before and after the homogenous reservoir was created.

4.2.3 Gassmann Fluid-Substitution

4.2.3.1 Theory

Gassmann (1951) derived a method of simulating fluid changes in a reservoir by measuring the saturated bulk modulus of the reservoir and then calculating the bulk modulus of the rock frame by assuming the original fluid parameters are known (Smith et al. 2003 and Kumar 2006). The bulk modulus of the rock frame is held constant throughout the fluid substitution as it is assumed that the rock frame will not undergo any lithological or structural changes throughout the fluid substitution process. The shear modulus will also remain constant as it is assumed that the fluids do not affect the shear modulus of the rock. When a well is drilled the p-wave sonic, s-wave sonic and density

can be logged (usually a dipole sonic is run which measures both P and S waves). From these measurements the saturated bulk modulus can be calculated by

$$K_{sat} = \rho \left(V_p^2 - \frac{4}{3} V_s^2 \right), \quad 5.7$$

where ρ is the density and the p-wave velocity (V_p) and s-wave velocity (V_s) can be calculated from the sonic logs. Whereas the shear modulus can be calculated by using

$$\mu = \rho V_s^2, \quad 5.8$$

The bulk modulus and density of the fluid and the mineral matrix need to be calculated using

$$\frac{1}{K_{fluid}} = \frac{S_{brine}}{K_{brine}} + \frac{S_{oil}}{K_{oil}} + \frac{S_{CO_2}}{K_{CO_2}}, \quad 5.9$$

where S_{xxx} is the saturation of fluid xxx and

$$K_{matrix} = \frac{1}{2} \left([v_{clay} K_{clay} + v_{qtz} K_{qtz}] + \left[\frac{v_{clay}}{K_{clay}} + \frac{v_{qtz}}{K_{qtz}} \right]^{-1} \right), \quad 5.10$$

where $v_{clay} = 80\% * v_{sh}$ and $v_{qtz} = 1 - v_{clay}$, we assume that shale is made up of a combination of 20% quartz particles and 80% clay. The bulk modulus of the rock frame can be calculated by

$$K_{frame} = \frac{K_{sat} \left(\frac{\phi K_{matrix}}{K_{fluid}} + 1 - \phi \right) - K_{matrix}}{\frac{\phi K_{matrix}}{K_{fluid}} + \frac{K_{sat}}{K_{matrix}} - 1 - \phi}, \quad 5.11$$

where ϕ is the porosity and can be calculated by

$$\phi = \frac{\rho_{matrix} - \rho_{bulk}}{\rho_{matrix} - \rho_{fluid}}, \quad 5.12$$

where ρ_{bulk} is the measured density and the fluid and matrix densities can be calculated by

$$\rho_{fluid} = S_{brine}\rho_{brine} + S_{oil}\rho_{oil} + S_{CO_2}\rho_{CO_2}, \quad 5.13$$

and

$$\rho_{matrix} = V_{clay}\rho_{clay} + V_{qtz}\rho_{qtz}. \quad 5.14$$

Once the bulk modulus of the rock frame has been determined the fluid changes can be modeled. Equations 5.9 and 5.13 can be recalculated for the new fluid fractions. The saturated bulk modulus can then be recalculated incorporating the new fluids, using

$$K_{sat} = K_{frame} + \frac{\left(1 - \frac{K_{frame}}{K_{matrix}}\right)^2}{\frac{\phi}{K_{fluid}} + \frac{(1-\phi)}{K_{matrix}} - \frac{K_{frame}}{K_{matrix}^2}}. \quad 5.15$$

From this result the velocities can then be recalculated in the interval by

$$V_s = \sqrt{\frac{\mu}{\rho}} \quad 5.16$$

and

$$V_p = \sqrt{\frac{K_{sat} + 4/3\mu}{\rho}}. \quad 5.17$$

Gassmann fluid substitution is a powerful tool but is only valid if the following assumptions hold true:

- The rock is homogenous and isotropic. The mineral composition must be equally distributed throughout the formation. Any anisotropic minerals can cause errors in the calculations (Smith et al. 2003). This also extends to the mineral composition and frame orientation not changing during the fluid substitution. For the Violet Grove model used in this thesis, the reservoir was deliberately made homogenous. In the more realistic settings this assumption is not held as the reservoir tends to be non-

homogenous and carbon dioxide often reacts with water and other minerals that can cause dissolution of the rock matrix or precipitation of new minerals depending on the lithology of the host rock and formation water properties.

- All pore spaces are connected and the fluid pressure is constant in the reservoir. (Smith et al. 2003). This either assumes that the fluids are homogeneously mixed throughout the reservoir or that there is patchy saturation. Patchy saturation requires a complicated fluid bulk modulus to be calculated, at seismic frequencies if the fluid patches are small then the rock can still be modeled using a homogeneous assumption (Cairns et al, 2010). In the Violet Grove model this assumption is valid. In the field differential buoyancies of gas, carbon dioxide, oil, and brine cause the fluids at equilibrium to become layered, requiring complicated calculations of the fluid bulk modulus.

Carbonate rocks tend to have pore spaces that are not connected violating the assumption of connected pore space. Since the Cardium formation is shaley sandstone, the shale can fill pores and cause reduced connectivity. In the Violet Grove model developed in this thesis, the reservoir is homogeneous so that the pore connectivity assumption is valid.

- The Gassmann equations are only valid for seismic frequencies. High frequencies, such as the recording frequencies of sonic logs may cause errors depending on the rock matrix (Smith et al. 2003). Shaley sands,

carbonates and low-porosity reservoirs tend to have larger errors than clean sand reservoirs at high frequencies.

4.2.3.2 Methodology

The fluid substitution in the Violet Grove simulation will go through three phases. Phase one contains the original fluids in the Cardium, which were assumed to be 50% oil, with dissolved gas and 50% brine with a salinity of 75,000 mg/L Chen (2006). Phase two represents the first attempt in recovering oil. The reservoir was flooded with fresh water thus reducing the salinity of the brine to 40,000 mg/L. During the production, it is assumed that some of the gas was driven out of the oil thus reducing the gas to oil ratio (GOR) from 100 to 4. The remaining fluids in the reservoir after the water flooding were 20% oil, and 80% diluted brine. To store carbon dioxide and ideally produce more oil, carbon dioxide was injected into the reservoir during the third fluid phase. The fluids remaining in the reservoir after this were 2% irreducible oil, 35% carbon dioxide and 63% diluted brine. Oil and carbon dioxide are more buoyant than brine therefore the fluids would normally produce layers. This invalidates the Gassmann equations so the fluids in this model will be assumed to be equally mixed throughout the formation. Figure 4.5 shows the saturation of the fluids in each phase.

Fluid properties are sensitive to the temperature and pressure in the reservoir. The Cardium formation is at approximately 1600m below the surface. In well 07-11 the temperature was recorded at 53°C at 1679m. This equates to about 50°C at the reservoir. To get the pressure at the reservoir a gradient of 22.17 MPa per kilometer of depth was used, which was derived using the density log average to calculate the lithostatic pressure

only. At 1600m the pressure is approximately 35.5 MPa. Plotting these parameters on a phase diagram, Figure 4.6, shows that the carbon dioxide will be in supercritical phase, thus acting like a gas but having a the density of a liquid (Bachu, 2000). The bulk modulus and density of the fluids can be calculated using the methods described in Batzel and Wang (1992) and Kumar (2006) and given in Table 4.1.

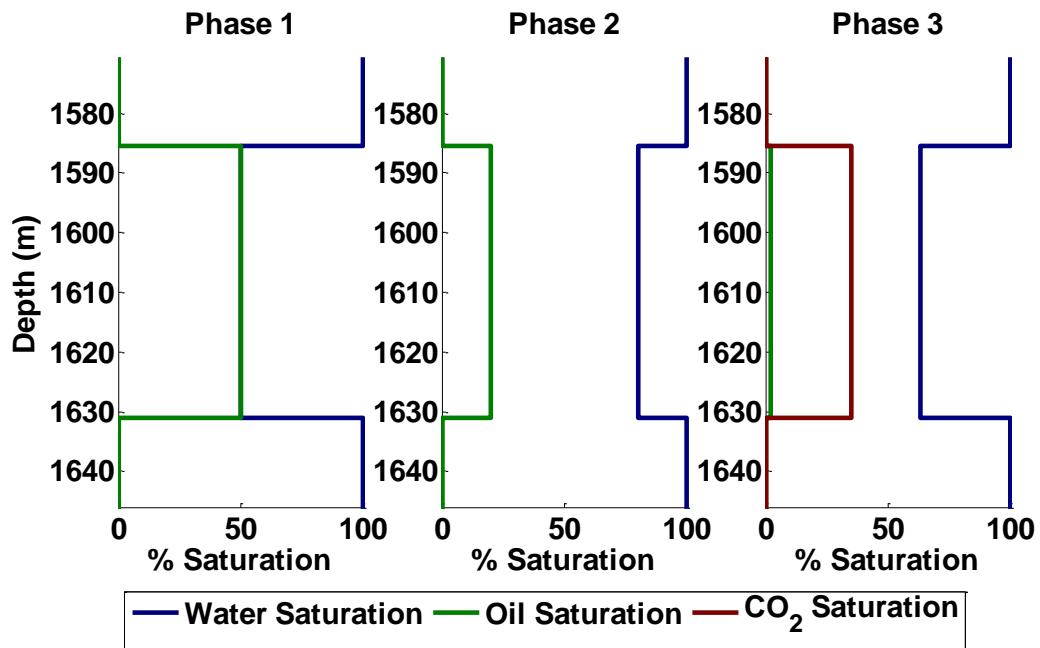


Figure 4.5: Fluid saturation for the three stages of field development. Phase 1- original fluids in place, Phase 2- after water injection, Phase 3- after carbon dioxide injection.

Table 4.1: Bulk modulus and density properties of fluids and minerals in the Cardium formation.

Material	Other Properties	Bulk Modulus (GPa)	Density (g/cm ³)
Clay		20.9	2.58
Quartz		36.6	2.65
Original Brine	Salinity = 75,000 mg/l	2.960	1.054
Diluted Brine	Salinity = 40,000 mg/l	2.776	1.030
Original Oil	40 API, 100 Gas to oil ratio, specific gravity of gas = 0.894	0.970	0.726
Oil after production	40 API, 4 Gas to oil ratio, specific gravity of gas = 0.894	1.573	0.804
Carbon Dioxide (Supercritical)	Temperature 50° and Pressure 35.5 MPa	0.287	0.874
Carbon Dioxide (Gaseous)	Temperature 50° and Pressure 5 MPa	0.005	0.149

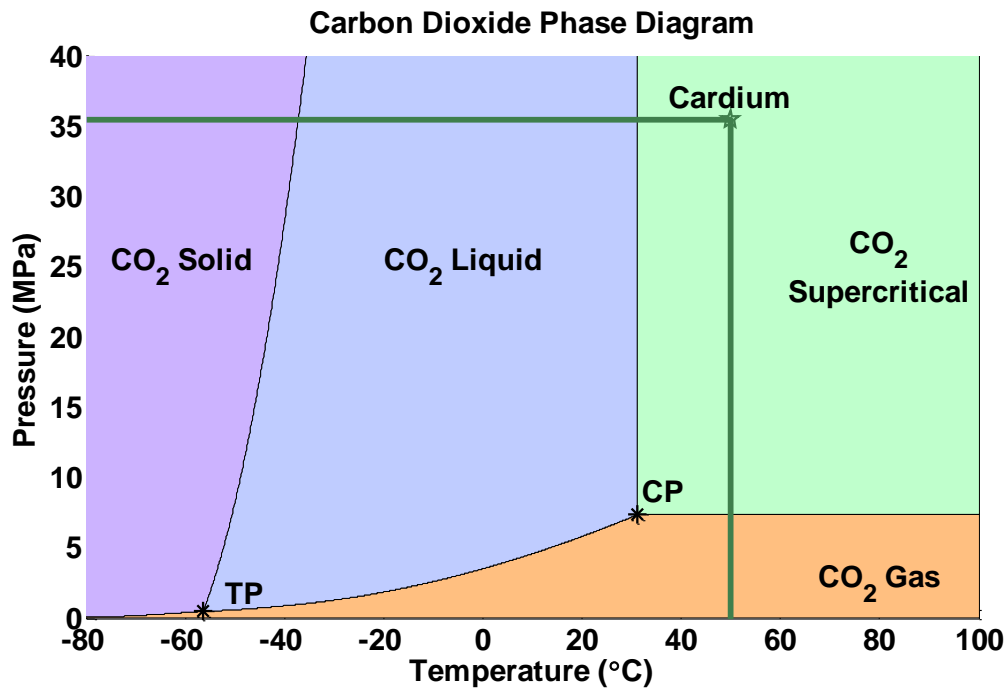


Figure 4.6: Phase diagram for carbon dioxide. The Cardium formation plots in the supercritical phase. TP is the triple point where at this temperature and pressure solid, liquid and gaseous phases exist in equilibrium. CP represents the critical point where the carbon dioxide enters into the supercritical phase. (Modified from Bachu, 2000)

The Batzle and Wang (1992) equations are empirical relationships used to calculate the bulk modulus and density of fluids at different pressures and temperatures. The gas equation can be extended for carbon dioxide. Batzle and Wang's gas equation uses the specific density of the gas to calculate the critical temperature and pressure, which is where the gas transfers to the supercritical stage. For carbon dioxide the actual critical point at 7.4 MPa and 31.1°C needs to be used in these equations or significant errors will be observed (Xu, 2006). Error can also be introduced if both the ratio of the formation temperature to the critical temperature in kelvin and the ratio of the formation pressure to the critical pressure are between 0.9 and 1.1 (Batzle and Wang, 1992). This may cause some difficulties when modeling carbon dioxide sequestration reservoirs as they can have temperatures and pressures close to the critical point.

The fluid substitutions that were calculated for each phase and the resulting velocity, density and P-wave impedance can be seen in Figure 4.7. Between the water injection phase and the carbon dioxide injection phase the p-wave velocity dropped 443 m/s (-11%). The s-wave velocity increased by 0.1 m/s. This increase is to be expected as the density of the rock is inversely proportional to the density which decreased. The fractional amount of change is also to be expected as the shear modulus is held constant through the Gassmann fluid substitutions. The density decreased by 0.3 kg/m^3 , which is also to be expected as the carbon dioxide replaced mostly oil during the fluid substitution and the densities of the oil and the supercritical carbon dioxide are very similar. The impedance decreased by $1156000 \text{ Kg}\cdot\text{m/m}^3\cdot\text{s}^2$ (-11%). The impedance of the reservoir is very similar to the impedance above the reservoir so it may not be fully detected in the seismic.

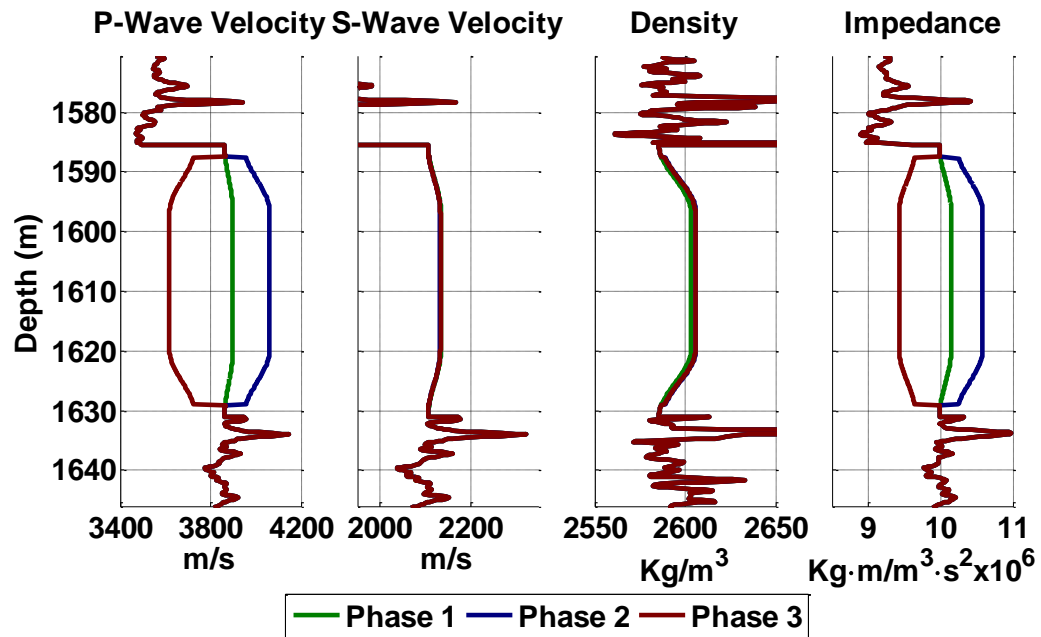


Figure 4.7: Velocity, density and impedance signatures in the Cardium reservoir for phase 1: original fluids, phase 2: water injection and phase 3: injection of supercritical carbon dioxide.

To investigate the effect of a gaseous carbon dioxide the fluid substitutions were repeated in the same interval. While the gaseous phase is unlikely to be found so deep in ground it represents the effect of the gaseous phase on inversions and any insights can be applied to shallower depths. The gaseous carbon dioxide bulk modulus and density can be seen in

Table 4.1. These values are significantly lower than the supercritical carbon dioxide. Figure 4.8 shows the signature of the injected gas. The difference between the water injection phase and the gaseous carbon dioxide phase for p-wave velocity is 1058 m/s (-26%). This is significantly higher than the supercritical result. The s-wave velocity increased by 2.7 m/s and the density decreased by 6.6 kg/m³. The impedance decreased by 2777000 Kg·m/m³·s² (-26%). The impedance in the reservoir is significantly less than the impedance in the rocks above. This will result in a clean reflection coefficient being produced and the reservoir being imaged.

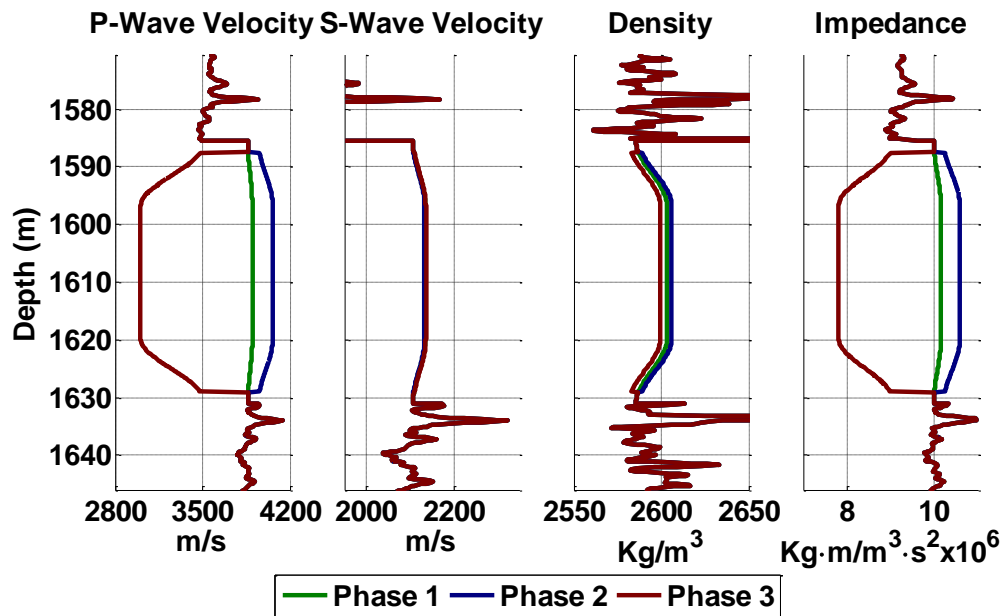


Figure 4.8: Velocity, density and impedance (P-wave) signatures in the Cardium reservoir for phase 1: original fluids, phase 2: water injection and phase 3: injection of gaseous carbon dioxide.

4.2.4 Synthetic-Seismic production

Before the synthetic seismic can be produced a velocity and density model are needed. These models were produced by blending the original log, the water injected log

and the carbon dioxide injected log together. Figure 4.9 shows the placement of the logs where the original well was placed at 0 and 3000 meters, the water injection well was placed at 500, 1000, 2000 and 2500 meters and the carbon dioxide well was placed at 1500 meters in the model. The pseudo-logs, at 2 meter intervals, were calculated by blending the two nearest wells with a weighting factor. This weighting factor was inversely proportional to the distance away from the well. An Impedance model was also produced for both the supercritical carbon dioxide (Figure 4.10) and the gaseous carbon dioxide (Figure 4.11). The gaseous carbon dioxide model has an observable impedance drop when compared with the supercritical model.

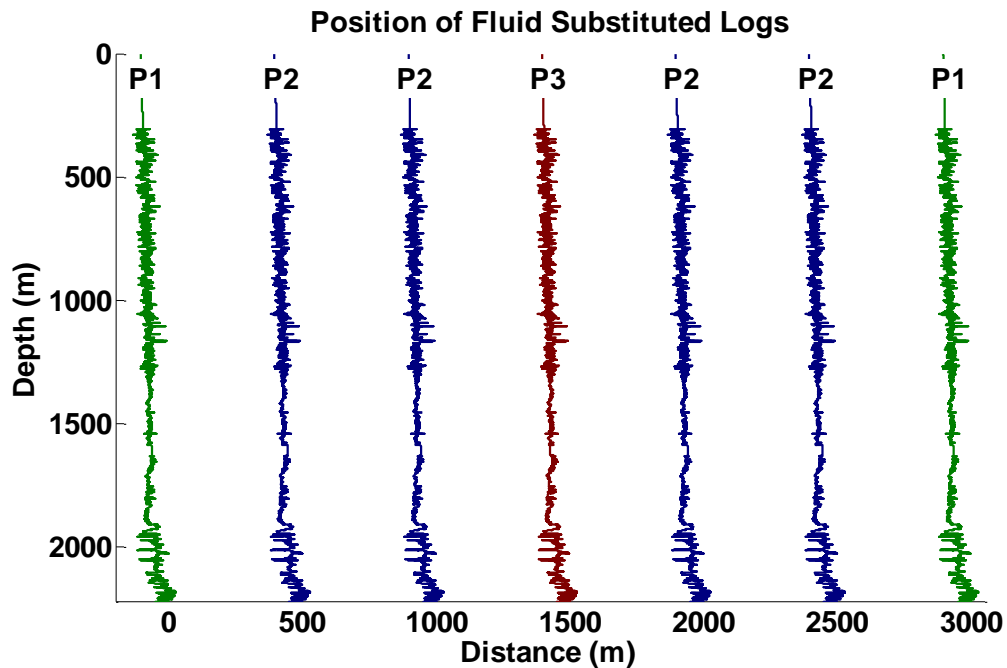


Figure 4.9: Log placement for creating the velocity and density model for the fluid substituted reservoir. P1 is the phase 1 logs that contain original fluids, P2 is the phase 2 logs which model the fluids after water injection, P3 is the phase 3 logs which model the fluids after the carbon dioxide injection.

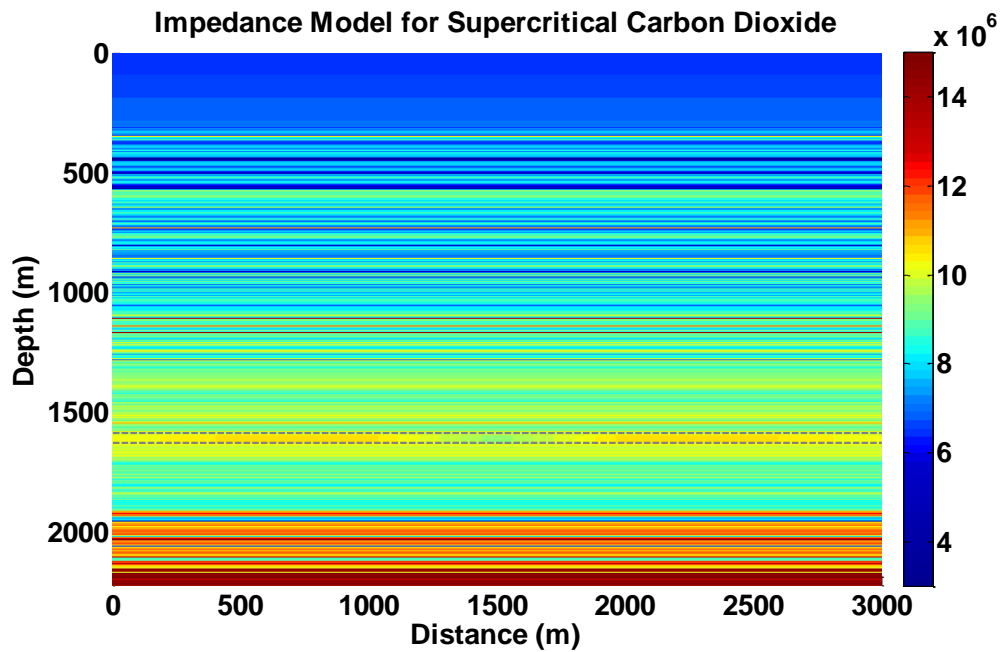


Figure 4.10: Impedance model using supercritical carbon dioxide. The horizontal grey lines near 1600m depth represent the top and bottom of the Cardium reservoir. If the carbon dioxide spread radially about the well bore this model would simulate the sequestration of about 58000 metric tonnes of supercritical carbon dioxide.

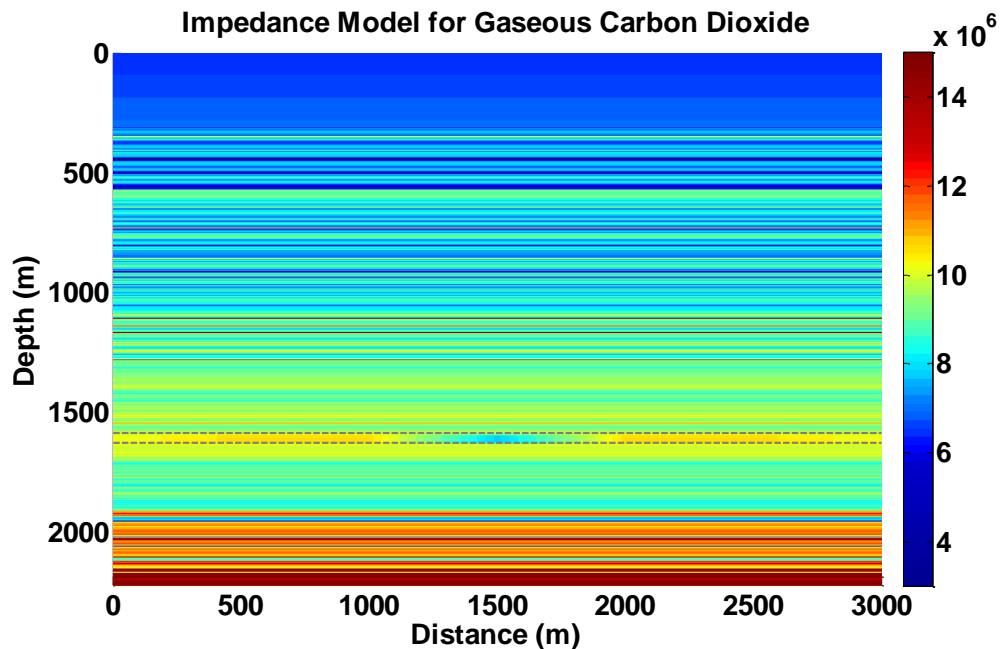


Figure 4.11: Impedance model using gaseous carbon dioxide. The horizontal grey lines near 1600m depth represent the top and bottom of the Cardium reservoir. If the carbon dioxide spread radially about the well bore this model would simulate the sequestration of about 8200 metric tonnes of gaseous carbon dioxide.

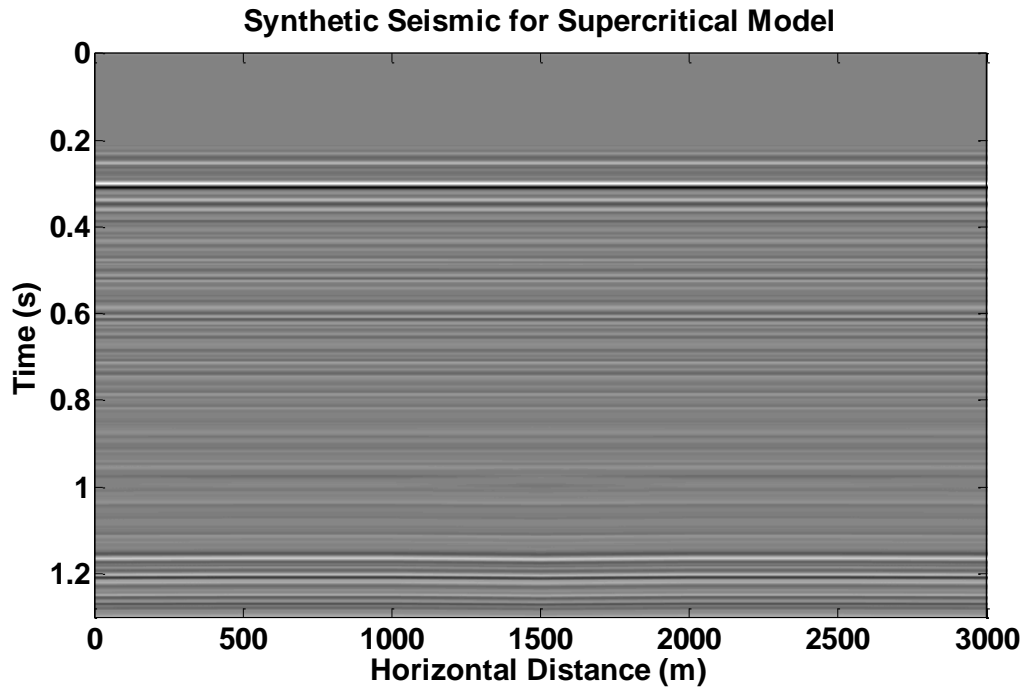


Figure 4.12: Synthetic seismic for supercritical model using a [8 10 50 125] zero phase Ormsby wavelet. The Cardium reservoir is located at about 1 second.

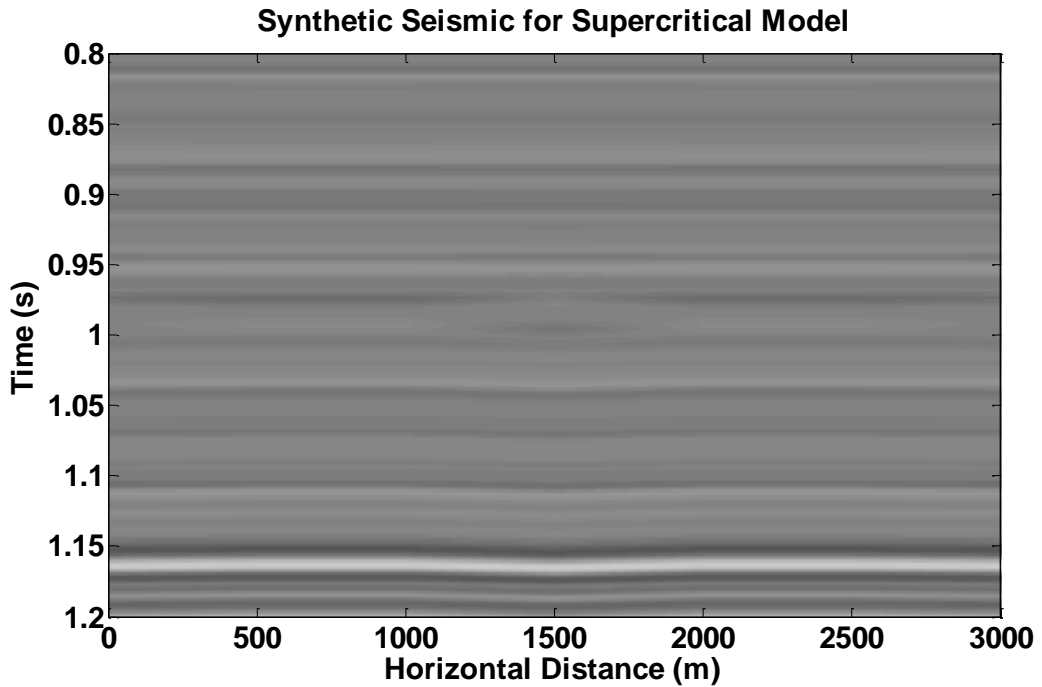


Figure 4.13: Synthetic seismic for supercritical model using a [8 10 50 125] zero phase Ormsby wavelet. This has been zoomed in to view the Cardium reservoir in more detail at about 1 second.

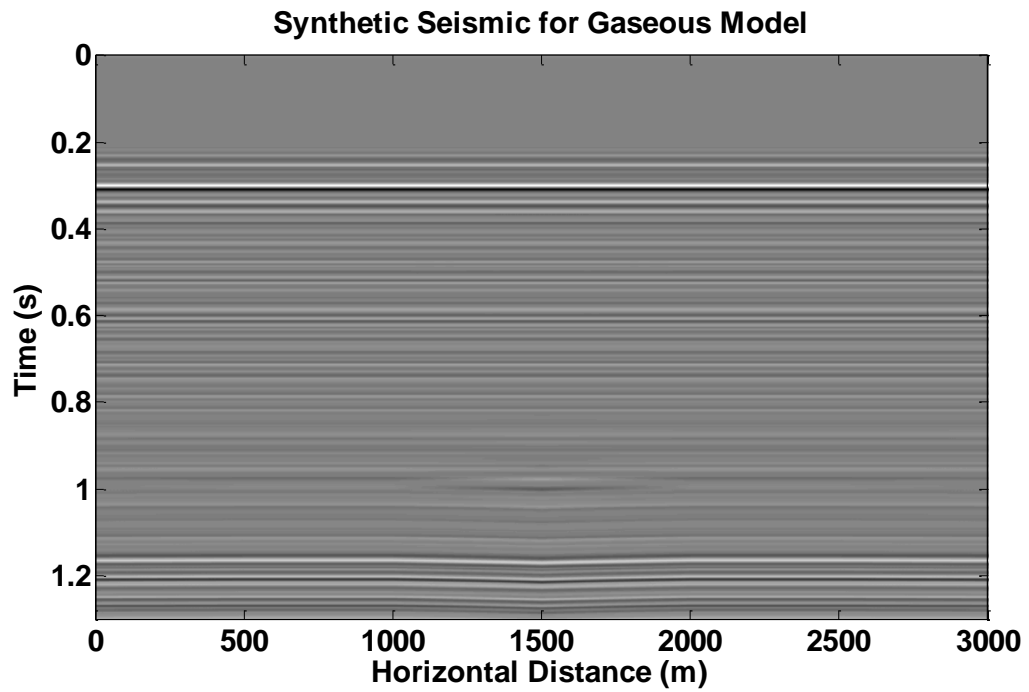


Figure 4.14: Synthetic seismic for gaseous model using a [8 10 50 125] zero phase Ormsby wavelet. The Cardium reservoir is located at about 1 second.

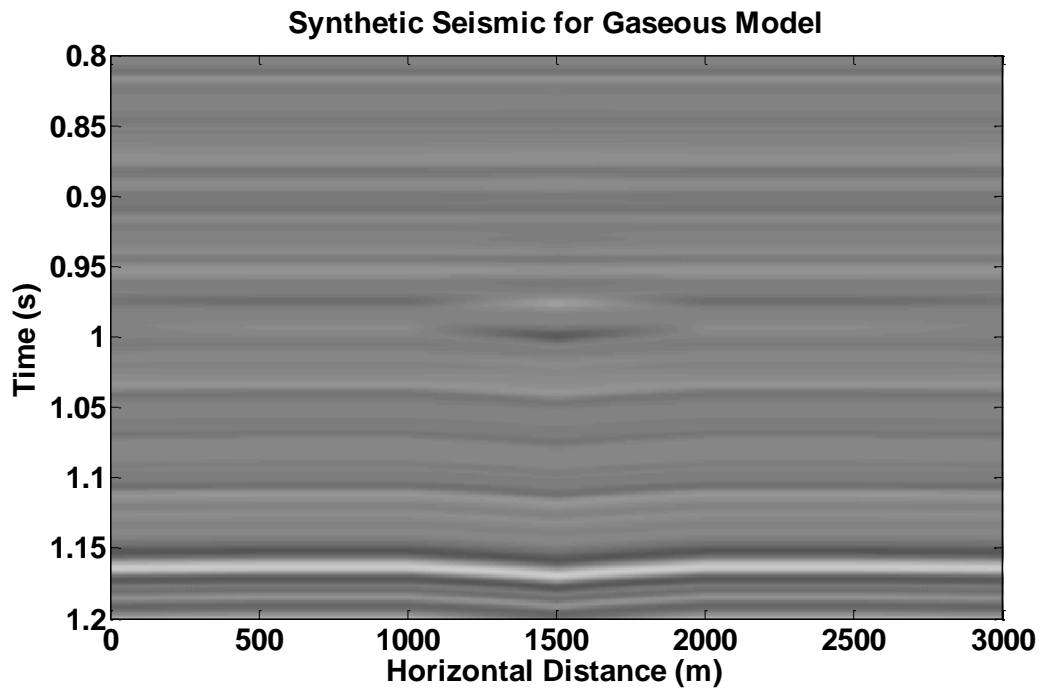


Figure 4.15: Synthetic seismic for gaseous model using a [8 10 50 125] zero phase Ormsby wavelet. This has been zoomed in to view the Cardium reservoir in more detail at about 1 second.

The synthetic seismic sections were calculated by computing primaries only normal-incidence seismograms for each pseudo-log in the impedance model, using a [8 10 50 125] zero phase Ormsby wavelet for both models. The carbon dioxide plume, at 1 second, is more visible in the gaseous section (Figure 4.14 and Figure 4.15) than in the supercritical section (Figure 4.12 and Figure 4.13). There are also more pull-down effects on the gaseous section than the supercritical section. An inversion is needed to detect where the supercritical carbon dioxide plume exists and delineate the gaseous carbon dioxide plume.

4.3 Inversions Using BLIMP

4.3.1 Introduction

Well logs are needed to provide low-frequency information to the impedance inversion. Since this is a time-lapse project, it is advantageous to investigate the consequences of using just a baseline log, or both baseline and monitor logs, in the inversion. The baseline log represents the model at time zero in a time-lapse case. There is a greater impedance contrast between the carbon injection log and the water injection log than between the original log and the carbon injection log. We will assume that the water injection occurred from an adjacent well and this new well that was drilled after the water injection will be used as baseline well. The monitor log represents the log at a time after carbon dioxide injection.

Obtaining a monitor log is very expensive and logistically difficult as production of the well must stop and be cleaned out so the logging tools can be put down the hole. It is very uncommon in industry to record a monitor log. If the monitor log were to produce

more accurate inversions it may be beneficial to record monitor logs on a regular basis for time lapse surveys.

The wavelet that was used has a low cut value of 10 Hz, which approximates a traditional processing flow. To remove unwanted low-frequency noise a high-pass filter is generally applied to seismic data. This filter often removes frequencies up to 10 Hz. Using this wavelet mimics the noise filter that is applied to the data and shows inversion results that would be seen when inverting a common survey. Since the wavelet is known the low-frequency cut off can be easily determined. For these inversions a low-frequency cut-off of 9 Hz will be used.

4.3.2 Supercritical Carbon Dioxide Model

Before any impedance inversions are calculated analyzing the ideal impedance section is important, if available. Figure 4.16 shows the true impedance of the supercritical model that has been low pass filtered to match the seismic data. The Cardium formation is depicted by the grey horizontal lines on the section. The top of the carbon dioxide plume is difficult to identify as it has a very similar impedance to the layer above it; but, it does show good contrast laterally against the water-injected logs. The bottom is easier as a high impedance layer occurs beneath it. The brine filled reservoir surrounding the plume has higher impedance. Adjusting the color map and scale can help illuminate impedance changes more easily.

BLIMP impedance inversions were calculated using both the baseline and monitor logs for the supercritical model. The baseline results using a low frequency cut off of 9 Hz can be seen in Figure 4.17. When compared to the true impedance this

inversion over estimates the impedance of the carbon dioxide plume making it appear laterally smaller than it actually is and has also overestimated the formation underlying the plume. Figure 4.18 shows the cross validation plots for wells at 250 meters, 750 meters and 1250 meters. Wells 250 and 750 had errors of 0.8% and 0.4% respectively and characterize the water flooded zone. Well 1250 is in the reservoir and the impedance can be seen to be larger than the true impedance by 1.8% in the reservoir interval depicted by the grey horizontal lines. When the impedance is overestimated the plume edges become smaller indicating that the plume has not spread as much as it actually has.

The BLIMP impedance inversion using the monitor impedance log is shown in Figure 4.19. In this inversion is clear that the inversion has underestimated the impedance around the reservoir interval. Figure 4.20 shows the cross validation plots where it is evident that the inversion is consistently lower at all three well intersections. Well 250, 750 and 1250 have errors of 2.9%, 3.2% and 2.0% respectively

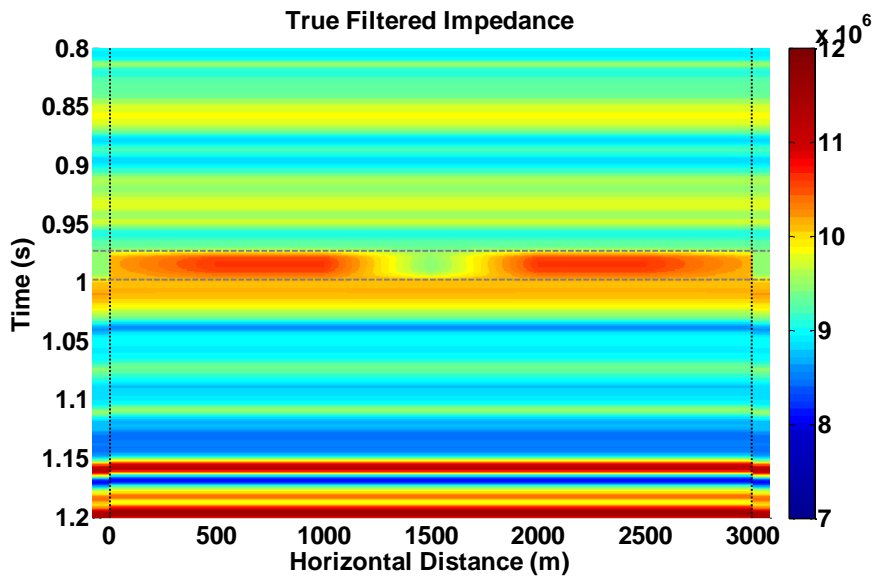


Figure 4.16: True filtered impedance for the supercritical carbon dioxide model. The filtered impedance at 1500 meters is plotted on each side of the impedance section for reference.

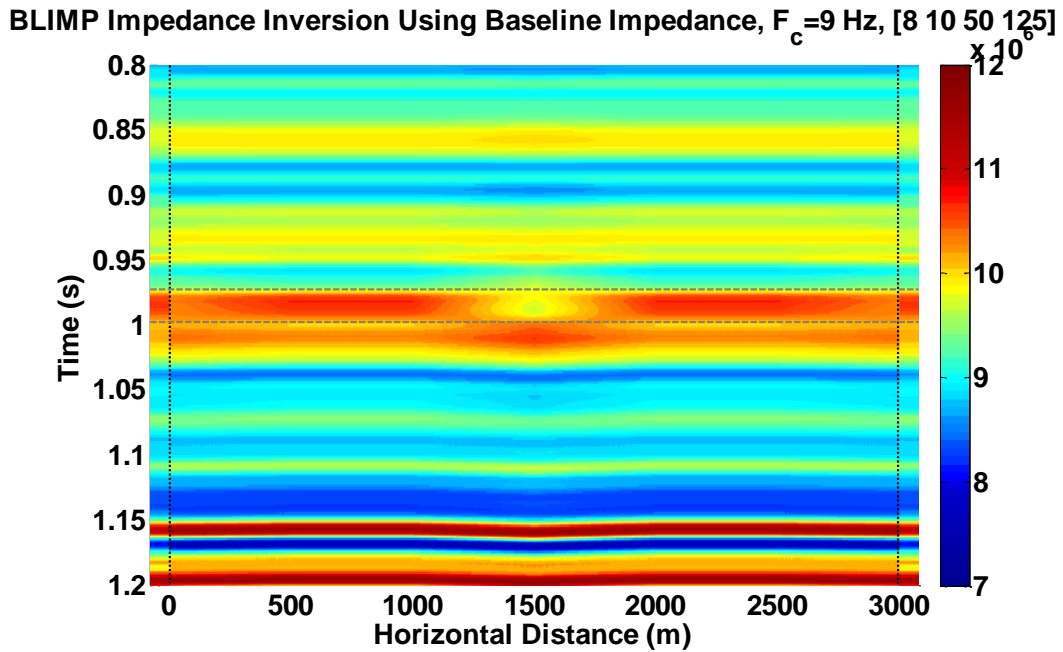


Figure 4.17: BLIMP inversion using the baseline impedance log and a low-frequency cut off of 9 Hz for the supercritical carbon dioxide model. The filtered baseline log is plotted at each side for reference.

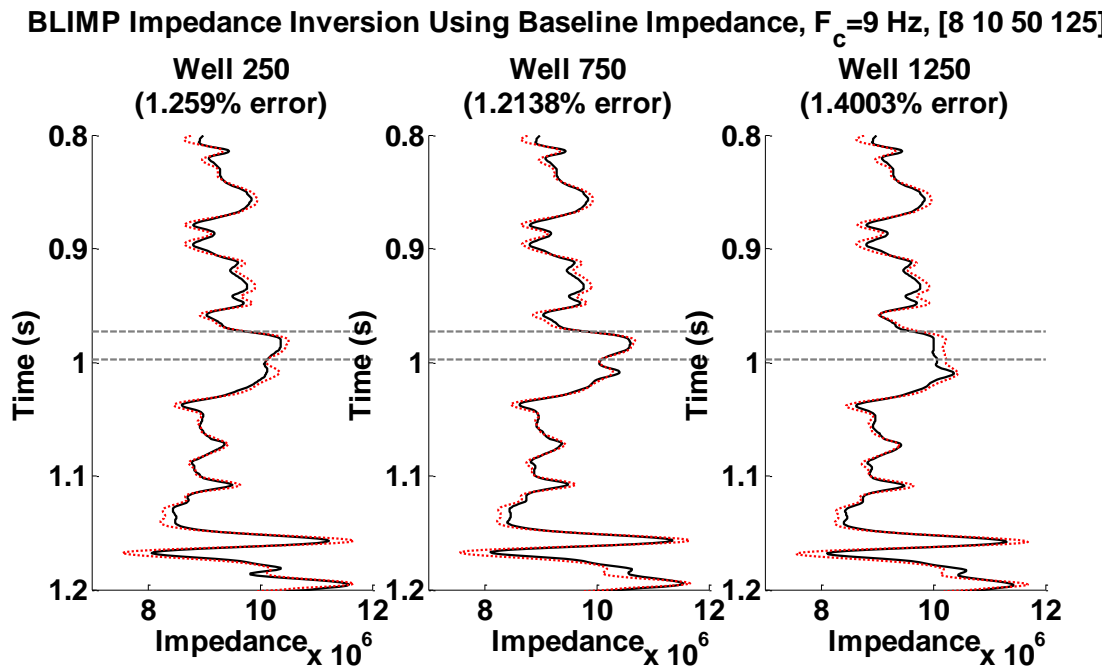


Figure 4.18: Cross validation plots for the baseline impedance log and a low-frequency cut off of 9 Hz for the supercritical carbon dioxide model. The black curve represents the true impedance and the red curve represents the inversion. Error is calculated between 0.8 and 1.2 seconds.

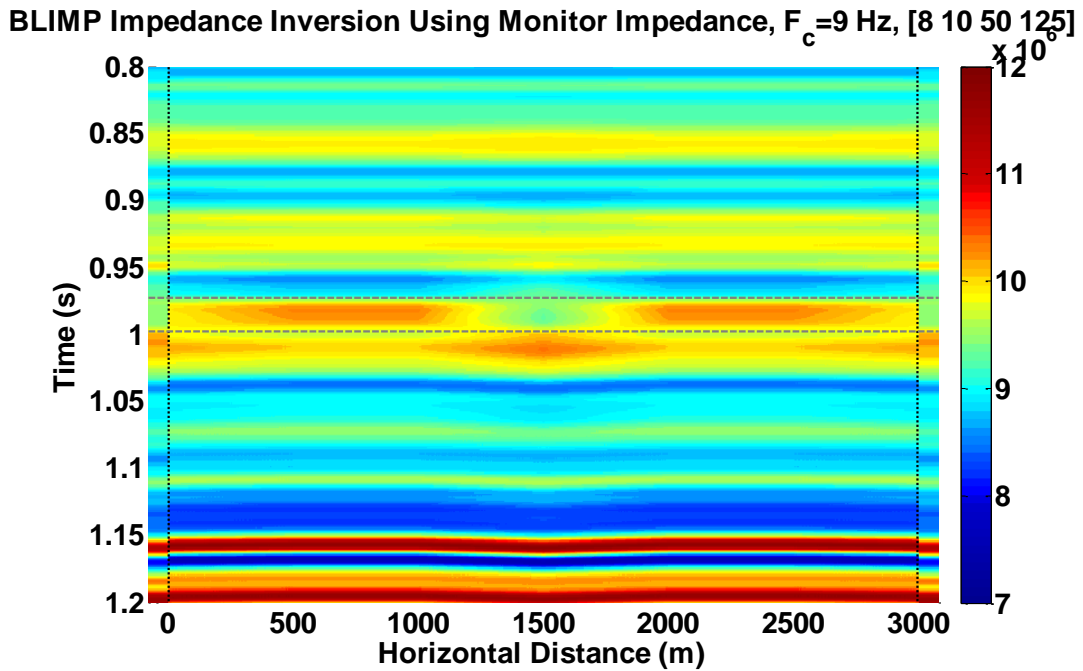


Figure 4.19: BLIMP inversion using the monitor impedance log and a low-frequency cut off of 9 Hz for the supercritical carbon dioxide model. The filtered monitor log is plotted at each side for reference.

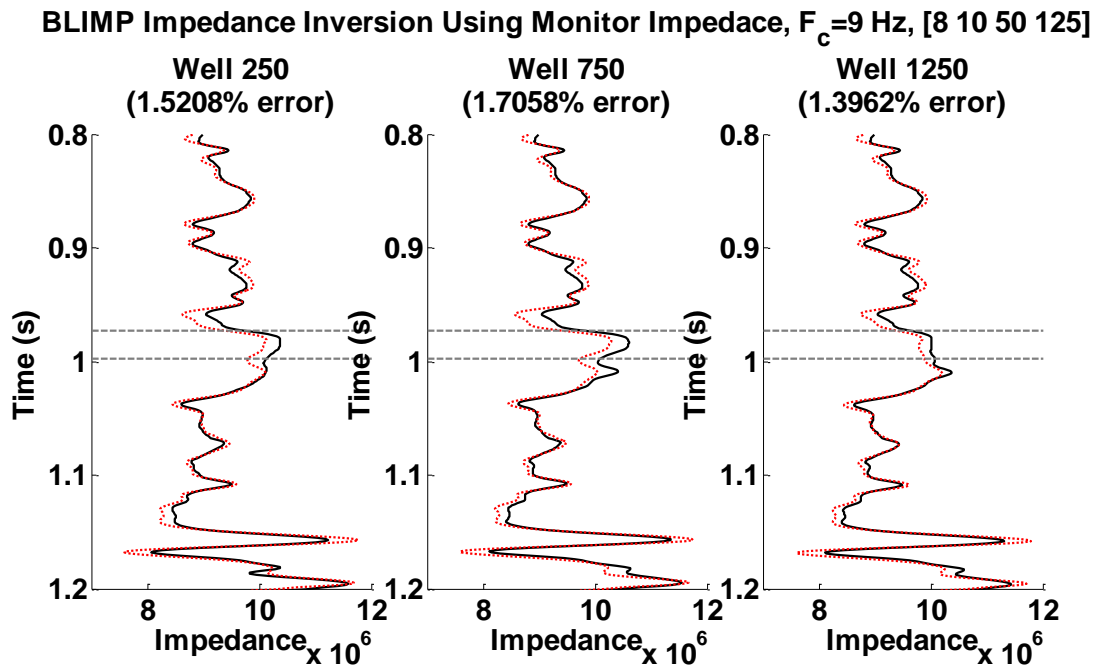


Figure 4.20: Cross validation plots for the monitor impedance log and a low-frequency cut off of 9 Hz for the supercritical carbon dioxide model. The black curve represents the true impedance and the red curve represents the inversion. Error is calculated between 0.8 and 1.2 seconds.

4.3.3 Gaseous Carbon Dioxide Model

The gaseous carbon dioxide model was created to amplify the differences between using the baseline log and the monitor log for impedance inversions. The true impedance of the gaseous model is shown in Figure 4.21. This section shows that there are significant pull-down effects caused by the gaseous plume. The impedance of the plume is also lower so it is easier to detect the top.

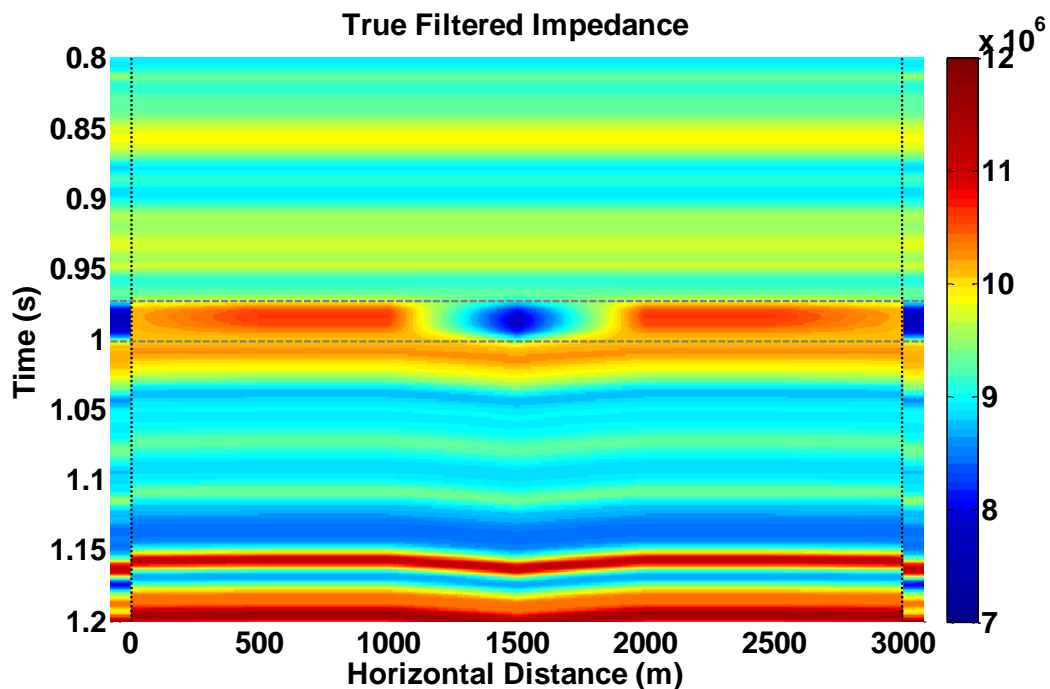


Figure 4.21: True filtered impedance for the gaseous carbon dioxide model. The filtered impedance at 1500 meters is plotted on each side of the impedance section for reference. The artifacts that are part of this section only appear in time and are pull down effects of the carbon dioxide plume.

BLIMP inversions were computed using the baseline impedance log (Figure 4.22) and using the monitor log (Figure 4.24), applying a low frequency cut off of 9 Hz. The baseline impedance log overestimates the impedance of the carbon dioxide plume but accurately estimates rest of the reservoir. The cross validation plots (Figure 4.23) show

these effects in greater detail with errors of 0.7%, 0.3% and 4.3% in the Cardium formation for wells 250, 750 and 1250, respectively. The monitor inversion greatly underestimates the impedance at the carbon dioxide plume as well as under estimating the rest of the reservoir and the lithology surrounding it. Figure 4.25 shows the cross validation plot supporting the severity of the impedance underestimation. Wells 250 and 750 had errors of 9.6% where as well 1250 only had an error of 7.1%. Underestimating impedance in a carbon dioxide monitoring program causes the plume to look like it is expanding faster than it actually is. The suitability of the reservoir can come into question, when really the problem is with the inversion.

In this case the baseline inversion had little effect but if the impedance value was abnormally high, high impedance smearing would have been seen similar to the low impedance smearing caused by the monitor log. In this case using the baseline impedance log to compute the inversion would be safer as it only slightly over estimates the plume. Caution needs to be used when overestimating the impedance as it can make the migration of the carbon dioxide plume harder to detect.

Expanding the signal band of the seismic data to record low-frequencies will cause the inversion to rely less on the well data and more on the seismic reflections. This will cause the inversion to show the fluid changes more accurately in the reservoir. The next section will discuss the gaseous carbon dioxide model using low-frequency data.

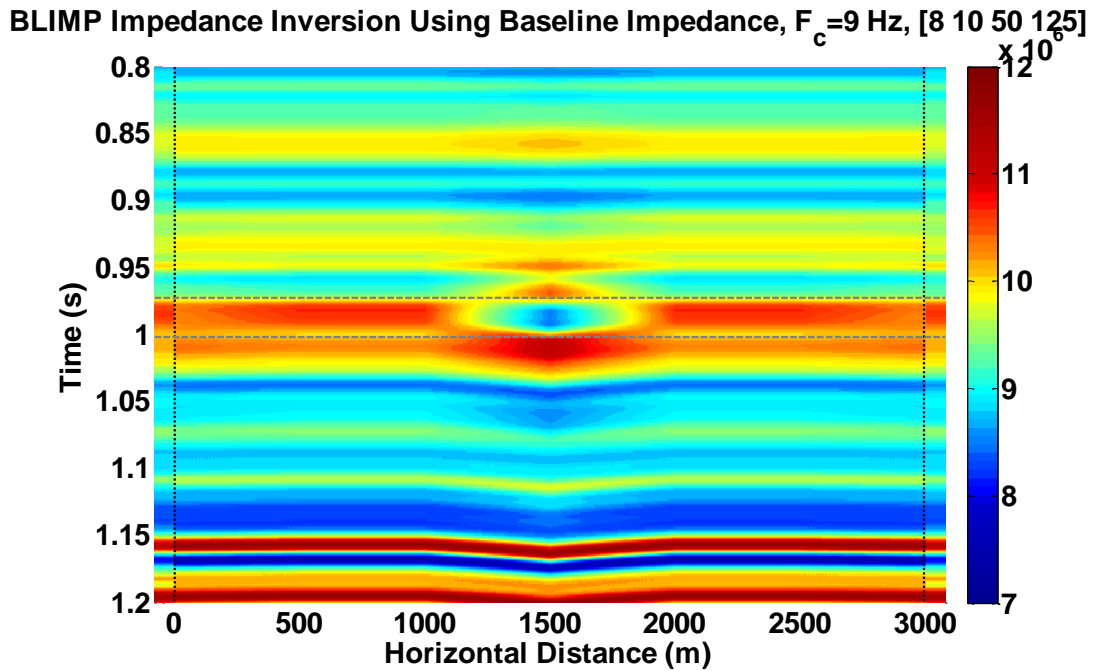


Figure 4.22: BLIMP inversion using the baseline impedance log and a low-frequency cut off of 9 Hz for the gaseous carbon dioxide model. The filtered baseline log is plotted at each side for reference.

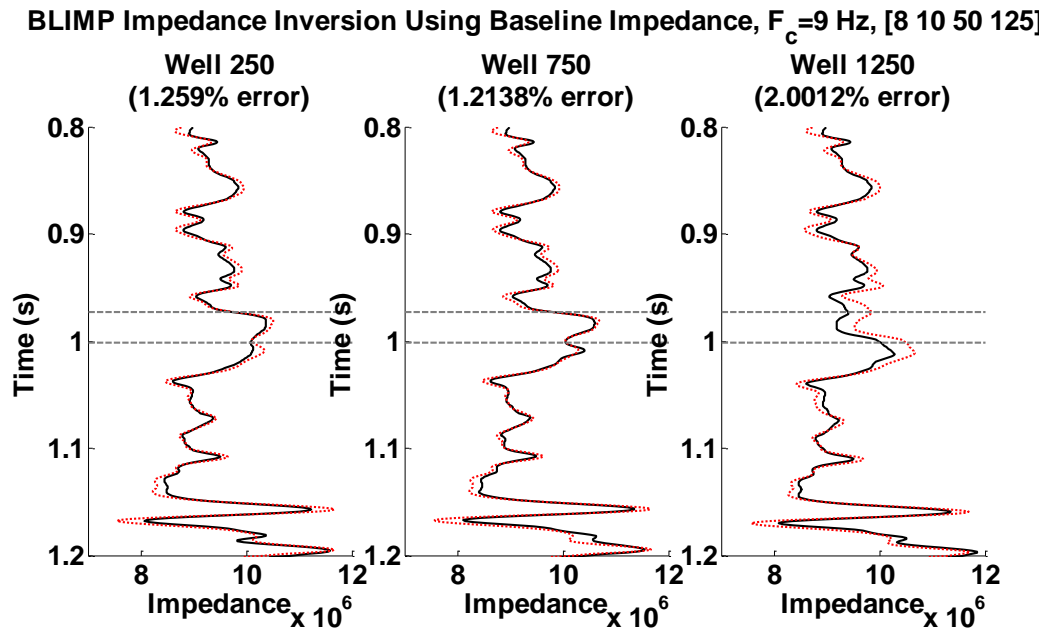


Figure 4.23: Cross validation plots for the baseline impedance log and a low-frequency cut off of 9 Hz for the gaseous carbon dioxide model. The black curve represents the true impedance and the red curve represents the inversion. Error is calculated between 0.8 and 1.2 seconds.

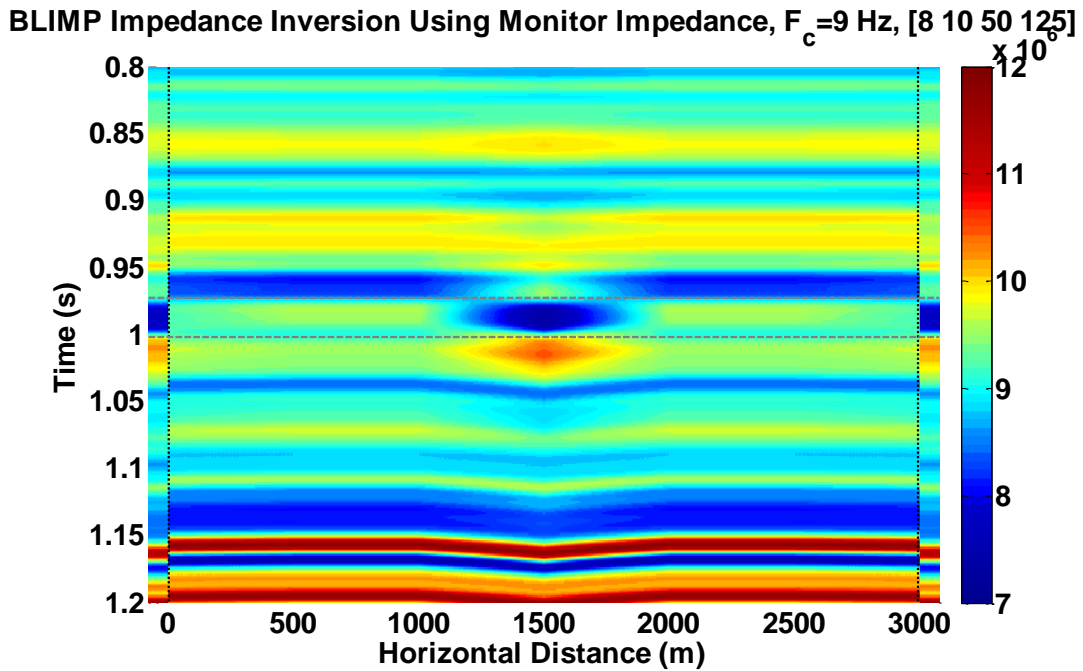


Figure 4.24: BLIMP inversion using the monitor impedance log and a low-frequency cut off of 9 Hz for the gaseous carbon dioxide model. The filtered monitor log is plotted at each side for reference.

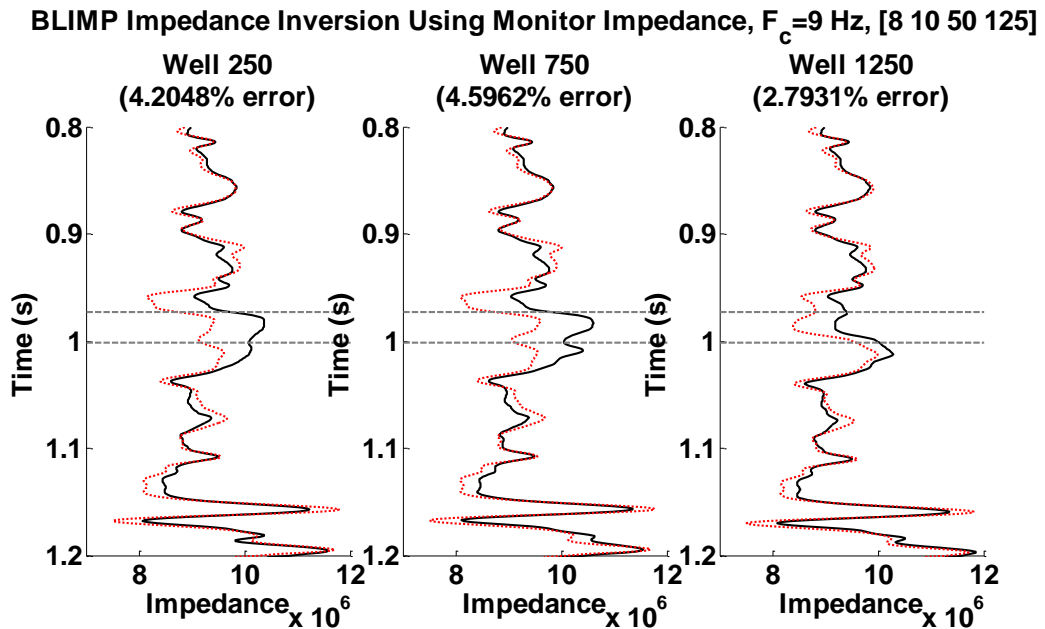


Figure 4.25: Cross validation plots for the monitor impedance log and a low-frequency cut off of 9 Hz for the gaseous carbon dioxide model. The black curve represents the true impedance and the red curve represents the inversion. Error is calculated between 0.8 and 1.2 seconds.

4.4 Inversions Using Low-Frequency Data

The gaseous carbon dioxide model was prepared by calculating normal incidence seismograms, using a zero phase [1.5 2 50 125] Hz Ormsby wavelet(Figure 4.26). This data contains reliable frequencies down to at least 2 Hz so a 2 Hz low-frequency cut off will be used for all inversions. The true impedance model can be seen in Figure 4.27, showing the carbon dioxide plume in the center of the section. The true impedance has been filtered with a 50 Hz high cut filter to match the frequency bandwidth of the seismic data.

BLIMP impedance inversions were computed using both the baseline impedance log and the monitor impedance log. The baseline log inversion(Figure 4.28) is very similar to the true impedance but overestimates in the Cardium reservoir. The cross validation plot shows this slight overestimation with errors of about 2% for each well for the Cardium formation. The monitor log inversion is also very similar to the true filtered impedance but underestimates the formation below the Cardium. The cross validation plot shows a very good match at well 250 with 0.5% error and 750 with 0.4% error but slightly underestimates at well 1250 with 1 % error for the Cardium formation.

By recording the low-frequency information the inversion relies more on the seismic and less on the well input. This creates a more stable inversion because using both the baseline and monitor logs can be used to produce reliable inversions. Since the monitor log is expensive and difficult to obtain, it is recommended that the baseline log be used when combined with low-frequency seismic.

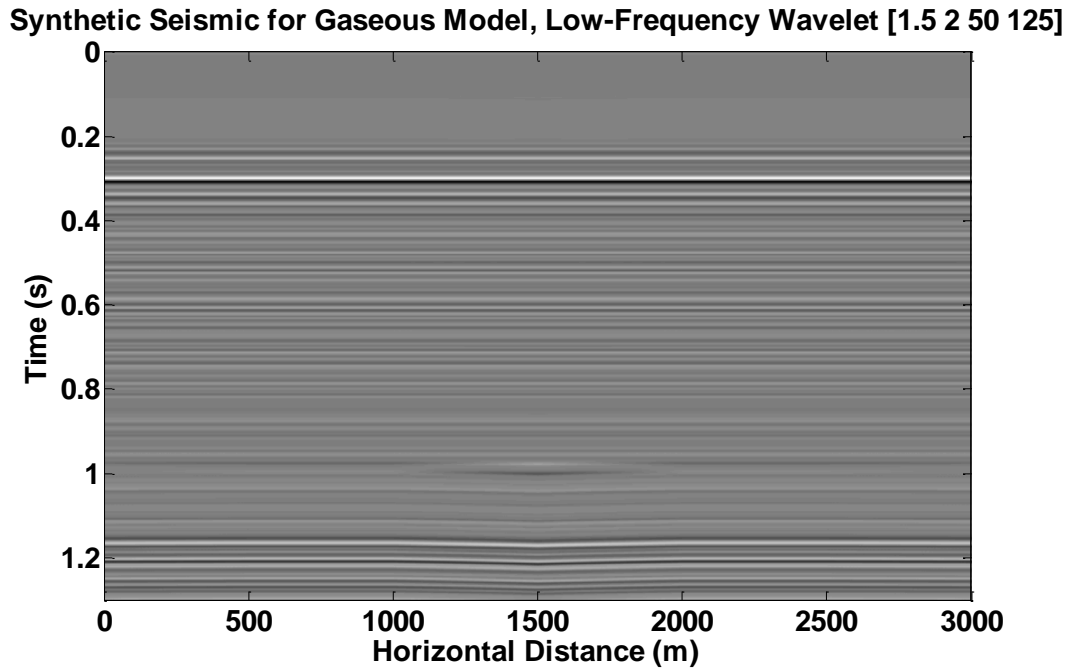


Figure 4.26: Seismic data for the low-frequency gaseous carbon dioxide model. The wavelet used was a zero phase [1.5 2 50 125] Hz Ormsby wavelet.

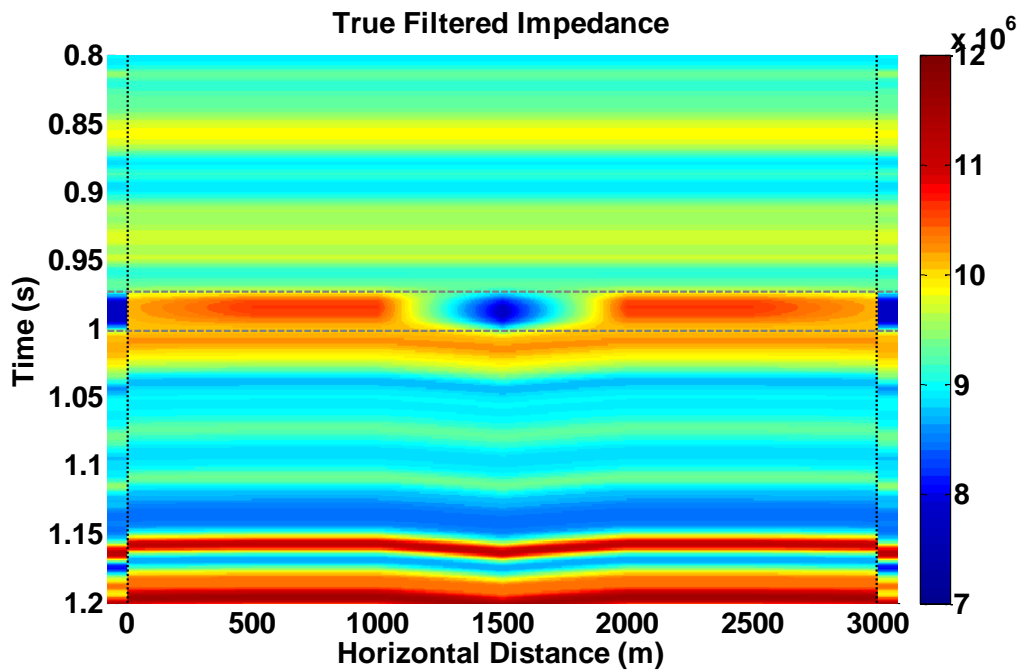


Figure 4.27: True filtered impedance for the gaseous carbon dioxide model. The filtered impedance at 1500 meters is plotted on each side of the impedance section for reference. The artifacts that are part of this section only appear in time and are pull down effects of the carbon dioxide plume.

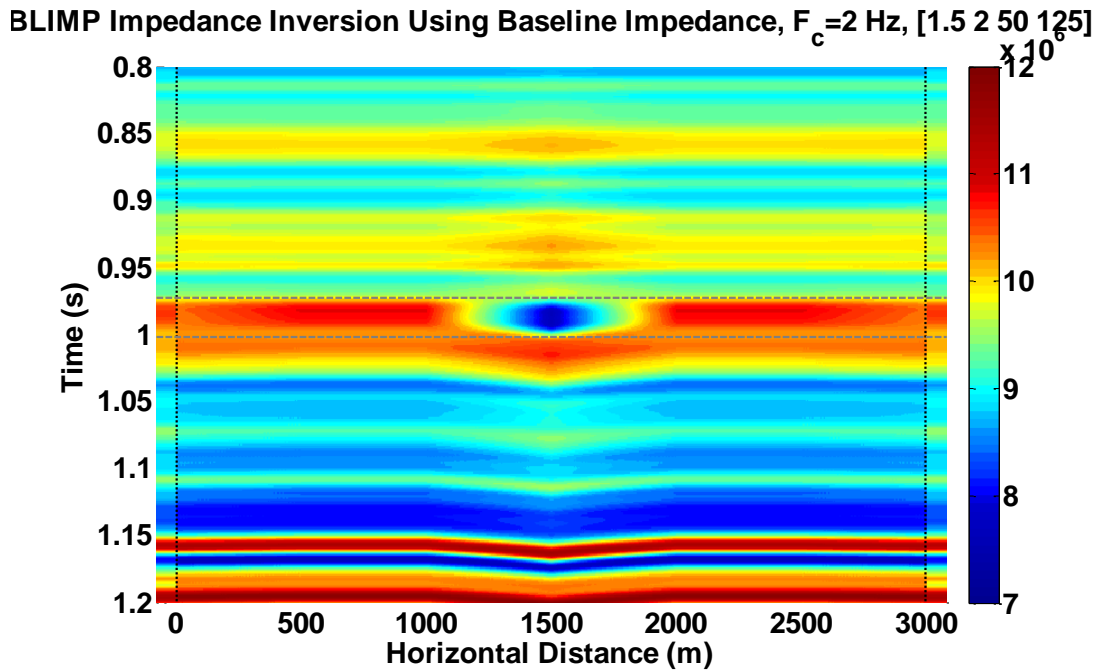


Figure 4.28: BLIMP inversion using the baseline impedance log and a low-frequency cut off of 2 Hz for the low-frequency gaseous carbon dioxide model. The filtered baseline log is plotted at each side for reference.

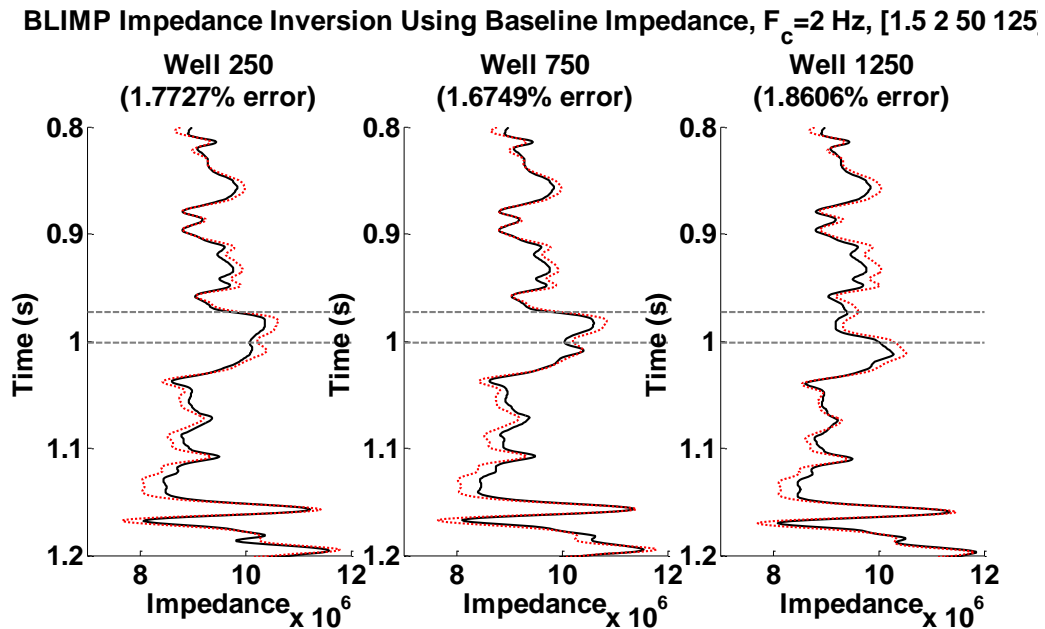


Figure 4.29: Cross validation plots for the baseline impedance log and a low-frequency cut off of 2 Hz for the low-frequency gaseous carbon dioxide model. The black curve represents the true impedance and the red curve represents the inversion. Error is calculated between 0.8 and 1.2 seconds.

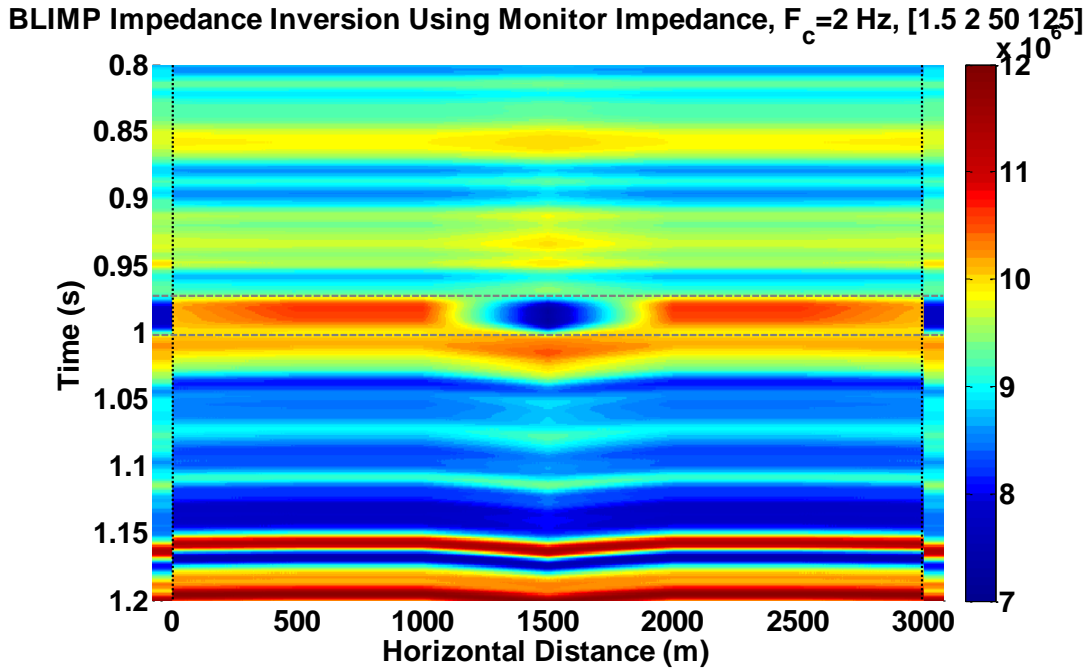


Figure 4.30: BLIMP inversion using the monitor impedance log and a low-frequency cut off of 2 Hz for the low-frequency gaseous carbon dioxide model. The filtered monitor log is plotted at each side for reference.

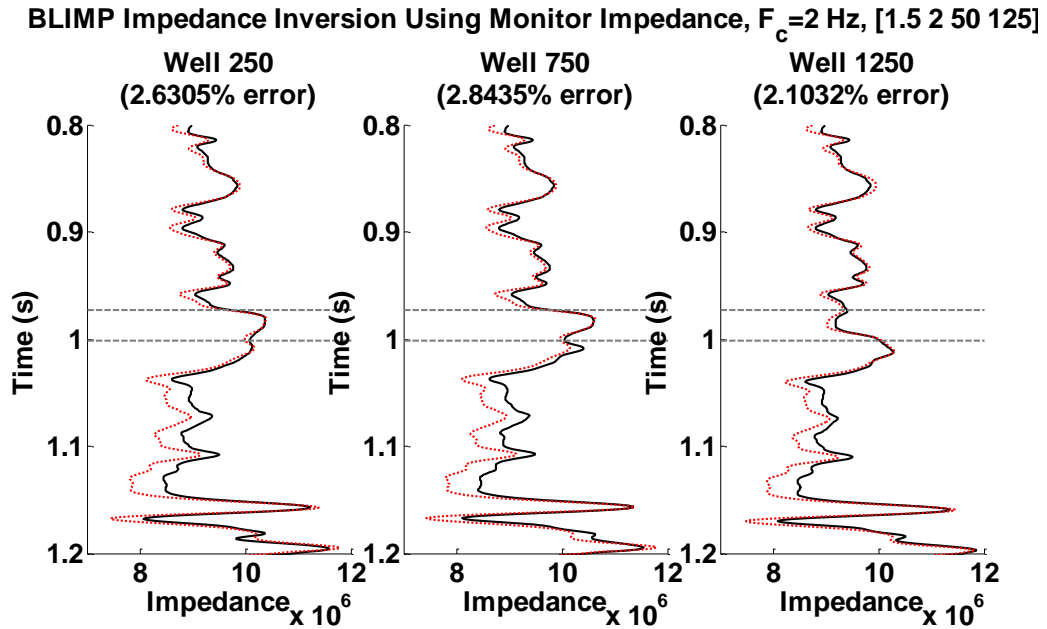


Figure 4.31: Cross validation plots for the baseline impedance log and a low-frequency cut off of 2 Hz for the low-frequency gaseous carbon dioxide model. The black curve represents the true impedance and the red curve represents the inversion. Error is calculated between 0.8 and 1.2 seconds.

4.5 Model of A Thin Cardium Reservoir

The Cardium formation contains three main sand bodies that are separated from each other by shale beds. The upper and mid sand layer had fluid connectivity whereas the lower sand was not connected (Alshuhail, 2011). These sands occur between 1605 meters and 1614 meters, making the reservoir 9 meters thick. Imaging this thin interval would require data with substantial power at the high frequencies. Since high frequencies in seismic data are attenuated, processing methods such as deconvolution are needed to increase the amplitudes of the high frequencies. Even with this effort it may not be possible to recover enough high frequencies to image this reservoir completely.

A model using the 9 meter thick reservoir was prepared in a similar fashion as the larger reservoir for supercritical carbon dioxide. Figure 4.32 shows the synthetic seismic data using an Ormsby [3 5 100 125] zero phase wavelet, for the supercritical model. The carbon dioxide plume is very difficult to see. A close up of the seismic, Figure 4.33, shows the plume. This could possibly be mistaken for a channel or another interpretation. An inversion can illuminate and add context to the interpretation, Figure 4.34. Since most of the signal is contained in the high frequencies, a thin layer is not as sensitive to the choice of well or the low-frequency cut-off used in the inversion. For the Violet Grove EOR Project the carbon dioxide plume was not detectable (Alshuhail, 2011). For this thin bed model the plume is barely detectable in an ideal situation with no noise or any processing issues. In the EOR Project the data was hindered by noise, less high frequencies and statics, which could make the signal of the plume nearly impossible to detect.

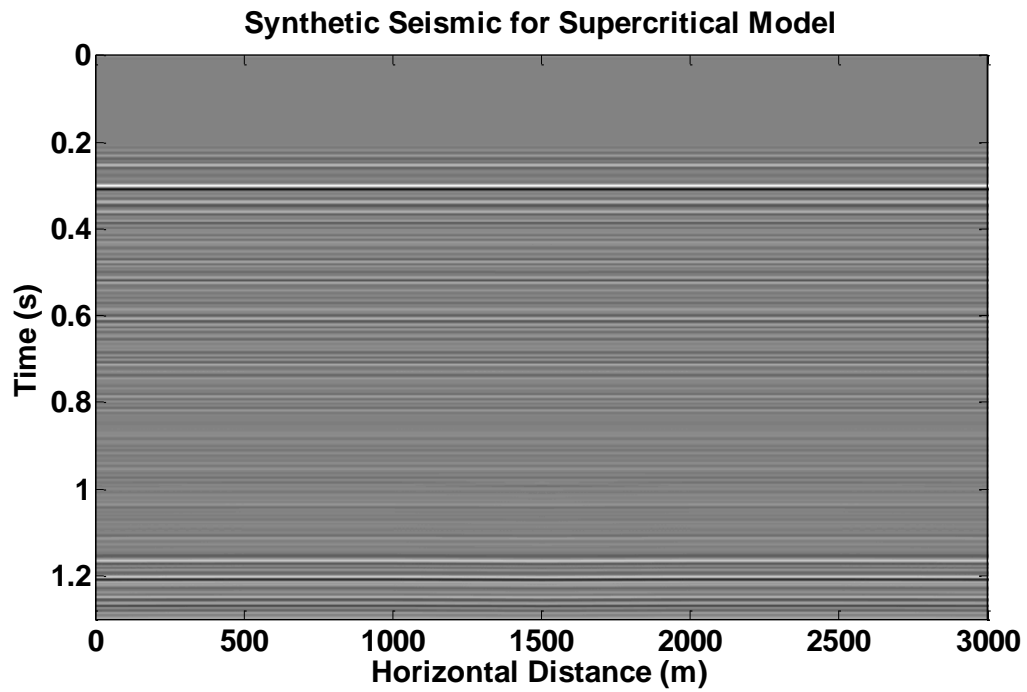


Figure 4.32: Seismic data for the thin Cardium reservoir. The wavelet used was a [3 5 100 125] Hz zero phase Ormsby wavelet. The Cardium reservoir is located at 1 second.

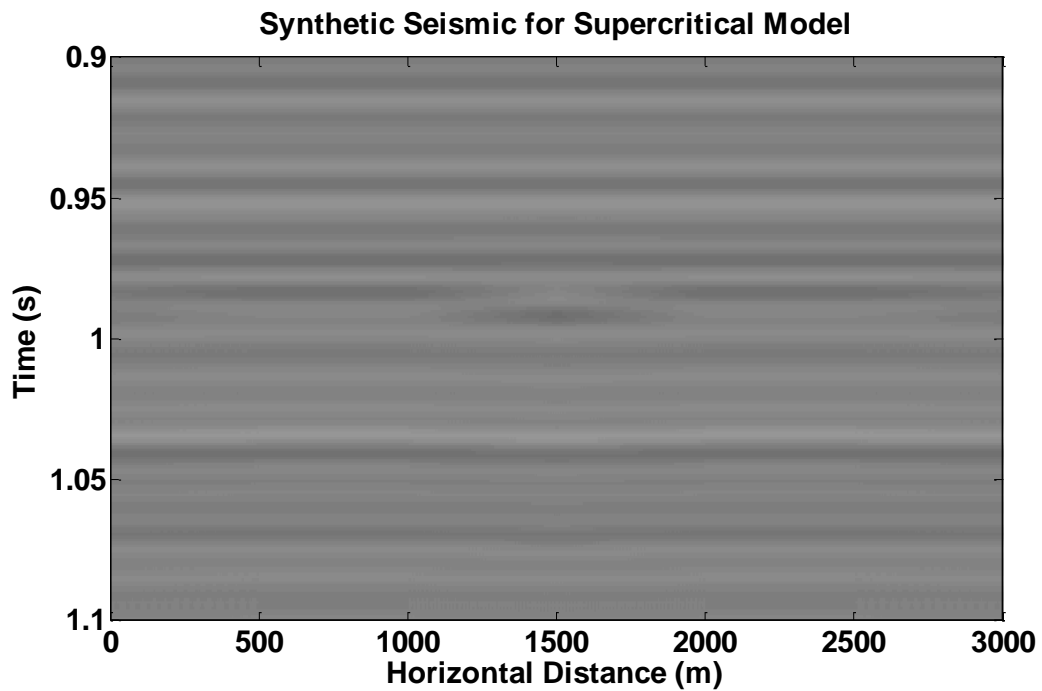


Figure 4.33: A close up of the seismic data showing the signature of the supercritical carbon dioxide plume.

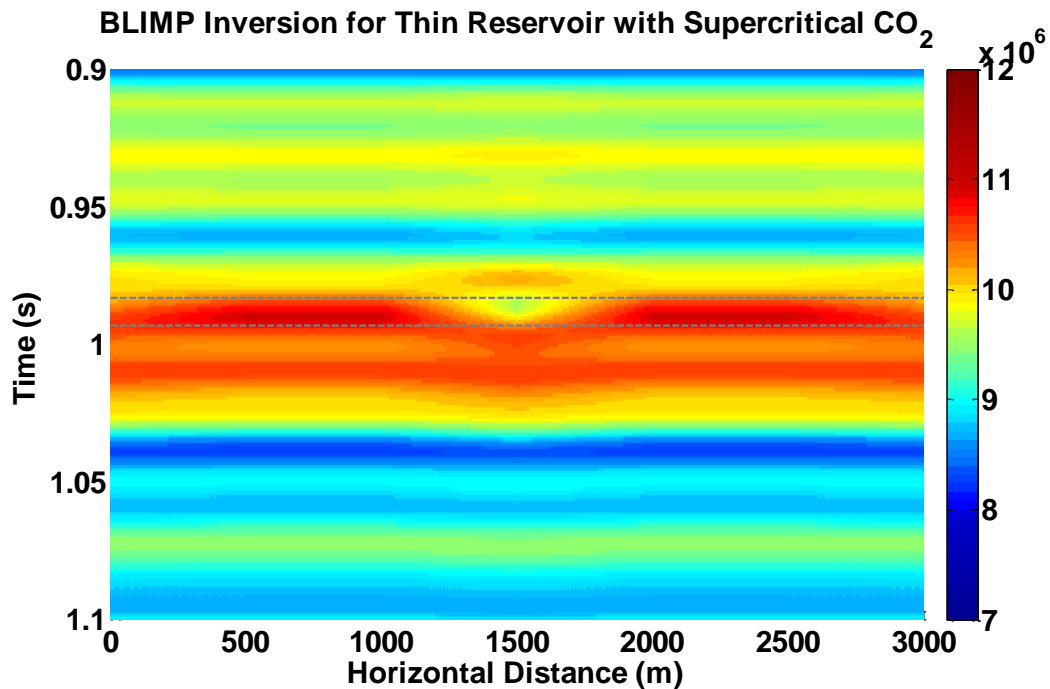


Figure 4.34: BLIMP inversion using the baseline impedance log and a low-frequency cut off of 4 Hz for the thin Cardium reservoir supercritical carbon dioxide model.

This shows that supercritical carbon dioxide in a small reservoir may be difficult to detect with normal seismic methods. Attempts to increase the amount of high frequencies and increase the temporal sample rate will help in imaging carbon dioxide plumes

4.6 Summary

- Gassmann fluid substitution can be used to model carbon sequestration reservoirs but care should be taken as carbon dioxide can react with formation rocks and fluids causing changes in lithology that will violate the assumptions of Gassmann.

- Fluid properties of the formation can be calculated using Batzle and Wang equations. When calculating the fluid properties of carbon dioxide care should be taken when the temperature and pressure of the formation are close to the critical temperature and pressure of carbon dioxide.
- The choice of using a baseline log, that represents the original fluids in a formation, or a monitor log, that represents the impedance changes after a fluid has been injected into the formation, can play a significant role in acoustic impedance inversion. If the monitor log has a strong low impedance response it will cause a lower impedance than expected. If the baseline log has a strong high impedance response it will cause higher impedance than expected.
- Recording low-frequencies is important when acquiring time-lapse surveys as the inversion becomes more dependent on the data and less dependent on the well log. This allows the baseline log to be used even though it does not represent the updated fluids in the reservoir.
- When reservoirs are thin effort needs to be made to record and recover as much high frequency information as possible. Thin reservoirs are characterized mainly by high frequencies and without this information they cannot be detected. This was observed during the Violet Grove EOR Project.

Chapter Five: **Conclusions**

- Processing can invalidate the amplitudes of seismic reflection events. Using time variant balancing with a reference well log is a valid way of restoring the amplitudes.
- Reasonable overburdens need to be applied to well logs to assist in the well tying process. It is preferable to use a linear gradient so that artificial reflection coefficients are not created.
- Reasonable underburdens should be applied to well logs to lengthen the logs to match the seismic length. For convenience this can be done in the time domain.
- Anomalous log values need to be removed by either clipping or smoothing operations.
- Calibration of the time-depth relationship is essential for producing accurate impedance inversions. When VSP or check-shot data is not available using reflection event matching or Hilbert envelope lobe matching programs can be used.
- Hilbert envelope lobe matching produces better calibration than reflection event matching as it is insensitive to constant phase errors.
- Polynomials can be used to fit the amplitude spectra of the seismic reflectivity data when estimating a wavelet. Using a fourth order polynomial fit to the log of the amplitude spectra produces a very good result.
- Deconvolution causes time variant phase rotation errors. This can be corrected by using time-variant phase rotations. It is preferred that the same phase rotation is

used on the entire reflectivity section, so phase angles calculated using a least squares method for all wells is preferred.

- The BLIMP algorithm is similar to the Lindseth method (1979) except it removes the linear trend and then applies a scalar to the integrated seismic data in the frequency domain. The linear trend is then added to the inversion result.
- The BLIMP algorithm adds low frequencies in two stages by estimating and removing the linear trend from the well impedance and adding it back to the inversion, and by adding low-pass frequencies from the well impedance to the inversion.
- The low-frequency cut off used in the low pass filter applied to the well impedance is very important. Selecting a value that is too low results in the impedance inversion being unreliable. Selecting a value that is too high will cause the seismic data to be overwritten with information from the well logs, causing subtleties that were present in the seismic to be erased.
- The BLIMP algorithm can be used with low-frequency information supplied by impedance logs from wells, impedance calculated from stacking velocities or a combination of stacking impedance and well impedance.
- The BLIMP algorithm applies a scalar to the integrated seismic. If this scalar is large enough it can amplify the low frequencies of the seismic and allow the low-frequency cut off to be lower than it would be for a smaller. This only applies to seismic data that contain very low frequencies.
- The low frequency cut off is a rough indicator of the low-frequency content of the seismic data.

- In the Hussar data set the low frequency content is time variant. For the shallow section the low-frequency content is about 3 Hz where as for the deeper section the low-frequency content is between 2 and 2.5 Hz. If the amplitude of the low-frequencies is boosted the low frequency content can be pushed down to 1.5 Hz.
- Gassmann fluid substitution can be used to model carbon sequestration reservoirs but care should be taken as carbon dioxide can react with formation rocks and fluids causing changes in lithology that will violate the assumptions of Gassmann (1951).
- Fluid properties of the formation can be calculated using Batzle and Wang (1992) equations. When calculating the fluid properties of carbon dioxide care should be taken when the temperature and pressure of the formation are close to the critical temperature and pressure of carbon dioxide.
- The choice of using a baseline log, that represents the original fluids in a formation, or a monitor log, that represents the impedance changes after a fluid has been injected into the formation, can play a significant role in acoustic impedance inversion. If the monitor log has a strong low impedance response it will cause a lower impedance than expected. If the baseline log has a strong high impedance response it will cause higher impedance than expected.
- Recording low-frequencies is important when acquiring time-lapse surveys as the inversion becomes more dependent on the data and less dependent on the well log. This allows the baseline log to be used even though it does not represent the updated fluids in the reservoir.

- When reservoirs are thin effort needs to be made to record and recover as much high frequency information as possible. Thin reservoirs are characterized mainly by high frequencies and without this information they cannot be detected. This was observed during the Violet Grove EOR Project.

References

- Aki, K. and P.G. Richards (2002) Quantitative Seismology, University Science Books, Sausalito, CA.
- Alshuhail, A A., 2011, CO2 Sequestration Site Characterization and Time-lapse Monitoring Using Reflection Seismic Methods: University of Calgary PhD Thesis, Vol 1.
- Bachu, S., 2000, Sequestration of CO2 in geological media: criteria and approach for site selection in response to climate change: Energy Conversion and Management, Vol 41, pp 953-970
- Bachu, S., 2002, Sequestration of CO2 in geological media in response to climate change: road map for site selection using the transform of the geological space into the CO2 phase space: Energy Conversion and Management, Vol 43, pp 87-102
- Batzle, M., and Wang, Z., 1992, Seismic properties of pore fluids: Geophysics, Vol 57, pp 1396-1408.
- Bertram, M. B. and Margrave, G. F., 2010, Recovery of low frequency data from 10Hz geophones: CREWES Research Report, Vol. 22.
- Bracewell, R. N., 2000, The Fourier transform and its Applications: McGraw-Hill.
- Castagna, J. P., Batzle, M. L., and Kan, T. K., 1993, Rock Physics– The link between rock properties and AVO response: in Castagna, J. P. and Backus, M. M., eds., Offset-dependent reflectivity – Theory and practice of AVO anomalies, SEG, Investigations in Geophysics no. 8, pp 135-171.
- Cairns, G., Jakubowicz, H., Lonergan, L., and Muggeridge, A., 2010 Issues regarding the use of time-lapse seismic surveys to monitor CO2 sequestration. SEG Technical Program Expanded Abstracts 2010: pp. 1236-1240.

- Chen, F., 2006, Interpretation of Time=lapse Surface Seismic Data at a CO₂ Injection Site, Violet Grove, Alberta: University of Calgary MSc Thesis
- Claerbout, J., 1976, Fundamentals of Geophysical Data Processing With Applications to Petroleum Prospecting: McGraw Hill, Inc. pp 20-23
- Cooke, D. A., and Schnider, W. A., 1983, Generalized linear inversion of reflection seismic data: Geophysics, Vol 48, pp 665-679.
- de Boor, C., 1978, A Practical Guide to Splines, Springer-Verlag
- Dix, H. C., 1955, Seismic velocities from surface measurements: Geophysics, 20, 68-86
- Evans, B.J., 1997, A Handbook for Seismic Data Acquisition in Exploration, SEG, geophysical monograph series no. 7, pp 135-171.
- Ferguson, R. J. and Margrave, G. F., 1996, A simple algorithm for bandlimited impedance inversion: CREWES Research Report, Vol. 8.
- Fritsch, F. N. and R. E. Carlson, 1980, Monotone piecewise cubic interpolation, SIAM J. Numerical Analysis, Vol. 17, 238-246.
- Gardner, G.H.F., Gardner, L.W., and Gregory, A.R., 1974, Formation velocity and density – the diagnostic basics for stratigraphic traps: Geophysics, 39,770-780.
- Gassmann, F., 1951, Über die Elastizität poroser Medien: Veierteljahrss-chrift der Naturforschenden Gesellschaft in Zürich, Vol. 96, pp 1–23.
- Henley, D. C. 2003, Coherent noise attenuation in the radial trace domain, Geophysics, 68. No. 4, pp1408-1416.
- Hall, K.W., G. F. Margrave and M. B. Bertram, 2009, Comparison of low-frequency data from co-located receivers using frequency dependent least-squares-subtraction scalars: CREWES Research Report, Vol. 21.

- Hall, K.W. and Margrave, G. F., 2011, Earthquake on the Hussar low-frequency experiment: CREWES Research Report, Vol. 23.
- Isaac, J. H., Margrave, G. F., Deviat, M., and Nagarajappa, P., 2012, Processing and analysis of Hussar data for low frequency content: CREWES Research Report Vol. 24.
- Kumar, D., 2006. A tutorial on Gassmann fluid substitution: formulation, algorithm and Matlab code: Geohorizons, pp 4-12.
- Lailly, P., 1983, The seismic inverse problem as a sequence of before stack migrations: Conference on Inverse Scattering, Theory and Application, Society of Industrial and Applied Mathematics, Expanded Abstracts, 206-220.
- Latimer, R. B., Davidson, R., and van Riel, P., 2000, An interpreter's guide to understanding and working with seismic-derived acoustic impedance data: The Leading Edge, Vol. 19, pp 242-256.
- Lavergne, M., 1975, Pseudo diagraphies de vitesse en offshore profond: Geophysical Prospecting, Vol 23, pp 695-711.
- Lavergne, M. and Willm, C., 1977, Inversion of seismograms and pseudo velocity logs: Geophysical Prospecting, Vol 25, pp 231-250.
- Lindseth, R. O., 1972, Approximation of acoustic logs from seismic traces: Journal of Canadian Well Logging Society, Vol.5, pp 13-26.
- Lindseth, R. O., 1979, Synthetic sonic logs – a process for stratigraphic interpretation: Geophysics, Vol. 44, No. 1.
- Lloyd, H. J. E, Lindseth, R.O., and Margrave, G. F., 2012, Investigating methods to transform acoustic impedance inversions into depth, CREWES Research Report, Vol. 24.

- Lowrie, W., 1997, Fundamentals of Geophysics, Cambridge University Press. pp 83-164.
- Margrave, G. F., 2010a, Methods of Seismic Data Processing – Geophysics 517/557
Course Notes: The Department of Geoscience, University of Calgary
- Margrave, G. F., Ferguson, R. J., and Hogan, C. M. , 2010b, Full waveform inversion with wave equation migration and well control: CREWES Research Report Vol. 22.
- Margrave, G. F., Mewhort, L., Phillips, T., Hall, M., Bertram, M. B., Lawton, D. C., Innanen, K. A. H., Hall, K. W. and Bertram, K. L., 2012, The Hussar low-frequency experiment: CSEG Recorder, Sept., pp 25-39..
- O’Doherty, R.F., and Anstey, N.A., 1971, Reflections on Amplitudes, Geophysical Prospecting, 19, 430-458.
- Oldenburg, D. W., Scheuer, T., and Levy, S., 1983, Recovery of the acoustic impedance from reflection seismograms: Geophysics, Vol. 48, No. 10.
- Oldenburg, D. W., Levy, S., and Stinson K., 1984, Root-mean-square velocities and recovery of the acoustic impedance: Vol. 49, No. 10. pp 1653-1663.
- Pendrel, J., 2006, Seismic Inversion – Still the best tool for reservoir characterization: CSEG Recorder,
- Rider, Malcolm.,2008, The Geological Interpretation of Well Logs- Second Edition: Rider-French Consulting Ltd. pp 78.
- Sheriff, R.E., and Geldart, L.P., 1995, Exploration Seismology: Cambridge University Press. pp 107-191
- Smith T., Carl H. Sondergeld, and Chandra S. Rai, 2003, Gassmann fluid substitutions: A tutorial: Geophysics, Vol. 68, pp. 430-440.

- Stewart, R.R., Huddleston, P.D., and Kan, T.K., 1984, Seismic versus sonic velocities: A vertical seismic profiling study: *Geophysics* 49, 1153-1168.
- Tarantola, A., 1984, Inversion of seismic reflection data in the acoustic approximation: *Geophysics*, 49, 1259-1256.
- Waters, K.H., 1978, *Reflection Seismology: A Tool for Energy Resource Exploration*, John Wiley and Sons, Inc.
- Wei, Z., and T. Phillips, 2011, Analysis of vibrator performance at low frequencies: *First Break*, 29, 55-61.
- White, R.E., 1980, Partial coherence matching of synthetic seismograms with seismic traces: *Geophysical Prospecting*, Vol 28. pp 333-358.
- White, R.E., 1997, The accuracy of well ties : practical procedures and examples: Expanded Abstract RC1.5, 67th SEG Meeting, Dallas.
- White, R.E., Thomas, R.T., Castoro, A., 1998, Stretch and squeeze – just keeping up appearances? EAGE 60th Conference and Technical Exhibition, Leipzig, Extended Abstract P138.
- White, R., and Simm, R., 2003, Tutorial: Good practice in well ties: *First Break*. Vol 21. pp75-83.
- Yilmaz, O., 2001, Seismic Data Analysis – Processing, Inversion and Interpretation of Seismic Data. SEG, *Investigations in Geophysics* no. 10, pp 81-90.
- Xu H., 2006, Short Note Calculation of CO₂ acoustic properties using Batzle-Wang equations: *Geophysics*, Vol. 71, p. F21-F23

APPENDIX A: MATLAB WELL-TYING PROGRAMS

A.1. Introduction

Three graphical user interface programs were designed to help with well ties. All of these programs were built in MATLAB and work with other import and export tools within the CREWES toolbox. *WaveletEstimator* estimates a wavelet using the amplitude spectra of a trace. *StretchWell* modifies the sonic log to adjust for any reflection discrepancies between the seismic data and a well synthetic. *EnvelopeMatch* is a variation of *StretchWell* but instead of matching reflection coefficients, Hilbert envelope lobes are matched allowing the calibration to become independent of constant phase rotations.

A.2. WaveletEstimator

Finding a wavelet that fits the trace data can be difficult. *WaveletEstimator*, in Figure A.1 uses polynomials to fit the amplitude spectrum of a trace. The program allows the user to analyze a selected time interval. The program allows the user to switch back and forth between three different wavelet types.

The first type is Spline which fits a series of cubic polynomials (de Boor, 1978) to the spectra. The sensitivity of this method is determined by the parameter *Percentage of Points*, where the percentage of points chosen will be used to create the approximation. As this parameter increases the approximation gets closer and closer to the trace spectra and requires at least two points to provide an approximation. This method can be fit to the amplitude spectra or the amplitude spectra in decibels. A frequency range of zero to half Nyquist can also be selected to avoid any imprint of the anti-alias filter that has been applied to the data. Approximations for this method are always shown in blue.

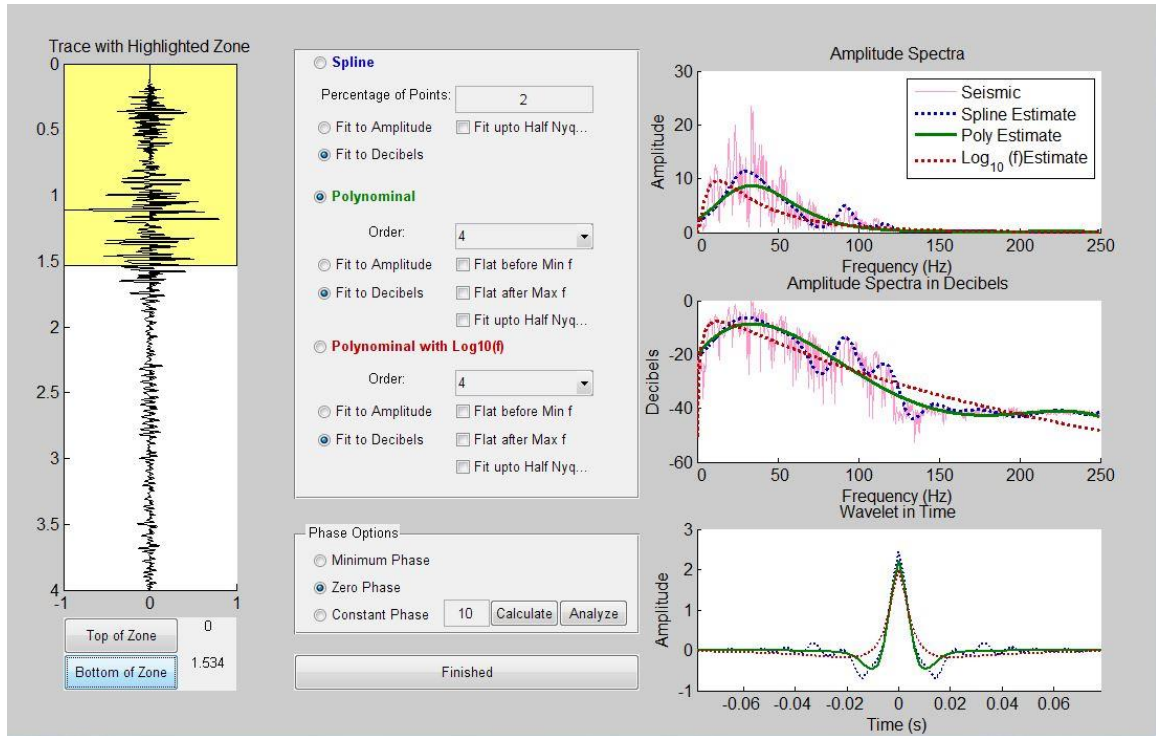


Figure A.1: The interface for *WaveletEstimator*. The zone that is used in calculating the amplitude spectra from the trace is indicated in yellow on the left-hand side. The amplitude spectra of the seismic trace and the estimated wavelet are shown in top right-hand corner, and in decibels just below. The wavelet is shown in the bottom right-hand corner in time. In the center are the wavelet options. Each wavelet type is identified by a separate color, which can be seen in each of the displays.

The second wavelet type is the polynomial. This method fits a polynomial, of the order specified by the user (orders 1-8), to the trace spectra. Again, this method offers the option of fitting the polynomial to the trace amplitude spectra or the trace amplitude spectra in decibels. The option of *Fit up to half Nyquist* allows the user to select frequencies between zero and half Nyquist instead of the default frequency range from zero to Nyquist. To prevent trace spectra from increasing exponentially at very low frequencies the *Flat before Min f* button finds the lowest positive root of the function.

From that point the value is copied for any frequencies that are less than that root. The *Flat after Max f* does a similar thing where it finds the largest positive root and copies the value for frequencies higher than that root. This provides a continuous amplitude spectrum estimate.

The third method is similar to the polynomial method however it fits the wavelet to the amplitude spectra where frequency is expressed using a logarithmic scale. This method is more reliable than the other two methods for matching the reflectivity found in well logs. This method has the same options as the polynomial method including *Flat before min*, *Flat after Max f*, *Fit up to Half Nyquist*, fitting the polynomial to the amplitude spectra, and the amplitude spectra in decibels.

This program allows the user to select a zero phase wavelet, a minimum phase wavelet and a constant phase wavelet that the user can specify. The program will automatically calculate the constant phase rotation needed by pressing the calculate button next to the constant phase option.

A.3. StretchWell

Sonic well logs in depth are used to produce time-depth curves which are then used in combination with density logs to calculate reflectivity and then convolved with a wavelet to create a synthetic seismic trace in time. The synthetic trace does not always match the seismic trace due to multiple reasons including:

- Non-ideal overburden
- Attenuation
- Source frequency differences

- Attenuation effects the velocity at which a wave travels. For a high frequency wave from a sonic source the velocity is higher than the velocity for a seismic frequency wave. The velocities are related by $v(f) = v \left(1 + \frac{1}{\pi Q} \ln \left(\frac{f}{f_o} \right) \right)$, where v is the velocity, Q is attenuation, f is the source frequency and f_o is the reference source frequency.
- Uncertain Wavelet

To compensate for these differences *StretchWell* has been developed which modifies the sonic log such that the events on the synthetic match the events on the seismic trace. Figure A.2 shows the synthetic trace in blue and the seismic in red in the right hand panel. The goal here would be to match the events at about 0.85 seconds.

If t_o is the time that the records match at the top of the interval, t_w is the event pick for the well and t_s is the event pick for the seismic, then we can write the following expressions

$$t_w = \frac{1}{10^6} \int_{z_o}^z S(z') dz' \quad \text{A.1}$$

$$t_s = \frac{1}{10^6} \int_{z_o}^z (S(z') + \Delta S(z')) dz' \quad \text{A.2}$$

where z_o corresponds to the depth associated at time t_o , z corresponds to the depth associated with time t_w , $S(z')$ is the sonic function and $\Delta S(z')$ is a perturbation of the sonic function.

If we let $\Delta S(z') = \alpha$, a constant we get the following

$$t_s = \frac{1}{10^6} \int_{z_0}^z (S(z')) dz' + \frac{1}{10^6} \int_{z_0}^z \Delta S(z') dz' \quad \text{A.3}$$

$$t_s = t_w + \frac{1}{10^6} \int_{z_0}^z \alpha dz' \quad \text{A.4}$$

$$t_s = t_w + \frac{1}{10^6} \alpha z' \Big|_{z_0}^z \quad \text{A.5}$$

$$\alpha = \frac{10^6 (t_s - t_w)}{(z - z_0)} \quad \text{A.6}$$

where t_s and t_w must be in one way time. The constant α is then added to the sonic log between the limits of z_0 and z .

The synthetic seismogram is then recalculated using the new sonic log and the events match at that time. Additional event picks are then chosen until the synthetic is matched to the seismic. Once the synthetic is adequate the program will then export the modified sonic log so that the user can create a better well tie.

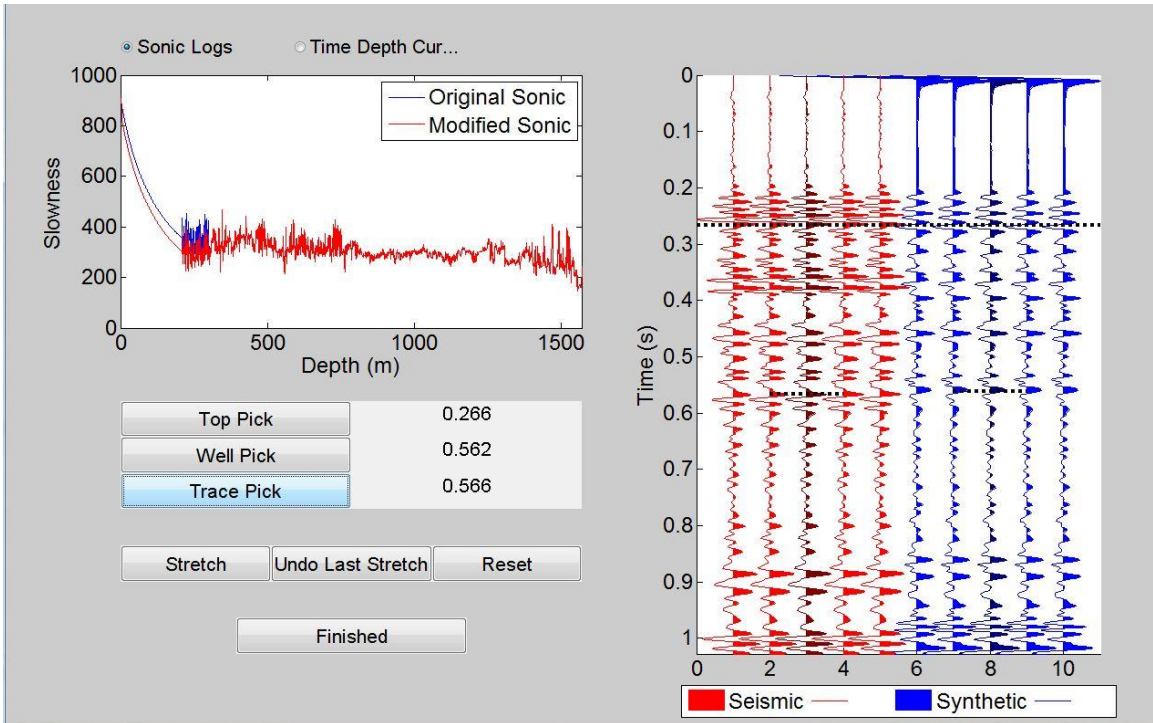


Figure A.2: The interface of *StretchWell*. The synthetic seismogram is shown in blue and the seismic data is shown in red. The two sonic curves are shown in the upper left hand corner of the display.

A.4. EnvelopeMatch

EnvelopeMatch is a modification of the *StretchWell* algorithm. The main difference is that it displays the Hilbert envelope which provides the events for matching (Figure A.3). This algorithm is not sensitive to phase changes like *StretchWell* is and can therefore provide a more unbiased well calibration.

A Hilbert envelope is formed by

$$HE = \sqrt{tr^2 + tr_q^2} \quad A.7$$

where HE is the Hilbert Envelope, tr is the trace and tr_q is the quadrature of the trace (rotated 90 degrees) (eg. Claerbout, 1976).

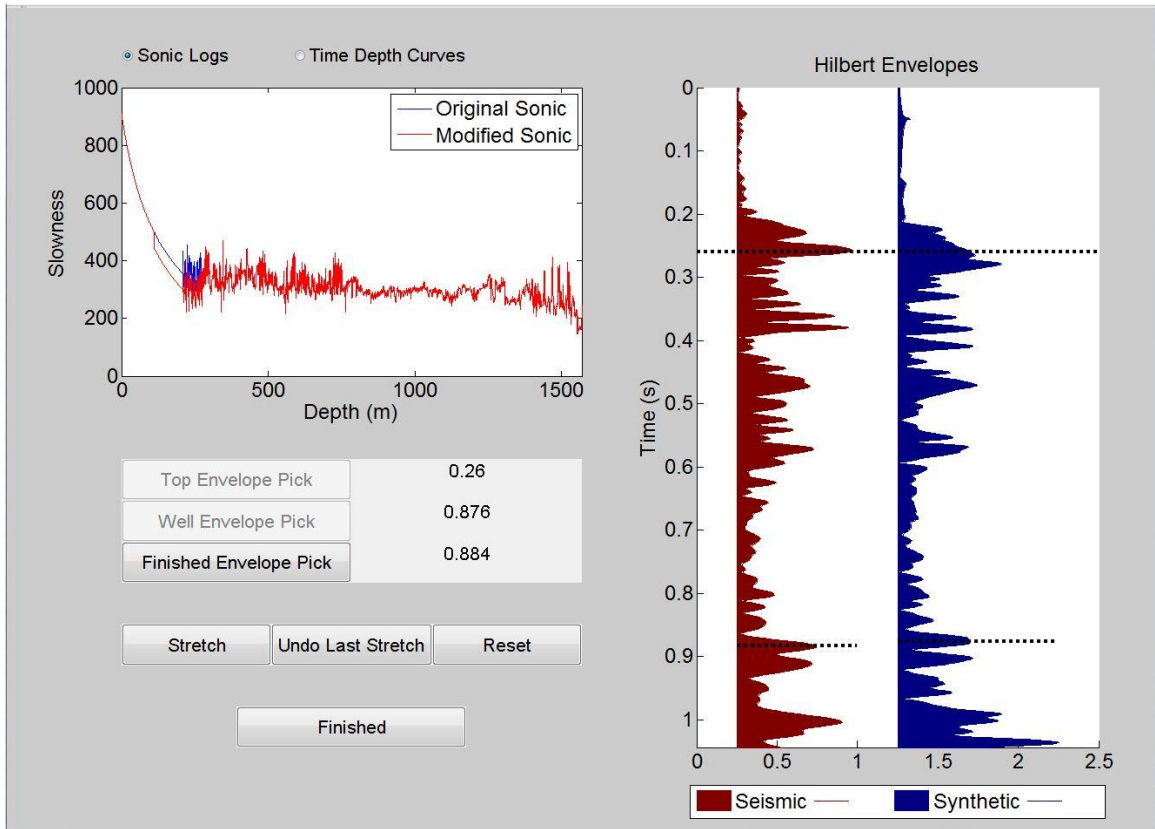


Figure A.3: The *EnvelopeMatch* interface has several features including the ability to toggle modified sonic log display and the time-depth curve change display. The seismic Hilbert envelope is displayed in red while the synthetic seismogram Hilbert transform is displayed in dark blue.